Adam Mickiewicz University

Faculty of Chemistry

M.Sc. Eng. Magdalena Bigaj-Józefowska

Application of cancer cell membrane-coated nanoparticles in advanced liver cancer treatment

Doctoral dissertation conducted at NanoBioMedical Centre
under the supervision of dr hab. Radosław Mrówczyński, prof. UAM

Supporting supervisor: dr inż. Bartosz Grześkowiak

The research was financed by The National Science Centre (NCN), Poland, under project number UMO-2018/31/D/ST8/02434.

Poznań. 2023

ACKNOWLEDGEMENTS

I have endured the painful loss of several beloved family members to cancer, including my dear grandfather. This doctoral thesis represents the realization of a longstanding dream, a testament to my unwavering commitment to contribute to the battle against this brutal disease. The work presented here is the culmination of immense dedication, often accompanied by tears and a relentless internal struggle during the toughest moments, as I persisted in pursuing my ultimate goal.

However, this achievement would not have been possible without the invaluable support and assistance of the people to whom I extend my deepest gratitude:

- My supervisors, especially dr inż. Bartosz Grześkowiak who entrusted me with his project and provided unwavering support and patience throughout the arduous four-year journey.
- Dr hab. Emerson Coy, prof. UAM, for his invaluable contribution in HR TEM-EDS measurements and for being a true friend.
- Dr Tomasz Zalewski, for his guidance in NMR and MRI measurements and his patient efforts to explain to me what it was all about.
- Dr Karol Załęski, for the SQUID measurements and his meticulousness and attention to detail.
- Dr Patrick Perrigue and Kaja Jaskot for the IFC measurements and their unbridled passion for science.
- Jakub Jagielski, for his invaluable guidance through the labyrinth of statistical analysis.
- And to all my colleagues at NBMC for their steadfast support and assistance, extending beyond the realm of research.

But most importantly – to my husband, Marcin, who was always there, cheering for me. I couldn't have done it without you (for real).

Dziękuję!

To Marcin

TABLE OF CONTENT

STRESZCZENIE

Choroby nowotworowe stanowią dla naukowców oraz ekspertów ochrony zdrowia na całym świecie ogromne wyzwanie, wymagające innowacyjnych podejść zarówno do leczenia, jak i diagnozowania. W ramach prezentowanej pracy badawczej stworzony został oparty na nanocząstkach system terapeutyczny do zastosowania w terapii nowotworowej. Zaproponowany układ bazuje na mezoporowatych, modyfikowanych żelazem nanocząstkach polidopaminy (MPDAFe), załadowanych lekiem chemioterapeutycznym - doksorubicyną (DOX). Nanocząstki MPDAFe są dodatkowo opłaszczone błoną komórkową, uzyskaną z komórek nowotworu wątroby linii HepG2, w celu uzyskania biomimetycznego systemu skutecznego dostarczania leków i obrazowania raka wątroby.

Głównym celem prowadzonych badań było opracowanie jednoetapowej syntezy nanocząstek MPDAFe oraz metody ich pokrycia błonami pochodzącymi z komórek HepG2. Tak opracowany system ma efektywnie dostarczać lek do homotypowych komórek nowotworowych, jednocześnie umożliwiając zastosowanie łączonej terapii fototermicznej i chemioterapii oraz obrazowania w rezonansie magnetycznym (MRI) w czasie rzeczywistym. Uzyskane nanocząstki zostały kompleksowo scharakteryzowane pod względem morfologii oraz właściwości fizykochemicznych. Potwierdzone zostały paramagnetyczne właściwości zsyntetyzowanego materiału, które umożliwiają zastosowanie go jako środka kontrastującego w MRI. Porowate nanocząstki MPDAFe wykazały ponadto wysoką wydajność w załadunku leku.

Potencjał terapeutyczny badanego układu został oszacowany z zastosowaniem zróżnicowanych testów cytotoksyczności. Proponowany system prezentował wysoką zdolność eliminacji komórek nowotworowych a jednocześnie znikomą toksyczność wobec zdrowych komórek. Co więcej, wykazano korzystny wpływ opłaszczania błoną komórkową na wychwyt nanoczastek przez komórki nowotworowe. Przeprowadzone zostały również pilotażowe badania *in vivo* na myszach Balb/c nude. Badania te nie potwierdziły jednoznacznie terapeutycznych właściwości proponowanego układu, jednak mogą stanowić podstawę do dalszego eksplorowania potencjału przeciwnowotworowego nanocząstek MPDAFe@DOX@Mem. Zastosowanie obrazowania MRI potwierdziło również możliwość wykorzystania nanocząstek MPDAFe do precyzyjnego diagnozowania raka wątroby i monitorowania terapii w czasie rzeczywistym.

Podsumowując, przedstawione badania otwierają nowe perspektywy w leczeniu i diagnozowaniu nowotworów, łącząc ukierunkowane dostarczanie leków, terapię fototermiczną i chemioterapię z obrazowaniem MRI. Przedstawiony system wykazuje ogromny potencjał w poprawie skuteczności leczenia i otwiera drogę do dalszych badań nad zastosowaniem rozwiązań opartych na biomimetycznych nanocząstkach polidopaminy w nowoczesnych terapiach przeciwnowotworowych.

SUMMARY

Cancer remains a formidable global health challenge, demanding innovative approaches for both treatment and diagnosis. The presented research aimed to tackle this issue by developing a multifunctional drug delivery system centered around doxorubicin (DOX)-loaded mesoporous polydopamine nanoparticles modified with iron (MPDAFe) and coated with membranes extracted from HepG2 cancer cells. The overarching goal was to create a targeted therapy tailored for liver cancer treatment while facilitating magnetic resonance imaging (MRI) for precise diagnosis and real-time monitoring.

The aims of this study are fourfold: Firstly, I aimed to engineer DOX-loaded PDAFe nanoparticles equipped with paramagnetic properties essential for their application in MRI imaging. Next, I coated these nanoparticles with HepG2 cell membranes, generating a biomimetic drug delivery system. Thirdly, I investigated the dual-therapy approach, harnessing the synergistic potential of photothermal therapy and chemotherapy to enhance cancer treatment outcomes. Finally, I evaluated the performance of these nanoparticles in liver cancer treatment scenarios, both within controlled *in vitro* environments and complex *in vivo* contexts.

The study resulted in the development of a one-pot synthesis of MPDAFe nanoparticles with confirmed porosity, paramagnetic properties, and efficient drug loading. The subsequent coating of these nanoparticles with HepG2 cell membranes creates a platform for targeted drug delivery. In the *in vitro* studies, I observed enhanced cellular uptake of these membrane-coated nanoparticles within liver cancer cells (HepG2). Various cytotoxicity assays confirmed the nanoparticles' effectiveness in inducing cancer cell death, while photothermal therapy with laser irradiation amplifies this effect. Furthermore, drug release studies conducted in different buffers, simulating biological conditions, reveal a controlled and sustained drug release profile - a critical aspect of effective chemotherapy.

My investigations extend to the pilot *in vivo* studies involving Balb/c nude mice. The obtained results were inconclusive about the potential of the multifunctional nanoparticles in liver cancer treatment. However, further investigation is required to evaluate the antitumor efficacy of MPDAFe@DOX@Mem NPs. Additionally, the MRI imaging showcased the nanoparticles' capacity for precise cancer diagnosis and real-time monitoring.

In summary, the presented research contributes significantly to the ongoing exploration of biomimetic theranostic nanoparticles in the realm of cancer treatment and imaging. The confluence of targeted drug delivery, dual therapy combining photothermal and chemotherapy and MRI-based diagnostics offers a holistic and promising approach to cancer management. These findings pave the way for potential side effects reductions, therapeutic outcomes improvements, and enhanced overall quality of life for cancer patients.

Looking forward, this work has far-reaching implications for developing more effective and personalized cancer therapies. It provides a solid foundation for future research endeavors and clinical applications in the dynamic field of cancer nanomedicine.

1

INTRODUCTION AND THEORETICAL BACKGROUND

The following chapter provides motivation and justification for undertaking the subject described in my doctoral thesis. By presenting the problem's current status, I aim to emphasize the relevance of my research. The introduction of the employed materials and solutions underlines the assumptions with which I undertook to fill the research gap in the field of cancer therapy.

Nanotechnology and nanomaterials

"There's Plenty of Room at the Bottom" – This iconic phrase coined by Dr. Richard Feynman during his groundbreaking lecture to the American Physical Society in Pasadena in December 1959 has since become a seminal moment in the history of science and technology. In his visionary speech, Dr. Feynman explored the untapped potential and boundless possibilities within the realm of miniaturization, laying the foundation for what would later blossom into the revolutionary field of nanotechnology [1]. Today, six decades later, his prescient words continue to resonate as nanotechnology has transformed from a developing concept into a dynamic discipline with an extensive array of practical applications.

Nanoscience focuses on investigating structures and molecules at the nanometer scale. It can be described as the science of matter and energy in the transitional scale between the atomic and macroscopic states [2]. Nanotechnology, conversely, pertains to the practical application of nanoscience in developing various devices and technologies [3]. Those two fields are symbiotically connected and share an unbreakable bond in the world of science and engineering. Nanotechnology stands as one of the most promising technologies in the 21st century [3]. It involves the observation, measurement, manipulation, assembly, control, and manufacturing of matter at the nanometer scale, unlocking its potential for a wide range of valuable applications. This level of fundamental control holds great promise, offering revolutionary technological advancements in various fields, including industry, biomedicine, environmental engineering, safety and security, food, water resources, energy conversion, and numerous others [3,4].

The general view on nanotechnology is that it deals with manipulating and engineering materials at the nanoscale [5]. Various definitions usually share three essential elements: Firstly, the consideration of material structure with dimensions typically ranging from single molecules

up to about 100 molecular diameters or approximately 100 nm. Secondly, nanotechnology involves the capability to measure and manipulate matter at the nanoscale, enabling new insights and technological advancements. Lastly, harnessing the unique properties and functions specific to the nanoscale, distinct from both macro and micro scales [4,6]. It is worth noting that although the theory mentions 100 nm as the upper threshold for nanomaterials, in practice, nanoscience and nanotechnology deal with structures often up to several hundred nanometers in size [2,7]. Selected aspects of nanotechnology are summarized in **Figure 1**.

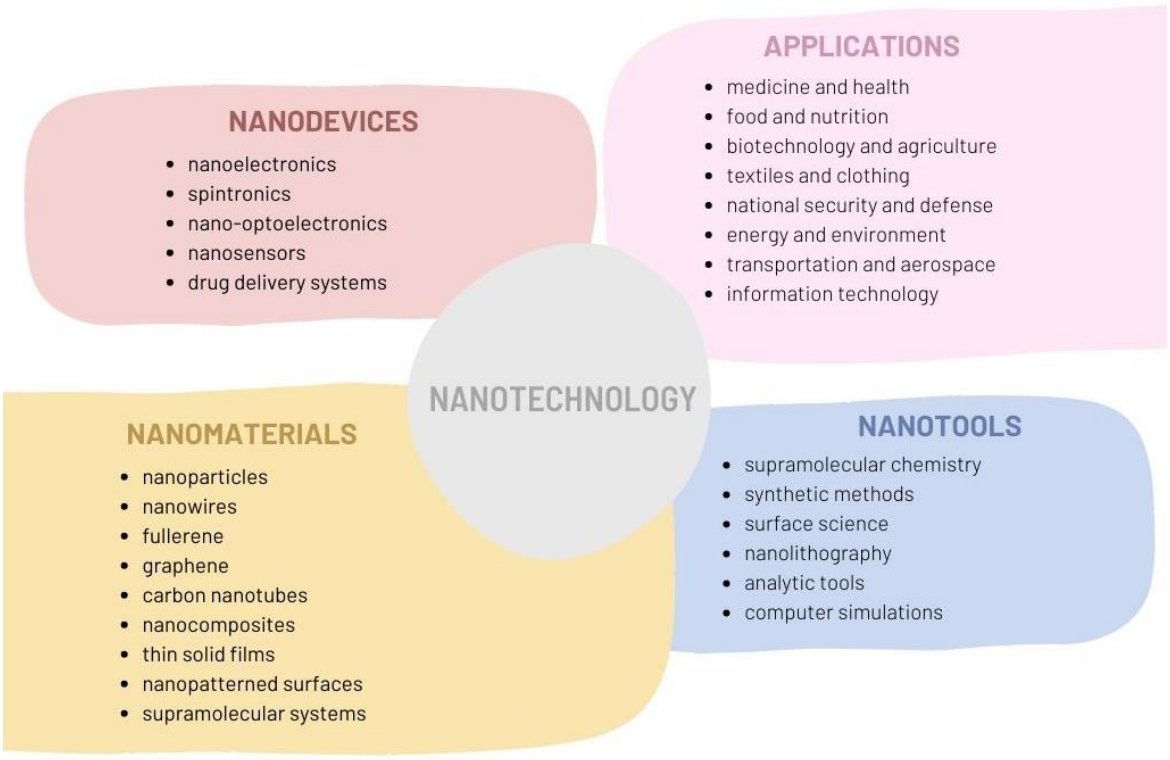

Figure 1. Representative aspects of nanotechnology. Based on [8].

Nanomaterials can be further classified based on their dimensions [5,9]:

- **Zero-dimensional (0D) nanomaterials**: nanoparticles with all three dimensions in the nanoscale range, typically less than 3 nm. Examples include quantum dots, fullerenes, and nanoparticles.
- **One-dimensional (1D) nanomaterials**: nanomaterials with two dimensions in the nanoscale range. Examples include nanowires, nanotubes, and nanorods.

- **Two-dimensional (2D) nanomaterials**: plate-like nanomaterials with one dimension in the nanoscale range. Examples include graphene, graphene oxide, and other 2D layered materials.
- **Three-dimensional (3D) nanomaterials**: equiaxed particles with all dimensions in the nanometric range but exceeding 4 nm. Examples include organic and inorganic nanoparticles.

Nano-scale phenomena are intricately linked to the remarkable surface-to-volume ratios exhibited by nanostructures. The inherent properties of nanomaterials and their subsequent manifestations, even at the macroscale, depend on both the shape and surface characteristics [2]. Numerous phenomena come into play at the nanoscale, where the small length scales impact energy band structures and the atomic arrangement, leading to alterations in the system's total energy (quantum confinement) [5]. Moreover, dimensional reduction can significantly influence chemical reactivity, as well as electrical, thermal, optical, and magnetic properties [5]. Even aspects such as mechanical strength can vary based on the size reduction of the structure [5]

Fabrication techniques are essential for creating nanomaterials with desired properties and dimensions. The concepts of the top-down and bottom-up approach to nanomaterial preparation have already been discussed by Dr. Feynman in his aforementioned visionary speech [1]. Various top-down and bottom-up techniques are employed for nanomaterial fabrication. The top-down methods involve creating smaller structural architectures by etching away bulk material, typically using lithographic processes, similar to sculpting an image from a block of stone [3]. This approach is widely applied for obtaining industrial materials such as semiconductors [8]. The bottom-up methods focus on building structures atom by atom or molecule by molecule through covalent or supramolecular interactions (i.e., π-π interactions, electrostatic, van der Waals or hydrogen bonding), analogous to constructing a house brick by brick [8]. This approach utilizes self-assembly and molecular recognition concepts and is often applied to obtain structures like nanoparticles, micelles, liposomes, or carbon nanotubes [3,8].

Comprehensive characterization of nanomaterials constitutes a fundamental aspect of nanoscience and nanotechnology, enabling the development and implementation of novel materials. Various methods are employed to evaluate their chemical, physical, and biological properties. Techniques like Fourier transform infrared (FTIR) spectroscopy, Raman scattering, liquid and solid nuclear magnetic resonance (NMR), as well as X-ray and UV-Vis

spectroscopies, allow investigation of atomic structure and chemical composition. To determine size, shape, and surface area, electron microscopy, gas adsorption/desorption isotherm with BET analysis, dynamic light scattering (DLS), and zeta potential analysis are employed [5]. Additionally, specific parameters can be evaluated using dedicated techniques like SQUID or electron plasmon resonance (EPR) for assessing magnetic properties or X-ray diffraction (XRD) to learn more about the crystallinity of the sample. Thermal stability can be evaluated using thermogravimetry (TGA) or differential scanning calorimetry (DSC).

There is a countless number of nanomaterials of various forms and shapes. Depending on the composition, nanoscale materials are usually divided into three classes: inorganic, carbon-based, and organic [10]. **Table 1** illustrates these most commonly utilized types of materials, accompanied by selected representative examples.

- **Carbon-based nanomaterials** are exclusively composed of carbon atoms and come in diverse forms, including fullerenes (e.g., C60), graphene, and carbon nanotubes [11]. They harness the unique properties of carbon, such as electrical conductivity, strength, and optical capabilities. Carbon-based nanoparticles have versatile applications ranging from drug delivery and energy storage to bioimaging and environmental sensing [10].
- **Inorganic nanomaterials** span a wide array of compositions, including metal, ceramic, and semiconductor nanoparticles. Whether monometallic, bimetallic, or polymetallic, metal nanoparticles exhibit distinctive optical, electrical, thermal, magnetic, and biological properties, making them vital in various scientific and technological domains [10]. Semiconductor nanoparticles, known for their bandgap tunability, are integral to applications like photocatalysis, optics, and electronics [10]. Ceramic nanoparticles, primarily composed of metal and metalloid oxides, carbonates, carbides, and phosphates, are celebrated for their stability and high load-bearing capacity, rendering them indispensable in biomedical, catalytic, and optoelectronic applications [10].
- **Organic nanomaterials** are constructed from various organic compounds such as proteins, carbohydrates, lipids, and polymers. They are characterized by their non-toxic and biodegradable nature, with some, like liposomes, featuring a hollow core. Organic nanoparticles are sensitive to thermal and electromagnetic radiation, and their formation often relies on non-covalent interactions [10,11]. These nanoparticles find extensive

application in biomedicine, particularly in targeted drug delivery and cancer therapy [10].

Table 1. Selected groups of nanomaterials with representative examples of their common forms. Based on [5,10].

Group of nanomaterials	Common forms
Carbon-based	Fullerenes: C60, C70, etc. Graphene, Carbon nanotubes (CNTs): Single-Walled (SWCNTs), Multi-Walled)MWCNTs), Nanofoam
Inorganic	Quantum dots (QD): CdSe, PbS, InP, etc., Nanoparticles: Ag, TiO2, ZnO, etc., Nanowires: Pt, Si, TiO_2, etc., Nanorods: Ag, Au, Cu, etc., Nanotubes: MoS_2, $NiCl_2$, etc.
Organic	Nanoparticles: poly(lactic-co-glycolic acid) (PLGA), polydopamine (PDA), lipid-based nanoparticles (liposomes, micelles, etc.), Dendrimers: poly(amidoamine) (PAMAM), poly(propylene imine) (PPI), etc., Nanowires: polypyrrole (PPy), polyaniline (PAN), etc., Nanotubes: polystyrene, polyvinylidene fluoride (PVDF), poly(methyl methacrylate) (PMMA), etc.

Polymeric nanoparticles

Polymeric nanoparticles are one of the most prominent examples of organic nanoparticles. Polymers are large molecules composed of numerous repeating units with diverse characteristics, leading to a wide range of compositions and properties. In the life sciences, both natural and synthetic polymers play significant roles. Natural polymers like nucleic acids, proteins, and peptides are fundamental components of biological structures and functions [5]. They support genetic and epigenetic processes. On the other hand, modern

synthetic methods enable the creation of synthetic polymers with unique physicochemical traits, such as robustness, viscoelasticity, and a tendency to form glasses and semicrystalline structures [12]. These polymers can be combined to form custom-designed supramolecular architectures. The versatility and resulting properties of polymer materials find numerous applications in the medical and pharmaceutical fields [12].

Polymeric nanoparticles can be synthesized using various methods. Standard synthesis techniques include nanoprecipitation, emulsification, salting out, ionic gelation, self-assembly, and polymerization [12–14]. **Nanoprecipitation** relies on the controlled mixing of a polymer solution in an organic/oil phase and an aqueous phase (usually water or another solvent), which induces the precipitation of nanoparticles. The rapid diffusion of the solvent from the polymer solution leads to the formation of nanoparticles [12]. **Emulsification** is a technique where an emulsion is formed by mixing an organic phase containing a water-immiscible solvent and a preformed polymer with an aqueous phase containing a stabilizing agent. The emulsification process involves high-shear agitation to achieve an oil-in-water (o/w) emulsion. Emulsification is the initial stage in several combined techniques, such as emulsification-solvent evaporation, emulsification-reverse sailing out, or emulsification-diffusion [12,14]. **The salting-out** technique involves creating an oil-in-water emulsion by mixing an organic phase with a water-insoluble with an aqueous phase containing a stabilizer and a high concentration of the salting-out agent. The obtained emulsion is then diluted to allow the organic solvent to diffuse into the aqueous phase, which results in the formation of polymeric nanoparticles [13,15]. **Ionic gelation** utilizes ionic interactions between oppositely charged molecules to form nanoparticles. Polymers with ionic groups are mixed with counterions or cross-linking agents, which induce gelation and nanoparticle formation [13,16]. **Self-assembly** techniques rely on the spontaneous organization of amphiphilic polymers or block copolymers to form nanoparticles with well-defined structures. The self-assembly process is governed by the hydrophobic and hydrophilic interactions, van der Waals attraction, and electrostatic interactions between polymer segments [13]. Polymer nanoparticle formation by **polymerization** involves initiating a chemical reaction where monomers come together to form long polymer chains. The polymerization process occurs in a controlled environment, allowing the nanoparticles to grow and eventually aggregate into larger structures [12]. Emulsion polymerization involves the polymerization of monomers in an emulsion system. Monomers are dispersed as droplets in an aqueous phase, along with surfactants to stabilize the emulsion.

The polymerization is then initiated, leading to the formation of nanoparticles in the dispersed phase [12].

Table 2 summarizes selected aspects of the presented techniques. Each synthesis method offers unique advantages and challenges, providing flexibility in tailoring polymeric nanoparticles for specific applications. The ability to control nanoparticle size, shape, composition, and surface properties allows for customization to meet the diverse demands of various fields [12].

Modifications of polymeric nanoparticles allow for fine-tuning of their properties and functionalities. Surface modifications can be achieved through various techniques. Chemical conjugation and "click chemistry" are popular techniques for immobilizing ligands on the surface of NPs. However, those methods typically involve modifying the ligand and/or polymer beforehand with a chemically active group [17]. Stable immobilization of ligands on polymeric nanoparticles can also be achieved through electrostatic interactions between oppositely charged species or physical adsorption driven by hydrogen bonding or hydrophobic interactions. This approach often eliminates the need for chemical modification of the ligand and/or nanoparticle termini [17]. Such modifications enhance the stability, biocompatibility, and targeting capabilities of polymeric nanoparticles. For example, the attachment of targeting ligands, such as small molecules (folate, galactose, estradiol, or biotin), antibodies, peptides, or aptamers, to the nanoparticle surface enables specific recognition and binding to target cells or tissues, enhancing their selectivity and uptake via receptor-mediated endocytosis [17]. While increasing functionality associated with nanoparticles is desirable, it is essential to consider scalability and robustness during preparation to ensure reproducible, large-scale production and compliance with high pharmaceutical quality standards for safe clinical translation [12].

Synthetic or natural polymers can be used to fabricate nanostructures for biomedical applications. A desirable polymer should possess biocompatibility, biodegradability, minimal toxicity, and non-pyrogenic properties. Additionally, it should have a high drug-loading capacity and offer protection against drug degradation [13]. Biodegradable and bioabsorbable matrices are generally favored, as they can degrade within the body through hydrolysis or enzymatic reactions, eliminating the need for surgical removal after implantation [13]. Examples of such polymers include PLGA, poly(caprolactone) (PCL), polyethylene glycol (PEG) derivatives, and polydopamine [13,18].

Table 2. Selected synthesis techniques of polymeric nanoparticles. [12,14,19,20]

Synthesis method	Types of NPs	Sizes	Size-determining factors	Benefits	Issues
Nanoprecipitation	Micelle, nanogel, nanospheres, nanocapsules	From >100 to 300 nm	Solution viscosity, polymer Mw and concentration, stirring rate	Simplicity, good reproducibility, well-defined size, narrow size distribution, scalability	Removal of the organic solvent and surfactant
Emulsification-solvent evaporation	Micelle, nanogel, nanocapsules, nanospheres	80-900 nm	Polymer concentration, ratios between the organic and aqueous phase, stirring	Scalability, quick, additional stabilizer not required	Removal of residual monomers not suitable for proteins and peptides, high volume of the aqueous phase
Ionic gelation	Nanospheres, nanogels	Typically 10-500 nm, suitable also for microparticles	The concentration of the polymer and the cross-linking agent, pH, and ionic strength of the solution	Relatively cheap (expensive equipment or reagents are not required) and fast (can be completed in less than 10 h)	Limited control over particle size and potential batch-to-batch variation
Sailing-out	Nanospheres	Several hundred nm	The concentration of salt and polymer, pH, and temperature	Monodispersed NPs, a variety of shapes and aspect ratios, unprecedented control over particle size, shape, chemical composition, cargo, modulus, and surface properties	Extensive purification procedure to remove the sailing-out agent
Self-assembly	Nanospheres, nanocapsules, micelles	Typically 10-100 nm	Polymer composition and Mw, self-assembly conditions	Well-defined structures with controlled size and stability	Complex synthesis, limited scalability
Polymerization	Nanospheres, nanocapsules, micelles, and other	From a few to hundreds of nm	Monomer concentration and Mw, reaction time, choice of initiators and stabilizers, polymerization methods	Ability to encapsulate various payloads (e.g., drugs, imaging agents)	Batch-to-batch variation, challenges in achieving uniform size distribution, and difficulty in scaling up the process for large-scale production

Polydopamine

Polydopamine is a synthetic form of melanin – a naturally occurring pigment ubiquitous in living organisms. Its origin can be traced to the discovery of the adhesive properties of dopamine, a catecholamine neurotransmitter found in humans. One notable characteristic is its adhesive nature, related to the abundance of catechol moieties assisted by amino groups, which allows the formation of conformal coatings on various substrates, including metals, ceramics, and plastic materials [21]. This property has led to its use as a surface modifier and adhesive in biomedical implants, tissue engineering scaffolds, and biosensors. In addition to its adhesive properties, PDA exhibits exceptional biocompatibility, biodegradability, and stability under physiological conditions, making it well-suited for biomedical applications. The properties such as antioxidant activity, free-radical scavenging, a broad range of light absorption, and efficient photothermal conversion are also desirable in designing multifunctional therapeutic agents [22]. Thus, PDA often serves in photoacoustic imaging (PAI) or photothermal therapy (PTT) applications. In 1960, Longuet-Higgins proposed that melanin consists of a conjugated chain of quinonoid units called a quinone-semiquinone copolymer [23]. However, the exact structure of melanin and PDA has remained a mystery for many years. A comprehensive analysis by Dryer and coworkers allowed a model of the PDA's structure to be proposed. The researchers suggest that PDA is not a covalent polymer but rather a supra-molecular aggregate of monomers held together by strong, noncovalent forces such as charge transfer, π-stacking, and hydrogen bonding [24]. Studies utilizing UV−Vis spectroscopy, crystallography, and density functional theory (DFT) calculations have pointed to a chemically disordered structure of melanin [25]. Moreover, it has been shown that the PDA structure contains at least two radical species [26].

Despite tremendous efforts put into elucidating the chemical composition of PDA, its structure remains not yet fully understood. However, it is established that PDA can be described as a mixture of different oligomers. High-resolution mass spectrometry (HR-MS) analysis confirmed the presence of dopamine units within the oligomeric PDA chain [27]. The investigation also revealed aminoethyl chains attached to the dopamine units. Liebscher et al. proposed another structural model for PDA, suggesting that it consists of a mixture of oligomers containing indole units with varying degrees of (un)saturation and open-chain dopamine units [27]. These oligomers coexist within the PDA structure, contributing to its overall composition. Furthermore, DFT calculations investigated the intermolecular interactions between PDA chains. The analyses indicated that charge-transfer interactions

between o-quinoid and catechol units play a significant role in the intermolecular interactions of PDA chains.

PDA synthesis can be performed in several ways but is generally based on spontaneous oxidation and polymerization of a precursor compound (most commonly commercially available dopamine hydrochloride) in alkaline conditions [28]. A simplified pathway of PDA formation is presented in **Figure 2**.

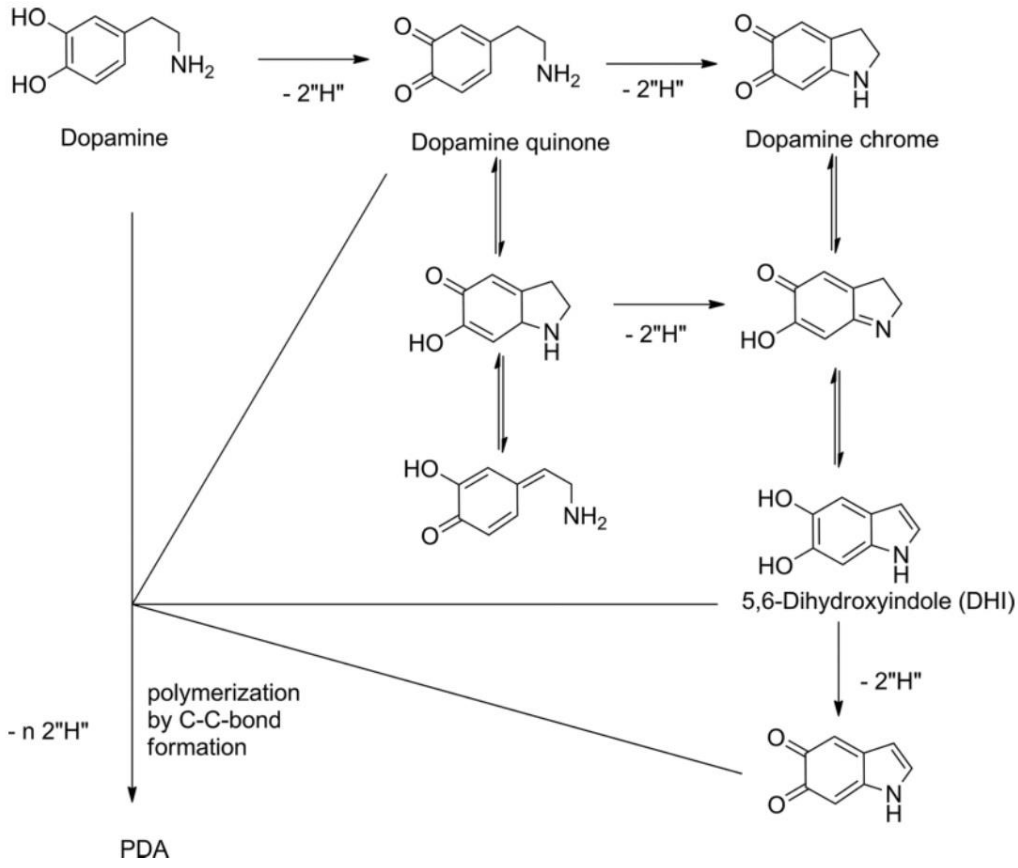

Figure 2. Schematic synthesis of PDA. [29]

The exact mechanism explaining PDA's structural features remains elusive, as it is a complex process involving multiple intermediates. However, evidence suggests that the synthesis begins with the formation of a semiquinone (rate-determining step, not shown in **Figure 2**) and dopamine quinone in the initial stages. The quinone species can undergo tautomerization, where the amino group attacks the β-position of the quinone Michael system. Further oxidative dehydrogenation of these intermediates can ultimately result in the formation of indole quinone units, also known as dopamine chrome [29]. During the synthesis, these various intermediates,

including semiquinone, dopamine quinone, and different tautomeric structures, can randomly combine through C-C bond formation to form oligomer species. The specific nature and mechanisms of these couplings still need to be better understood [29]. Depending on the oxidizing agent used in the synthesis, single electron transfer steps may also be involved, generating radical species capable of combining with other radicals or close-shell species. This highlights the potential involvement of radical reactions during PDA formation.

The synthesis conditions, such as temperature, duration, pH, or dopamine (DA) concentration, determine the size and morphology of the resulting nanoparticles. PDA provides a valuable platform for secondary reactions. Hence, PDA-based NPs can be further modified with various functional moieties.

PDA's versatile properties were employed in various biomedical applications – including enzyme immobilization [48], fluorescence imaging [47], sensors [49], ant-bacterial strategies [50], and cancer treatment [51]. While the debate regarding its structure is still ongoing, there is an agreement that it is composed of indole units with varying degrees of hydrogenation, primarily linked by C-C bonds connecting the benzene rings [27]. The vicinity of aromatic rings and various functional groups makes PDA nanoparticles potent carriers of different hydrophilic and hydrophobic drugs. All the features mentioned above contribute to polydopamine being a promising material for creating therapy-combining, imaging-guided nano-drug delivery systems (DDS) for cancer treatment.

Polydopamine-based theranostic cancer treatments

Cancer is a complex and devastating group of diseases characterized by uncontrolled cell growth and the ability to invade nearby tissues and spread to other parts of the body [30]. Despite significant advancements in research and treatment, it remains a major global health challenge (**Figure 3A**) [31]. Liver cancer is among the most common cancer cases with a high mortality rate (**Figure 3B**). Cancer is a problematic health issue because it can affect various organs and tissues, and its heterogeneity makes the development of universal treatment approaches highly challenging [30].

Traditional cancer treatments like surgery, chemotherapy, and radiation therapy often come with side effects and limitations, particularly in advanced cases [32–34]. However, pursuing novel cancer research and therapeutic solutions is paramount to overcome these challenges and enhance patient outcomes. Researchers and healthcare experts are dedicated to understanding

the underlying mechanisms of cancer development and progression, identifying precise molecular targets, and crafting more personalized, targeted therapies. This includes cutting-edge nanoparticle-based approaches like immunotherapies, precision treatments, gene therapies, and drug delivery systems [35–39], generally referred to as cancer nanomedicine.

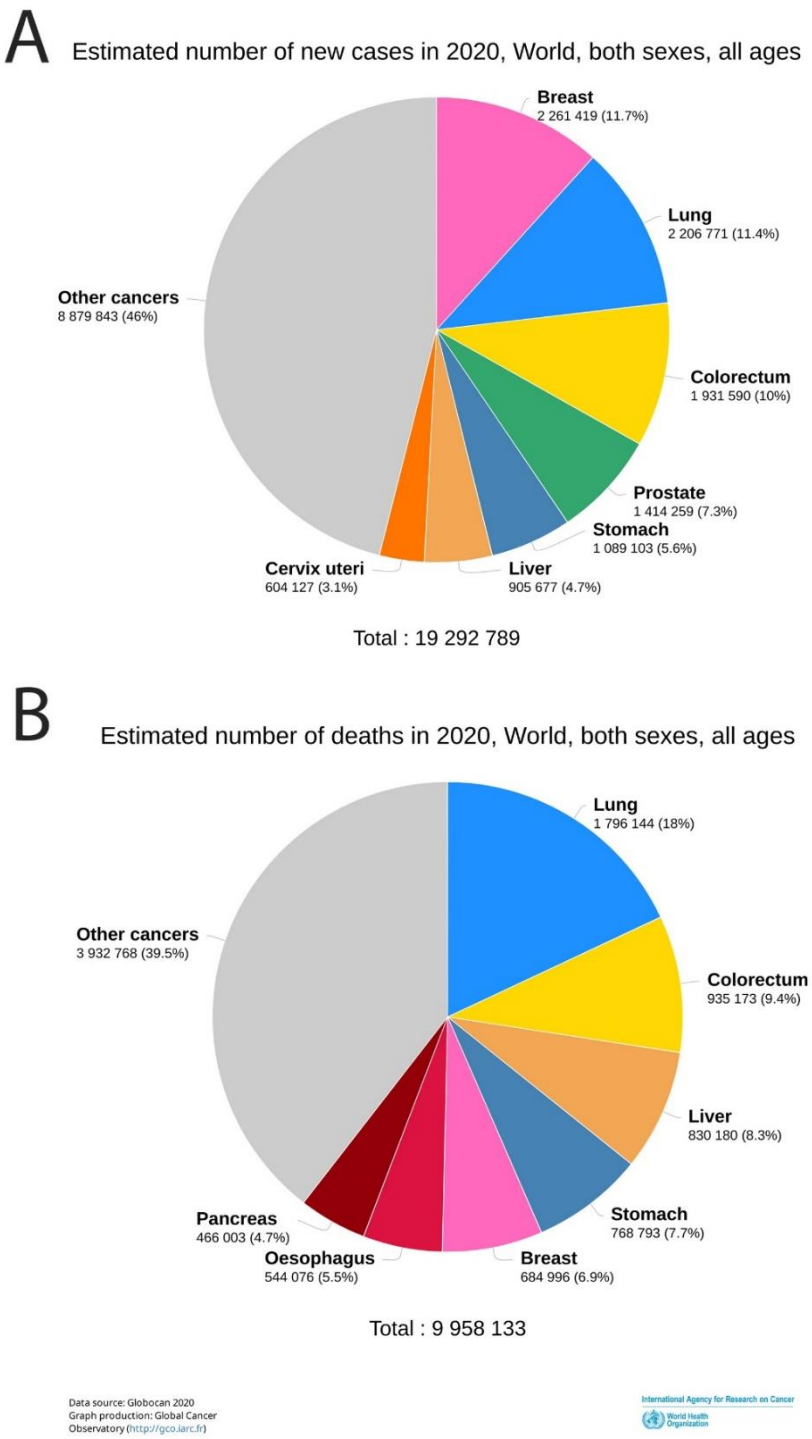

Figure 3. Cancer statistics. Estimated number of **A)** new cases of cancer and **B)** cancer-related deaths in 2020 worldwide. [31]

Nanomedicine is a field of medical science leveraging nanotechnology to diagnose, treat, and prevent diseases, including cancer [2]. By employing nanoscale materials to interact with biological systems at the molecular and cellular levels, nanomedicine offers unique advantages like targeted drug delivery, enhanced imaging capabilities, and the capacity to overcome biological barriers, making it a promising avenue for more effective and precise medical interventions [2,12]. One exciting frontier in this battle against cancer involves harnessing nanoparticles in DDS, allowing for targeted delivery of therapeutic agents directly to the tumor while minimizing harm to healthy tissues. Furthermore, nanoparticles introduce additional modalities to anticancer strategies, such as supplementary therapeutic or imaging techniques.

Multimodal therapy combines multiple treatment approaches, such as chemotherapy, radiotherapy, phototherapy, or immunotherapy, to augment therapeutic efficacy [40]. This strategy capitalizes on the complementary mechanisms of different therapies to target cancer cells from multiple angles, resulting in synergistic effects and potentially overcoming drug resistance. Advances in research and therapeutic approaches hold the promise of more effective, less toxic, and individualized treatments, ultimately leading to improved survival rates and better quality of life for patients. The continuous advancement of our understanding and treatment options aims to attain better control and hopefully eradicate cancer.

Multimodal therapy and theranostic DDS are highly attractive in biomedical applications, particularly in cancer treatment, due to their potential to address multiple challenges in cancer management. Theranostic DDS refer to nanoscale carriers that not only deliver therapeutic agents to specific sites but also enable simultaneous diagnostic imaging, allowing real-time monitoring of treatment efficacy. By integrating therapy and diagnostics in one platform, theranostic systems offer personalized treatment strategies, improved targeting of cancer cells, and reduced off-target effects [41]. This holds a promise of better patient outcomes and minimized side effects compared to traditional treatments [41].

Polymeric nanoparticles play an important role in research on novel therapies based on the theranostic concept. They serve as carriers for therapeutic agents, including drugs, genes, and imaging agents, enabling controlled release, improved bioavailability, and targeted delivery to specific cells or tissues [42]. Polymeric nanoparticles can encapsulate hydrophobic and hydrophilic drugs, protecting them from degradation, improving their stability, and enhancing their therapeutic efficacy [12]. Additionally, the nanoparticles can be functionalized to enhance

their interactions with biological systems, improve stability, and facilitate specific targeting mechanisms [43].

Polydopamine is an attractive material for multimodal therapy and theranostic approach due to its unique properties (**Figure 4**) [44]. PDA is biocompatible, biodegradable, and exhibits excellent photothermal conversion ability, enabling photothermal therapy [45]. PTT uses laser irradiation to heat and ablate tumor cells locally, leading to cancer cell death while sparing healthy tissue [46]. PDA can also be a versatile coating material, allowing easy functionalization with various therapeutic agents, imaging probes, and targeting ligands for specific cancer cell recognition [18]. Furthermore, PDA possesses intrinsic fluorescence, making it suitable for imaging and tracking the distribution of nanoparticles *in vitro* [47]. The abundance of aromatic rings favors an ability to chelate metal ions, such as Zn^{2+}, $Fe^{2+/3+}$, Gd^{3+}, Mn^{2+}, and ^{64}Cu, which enables the synthesis of PDA-based probes for various bioimaging techniques, including positron emission tomography (PET) [48], computed tomography (CT), and MRI [49,50].

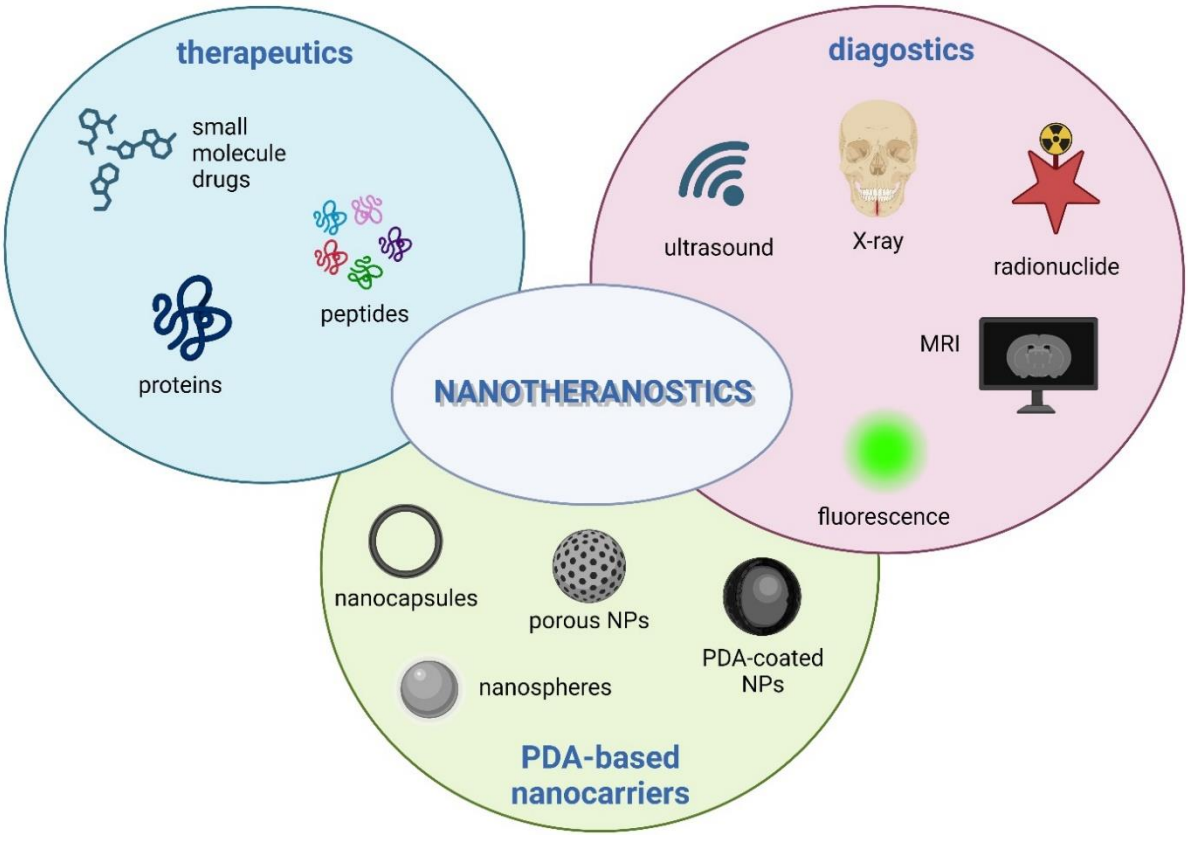

Figure 4. Elements of PDA-based nanotheranostic systems. Created with BioRender.com. Based on [51].

As stated earlier, PDA serves not only as an effective drug carrier but also as a proficient photothermal agent. This enables the potential for simultaneous implementation of PTT and chemotherapy by integrating chemotherapeutics with nanoformulations containing PDA. Examples of PDA-based combined therapy include PEG-modified cisplatin (CP)-loaded PDA (PDA-PEG-CP) NPs for combined PTT and chemotherapy [52]. A similar system but loaded with DOX or SN38 was proposed by Wang *et al.* [53]. Li and co-workers reported on PDA-arginine-glycine-aspartic-cysteine acid/doxorubicin (PDA-RGDC/DOX) for photoacoustic imaging-guided targeted PTT and chemotherapy [54]. Other examples include simultaneous PTT and photodynamic therapy (PDT) achieved using nanoformulations incorporating PDA with photosensitizers (PSs) such as Ce6 [55,56]. Other multimodal systems include nuclear-imaging-guided combined radioisotope therapy (RIT) and chemotherapy [57] or PTT and immunotherapy with dual-mode fluorescence and multispectral optoacoustic tomography (MSOT) imaging [58]. Whan and co-workers proposed an exciting strategy for anticancer treatment by combining PTT, immunotherapy, and chemodynamic therapy within a single DDS [59]. Additionally, the polydopamine-multiprotein conjugates (DmPCs) enabled fluorescence-based real-time tumor imaging.

Overall, polydopamine's adhesive nature, biocompatibility, surface functionalization capabilities, and straightforward synthesis make it a promising material for various biomedical applications, including novel cancer treatment strategies. Its beneficial properties offer exciting avenues for biomedical research and technology advancements.

Delivery of nanoparticles to cancer cells

The efficient delivery of nanoparticles to cancer cells is critical for achieving therapeutic efficacy and minimizing off-target effects. Several strategies have been developed to enhance the delivery of NPs to tumors, including the enhanced permeability and retention (EPR) effect, targeted delivery, and biomimetic approach.

Passive targeting to the tumor sites relies on the EPR effect - a phenomenon observed in solid tumors characterized by leaky blood vessels and impaired lymphatic drainage [60]. The abnormal tumor vasculature allows nanoparticles to passively extravasate and accumulate within the tumor tissue, driven by enhanced permeability and reduced clearance [60]. The EPR effect is influenced by factors such as tumor type, stage, and vascular permeability [61]. Nanoparticles with sizes of 50-300 nm are considered optimal for EPR-based tumor

accumulation. EPR offers several advantages for nanoparticle delivery to cancer cells [43]. It can increase the local concentration of therapeutic agents while reducing their systemic distribution [61]. Long-term blood circulation is essential for effective passive targeting [43]. Modifications of the nanoparticle surface to avoid preliminary clearance by the reticuloendothelial system (RES) include anti-fouling and/or stabilizing agents [61]. Surface functionalization with PEG is one of the most common methods for prolonging blood circulation [43]. However, there have been reports about the unexpected clearance of PEGylated materials *in vivo* after repeated administration [62]. Moreover, it is important to note that the extent of the EPR effect can vary among different tumors and patients, emphasizing the need for personalized medicine approaches [43].

Actively targeted delivery aims to guide nanoparticles to cancer cells by exploiting specific interactions between the nanoparticles and cancer cell receptors or antigens. This approach enhances the specificity of nanoparticle accumulation in cancer cells, increasing therapeutic efficacy while minimizing side effects [43]. Targeted delivery can be achieved through various strategies:

- **Ligand-based targeting:** Nanoparticles can be functionalized with targeting ligands such as antibodies, peptides, or aptamers with high affinity and selectivity for cancer cell markers [61]. These ligands recognize and bind to specific receptors or antigens overexpressed on the surface of cancer cells, enabling specific nanoparticle-cell interactions [43]. Ligand-based targeting enhances the cellular uptake of nanoparticles by cancer cells and improves their therapeutic efficacy [51].
- **Magnetic targeting**: Magnetic nanoparticles can be guided to the tumor site using an external magnetic field [63]. This approach enables the precise localization of nanoparticles to the tumor, increasing their accumulation and contact with cancer cells.
- **Biomimetic approach:** Biomimetic nanoparticles represent a promising strategy inspired by the natural cell structures and behaviors [64]. These nanoparticles mimic the surface characteristics, functionalities, and interactions of biological entities, including cells, to enhance their delivery to tumors [65]. Biomimetic nanoparticles offer several advantages for cancer cell targeting and delivery. They can improve nanoparticle stability, enhance cellular uptake, and enable specific interactions with cancer cells [66]. By mimicking the natural characteristics of cells, biomimetic nanoparticles show improved selectivity and efficiency in delivering therapeutic agents [65].

Cell membrane-coating technology

The fusion of biomimicry and advanced nanotechnology has sparked revolutionary advancements in the field of biomedicine. Among the trends shaping this field, membrane coating technology plays a pivotal role. This innovative approach leverages the intrinsic properties of cellular membranes to enhance the functionality of synthetic nanoparticles, promising breakthroughs in precision-targeted and personalized therapeutic strategies.

The choice of cellular membranes as coating materials for nanoparticles is essential in engineering biomimetic nanosystems. Different sources of cellular membranes offer distinct attributes that contribute to the multifunctionality and therapeutic potential of the resulting nanocomplexes. The most common membrane sources for biomimetic anticancer systems include:

- **Red blood cells (RBC)** – the inherent biocompatibility of RBC membranes, coupled with their stealth-like characteristics, enables coated nanoparticles to navigate the bloodstream and prolong the circulation with minimal immune recognition [67]. The inherent RBC membrane protein can prevent the nanocarrier from phagocytosis [68].
- **Cancer cells** - these membranes harbor tumor-specific antigens and receptors, facilitating the homing of coated nanoparticles to cancerous tissues. Cancer cell membranes can enhance site-specific drug delivery, reduce off-target effects, and hold potential for early cancer detection through biomarker recognition [69].
- **Platelet cells** - platelet membrane-coated nanoparticles can exploit the natural tendency of platelets to accumulate at sites of injury, including tumor sites. This biomimetic approach can enhance the specific delivery of therapeutics to tumors, leading to increased therapeutic efficacy and reduced off-target effects [70].
- **Stem cells** - Stem cells have the ability to migrate toward areas of inflammation, which is often a characteristic of tumor microenvironments [71]. Stem cell membrane-coated nanoparticles can leverage this property to improve targeted drug delivery [72].
- **White blood cells (WBC)** – WBC, including macrophages, leukocytes, lymphocytes, and neutrophils, possess immunomodulatory and antigen-presenting capabilities [65]. When applied as DDS coating, WBC membranes enhance tumor targeting of the nanoformulations [73,74].
- **Hybrid membranes** - created by fusing membranes from different cell types. The hybrid membrane-coated nanoparticles can combine the advantageous properties

of multiple cell types for enhanced cancer treatment [75]. For instance, combining cancer cell and macrophage cell membranes can potentially increase drug delivery efficiency by combining the macrophage cells' ability to follow inflammation sites and the homologous targeting properties of cancer cells [76].

In the field of cancer treatment, utilizing membranes from different cell sources for coating nanoparticles offers a biomimetic approach that enhances targeting, drug delivery, and therapeutic efficacy (**Figure 5**). By mimicking the natural properties of these cells, membrane-coated nanoparticles hold promise for improving the precision and success of cancer therapies.

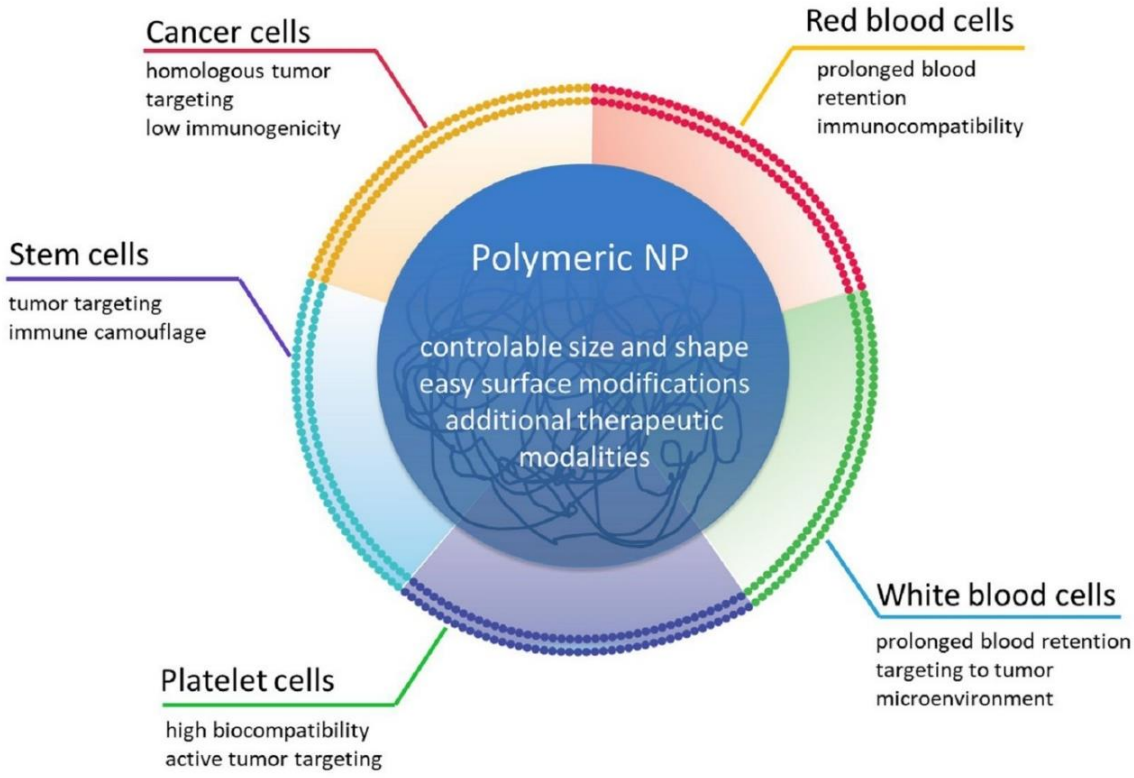

Figure 5. Selected aspects of different membrane sources for polymer-based membrane-coated anticancer drug delivery systems. [65]

The process of isolating cellular membranes plays a crucial role in the development of cell membrane-coated nanoparticles. The method employed depends on the cell type under consideration. For akaryote cells like erythrocytes and platelets, differential centrifugation is commonly utilized to separate these cells from blood samples [77,78]. Subsequently, the cells are lysed, and the membrane fraction is purified. On the other hand, karyocyte cells, such as

cancer cells, require a preliminary lysis step before isolating the membranes. This is often accomplished through techniques such as hypotonic buffer treatment or extrusion. Purification of the membrane fraction can be achieved using discontinuous sucrose gradient centrifugation, facilitating the separation of various fractions of cellular biomacromolecules [79]. Commercially available membrane protein extraction kits are also employed for this purpose. Careful handling of the isolation procedure is paramount to maintaining the membranes' biological functionality. The addition of protease inhibitors is recommended to prevent enzymatic degradation.

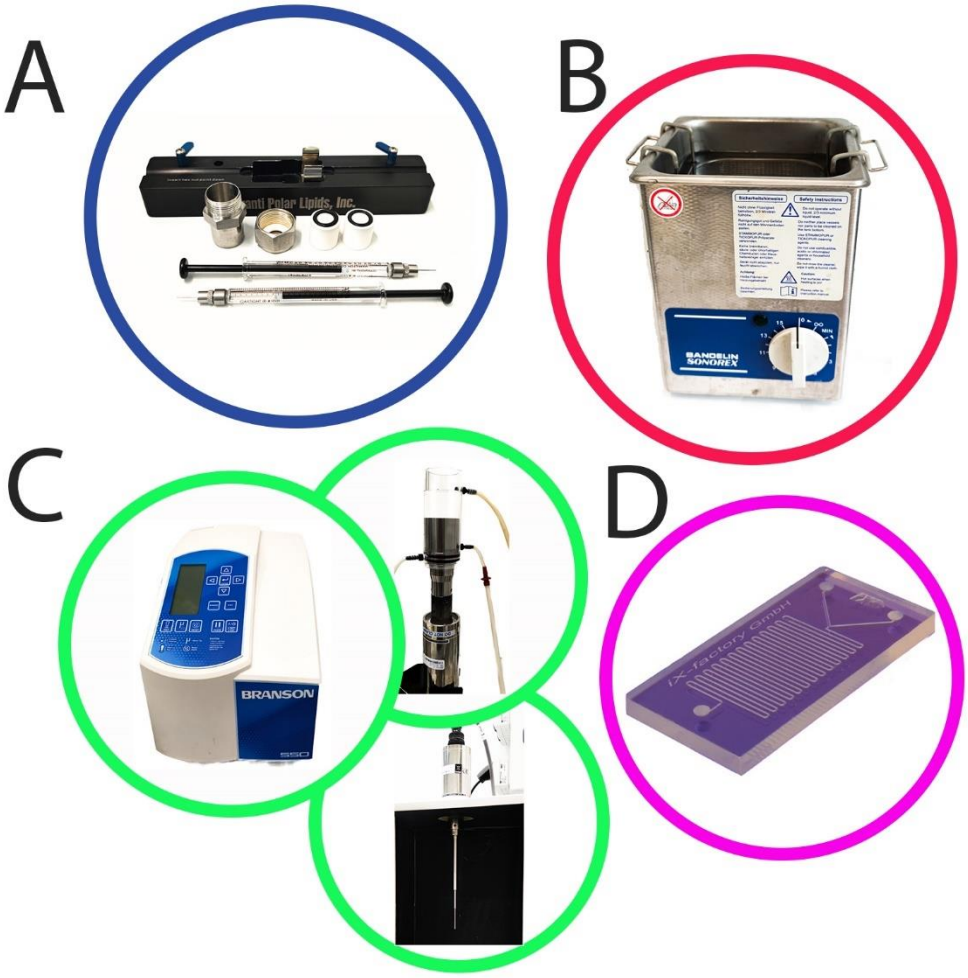

Figure 6. Standard techniques used in membrane-coating technology. **A)** Mini-extruder, **B)** Bath sonicator, **C)** High power sonicator with two sonication setups: head with a water tank (top right) and tip sonicator (bottom right), **D)** A chip used in a microfluidics technique.

Various techniques are employed to coat nanoparticles with isolated cellular membranes, each with advantages and limitations. The most commonly used methods are co-extrusion, sonication, and microfluidic systems with electroporation (**Figure 6**). **Co-extrusion** involves the sequential passage of the membrane vesicles and the nanoparticles through a porous polycarbonate membrane [80]. This creates fused structures through mechanical adsorption forces between the membrane vesicles and the nanoparticle surface. Although efficient, **sonication** requires careful sonication power control to prevent the temperature-induced denaturation of functional receptors on the cell membrane vesicles [81]. **Microfluidic systems** coupled with electroporation offer a high degree of control and flexibility in the coating process, allowing for the optimization of the membrane coating procedure in terms of uniformity, fusion efficacy, and minimal protein denaturation [82].

Integrating cellular membranes onto nanoparticles has significantly enhanced their colloidal stability [62]. Research indicates that these coated formulations can be stored for up to 15 days in aqueous media, such as phosphate-buffered saline (PBS) buffer. It has been suggested that the lyophilization process could further extend the shelf-life of cell membrane-coated nanoparticles, contributing to their long-term stability during storage [83].

The properties of nanoparticles significantly impact the success and quality of cellular membrane coating. Recent investigations into nanoparticle size (ranging from 80 to 200 nm) have revealed that while macrophage uptake remains unaffected, larger particles tend to accumulate more in the liver and exhibit accelerated clearance from the bloodstream [84]. An exploration of the interaction between polymeric cores and RBC membrane coatings showcased that successful coating occurs within a size range of 65 to 340 nm [85]. Notably, it was shown that the negative charge of the nanostructures was necessary for the proper translocation of the cell membrane onto their surface. Coating of positively charged NPs may result in unfavorable interactions between the coating and the core, leading to particle aggregation. The shape is another essential factor influencing cell membrane coating. Despite their increased curvature, anisotropic nanoparticles can be coated successfully with cell membrane vesicles, similarly to their spherical counterparts [86]. However, the geometry of nanoparticles influences biodistribution, therapeutic efficacy, and interactions with cells, presenting a complex relationship between shape and functional outcomes. Nanoparticles with a discoidal shape exhibit heightened resistance to non-specific cellular elimination upon systemic administration compared to their spherical counterparts [87]. Diverse morphologies can influence cellular interactions by virtue of variations in surface area-to-volume ratios,

potentially activating numerous intracellular signaling pathways [88,89]. Additionally, the membrane coating's integrity emerges as a pivotal factor in this context. Investigations reveal that approximately 10% of coated nanoparticles exhibit complete encapsulation, while roughly 40% exhibit a coating degree surpassing 20% [90]. Nevertheless, even partially coated nanoparticles can still harness the benefits of the membrane fragments on their surface, facilitating cancer cell targeting and evading immune surveillance.

Characterizing the successful coating of nanoparticles with cellular membranes requires a combination of physicochemical and biological techniques. Transmission electron microscopy (TEM) imaging confirms the core-shell structure of the coated nanoparticles. DLS measurements provide insights into particle size distribution and stability. Zeta potential measurements assess surface charge, which can influence particle interactions. Sodium dodecyl-sulfate polyacrylamide gel electrophoresis (SDS-PAGE) analysis and western blotting are employed to analyze the protein content of the coated nanoparticles. While these techniques confirm protein presence, they cannot quantify encapsulation efficiency accurately [65].

Numerous studies have previously explored the integration of PDA NPs into cell-coating technologies for cancer treatment. However, this area was not extensively exploited at the start of this project (October 2019). In 2018, Mu and co-workers developed Fe_3O_4@PDA NPs coated with mesenchymal stem cells, serving as siRNA carriers gene and photothermal therapy [91]. In the same year, Liu *et al.* introduced hemoglobin-bearing PDA NPs coated with RBC membranes for combating hypoxia-mediated tumor resistance to photodynamic therapy [92]. In 2019, Pan *et al*. developed aspirin-loaded PDA nanocapsules coated with 4T1 cancer cell membrane – an anti-inflammatory DDS for tumor-targeted PTT [93]. In 2020, Zhang and collaborators proposed a novel DDS composed of umbilical cord mesenchymal stem cell membrane-coated polydopamine nanoparticles encapsulating SN38, designed for the treatment of malignant bone tumors [94]. Another system was proposed in 2021 by Cao e*t al*., who reported on a two-photon excited PDA-Mn^{2+} coated with cancer cell (HeLa) membrane to create a targeted antitumor therapy system [95]. In the same year, Mu *et al.* developed stem cell membrane-camouflaged PDA NPs carrying DOX and PD-L1 siRNA for targeted chemoimmunotherapy of prostate cancer bone metastases [72]. Moving forward to 2022, Guo *et al.* published a notable study on PDA-based DDS coated with MNNG/HOS cell (osteosarcoma) membranes for the purpose of targeted therapy in hypoxic tumors, aiming to remodel the tumor microenvironment [96]. In the same year, Ren and co-workers reported on DOX-loaded mesoporous PDA NPs coated with platelet cell membranes for combined

chemotherapy and PTT of human breast cancer [97]. An interesting approach was proposed by Xiao *et al.* in 2023. The researchers developed a DDS composed of PDA-modified gold nanostar NPs coated with cell membrane isolated from anti-PD-L1 single-chain variable fragment (scFv) over-expressing cells for enhanced colorectal cancer immunotherapy [98]. **Table 3** shows representative examples of membrane-coated PDA-based DDS for cancer treatment. This research seeks to approach this topic from a novel perspective, offering fresh insights and innovative contributions to the field.

Table 3. Representative examples of membrane-coated PDA NPs for anticancer treatment. [99]

Membrane source	**Tumor**	**Targeting**	**Application**	**Ref.**
stem cells	prostate cancer bone metastases	active cancer cells targeting by stem cell membrane	chemoimmuno-/ gene therapy (DOX, PD-L1-targeting siRNA)	[72]
cancer cells (HeLa)	cervical carcinoma	homologous targeting	chemodynamic/photothermal therapy, two-photon/photoacoustic/magnetic resonance imaging (Mn^{2+})	[95]
platelet cells	breast cancer	specific targeting of tumor cells by platelet membrane	chemo-/photothermal therapy (DOX)	[97]
umbilical cord mesenchymal stem cells	malignant bone tumor	tumor-specific targeting of stem cell membrane	chemo-/photothermal therapy (SN38)	[94]
red blood cells	triple-negative mouse breast cancer	passive targeting	photodynamic therapy, photoacoustic imaging (Hb, MB)	[92]
cancer cells (4T1)	triple-negative mouse breast cancer	homologous targeting	photothermal treatment, drug delivery (Aspirin)	[93]

Overall, in the realm of cancer treatment, the evolution of membrane-coated nanoparticle systems stands as a promising stride toward precision therapy. By harnessing the biomimetic properties of diverse cellular sources, these systems hold the potential to redefine therapeutic approaches, offering enhanced targeting, reduced immunogenicity, and synergistic multimodal therapies for more effective and personalized cancer interventions.

2

AIM OF THE STUDY

This chapter outlines the primary objectives established for this research, driven by a deliberate interdisciplinary approach aimed at harnessing the collective expertise and insights from diverse fields. These objectives were formulated to leverage the multifaceted knowledge acquired throughout the study, contributing to a comprehensive and holistic understanding of the research landscape.

The primary objective of this study was **the development of a biomimetic drug delivery system coated with membranes designed for precise tumor targeting while enabling multimodal therapy and real-time imaging**. Porous polydopamine NPs were judiciously chosen as the core material for the nanocarriers, given their inherent photothermal properties and remarkable drug-loading capacity. At the outset of this project, the realm of membrane-coated PDA-based nanoformulations remained relatively uncharted, presenting an opportune research niche. As previously discussed, the spectrum of membrane sources encompasses various origins. In this study, cancer cells were selected as the primary source for membrane coating due to their remarkable homologous targeting potential. Liver cancer was selected as a model cancer type for the study. Hence, the hepatocellular carcinoma cell line (HepG2) was used as the membrane source. The development of this theranostic system was meticulously pursued with keen attention to the following aspects:

- **Synthesis of PDAFe Nanoparticles**: Developing a one-pot synthesis method to fabricate Fe-modified porous PDA nanoparticles with desirable properties, including controlled size and paramagnetic characteristics.
- **Membrane Coating:** Investigating the process of coating the PDAFe nanoparticles with membranes extracted from HepG2 cancer cells, ensuring successful integration and stability of the biomimetic nanoparticles.
- **Drug Loading and Release:** Developing a drug delivery system by loading the nanoparticles with doxorubicin (DOX) and characterizing the drug release profiles under different biological conditions to optimize therapeutic efficacy.
- ***In Vitro* Studies:** Conducting comprehensive *in vitro* studies to evaluate the cellular internalization, cytotoxicity, and therapeutic effectiveness of the membrane-coated

DOX-loaded nanoparticles on liver cancer cells (HepG2) compared to non-coated nanoparticles.

- **Combined Therapy:** Assessing the potential for combined photothermal therapy and chemotherapy by exploiting the photothermal properties of the nanoparticles and evaluating their efficacy in eradicating liver cancer cells.
- **MRI Imaging:** Investigating the nanoparticles' suitability for magnetic resonance imaging (MRI) as a dual-function theranostic agent, providing real-time monitoring and imaging capabilities during treatment.
- **Characterization and Analysis**: Performing extensive physico-chemical and biological analyses to characterize the nanoparticles, assess their stability, and gain insights into their interactions with biological systems.
- **Targeted Liver Cancer Treatment**: Evaluating the potential of the developed drug delivery system for targeted treatment and imaging of liver cancer, with a focus on enhancing therapeutic outcomes while minimizing off-target effects.
- **Contribution to Nanomedicine:** Contributing to the field of nanomedicine by addressing the gap in the literature regarding the synthesis and application of membrane-coated PDA-based nanoparticles for liver cancer therapy and imaging.

3

MATERIALS AND METHODS

This chapter summarizes all of the reagents, techniques, and methods that were applied to achieve the goals of my doctoral thesis. The methods and techniques used for nanoparticle synthesis, characterization, and *in vitro* and *in vivo* examination are concisely introduced to justify their use and assure that the presented analyses were carried out reliably.

Materials

Citric acid (≥99.5%), (Gadolinium(III) chloride hexahydrate (99%), Iron (III) chloride hexahydrate (98.0-102%), L-Glutathione reduced (GSH, ≥98.0%), Mesitylene (1,3,5-trimethylbenzene, TMB, 97%), Pluronic® F-127, Trizma® base (Tris(hydroxymethyl)aminomethane), ≥99.9%, Hank's Balanced Salt Solution (HBSS) buffer, Fetal Bovine Serum (FBS), phosphate-buffered saline (PBS) buffer (with or without Ca^{2+} and Mg^{2+}), SDS Gel Preparation kit, antibiotic antimycotic solution (10000 units penicillin, 10 mg/ml streptomycin, 25 µg/ml amphotericin B), Menadione, Sodium citrate tribasic dihydrate ≥99.0%, Sodium dodecyl sulfate (SDS), Glycine, Tween® 20, Muse® Oxidative Stress Kit, Muse® Count&Viability Assay Kit, primary antibodies (Anti-Glypican 3, Anti-Glyceraldehyde-3-Phosphate Dehydrogenase (GAPDH), Anti-Na+/K+ ATPase α1), and secondary antibody: Anti-Rabbit IgG (H+L), CF™ 488A produced in F(ab') fragment of goat were purchased from Sigma-Aldrich. Methanol (r.g.) was purchased from P.P.H. "STANLAB" Sp. z o.o. Dopamine hydrochloride (99%) was purchased from Alfa Aesar. Ethanol (99.6%) and acetone (r.g.) were purchased from Avantor Performance Materials Poland S.A. (formerly POCH S.A.). ATTO 550 was purchased from ATTO-TEC GmbH. RED-NHS was purchased from NanoTemper Technologies GmbH. Fluorescent dyes (calcein AM, ethidium homodimer1, Hoechst 33342, concanavalin A AlexaFlour 647 conjugate, SYTOX Green), 16% formaldehyde solution, trypsin-EDTA (0.25%) solution, cell media Dulbecco's Modified Eagle Medium (DMEM 4.5 g/l glucose, L-glutamine and 3.7 g/l sodium bicarbonate, w/o sodium pyruvate), Minimum Essential Medium Eagle (MEM 4.5 g/l glucose, L-glutamine and 3.7 g/l sodium bicarbonate, w/o sodium pyruvate), sodium pyruvate (100 mM), non-essential amino acids solution (100X), Dulbecco's Phosphate Buffered Saline (DPBS), secondary antibody: Goat anti-Mouse IgG (H+L) Highly Cross-Adsorbed (Alexa Fluor™ Plus 488),

Mem-PER™ Plus Membrane Protein Extraction Kit, Pierce BCA Protein Assay Kit, and Click-iT™ Plus EdU Cell Proliferation Kit for Imaging, Alexa Fluor™ 488 dye were purchased from Thermo Fisher Scientific Inc. WST-1 Cell Proliferation Reagent was purchased from Takara Bio. Doxorubicin (DOX), Hydrochloride Salt, >99%, was purchased from LC Laboratories. Manganese (II) chloride tetrahydrate, 98%, was purchased from ROTH. Uranyl acetate, 98%, was purchased from Polysciences.

Slide-A-Lyzer™ Dialysis Cassettes, 3.5K MWCO and 8-well Nunc Lab-Tek II Chambered Coverglass were purchased from Thermo Fisher Scientific Inc. Avanti® mini-extruder and extruder polycarbonate membranes were purchased from Avanti Polar Lipids. TEM grids (Lacey Formvar/Carbon, 300 mesh, Copper approx. grid hole size: 63µm) were purchased from Ted Pella Inc. Disposable folded capillary cells were purchased from Malvern Panalyical Ltd. Polystyrene cuvetted (10x10x45 mm) were purchased from SARSTEDT AG & Co. KG.

Cell lines: HepG2, MRC-5, and U-118 MG cells were purchased from the American Type Culture Collection (Manassas, VA, USA).

Methods

Preparation of membrane-coated nanoparticles

Synthesis of porous PDAMe nanoparticles

The synthesis method was based on a previously established protocol [100]. Briefly, Pluronic® F-127 (0.36 g, 0.03 mmol) was dissolved in 60 mL ethanol and 65 mL water. Subsequently, TMB (0.36 g, 2.99 mmol) was added to the solution and stirred for 30 min. Then, Trizma® base (90 mg, 0.74 mmol) in 10 mL of water was added to the reaction, followed by dopamine hydrochloride (60 mg, 0.32 mmol). The reaction solution was stirred at RT for 24 h. A metal source was added at a chosen time point to obtain metal-PDA nanoparticles. The metal sources used include $FeCl_3 \cdot 6H_2O$ (72 – 150 mg, 1.29 – 2.69 mmol of metal), $GdCl_3 \cdot 6H_20$ (72 – 150 mg, 0.46 – 0.95 mmol of metal), and $MnCl_2 \cdot 4H_20$ (72 – 150 mg, 1.31 – 2.73 mmol of metal). The tested addition time points were between 1 and 21 h after the synthesis was started. The obtained nanoparticles were purified by four series of 30-min bath sonication followed by high-speed centrifugation (22 000 rpm, 15 min) with a mixture of ethanol and acetone (2:1 v/v%, 40 mL). The nanoparticles were stored in ethanol in cold conditions.

Fluorescent staining

Several biological assays required the use of fluorescently stained nanoparticles. Hence, 2 mL of NPs solution in water (1 mg/mL) was mixed with 995 µL borate buffer pH 8.5 and 5 µL of ATTO 550 or RED NHS dye. The solution was stirred in darkness for 24 h (300 rpm) and then dialyzed for 72 h against water using Slide-A-Lyzer™ Dialysis Cassettes, 3.5K MWCO.

Drug loading and release

The MPDAFe NPs were loaded with a doxorubicin drug. Briefly, a DOX stock solution (1 mg/mL) was prepared by dissolving doxorubicin·HCL powder in PBS buffer (10 mM, pH 7.4) and then sonicating until a clear solution was obtained. Then, 1 mL of diluted stock DOX solution (0.5 mg/mL) was added to 1 mg of NPs and left overnight under shaking (550 rpm). Next, the free drug and physically absorbed DOX were removed by several series of washing with pH 7.4 PBS buffer, followed by centrifuging the drug-loaded NPs until no DOX signal was observed in the supernatant. The supernatant was collected and subsequently measured using UV-Vis spectroscopy to evaluate the amount of unloaded DOX. The following formulas were applied to calculate the drug loading and encapsulation efficiency:

$$\%\, drug\ loading = \ m_d/m_{NPs} \cdot 100\% \quad (1)$$

$$\%\, encapsulation\ efficiency = \ (m_0 - m_f)/m_0 \cdot 100\% \quad (2)$$

where $\boldsymbol{m_d}$ is the amount of the drug entrapped in NPs, $\boldsymbol{m_{NPs}}$ is the total weight of the NPs, $\boldsymbol{m_0}$ is the initial amount of the drug, and $\boldsymbol{m_f}$ is the amount of the free (not loaded) drug.

The drug release was examined using buffers mimicking different physiological conditions and with and without 808 nm NIR laser irradiation. Briefly, 1 mg of MPDAFe@DOX was mixed with 1 mL of appropriate buffer (citric buffer (10 mM, pH = 4.5); citric buffer (10 mM, pH = 4.5) with 10 mM GSH; PBS buffer (10 mM, pH = 7.4); PBS buffer (10 mM, pH = 7.4) with 10 mM GSH) at 37 °C under shaking (550 rpm) to determine the effect of pH and laser irradiation on the character of drug release. The samples were collected at various time intervals (1 h, 2 h, 4 h, 6 h, 24 h, 48 h, and 72 h). The collected supernatant was evaluated for the DOX content using a standard curve method, based on which the release curve was prepared. The experiment involving laser irradiation began with irradiating the samples for 5 min with an 808 nm laser (6 W/cm^2). The first control of the release was collected immediately after

the irradiation (time = 0 h), and then the experiment was carried on in the same manner described above. Three repetitions of each experiment were performed, and the mean value with standard deviation was used to express the results of active ingredient release. Following this, the data were fitted into five different mathematical models: zero-order, first-order, Higuchi's, Korsmeyer-Peppas, and Hixson-Crowell [101]. This analysis aimed to study the kinetics and the mechanism of the process. The correlation coefficient (R^2) was calculated to determine each model's fit.

Membrane isolation

The cancer cell membranes were sourced from HepG2 cells. A Mem-PER™ Plus Membrane Protein Extraction Kit was used to isolate the cell membranes containing the natural membrane proteins. The cells were grown in MEM medium supplemented with 10% FBS, 1% antibiotics, non-essential amino acids, and sodium pyruvate. The experimental procedure involved a series of sequential steps to prepare and isolate cells. Initially, the cells were resuspended in the growth media by gently scraping them off the plate surface using a cell scraper, resulting in a suspension of 5×10^6 cells. This suspension was then centrifuged at 300 × g for 5 min to form a cell pellet. To eliminate potential contaminants, the cell pellet was washed with 3 mL of Cell Wash Solution and centrifuged at 300 × g for 5 min. Following the removal of the supernatant, the cells were resuspended in 1.5 mL of Cell Wash Solution and transferred to a 2 mL centrifuge tube. Another centrifugation step at 300 × g for 5 min was performed, and the resulting supernatant was discarded. For permeabilization, the cell pellet was treated with 0.75 mL of Permeabilization Buffer, briefly vortexed to ensure a uniform cell suspension, and incubated at 4 °C with continuous mixing for 10 min. Subsequently, the permeabilized cells were centrifuged at 16 000 × g for 15 min, and the supernatant, containing cytosolic proteins, was cautiously collected and transferred to a new tube. To solubilize the pellet, 0.5 mL of Solubilization Buffer was added, and the mixture was resuspended by gentle pipetting. The tubes were then incubated at 4 °C for 30 min with continuous mixing. Finally, the tubes underwent centrifugation at 16 000 g for 15 min at 4 °C, and the resulting supernatant, containing solubilized membrane and membrane-associated proteins, was carefully transferred to a fresh tube. After isolating the membranes, the protein content was determined using a BCA assay, and the membrane isolates were lyophilized and stored at – 80 °C until used.

Nanoparticle coating with cell membranes

Membrane fragments obtained from the membrane isolation described above were used to coat the nanoparticles in order to develop a membrane-coated drug delivery system and benefit from the inherent properties of natural cell membranes. Before use, the membrane isolates were reconstituted in water and sonicated using a bath sonicator for 10 min. The membrane vesicles were then obtained by extruding the membrane solution 20 times through polycarbonate filters (0.8 µm) using an Avanti® mini-extruder equipped with gas-tight syringes. MPDAFe or MPDAFe@DOX nanoparticles (1 mg/mL in water) were mixed with the membrane vesicles (1 mg of protein/mL in water). The mixture was sonicated with a high power sonicator with a water-tank head (**Figure 6C**), and then the solution was extruded 10 times through polycarbonate filters (0.8 µm). The coated nanoparticles (MPDAFe@Mem or MPDAFe@DOX@Mem) were lyophilized and stored at -80 °C if not used immediately.

Physicochemical characterization of nanoparticles

Transmission Electron Microscopy and Energy-dispersive X-ray spectroscopy

TEM is a powerful technique that allows obtaining high-resolution images and detailed structural information of materials at the atomic scale. The electron beam used in TEM has a significantly shorter wavelength than photons in visible light, making it possible to achieve subnanometer resolution. In fact, TEM can achieve resolutions under 1 nm, well below the capabilities of even the highest-resolution light microscopes, which typically have a resolution of around 200 nm [102]. In a typical TEM setup, a beam of high-energy electrons is focused onto a thin sample. The electrons that pass through the sample are collected and projected onto a screen or detector to form an image [103]. The interaction between the electron beam and the sample can reveal information about the sample's composition, crystal structure, defects, and other properties. By manipulating the electron beam and sample position, it is possible to perform various analytical techniques, such as diffraction, imaging, and spectroscopy, to study the material's properties in detail [9].

Although TEM is a powerful tool for studying materials at the atomic scale, there are also some limitations to this technique. It is unsuitable for studying bulk materials, as the electron beam can only penetrate a few hundred nanometers into the sample. Additionally, TEM samples must be under vacuum, which limits the study of certain biological or hydrated samples [102]. TEM is also limited in its ability to provide information about the sample's chemical composition. Energy-dispersive X-ray spectroscopy (EDS) can be used in conjunction with TEM to obtain chemical information. EDS works by detecting the X-rays emitted when electrons in the sample

are excited by the electron beam used in TEM. When the electron beam interacts with the sample, it can cause the electrons in the sample to move to higher energy levels. When these electrons return to their original energy levels, they release energy in the form of X-rays [104]. The energy of these X-rays is characteristic of the element from which they were emitted. EDS detects and measures these X-rays, allowing the sample's composition to be determined. To perform EDS in TEM, a detector is positioned behind the sample, and the X-rays emitted from the specimen pass through a thin window and into the detector. The detector measures the energy of the X-rays, and the resulting spectrum can be used to identify the elements present in the sample [104].

Limitations to EDS include sensitivity and spatial resolution. Although virtually all elements (apart from hydrogen and helium) can be detected by modern EDS systems, some, such as beryllium and lithium, require dedicated analysis conditions. Moreover, reliable EDS analysis requires a certain amount of material to obtain a detectable signal. It has been estimated that the minimum detectable concentration in EDS when using a standard specimen is 1 at% [104,105]. Additionally, the spatial resolution of EDS is typically lower than that of TEM imaging, meaning that the elemental information obtained may not be as precise in terms of identifying the location of specific elements within the sample. Overall, TEM and EDS are essential tools for materials science, nanotechnology, and other fields where understanding the atomic-level structure and properties of materials is crucial.

The samples for the TEM imaging were prepared using drop-casting: A tiny droplet of the nanoparticle solution is placed onto a TEM grid Lacey Formvar/Carbon, 300 mesh, Copper approx. grid hole size: 63µm), which is a small, thin piece of material with a mesh structure that allows the electron beam to pass through. The solvent in the droplet is then allowed to evaporate, leaving behind a thin film of nanoparticles on the grid. To visualize the membrane coating, a drop of 1% uranyl acetate was added to the grid with an MPDAFe@Mem sample. The access of the uranyl acetate solution was removed, and the grid was further proceeded to drying. The images were obtained using a Transmission Electron Microscope Jeol 1400 (JEOL Ltd., Tokyo, Japan) with a maximum accelerating voltage of 120 kV and a maximum resolution of 0.2 nm. EDS analysis was performed using a High-Resolution Transmission Electron Microscope HRTEM Jeol ARM 200F (JEOL Ltd., Tokyo, Japan) with a maximum accelerating

voltage of 200 kV and a maximum resolution of 0.63 Å equipped with energy-dispersive X-ray (EDX) detector.

Dynamic Light Scattering

DLS is used to measure the size and charge of particles in a solution. It is based on the principle that when a light beam hits a particle, the light will be scattered in all directions. The scattered light intensity is then measured and analyzed to determine the particle properties [106].

Hydrodynamic diameter: In DLS, the hydrodynamic diameter of a particle is measured, which is the diameter of a sphere that diffuses at the same rate as the particle. The Brownian motion of the particles in solution causes them to move randomly, and this movement can be detected by monitoring the fluctuations in the scattered light intensity. The particle size is then determined by analyzing the intensity fluctuations using the Stokes-Einstein equation [106].

Polydispersity: Polydispersity is an indicator of the distribution of particle sizes in a sample. DLS can measure polydispersity by analyzing the intensity of light scattered by various fractions of the particles differing in size and is calculated by $(\text{width/mean})^2$ for each peak [107]. Therefore, a sample with a narrow distribution of particle sizes has a low polydispersity index (PDI). In contrast, a sample with a wide distribution of particle sizes has a high polydispersity index [106].

Zeta potential: The zeta potential is the electrical potential difference between the surface of a particle and the surrounding fluid. Zeta potential measurements are based on the electrophoretic mobility of particles in a solution under an applied electric field [107]. The mobility is related to the zeta potential by the Henry equation [108]. The software can calculate the zeta potential by measuring the velocity of the particles in the electric field.

The size distribution of the obtained nanoparticles, polydispersity, and zeta potential were investigated using the Zetasizer Nano ZS (Malvern Panalytical Ltd) dynamic light scattering (173 ° detector) and electrophoretic mobility measurements. Solutions of 5 µl NPs (1 mg/mL) in 1.45 mL deionized water were used for the analysis. The results are presented as the arithmetic mean ± standard deviation of three measurements.

Colloidal stability

The colloidal stability of the MPDAFe@DOX@Mem NPs in water was examined using the DLS. The sample (0.25 mg/mL) was stored at RT, and the hydrodynamic diameter, PDI, and zeta potential measurements were performed for 15 days. The colloidal stability of the lyophilized MPDAFe@Mem and MPDAFe@DOX@Mem samples resuspended in 10 mM pH 7.4 PBS buffer was examined for 13 days. The measurements were performed daily for the given period. The results are presented as the arithmetic mean ± standard deviation of three measurements.

Metal content evaluation

Inductively Coupled Plasma Optical Emission Spectroscopy (ICP-OES) is a widely used analytical technique for determining elemental concentrations in various samples. ICP-OES enables rapid analysis of multiple elements with a detection limit of 1-10 ppm [109]. A sample is introduced into an inductively coupled plasma, which is generated by applying a high-frequency electric field to a gas such as argon. The plasma heats the sample to a temperature of several thousand degrees Celsius, causing the sample to vaporize and ionize. The excited ions and atoms emit characteristic light at specific wavelengths, which are detected and analyzed by an optical spectrometer. The intensity of the emitted light at each wavelength is proportional to the concentration of the corresponding element in the sample, allowing for the determination of the sample's elemental composition [110].

To ensure accurate and precise measurements, the sample must be appropriately prepared. Liquid samples are typically acidified to minimize interferences from other elements and to prevent the precipitation of dissolved species. Solid samples must be first dissolved in acid to extract the analytes, and then the solution is filtered to remove any particulate matter that could block the plasma torch. The sample must also be sufficiently homogeneous to ensure that a representative portion is analyzed. The accuracy and precision of ICP-OES measurements can be affected by various factors, including the matrix effects and spectral interferences [109]. To minimize these effects, it is crucial to use appropriate calibration standards and analytical techniques and to perform quality control checks on the instrument and sample preparation procedures.

ICP-OES measurements were performed to determine the metal content of the MPDAMe nanoparticles, where Me = Fe, Gd, or Mn. The initial MPDAMe NPs solutions were dried and subsequently dissolved in 65% nitric acid to a concentration of 1 mg/mL. The acidified solution

was then heated overnight at 80 °C to ensure the complete dissolution of the nanoparticles. The measurements were conducted at the Faculty of Chemistry, Adam Mickiewicz University in Poznań, using a Varian ICP-OES VISTA-MPX instrument with a wavelength range of 165-845 nm. The instrumental parameters included a detection limit of 0.1 μg/mL, an integration time of 2 seconds, and a plasma flow rate of 15 L/min. The metal content of the MPDAMe nanoparticles was determined based on the intensity of the emitted light at specific wavelengths, which was proportional to the concentration of the corresponding metal element in the sample.

Thermal analysis

TGA coupled with FTIR (Simultaneous thermal analysis and Fourier-transform spectroscopy, STA/FTIR) is a powerful analytical technique for investigating the thermal behavior and chemical composition of complex materials. STA/FTIR enables simultaneous control of the weight change of a sample under heating and collecting infrared spectra of the atmosphere in the measurement chamber (hence, the product of sample decomposition) [111,112]. The technique is particularly useful for characterizing polymeric materials, as it can provide information on their thermal properties, such as glass transition temperature, decomposition temperature, and thermal stability. It can also be used to monitor the decomposition of polymers and biomass as well as ceramic and inorganic samples [111].

30 mg of MPDA NPs was dried prior to the measurements. The heating was performed at 10 °C/min in the range from 26 to 970 °C in a nitrogen atmosphere. The measurements were performed using Simultaneous Thermal Analyzer (STA) 6000 (Perkin Elmer) at the Centre for Advanced Technologies, Adam Mickiewicz University in Poznań.

Gas adsorption/desorption measurements

Gas adsorption/desorption measurements and BET analysis are essential techniques for the characterization of porous materials and provide valuable information about the surface area and pore size distribution of a wide range of materials. Nitrogen adsorption/desorption measurements are typically performed using a surface area or gas adsorption analyzer. The sample material is first outgassed at an elevated temperature under a vacuum to remove adsorbed gases. Then, the sample is placed in the analyzer, and nitrogen gas flow is introduced at a controlled pressure and temperature. Nitrogen adsorbs onto the surface of the porous material, filling the available pore space. As the pressure gradually increases, more nitrogen gas is adsorbed until the pores become saturated. The pressure gradually decreases, causing

nitrogen to desorb from the material. The amount of nitrogen adsorbed or desorbed at each pressure step is measured, and this data is used to construct an adsorption/desorption isotherm [113].

The BET analysis is a mathematical model based on the theory proposed by Brunauer, Emmett, and Teller and is widely used to calculate the surface area of porous materials from the adsorption isotherm data [114]. The model is based on the adsorption of monolayers of gas molecules onto the material's surface, and it considers the forces of attraction between the gas molecules and the material's surface [113]. The BET model is widely used in the analysis of porous materials because it provides a simple and reliable way to calculate the surface area of the material.

BET analysis of N_2 adsorption/desorption isotherm was performed to evaluate the surface area and pore volume of MPDA NPs. Before the measurements, the particles were analyzed with STA-FT-IR to establish the temperature limit of the outgassing phase. N_2 adsorption/desorption measurements were performed using 200 mg of dry MPDA NPs sample. The measurements were performed using ASAP 2420 (Micromeritics Instrument Corporation) at the Centre for Advanced Technologies, Adam Mickiewicz University in Poznań.

Magnetic properties

Magnetic Property Measurement System (MPMS) is a type of magnetometer using a Superconducting Quantum Interference Device (SQUID) as the magnetic field sensor. The system allows for measuring the magnetic properties of materials as a function of temperature and magnetic field. SQUID is a highly sensitive detector consisting of two superconducting electrical contacts separated by a very thin insulating layer known as a Josephson junction, allowing for the flow of Cooper pairs of electrons [115]. When a voltage is applied across the junction, a supercurrent can flow, which is a result of quantum tunneling. The supercurrent is highly sensitive to magnetic fields, which makes SQUID an excellent device for detecting small changes in magnetic fields. The device is capable of detecting magnetic fields as small as 10^{-15} Tesla, which is approximately 1 000 times weaker than the magnetic field of the Earth [115]. The MPMS measurements are used in various applications, including biomagnetism, geophysics, and materials science. By observing how the magnetization (degree of magnetism) varies in response to changes in temperature and the intensity of the magnetic field, we can identify the type of magnetism and other significant associated factors. The MPMS measurements can be divided into two categories: measurements

of magnetization as a function of applied magnetic field or measurements of magnetization as a function of temperature [115]. **Magnetization *(M)*** is a quantity that indicates the degree to which a material can be magnetized. **Magnetic susceptibility (χ)** is a measure of how much material is affected by an applied magnetic field (H). It is commonly used to study magnetic materials and is often expressed as a function of temperature and magnetic field strength. In MPMS, susceptibility can be measured by applying a small alternating magnetic field and measuring the resulting response of the material in the range of temperatures. The susceptibility measurements can provide valuable information about the magnetic properties of a material, including its magnetic ordering and magnetic anisotropy [115]. The information obtained from the susceptibility and magnetization measurements ($\chi(T)$ and $M(H)$, respectively) allows for the determination of the magnetic nature of the tested sample.

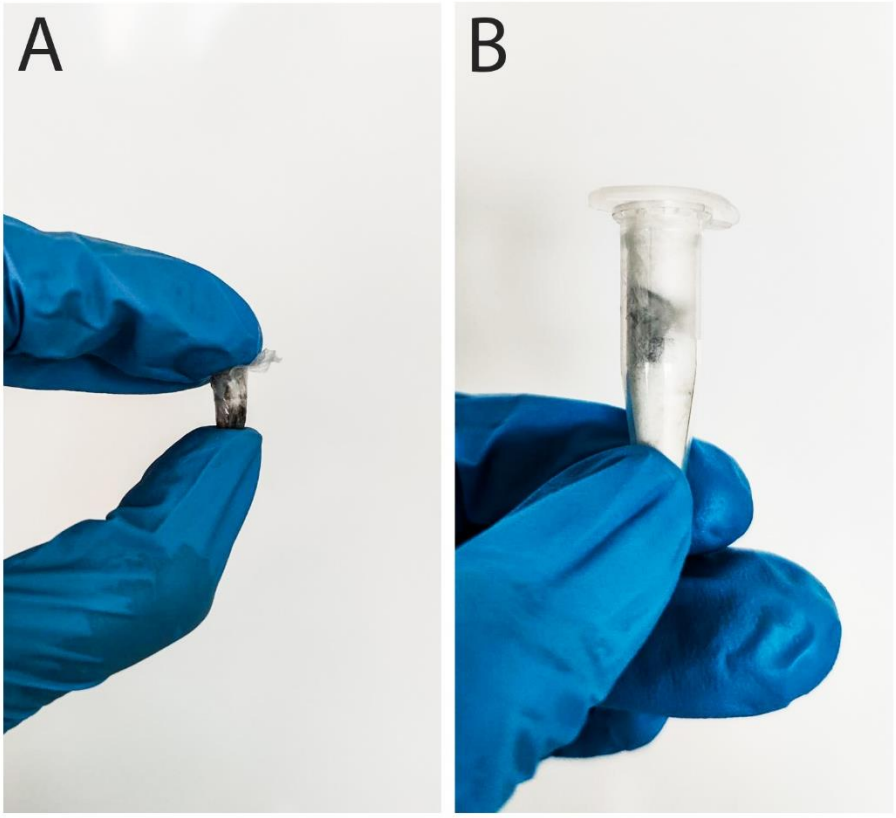

Figure 7. Sample preparation for the SQUID measurements. **A)** Leak-proofed polycarbonate capsule, **B)** Capsule fixed in an upright position in an Eppendorf tube for centrifugation.

In preparation for the measurements, 100 μL of MPDAMe (Me = Fe, Gd, or Mn) or MPDA NPs in water (1 mg/mL) was placed in a polycarbonate measurement capsule. A dedicated centrifugation technique was developed due to the small size of the capsules. First, the sample

solution in water was placed in the capsule. Then, the capsule was tightly wrapped with parafilm sealing film to avoid leakage during centrifugation (**Figure 7A**). The leak-proofed capsule was then placed in a 1.5 mL Eppendorf tube filled with cotton wool to fix the capsule in an upright position (**Figure 7B**). The solution was centrifuged, the supernatant removed, and the pellet was left to dry. Magnetic susceptibility was investigated by measuring changes in the magnetic moment of the sample in the temperature range from 2 to 300 K in the field of 1 kOe. Magnetization was measured for the changing magnetic field from -70 kOe to 70 kOe at two temperatures: 2 and 300 K.

Relaxivity studies

NMR is a technique that investigates the behavior of atomic nuclei in a magnetic field and provides insights into the structure, dynamics, and composition of molecules. It relies on the phenomenon of nuclear spin, which arises from the intrinsic property of atomic nuclei to possess angular momentum.

In an NMR experiment, a sample is placed in a strong and uniform magnetic field. The magnetic field causes the nuclear spins to align either parallel (low energy state) or antiparallel (high energy state) to the magnetic field direction. By applying a precisely tuned radiofrequency (RF) pulse, the energy levels of the nuclear spins can be manipulated. This pulse causes a transition between the energy states, wherein the spins absorb or emit energy, which is detected by specialized RF coils.

Upon completion of the RF pulse, the nuclear spins return to their original alignment, a process known as relaxation. During relaxation, the spins release the absorbed energy, which is detected and recorded as a signal by the NMR instrument. **Relaxation times T_1 and T_2** are fundamental properties of nuclear spin systems and are important parameters for characterizing the behavior of paramagnetic materials in solution. T_1 describes the rate at which the net magnetization of the sample returns to its equilibrium value along the direction of the applied magnetic field after being perturbed by the RF pulse. T_2 describes the rate at which the magnetization transverse to the magnetic field decays due to spin-spin interactions, which causes the phase of the signal to change and ultimately decay. In the presence of a paramagnetic species, T_1 and T_2 can be shortened due to the interaction between the nuclear spins and the unpaired electrons in the paramagnetic species. The extent to which T_1 and T_2 are shortened is proportional to the concentration of the paramagnetic species and is described by **relaxivity**, which is an indicator of the ability of the paramagnetic species to induce relaxation in the surrounding

protons. Relaxivity can be determined by measuring T_1 and T_2 at different concentrations of the paramagnetic species.

Relaxivity measurements were performed on MPDAMe NPs (Me = Fe, Gd, or Mn) using NMR spectrometers with a working frequency of 16.5 MHz or 200 MHz for protons to investigate the effect of the paramagnetic NPs on the relaxation behavior of protons in surrounding water molecules. The MPDAMe NPs were prepared by dissolving them in water at concentrations ranging from 0.1 to 1 mg/mL, which corresponds to 0.2-1.0 mM of Fe for MPDAFe NPs, 0.3 - 1.7 mM of Fe for Ferritis NPs, 0.67-1.34 mM of Gd for Gadolinis NPs, and 0.39-1.56 mM of Mn for Manganis NPs. Pure water was used as a control. The measurements were performed at RT and 37 °C. The T_1 times were measured using the **inversion-recovery** method (180 ° – τ – 90 °), based on inverting the spin magnetization and subsequent observation of its recovery to the equilibrium state. The NMR T_1 relaxation rate (R_1) was then determined, and relaxivity values were determined by fitting the relaxation rate data to the following equation using GraphPad Prism 7 software:

$$R_1 = r_1 \cdot C_{Me} + R_{water} \quad (3)$$

where $\boldsymbol{R_1}$ is the $\boldsymbol{T_1}$ relaxation rate of the sample, $\boldsymbol{r_1}$ is relaxivity, $\boldsymbol{C_{Me}}$ is the molar concentration of metal, and $\boldsymbol{R_{water}}$ is the T_1 relaxation rate of pure solvent (water).

Magnetic Resonance Imaging *in vitro*

MRI is an imaging technique that utilizes the principles of nuclear magnetic resonance to create detailed and high-resolution images of the internal structures of the human body. It provides valuable diagnostic information about various anatomical and physiological characteristics, aiding in detecting and evaluating numerous diseases and conditions.

At its core, MRI relies on the behavior of atomic nuclei, particularly those of hydrogen, when subjected to a strong magnetic field and specific RF pulses. Within the human body, these protons (^{1}H) are abundant in water and fat molecules, which are prevalent in biological tissues.

A strong and uniform magnetic field is applied when a subject is positioned inside the MRI scanner. This field aligns the spinning axes of the protons within the subject along the direction of the magnetic field. Subsequently, RF pulses are emitted, causing the protons to absorb energy and deviate from their aligned state. Once the RF pulse is ceased, the protons gradually return to their aligned state, releasing the absorbed energy. This energy emission is detected by

specialized RF coils positioned around the subject. To spatially encode the MRI signals and generate detailed images, gradient magnetic fields are applied along three orthogonal axes (x, y, and z), which alter the main magnetic field in a spatially specific pattern [116]. These gradients vary in strength across the imaging volume. By changing the strength and timing of these gradients, specific locations within the body can be selected for imaging. The gradients affect the resonant frequency of protons, allowing the MRI system to distinguish where the signals are coming from. The slice selection gradient is used to select a specific slice or cross-section of the body for imaging along the z-axis. Different slices can be imaged by varying the strength and duration of this gradient. Phase encoding gradient encodes spatial information along the y-axis by varying the phase of the MRI signals to distinguish positions along this axis. Finally, the frequency encoding gradient encodes spatial information along the x-axis [117]. A computer then processes the emitted signals to generate detailed images.

Different tissues within the body have distinct relaxation times, which refer to the time it takes for the protons to return to their aligned state. MRI can differentiate between various types of tissues by analyzing the differences in relaxation times, creating contrast in the resulting images. The generated MRI images display cross-sectional slices of the body with exceptional clarity and anatomical detail. To visualize different tissues and organs with MRI, contrasting agents are used. Paramagnetic sample solutions are one type of contrasting agent that can be used to enhance the contrast between tissues. The contrasting potential of such samples can be initially examined in solution to evaluate the nanoformulations' behavior when exposed to a high magnetic field.

The **Single-echo multi-slice (SEMS)** technique is used to acquire multiple image slices in a single excitation pulse, thereby reducing imaging time and improving efficiency. This technique utilizes a single RF pulse designed to excite a specific slice thickness and position within the imaged volume. After the excitation pulse, the signal from each slice is spatially encoded and acquired using the appropriate gradient fields. By obtaining multiple slices with a single excitation pulse, SEMS significantly reduces the total imaging time compared to acquiring each slice individually. **Multi-echo multi-slice (MEMS)** is an MRI technique that enables the acquisition of multiple images with different echo times and slice positions in a single scan. This technique is particularly useful in the measurement of paramagnetic samples because it allows for the detection of subtle changes in signal intensity that can be missed with conventional MRI techniques. Multiple echoes are acquired within a single repetition time (TR) for each excitation pulse. This is achieved by applying a series of spin echoes with different

times of echo (TEs) during the same TR. In both MEMS and SEMS techniques, multiple images are acquired with different slice positions. The images are then combined to create a composite image that highlights areas with short T_1 relaxation times or long T_2 relaxation times.

The contrasting potential of MPDAFe@Mem NPs was evaluated using a 9.4 T (400 MHz for protons) Agilent MRI scanner. Six concentrations of the NPs solutions in water (between 1 and 0.1 mg/mL, 0.2-1.0 mM of Fe) with water as a control were measured in both T_1-weighted (inversion-recovery) and T_2-weighted (MEMS) modes. The experimental parameters are presented in **Table 4**. T_2 maps were created out of the obtained images using ImageJ software.

Table 4. Experimental parameters applied to acquire T_1- and T_2-weighted images of paramagnetic nanoformulations using an MRI scanner.

Parameter	**Inversion-recovery (T_1- weighted)**	**MEMS (T_2-weighted)**
TR	12.5 s	15 s
TE	8 ms	14.28 ms
Field of view	25x25 mm	25x25 mm
Matrix	256x256 points	128x128 points
Slice width	1 mm	1 mm

Photothermal measurements

The photothermal properties of nanoparticles can be measured using various techniques. One standard method involves irradiating the nanoparticle solution with a laser of a specific wavelength and power and monitoring the temperature increase of the solution using a thermocouple or a thermal camera.

The photothermal properties of MPDAMe (where Me = Fe, Gd, or Mn) NPs were measured by irradiating 1 mL of nanoparticle solution in water (concentrations of 10, 25, or 50 μg/mL) in a quartz cuvette with an 808 nm NIR laser (Changchun New Industries Optoelectronics Tech. Co., Ltd.) placed at a distance of 5 cm from the cuvette at various power levels (between 2 and 6 W/cm^2) for 5 min. The temperature changes were monitored using a thermocouple or a KT-650 thermal camera (SONEL S.A.). The solution was stirred during the experiment to prevent nanoparticle sedimentation and ensure an even heat distribution within the solution. Water was measured as a control. The thermal stability of the nanoformulations (1 mL, 50 μg/mL) was

evaluated by performing five cycles of heating and cooling of the nanoparticle solution under constant temperature control. All measurements were performed in triplicates.

Biological characterization of nanoparticles

Gel electrophoresis

The sodium dodecyl-sulfate polyacrylamide gel electrophoresis (SDS-PAGE) protein separation was performed to compare the protein composition of the three fractions isolated from living cells: whole cell, cytosol, and membrane fraction. SDS-PAGE is a widely used technique for separating proteins based on their size. SDS denatures and binds to the protein, giving it a negative charge proportional to its molecular weight. This allows for separation based on size alone when subjected to an electric field [118]. The protein separation was also performed as the pre-step for the Western blotting analysis. The gel was prepared using the SDS Gel Preparation Kit according to the manufacturer's instructions. Briefly, the kit components, including acrylamide (30%)/bisacrylamide(0.8%) stock solution (PAA), separation gel concentrate, stocking gel concentrate, 10% N,N,N',N' - Tetramethylethylenediamine (TEMED) solution, and ammonium persulfate (APS) were mixed in specific proportions to obtain a 10% separation gel and a 3% stacking gel (**Table 5**). The pre-casted gels were stored wet at 4 °C for up to 7 days. Prior to gel separation, the protein samples were diluted to a concentration of 5 µg/mL and mixed with loading buffer at a 3:1 (sample:loading buffer) ratio. The samples were then heated at 95 °C for 5 min and cooled on ice for 2 min. A total of 8 µL of protein marker and 10 µL of the sample were loaded onto the wells of the stacking gel. The gels were placed in a Mini-PROTEAN Tetra Vertical Electrophoresis Cell tank equipped with PowerPac™ Basic Power Supply (BioRad Laboratiories, Inc.) filled with a running buffer (**Table 6**). The initial voltage applied was 80 V until the samples reached the stacking gel, followed by an increase to 120 V until separation was completed over 1.5 h. The gels were either transferred to a membrane for Western blotting or stained with a Coomassie blue solution (preceded by gel fixing in 15% ethanol and 1% citric acid for 1 h each) to visualize the protein bands.

Table 5. Quantities used to prepare separation gel (15 mL) and stacking gel (5 mL) for SDS-PAGE electrophoresis.

Gel type	Separation gel (10%)	Stacking gel (3%)
PAA stock solution/mL	5	0.5
Separation (stacking) gel Concentrate/mL	5	(1.0)
Ultrapure water/mL	4.75	3.4
TEMED solution/mL	0.25	0.1
APS solution*/mL	0.1	0.03

*10% (w/v) APS solution in ultrapure water was prepared in advance

Western blotting

Western blotting analysis was performed to prove the successful separation of cytosolic and membrane fractions by detecting the fraction-specific proteins. Western blotting, also known as protein blotting or immunoblotting, is a widely used technique in molecular biology for detecting and quantifying a specific protein within a complex mixture. This method is based on the principle of antibody-antigen recognition, where a specific antibody is used to recognize and bind to the target protein. Western blotting involves three significant steps: separation of proteins using electrophoresis, transfer of proteins onto a membrane, and detection of the target protein using a specific antibody [119].

Table 6. Composition of electrophoresis buffer and transfer buffer in ultrapure water.

Buffer component	Running buffer	Transfer buffer
Tris	25 mM	25 mM
Glycine	190 mM	190 mM
SDS	0.1%	-
Methanol	-	20%

The electrophoretic protein separation was performed as described above. After the separation, the gels were preceded to the transfer of the proteins to PVDF membranes. Before the transfer, the PVDF membranes were activated in methanol (2 min) and then washed with deionized water (10 min) and the transfer buffer (**Table 6**). The transfer sandwich was prepared as follows: a sponge, 3x Whatman® gel blotting paper (3 MM), gel, PVDF membranes,

3x Whatman® gel blotting paper (3 MM), and a sponge. All of the sandwich elements were soaked with the transfer buffer before assembling, and the absence of bubbles between the layers was ensured. The transfer was performed at a constant power of 130 A from 30 min to 1 h 30 min (depending on the size of the proteins of interest) in a Mini-PROTEAN Tetra Vertical Electrophoresis Cell equipped with PowerPac™ Basic Power Supply. After the transfer, the gels were fixed with 15% ethanol and 1% citric acid and stained with a Coomassie blue solution overnight. The membranes were blocked with 5% skimmed milk solution in 10 mM pH 7.4 PBS + 0.1% Tween® 20 for 1 h under rotation. Then, the membranes were washed three times with 10 mM pH 7.4 PBS + 0.1% Tween® 20, and the primary antibodies were added (**Table 7**). The antibodies were incubated with the membranes overnight at 4 ºC under rotation.

Table 7. Primary antibodies and the dilutions used in the Western blotting experiments.

Antibody	**Origin**	**Target protein location**	**Dilutions tested**
Anti-Glypican 3	Rabbit	Membrane	1:500, 1:1000, 1:2000 1:10 000
Anti-GAPDH	Mouse	Membrane	1:1000, 1:10 000
Anti-Na^+/K^+ ATP-ase α-1	Rabbit	Membrane	1:1000
Anti-Glypican 3	Rabbit	Membrane	1:500, 1:1000, 1:2000 1:10 000

Subsequently, the membranes were washed two times with 10 mM pH 7.4 PBS buffer and one time with 10 mM pH 7.4 PBS + 0.1% Tween® 20 prior to incubation with the fluorescently labeled secondary antibody (**Table 8**) under rotation for 1 h. Eventually, the membranes were washed three times with PBS buffer and imaged using the Molecular Imager® PharosFX™ Systems (BioRad Laboratories Inc.).

Table 8. Primary antibodies and the dilutions used in the Western blotting experiments.

Antibody	Origin	Excitation/emission wavelength	Dilutions tested
Anti-Rabbit IgG conjugated with CF™ 488A	F(ab')2 fragment of goat	490 nm/515 nm	1:2000
Anti-Mouse IgG conjugated with Alexa Fluor™ Plus 488	Goat	499 nm/520 nm	1:100, 1:200

Biological studies *in vitro*

Cell lines

HepG2 hepatocellular carcinoma cell line isolated from the human liver, U-118 MG glioblastoma cell line derived from a glioblastoma multiform, and MRC-5 cell line isolated from the human lung tissue were maintained at 37 °C in a 5% CO_2 humidified environment. HepG2 cells were cultured in MEM medium supplemented with 10% FBS, 1% antibiotics (penicillin 100 µg/mL, streptomycin 100 µg/mL), non-essential amino acids, and sodium pyruvate. U-118, MRC-5 cells were cultured in DMEM medium supplemented with 10% FBS and 1% penicillin-streptomycin antibiotic. The cell lines were stored in liquid nitrogen in the NBMC AMU cell culture bank.

Cytotoxicity assays

A series of robust and reliable assays were conducted to assess the potential cytotoxicity of nanoparticles. These assays aimed to provide practical insights into the impact of nanoparticles on cellular systems and determine their potential risks. The following methodology outlines the experimental procedures employed to evaluate nanoparticle cytotoxicity:

Nanoparticle concentrations: Before the experimental procedures, a series of dilutions in water was prepared for each type of nanoparticles of interest. The final NPs concentrations used for the cytotoxicity evaluation included 40, 20, 10, 5, 2.5, and 1.25 µg/mL.

Cell Viability Assays: Cells were seeded in 96-well plates at a specified density according to the cell type (HepG2: 2 x 10^4 cells/well, MRC-5: 5x10^3 cells/well, U-118: 5 x 10^3 cells/well) and allowed to adhere overnight. The range concentrations of nanoparticles were added to the wells, and the cells were incubated for a predetermined period. Cell viability was then assessed using colorimetric or fluorometric assays following the manufacturer's instructions.

To investigate **photothermal therapy potential**, each well was irradiated with an 808 nm NIR laser for 5 min with the power of 3 or 6 W/cm^2 4 h after the addition of nanoparticles.

Data Analysis: All experimental data were analyzed using appropriate statistical methods. Statistical significance was determined using GraphPad Prism software.

WST-1 assay

The WST-1 assay is a colorimetric assay commonly used to measure cell viability and proliferation. This assay is based on the reduction of a tetrazolium salt, WST-1, to a soluble formazan dye by mitochondrial dehydrogenase enzymes in the presence of an intermediate electron acceptor in viable cells [120]. The formazan dye is then quantified using a spectrophotometer, with the amount of dye formed being proportional to the number of viable cells.

To perform the WST-1 assay, HepG2, MRC-5, and U-118 cells were seeded on a 96-well flat bottom plate. 24 h after the seeding, nanoparticle solutions of various concentrations in water were added (50 µL/well). Following another 48 h, 10 µL of the WST-1 Cell Proliferation Reagent was added to the culture medium, and the UV-Vis measurement was performed after 4 h. The absorbance at 450 nm (reference wavelength 620 nm) was recorded against the background control using a multi-well plate reader (Anthos Zenyth 340rt, Biochrom). The cell viability was expressed as the respiration activity normalized to untreated cells.

EdU cell proliferation assay

The cell proliferation evaluation using the EdU cell proliferation assay relies on High-Content Analysis (HCA). This sophisticated imaging-based technique combines automated microscopy with advanced image analysis algorithms to quantitatively analyze cellular features and processes at a high throughput level.

In HCA, cells or biological samples are typically cultured and treated with various perturbations, such as drugs, nanoparticles, or genetic manipulations. Fluorescently labeled probes or dyes selectively stain specific cellular components, allowing for the visualization of cellular structures or molecular targets of interest [121]. The imaging process involves capturing multiple images of cells or regions of interest using high-resolution microscopy

systems. Once the images are obtained, sophisticated image analysis algorithms are applied to extract quantitative data from the images [121].

To perform the EdU cell proliferation assay, the Click-iT™ Plus EdU Cell Proliferation Kit was used. This kit is based on the incorporation of 5-ethynyl-2'-deoxyuridine (EdU), a nucleoside analog to thymidine, into newly synthesized DNA during the S-phase of the cell cycle. The EdU is subsequently detected via a copper-catalyzed click reaction with an azide-containing fluorophore, allowing for easy visualization and quantification of proliferating cells [122].

To perform the EdU assay, HepG2 and MRC5 cells were seeded on a black 96-well flat bottom plate with transparent bottom. 24 h after the seeding, nanoparticle solutions of various concentrations in water were added (50 µL/well). Following 24 h incubation with the nanoparticles, cells were labeled with 1x EdU solution for 24 h at 37 °C. The cells were then fixed using 4% formaldehyde in PBS (fixation solution) and permeabilized using 0.5% Triton® X-100 in PBS (permeabilization solution), allowing the EdU to access the DNA. The click reaction is then performed with the fluorophore, which can be visualized using a fluorescence microscope or flow cytometer. For EdU detection, the cells were incubated with a reaction cocktail containing 10 mM dye azide. Subsequently, the cells were imaged using the IN Cell Analyzer 2000 (GE Healthcare Life Sciences, Pittsburgh, PA, USA). All cells (proliferating and non-proliferating) were imaged using the DAPI/DAPI excitation/emission filters, while the Cy5/Cy5 ex/em filters were applied for the proliferating cells. 20 fields of view were taken per well with a 20x magnification.

Live/Dead assay

Live/Dead assay is another example of cell viability evaluation based on the abovementioned HCA technique. It is a commonly used method for distinguishing between live and dead cells in a population. The assay utilizes two fluorescent dyes, one of which stains live cells and the other stains dead cells [123]. To perform the assay, cells are first treated with the dyes and then visualized under a fluorescence microscope or analyzed using flow cytometry. Live cells will fluoresce green due to esterase activity, which converts the non-fluorescent calcein-AM to a green fluorescent calcein [123]. Simultaneously, dead cells are labeled with

red fluoresce due to ethidium homodimer-1 uptake, which only enters cells with damaged membranes and binds to nucleic acids, emitting a red fluorescence signal [123].

To perform a Live/Dead cell viability assay, HepG2 and MRC5 cells were seeded on a black 96-well flat bottom plate with transparent bottom. 24 h after the seeding, nanoparticle solutions of various concentrations in water were added (50 µL/well). Following 48 h incubation with the nanoparticles, cells were labeled with 2 µM calcein AM and 2 µM ethidium homodimer-1 in Dulbecco's phosphate-buffered saline (DPBS) (100 µL/well) for 30 min at 37 °C. Subsequently, the cells were imaged using the IN Cell Analyzer 2000. Living cells were imaged using the FITC/FITC excitation/emission filters, while the TexasRed/TexasRed ex/em filters were applied for the dead cells. 20 fields of view were taken per well with a 20x magnification.

Count and viability assay

Cell count and viability dependence on nanoparticle exposure were investigated using a flow-cytometry-based device. Flow cytometry is a powerful technique for analyzing and characterizing individual cells or particles within a heterogeneous population. It involves detecting and quantifying fluorescently labeled cells or particles as they pass through a focused laser beam. The sample is prepared by labeling cells or particles with specific fluorescent probes or dyes that selectively bind to cellular targets or molecules of interest, allowing for the identification and quantification of specific cell populations or markers. Once the sample is prepared, it is introduced into a fluidic system that transports the sample in a controlled manner to the flow cell, where the cells or particles pass through the laser beam one at a time. As the passing cells traverse the laser beam, they scatter and emit fluorescence. Fluorescence emission signals are detected in specific wavelength ranges corresponding to the fluorochromes used in the labeling process. The Muse® Cell Analyzer (Luminex Corporation, USA) is a flow cytometry-based device designed for simplified and rapid analysis of samples.

The Muse® Count & Viability Reagent is a tool that can differentiate between viable and non-viable cells based on their permeability to two DNA-binding dyes present in the reagent. The Muse® Count & Viability Software Module is then used to perform calculations automatically and present the data in two dot plots. The reagent contains a DNA-binding dye that stains the nucleus of dead and dying cells and a membrane-permeant DNA staining dye that stains all cells with a nucleus. These parameters are displayed as *viability* and *nucleated cells*, respectively. *Viability* is used to distinguish between viable and non-viable cells, while

nucleated cells are used to differentiate cells with a nucleus from debris and non-nucleated cells. The Muse® System relies on flow cytometry to count the stained nucleated events accurately and uses cellular size properties to distinguish free nuclei and cellular debris from cells, providing an accurate total cell count.

To perform a Count and viability assay, HepG2 cells were seeded on a 96-well flat bottom plate. 24 h after the seeding, nanoparticle solutions of various concentrations in water were added (50 µL/well). Following 24 h incubation with the nanoparticles, the cell preparation process included several steps, such as washing and detachment of the cells. Eventually, 10 µL of cells were combined with 190 µL of Muse® Count&Viability Reagent, and the measurements were conducted after 5 min of incubation at RT in the dark. Negative and positive controls were also utilized: non-treated cells (without nanoparticles) and cells treated with 200 µM Menadione, respectively. The Muse® Cell Analyzer was used to determine the results.

Oxidative stress assay

Investigation of the nanoparticle-induced oxidative stress in cells was performed using a Muse® flow cytometer. HepG2 cells were exposed to nanoparticles to evaluate the cellular populations experiencing oxidative stress by detecting Reactive Oxygen Species (ROS). ROS are reactive radicals and non-radical molecules derived from molecular oxygen, including superoxide, singlet oxygen, and peroxide, which play a role in several cellular processes, including apoptosis and alternate death pathways. The Muse® Oxidative Stress Kit was used to determine the relative percentage of ROS-negative and ROS-positive cells by detecting intracellular superoxide radicals. The kit utilizes the Muse® Oxidative Stress Reagent, which is based on dihydroethidium (DHE), a well-established compound used for detecting reactive oxidative species in cellular populations. The cell-permeable DHE reacts with superoxide anions, undergoing oxidation to form a DNA-binding fluorophore, such as ethidium bromide, which intercalates with DNA and emits red fluorescence. The assay distinguishes two cell populations: ROS(-) represents live cells, while ROS(+) indicates cells exhibiting ROS-induced oxidative stress.

The experimental procedure involved seeding HepG2 cells on a 96-well plate, adding 50 µL of NPs solutions of varying concentrations in water to the cell-seeded wells after 24 h incubation, and performing measurements after 24 h incubation with the NPs. The sample preparation

process included several steps, such as washing and detachment of the cells. To perform a Count and viability assay, HepG2 cells were seeded on a 96-well flat bottom plate. 24 h after the seeding, nanoparticle solutions of various concentrations in water were added (50 μL/well). Following 24 h incubation with the nanoparticles, the cell preparation process included several steps, such as washing and detachment of the cells. Eventually, 10 μL of cells were combined with 190 μL of Muse® Oxidative Stress working solution, and the measurements were conducted after 30 min of incubation at room temperature in the dark. Negative and positive controls were also utilized, consisting of non-treated cells (without nanoparticles) and cells treated with 200 μM Menadione, respectively. The Muse® Cell Analyzer was used to determine the results.

Internalization of nanoparticles

The uptake of the nanoformulations by HepG2 cancer cells was evaluated using imaging flow cytometry and confocal laser scanning microscopy (CLSM).

Imaging flow cytometry (IFC) is a powerful analytical technique used in biological and medical research to assess and characterize cells and particles. It integrates the advantages of traditional flow cytometry, such as its ability to handle multiple parameters rapidly, with the added benefits of capturing detailed information about cell shape and location at the single-cell level [124,125]. It can quickly generate multi-channel digital images of numerous individual cells, which encompass various fluorescence channels, as well as bright field (transmitted light) and dark field (scattered light) data. It involves passing a suspension of the subject of the study, such as cells, through a laser beam one at a time. As each cell passes through the laser beam, it scatters light in various directions and emits fluorescence if labeled with fluorescent dyes or markers. Detectors capture these scattered and emitted signals, providing information about each cell. This technique has the capability to measure various characteristics of specific components, like proteins, nucleic acids, and glycolipids, within different subcellular regions such as the nucleus or mitochondria [124]. This wealth of data makes imaging flow cytometry well-suited for in-depth analysis of nanoparticle interactions with living cells.

Nanoparticle uptake by HepG2 cells was assessed employing an Amnis Flowsight Imaging Flow Cytometer (Luminex Corp., USA). Cells were seeded at a density of 6×10^5 cells/well in a 6-well plate and cultured for 24 h. Subsequently, 500 μL of RED-NHS labeled NPs at a concentration of 20 μg/mL per well were added, and cells were incubated for 1 and 4 h.

Afterward, cells were trypsinized and fixed with 4% formaldehyde for 15 min. SYTOX Green was used to stain cell nuclei at a concentration of 167 nM. To ensure the analysis exclusively considered internalized NPs, cells underwent PBS buffer washing and centrifugation (1200 rpm for 5 min) between each step. During data collection, a flow rate setting with the slowest speed was employed to capture high-quality images. DNA and nanoparticle dyes were activated using 488 nm and 642 nm lasers. Each sample measurement involved four repetitions, each consisting of 250 events. A gating strategy was employed to identify individual cells while minimizing the presence of dead cells and debris, focusing on "size" and "aspect ratio." Only in-focus cells were analyzed by selecting those with high "Gradient RMS" values. Compensation controls were established using the "compensation wizard" option in the instrument's acquisition software. IDEAS® 6.3 Software (EMD Millipore, USA) was utilized to generate histograms and determine the fluorescence signal from nanoparticles using the "Set Range to Pixel Data" function, with a consistent template for gating and compensating fluorescence signals applied across all data sets.

CLSM and fluorescent imaging have revolutionized the field of microscopy by enabling scientists to visualize and study biological samples in unprecedented detail. The principles of CLSM are based on the ability to selectively focus on a thin section of a sample using a pinhole, which eliminates out-of-focus light and allows for improved resolution and contrast [126]. The procedure involves illuminating the sample with a laser beam and scanning the sample point-by-point to generate a three-dimensional image. Fluorescent imaging utilizes fluorescent molecules that emit light when excited by a specific wavelength of light. This allows for the visualization of specific structures or molecules within a sample. The experimental procedure for fluorescent imaging involves labeling the target molecules with fluorescent dyes or using genetically encoded fluorescent proteins. The sample is then excited with a specific wavelength of light, and the emitted light is captured using a detector [127]. Together, CLSM and fluorescent imaging have provided researchers with powerful tools to study cellular and molecular processes in a non-invasive and high-resolution manner [126].

The cell internalization of DOX-loaded nanoparticles was established using 8-well Nunc Lab-Tek II Chambered Coverglass. Briefly, HepG2 cells were seeded in each well (5×10^4 cells/well in 500 µL of cell medium). On the following day, the nanoparticle solutions were added. After 4 h of incubation, the cells were fixed using 4% formaldehyde. The nuclei were stained with DRAQ5, whereas the cell membranes were stained with Concanavalin A

AlexaFlour 647 dye. The preparations were imaged using a Leica TCS SP5 high-resolution confocal microscope (Leica Microsystems SAS, France).

Biological studies *in vivo*

The following studies were performed in consortium with the Department of Toxicology, Poznań University of Medical Sciences, under the supervision of Prof. Ewa Florek. Animal experiments were performed in accordance with the EU Directive 2010/63/EU for animal experiments and respective local regulations. Animal research followed internationally accepted guidelines for the care and use of laboratory animals, including the National Institute of Public Health – National Institute of Hygiene (NIPH – NIH) guidelines, and was approved by the respective Local Ethical Committee for Animal Experimentation (Uchwała nr 5/2020). All animal experiments were performed in accordance with relevant policies and regulations.

Animal model

Balb/c nude mice are a strain of laboratory mice that lack T and B lymphocytes and have a compromised immune system, making them suitable for studies that require the implantation of human cancer cells without rejection by the immune system. Subcutaneous tumor models involve the injection of tumor cells into the subcutaneous tissue of the mouse, allowing the tumor to grow and develop in a controlled environment. The subcutaneous tumor model was established by inoculating 2 x 10^6 HepG2 cells in 10 mM pH 7.4 PBS buffer into the left leg of each mouse. The mice were then monitored, including body weight and tumor measurements, every 2 days.

Therapeutic potential

In vivo studies are conducted to investigate the effectiveness of novel therapeutics and drug delivery systems as potential anticancer therapy. Subcutaneous tumor models are relatively easy to establish, and tumors can be monitored and measured non-invasively over time [128]. Immunodeficient mice like Balb/c nude mice reduce the likelihood of an immune response to the tumor, providing a more accurate representation of the efficacy of the applied treatment [129]. There are certain limitations to using xenograft subcutaneous tumor models in mice. One of the main limitations is that subcutaneous xenografts do not recapitulate the complexity of the human tumor microenvironment, including the interactions between

tumor cells and other cells, such as stromal cells and vasculature. Additionally, xenograft tumors lack the capacity to metastasize, which is a critical aspect of many human cancers [129]. Nevertheless, the xenograft mice models are commonly used in biomedical studies, especially for carcinogenesis and response to therapeutics [129].

For the *in vivo* evaluation of anticancer potential, the Balb/c nude female mice were divided into 8 groups: I) PBS (vehicle, control group), n=8; II) PBS + laser irradiation (phototherapy), n=8; III) anticancer drug DOX (chemotherapy), n=8; IV) MPDAFe@Mem NPs, n=8; V) MPDAFe@DOX@Mem NPs (chemotherapy), n=8; VI) MPDAFe@Mem NPs + laser irradiation (phototherapy), n=8; VII) anticancer drug DOX + laser irradiation (chemo- + phototherapy), n=8; VIII) MPDAFe@DOX@Mem NPs + laser irradiation (chemo- + phototherapy), n=8. When the tumor reached 5-10 mm in size, the animals were intravenously injected with a solution specific to their experimental group. The concentration of DOX was 2 mg/mL, resulting in a concentration of NPs of 4.44 mg/kg. In the groups that involved photothermal therapy, the tumors were irradiated with an 808 nm laser (6 W/cm^2) for 5 min on the day after the administration of the nanoformulations/buffer. The local temperature after irradiation was measured with a photothermal camera. The animals were monitored for 38 days, including body weight and tumor measurements.

Magnetic Resonance Imaging *in vivo*

MRI is widely used in preclinical research to study the anatomy, function, and pathology of various organs and tissues in small animals, including mice. In a typical MRI experiment, a mouse is anesthetized and placed inside a dedicated MRI scanner with an RF coil positioned around the region of interest. The generated strong magnetic field aligns the magnetic moments of protons in the body's water molecules. Subsequently, the applied RF waves cause the protons to rotate out of alignment. When the protons return to their original alignment, they release energy that is detected by the RF coil. The scanner can create high-resolution images of the mouse's anatomy and physiology by analyzing the signal generated by the protons. MRI imaging can be used to study a wide range of biological phenomena, including tissue morphology, blood flow, and metabolic activity. The technique is particularly useful for studying diseases such as cancer, neurological disorders, and cardiovascular diseases, where changes in tissue morphology and function are important diagnostic and prognostic indicators.

MPDAFe@Mem nanoparticles were evaluated for their contrasting potential and biodistribution *in vivo* in Balb/c nude female mice using MRI imaging. When the tumor reached 5-10 mm in size, the animals were intravenously injected with MPDAFe@Mem nanoparticles. The mice were anesthetized with the volatile anesthetic agent isoflurane and imaged at various time points post-injection (pre-administration, immediately after administration, 20 min, 24 h, and 7 days) using an MRI tomograph with a magnetic field strength of 9.4 T (400 MHz for protons) to acquire T_1-weighted images using fSEMS sequence with the following parameters: TR = 0.5 s, TE = 8 ms, ETL = 2, number of slices = 10. To evaluate the contrasting effect, the first image was taken before the administration of the nanoparticle solution, which was subsequently injected into the mice via the tail vein at a concentration of 4.44 mg/kg in a 10 mM pH 7.4 PBS buffer. The injection was performed using a catheter.

Statistical analysis

Appropriate statistical tests were employed to determine the significance of observed differences between experimental groups. The two-sample t-test or analysis of variance (one-way ANOVA) followed by post-hoc Turkey analysis was utilized for parametric data, such as normally distributed continuous variables. The significance level was set at $p < 0.05$ to determine statistical significance. All statistical analyses were performed using GraphPad Prism software.

4

RESULTS AND DISCUSSION

The following chapter provides a thorough overview of the data obtained from my research. The results were divided into sections. Each section presents the selected aspects of the conducted research and a careful analysis and discussion of the presented data.

Nomenclature of the nanoformulations

For the sake of clarity as to the subjects of subsequent analyses, **Table 9** defines the nomenclature used to describe the individual nano-formulations discussed in the chapter.

Table 9. Nomenclature of the investigated nanoformulations.

Sample name	Description
MPDA	Porous PDA NPs without iron
MPDA@Fe	Porous PDA NPs modified with Fe post-synthesis
MPDAFe	Porous PDAFe NPs obtained in a one-pot synthesis with 75 ug Fe^{3+} added (MPDAFe(L) in **Table 12**)
MPDAFe@DOX	MPDAFe NPs loaded with DOX
MPDAFe@Mem	Membrane-coated MPDAFe NPs
MPDAFe@DOX@Mem	Membrane-coated MPDAFe@DOX NPs
Ferritis	Porous PDAFe NPs obtained in a one-pot synthesis with 150 ug Fe^{3+} added (MPDAFe(H) in **Table 12**)
Gadolinis	Porous PDAFe NPs obtained in a one-pot synthesis with 150 ug Gd^{3+} added (MPDAGd (H) in **Table 12**)
Manganis	Porous PDAFe NPs obtained in a one-pot synthesis with 150 ug Mn^{2+} added (MPDAMn(H) in **Table 12**)

Synthesis and characterization of porous PDA nanoparticles

PDA attracts a growing interest as a multifunctional material suitable for biomedical applications due to its beneficial characteristics, such as inherent biocompatibility, low toxicity, near-infrared absorption, efficient photothermal conversion, and metal ion chelation [130]. The properties presented in the literature review section and the wide application of polydopamine nanoparticles in drug delivery influenced the use of this material in this study as

the basis for creating a functional liver cancer treatment system. The main idea of the formation and functionalization of the PDA-based nanoparticles and their goal application is presented in **Figure 8**.

PDA nanoparticles are synthesized through an oxidative polymerization method. In this process, dopamine, typically in the form of a dopamine hydrochloride salt, is dissolved in a buffered alkaline solution, commonly using Tris or phosphate buffers [27,29]. The alkaline pH (typically around 8-9) is crucial for the initiation of polymerization. The oxidative polymerization is triggered by the presence of oxygen in the air or by the addition of an oxidant, such as ammonium persulfate or hydrogen peroxide [27,29]. These oxidants facilitate the oxidation of dopamine to dopamine quinone, which then undergoes self-polymerization to form the PDA nanoparticles [27]. The reaction is typically carried out at room temperature under gentle stirring for several hours to allow sufficient polymerization and particle growth. During this time, the color of the solution changes to dark brown or black due to the formation of PDA nanoparticles [29]. The synthesis of PDA nanoparticles has several inherent advantages, including simplicity, scalability, and versatility. The process can be easily adapted to different substrates and particle sizes. Moreover, the PDA nanoparticles' surface can be further modified through various functionalization strategies, including covalent conjugation or non-covalent interactions, to introduce specific functionalities or improve their compatibility with targeted biomedical applications [131].

According to the previous research focused on PDA-based materials, the formation of porous PDA nanoparticles proceeds through several stages. Initially, small PDA nanoparticles with diameters in the 2-5 nm range are observed after a certain reaction time. These nanoparticles can interconnect with each other, leading to the formation of larger aggregates. As the reaction progresses, porous PDA structures start to emerge, characterized by the presence of spherical particles with sizes larger than the primary nanoparticles [100]. The interaction between the PDA nanostructures and the surrounding environment facilitates the formation of MPDA. In particular, a strong affinity between the primary PDA nanoparticles and π-electron rich TMB leads to the emulsion-templated self-assembly. The adsorption of PDA nanoparticles onto the emulsion droplets stabilizes the emulsion and prevents droplet coalescence.

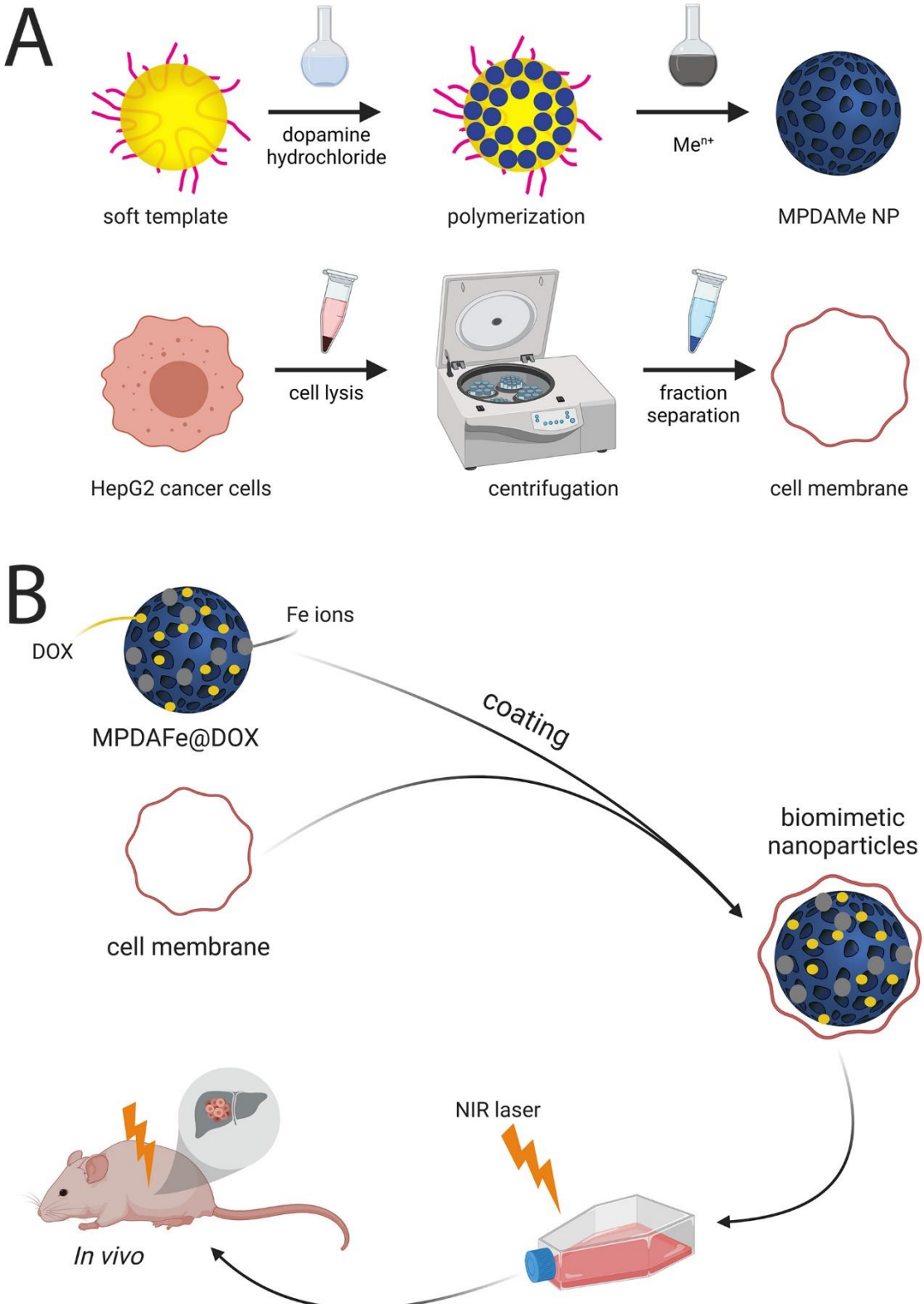

Figure 8. Schematic illustration of the main research idea of the study. **A)** Soft-template synthesis of MPDAMe NPs, Me = Fe, Gd, or Mn (upper row, based on [100]) and cell membrane isolation (bottom row). **B)** Functionalization and coating of the NPs results in formation of biomimetic nanoparticles which anticancer potential was evaluated *in vitro* and *in vivo*. Created with BioRender.com.

This stabilization is attributed to the formation of a protective layer comprising PDA nanoparticles and Pluronic® F-127 at the interface between the continuous and dispersed phases of the emulsion [100]. As the reaction proceeds, the primary PDA nanoparticles continue to grow in size, and the proportion of porous PDA (MPDA) particles increases. The growth and organization of PDA nanoparticles within the emulsion droplets lead to the formation of the porous structure.

A previously established synthesis protocol was used as the starting point for the synthesis of MPDA NPs [100]. Representative examples of the different synthesis conditions tested and the resulting NPs characteristics measured with DLS are presented in **Table 10**. The constant conditions for the presented syntheses were: 0.36 g of Pluronic® F-127, 65 mL of Mili-Q water, 60 mL of 99 % ethanol, 90 mg of Trizma base in 10 mL Mili-Q water, and 60 mg of dopamine chloride. TEM images are presented in **Figure 9**.

Table 10. Selected conditions tested for the synthesis of MPDA NPs and corresponding DLS characterization of the obtained nanostructures.

Sample number	Synthesis conditions	DLS		
		Z-average/d.nm	PDI	Zeta potential/mV
1	0.36 g TMB, RT, 100 rpm	1793.0±71.6	0.86±0.12	-14. ±0.4
2	0.4 g TMB, RT, 300 rpm	323.3±6.9	0.24±0.01	-9.43±0.6
3	3.2 g TMB, RT, 300 rpm	275.3±3.9	0.11±0.05	-32.5±0.4
4	0.36 g TMB, 50 ^{o}C, 300 rpm	380.2±6.8	0.29±0.03	-9.8±0.6
5	0.37 g TMB, RT, 350 rpm	253.9±6.6	0.22±0.04	-15.4±0.6
6	0.36 g TMB, RT, 1000 rpm	777.5±25.2	0.43±0.03	-9.3±0.2

RT – room temperature, rpm – rounds per minute (stirring speed)

The results of the DLS measurements and the structures observed on the TEM images indicate the importance of the selection of reaction parameters and the exact amounts of reagents used, and even the reaction mixing speed, in order to obtain nanoparticles with appropriate properties. The decisive features were the spherical shape, porosity, and homogeneity of the resulting nanoformulations. All of the obtained nanoparticles were of spherical shape and had negative zeta potential; however, in some cases (e.g., **Sample 5** in **Table 10**/**Figure 9D**), the particles were interconnected. In other cases, much larger structures were received together with small

nanoparticles (**Sample 1** in **Table 10/Figure 9A**) or even additional structures (**Sample 6** in **Table 10/Figure 9F**). The following conditions were selected as optimal for the expected outcome based on the negative zeta potential, preferred sample size, and polydispersity: **0.37 g of TMB, RT, mixing speed: 350 rpm** (**Sample 5** in **Table 10**). The MPDA NPs obtained using those conditions were further characterized for their thermal stability, pore volume, and surface area.

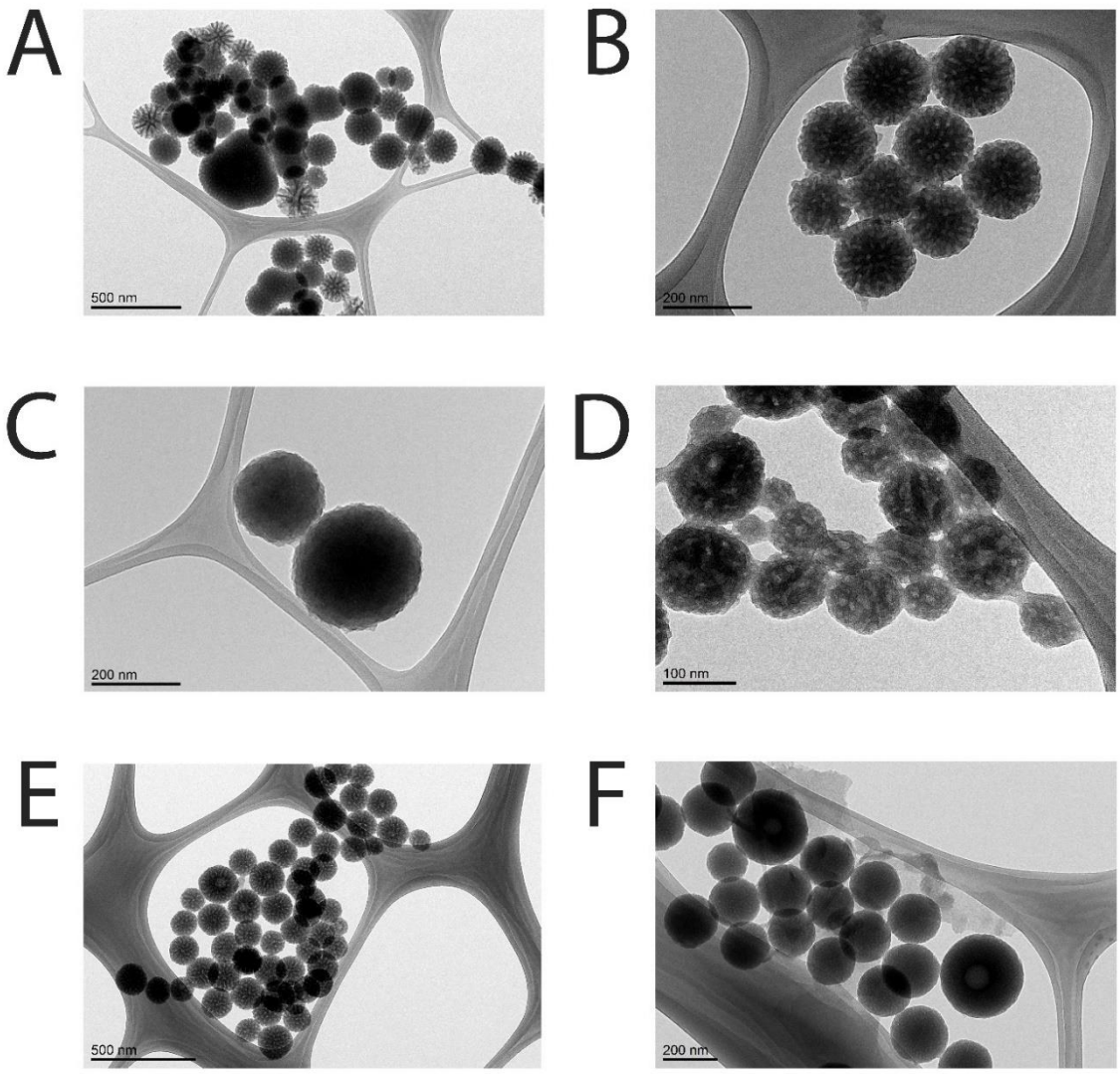

Figure 9. TEM images of MPDA NPs synthesized using different conditions. The images correspond to samples listed in **Table 10**: **A)** Sample 1, **B)** Sample 2, **C)** Sample 3, **D)** Sample 4, **E)** Sample 5, **F)** Sample 6.

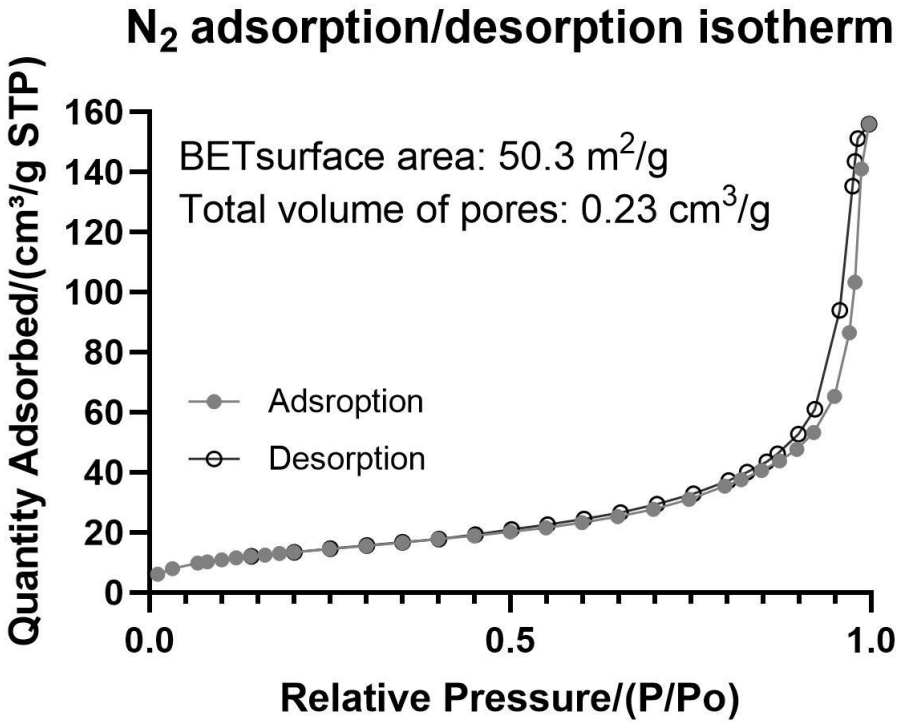

Figure 10. N_2 adsorption/desorption isotherms of MPDA NPs.

BET surface analysis

The N_2 adsorption/desorption measurements and subsequent BET analysis provided valuable insights into the porosity and surface area of the porous PDA nanoparticles (**Figure 10**). The MPDA NPs, obtained using the synthesis conditions described above, exhibited a specific surface area of 50.3 m^2/g and total pore volume of 0.23 cm^3/g, which is in line with a previously reported surface area (45 m^2/g) and pore volume (0.17 cm^3/g) of porous PDA NPs obtained using a similar protocol [100]. It was shown that increased surface area resulted in a significantly higher drug loading capacity of porous PDA NPs compared to their nonporous counterparts [132]. The N_2 adsorption/desorption isotherm analysis revealed a wide capillary condensation step with a type-IV isotherm according to IUPAC nomenclature with a type-H4 hysteresis loop. These types of loops are typically associated with adsorption-desorption processes occurring in narrow slit-like pores and confirm the presence of mesoporous structure [133–135]. This behavior was observed in the P/P_0 range of 0.45–0.9, indicating a relatively broad pore size distribution. Indeed, the pore volume analysis revealed the pore diameter ranging from 4 to 30 nm (not shown). The peak pore size was determined to be around 19 nm. The determination of a total pore volume of 0.23 cm^3/g further indicates the presence of substantial pore space within the MPDA NPs. The existence of such pores

suggests the potential for efficient loading and encapsulation of therapeutic agents. Pores can also facilitate improved diffusion of substances into and out of the nanoparticles, which is critical for effective drug release and interactions with target sites. Based on the established surface area and pore size, the MPDA nanoparticles hold promise as carriers for a wide range of drug sizes, including small molecule chemotherapeutics such as doxorubicin [136,137]. The versatility of these nanoparticles in accommodating different drug sizes makes them attractive candidates for targeted drug delivery and controlled release applications.

In conclusion, the N_2 adsorption/desorption measurements and BET analysis of the porous PDA nanoparticles revealed a high surface area and significant pore volume, highlighting their potential for various biomedical applications. These nanoparticles possess favorable characteristics for efficient drug delivery, adsorption, and other related processes.

Thermal stability

Understanding the thermal behavior of materials for biomedical applications provides valuable insights into their stability, integrity, and potential for application in controlled drug release. Thermal stability studies, such as STA-FTIR, enable the investigation of the material's response to temperature changes and the identification of any thermal degradation or decomposition processes. This information is vital for ensuring the efficacy, safety, and long-term stability of drug delivery systems, as it helps to optimize formulation parameters and select suitable materials with the desired thermal properties. The thermal stability and decomposition behavior of the MPDA NPs were investigated using the STA-FTIR system, which combines TGA with FTIR analysis. The experiment involved heating the sample from about 26 to 970 °C at a rate of 10 °C/min under N_2 atmosphere. The aim of this study was to evaluate the thermal stability and degradation behavior of the MPDA NPs and identify the products of their decomposition.

In the weight change curves (**Figure 11A**), a peak was observed at around 60 °C, indicating the occurrence of an initial thermal event. At this temperature, any residual moisture or volatile components adsorbed onto the surface of the polydopamine nanoparticles may start to evaporate or desorb, resulting in a weight loss [138]. This could explain the initial decrease in weight observed in the derivative weight change (red curve in **Figure 11A)**. As the temperature increased further, a gradual decrease in weight was observed, starting around 270 °C. This weight loss can be attributed to the decomposition and oxidation of the polydopamine structure.

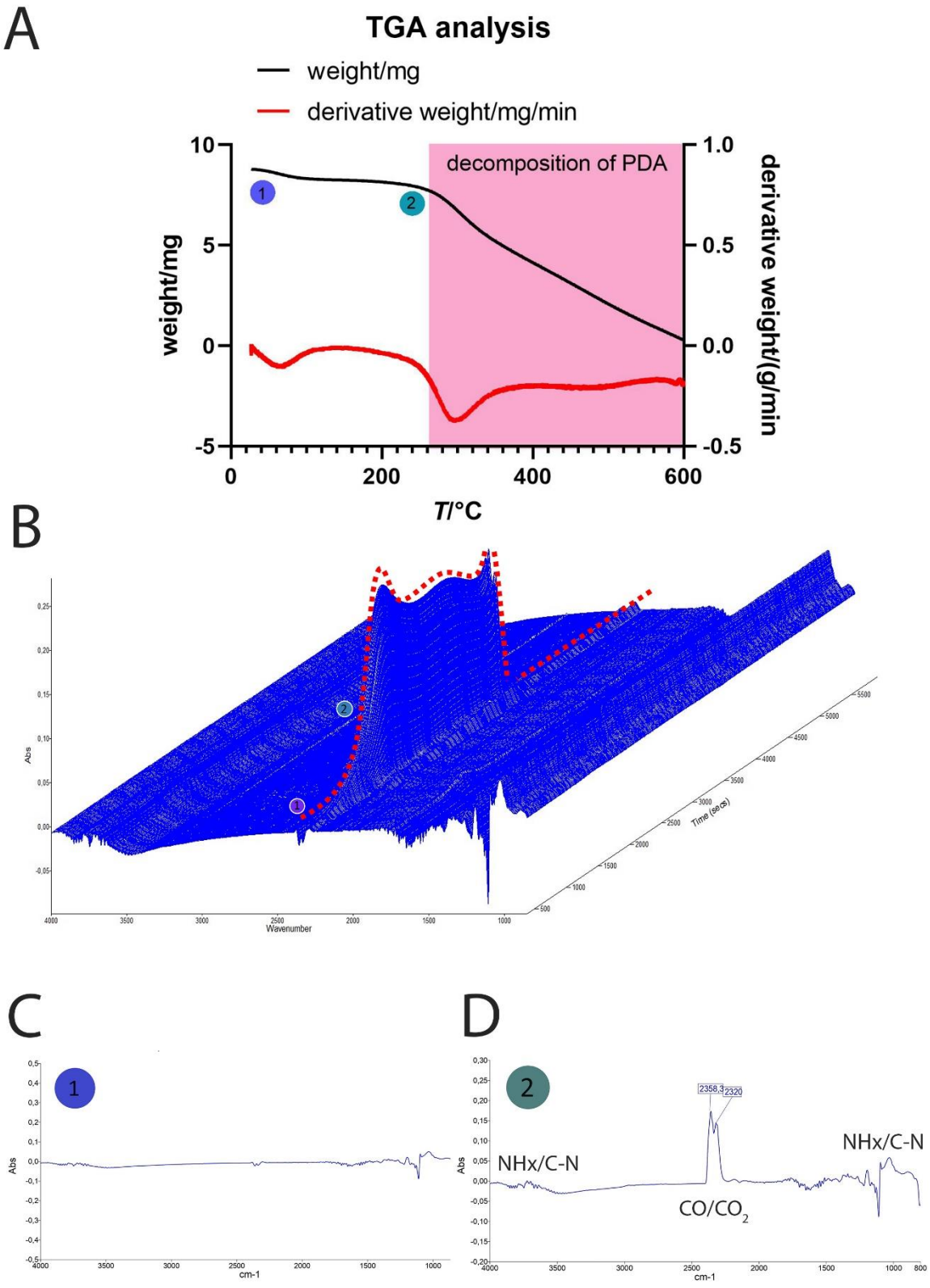

Figure 11. STA/FTIR analysis of MPDA NPs. **A)** Weight change curves between about 26 and 600 ºC; **B)** 3D map of FTIR spectra during the entire combustion process; **C)** FTIR spectrum at t = 4.5 min (marked as ①), **D)** FTIR spectrum at t = 25 min (marked as ②).

The 3D map of FTIR spectra (**Figure 11B**) provides additional information about the chemical changes occurring during the combustion process. Two representative FTIR spectra at different time points were analyzed to gain insights into the molecular transformations. **Figure 11C** shows the FTIR spectrum at t = 4.5 min (marked as ① **Figure 11**), corresponding to the initial stage of the combustion process and the weight loss peak observed at 60 °C. The spectrum does not exhibit any distinctive peaks, confirming that the weight loss could be attributed to residual moisture evaporation from the porous structure. In contrast, the FTIR spectrum at t = 25 min (marked as ② **Figure 11**), representing a later stage of the combustion process, reveals several characteristic peaks. The presence of low-intensity peaks at around 3700 cm^{-1} and between 1200-100 cm^{-1} could be associated with the stretching vibration of N-H bonds or C-N bonds. These bonds are present in amine or amide functional groups. Additionally, two major peaks are observed at 2358 cm^{-1} and 2320 cm^{-1}, which could be attributed to carbon dioxide (CO_2) or carbon monoxide (CO) gas evolution during the decomposition process. The peak at around 2358 cm^{-1} is characteristic of the asymmetric stretching vibration of CO_2, however, the presence of CO cannot be ruled out [139–142]. The presence of CO_2 is commonly observed in thermal analysis or combustion processes, where carbon-containing materials undergo oxidation. Therefore, the presence of CO_2 peaks would be expected during the thermal treatment of the PDA sample. On the other hand, the presence of CO could also contribute to the observed peaks. CO is a colorless and odorless gas that can form as a byproduct of incomplete combustion or thermal degradation processes. To conclusively distinguish between CO and CO_2 contributions to the observed peaks in the FTIR spectrum, additional analysis is necessary. The appearance of these peaks indicates the release of gaseous byproducts as the polydopamine structure undergoes thermal decomposition. Furthermore, additional peaks in the range of 1200-1000 cm^{-1} may be observed, which could correspond to various functional groups or molecular fragments formed during the combustion process.

The presence of these specific peaks in the FTIR spectrum at t = 25 min provides insights into the chemical changes occurring as the polydopamine nanoparticles undergo thermal decomposition. The observed release of carbon dioxide/monoxide gas indicates the breakdown of the polydopamine structure and the generation of volatile byproducts. Overall, the TGA experiment and FTIR analysis suggest the thermal stability of MPDA nanostructures up to 270 ºC.

Synthesis and characterization of porous MPDAMe nanoparticles

The introduction of metal ions into PDA nanoparticles serves as a pivotal strategy to impart them with unique and desirable properties. In particular, the incorporation of specific metal ions can result in obtaining paramagnetic PDA-based NPs, thereby rendering them highly suitable for MRI applications. This deliberate modification enhances their versatility and opens up new paths for non-invasive imaging, diagnostics, and therapeutic interventions in the field of nanomedicine. Thus, the next step of this study involved modification of the MPDA NPs with iron using $FeCl_3 \cdot 6H_2O$ as the Fe source, $GdCl_3 \cdot 6H_2O$, and $MnCl_2 \cdot 4H_2O$ as the Mn source. PDA has a high affinity towards various metals, including noble metals. Incorporating metals such as Gd, Mn, or Fe into PDA nanoparticles can enhance their magnetic properties and increase their multimodality by adding contrasting properties, which could be useful for MRI imaging. Initially, the modification was performed as a post-synthesis step on purified MPDA NPs. Different NPs:Fe ratios were investigated. The results are summarized in **Table 11**.

Table 11. DLS measurements of MPDA@Fe NPs obtained using different MPDA:Fe mass ratios.

MPDA:Fe*	Z-average/d.nm	PDI	Zeta potential/mV
1:3	452.1±5.8	0.26±0.01	23.4±0.8
1:3	328.6±4.1	0.15±0.02	25.4±0.6
1:1	924.4±90.8	0.62±0.07	-8.4±0.4
1:0.5	741.2±75.1	0.055±0.01	-16.1±0.7
1:0.25	2506.0±559.2	0.89±0.14	-17.5±7.1
1:2	327.2±1.2	0.12±0.03	3.9±1.4
1:1	430.8±13.6	0.26±0.04	2.8±1.1
1:0.5	485.0±7.8	0.28±0.05	2.2±0.2

*mass ratio

The presented results varied between batches and repetitions in both size and zeta potential parameters. Moreover, the nanoparticles with a negative zeta potential experienced extensive aggregation, which would impede the further modification steps, namely coating with cancer cell membranes. Thus, I decided to explore the possibility of incorporating metal ions directly at the synthesis stage. A one-pot synthesis of porous PDAMe nanoparticles has not been

extensively explored. Below, I report my attempts at synthesizing porous PDAMe nanoparticles (Me = Gd, Mn, or Fe) and optimizing the synthesis conditions.

A high abundance of catecholic moieties in the PDA structure enables the chelation of the metal ions, however, the addition of a metal source could disturb the previously established polymerization process [143]. Hence, conditions such as the time point of the metal source introduction and its concentration needed to be designed carefully. Various amounts of the metal source and the time points of its addition were tested. The resulting NPs morphology was evaluated to establish optimal conditions for metal-MPDA NPs synthesis. Examples of such evaluation are presented in **Figure 12**. The details of the source type and amount, as well as DLS physicochemical characterization of the selected examples of MPDAMe synthesis, are summarized in **Table 12**.

TEM images of the selected MPDAMe samples show that all of the selected nanoparticles were of spherical shape and visible porosity. In all investigated examples, nanoparticles with empty cavities of various sizes were observed. Additionally, all of the MPDAMe NPs were of similar size, roughly below 200 nm. However, it was observed that MPDAFe NPs (both (**L**) and (**H**)) were of spherical shape without additional structures, whereas both MPDAGd and MPDAMn NPs had additional structures attached to spherical NPs, which could not be washed off even after several additional cycles of sonication-centrifugation steps. The DLS measurements of the hydrodynamic diameter confirmed the comparable sizes of all of the presented structures. However, the zeta potential differed between the metals. The lowest values were registered for MPDAMn, whereas MPDAGd presented the highest zeta potential among the samples. Interestingly, for MPDAFe and MPDAGd, there was a trend that the samples with a higher amount of metal added (denoted with (**H**)) had higher zeta potential values than the samples with a lower amount of metal (denoted with (**L**)). However, this was not the case for the MPDAMn samples, which both showed similar zeta potential values.

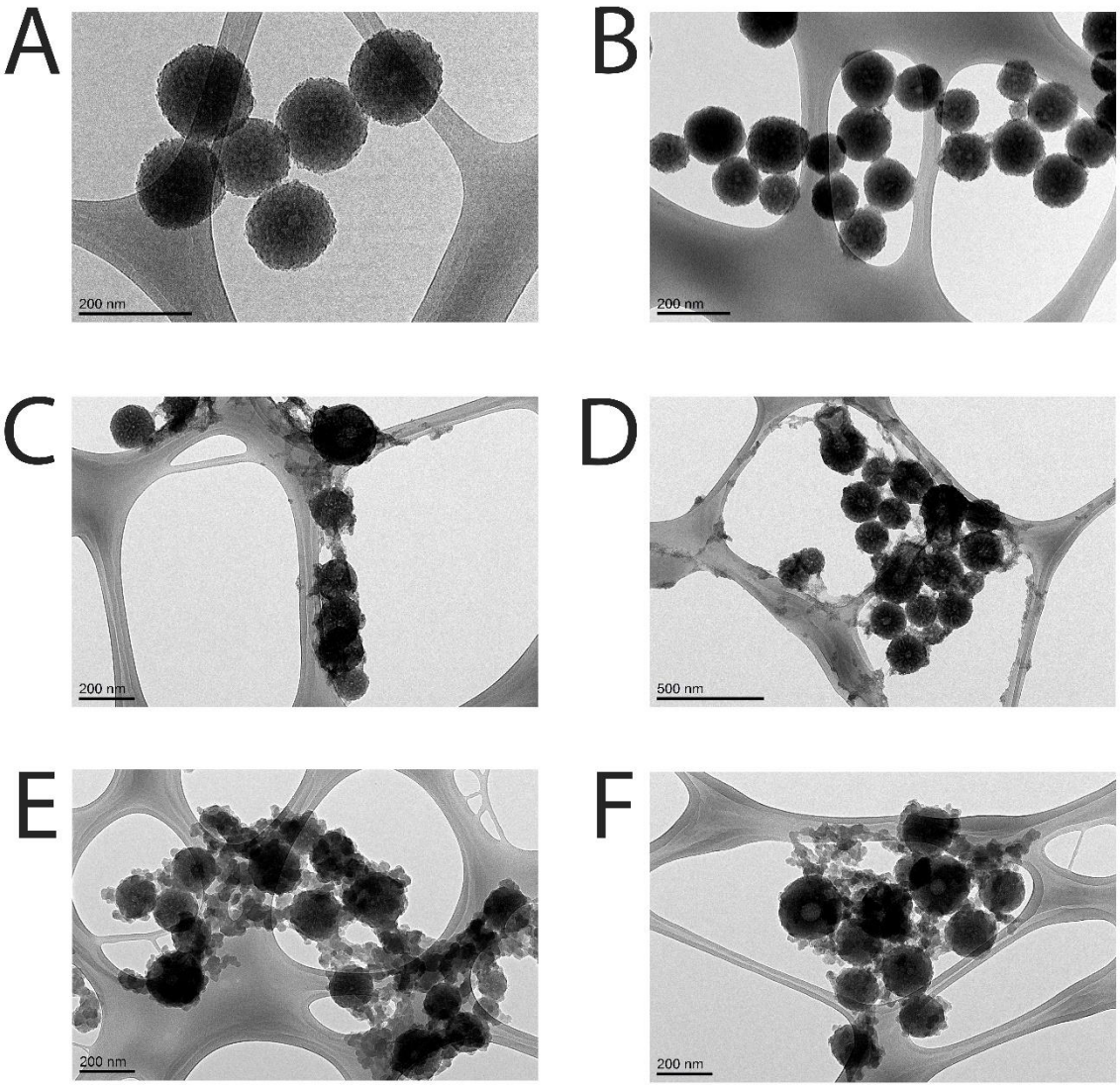

Figure 12. TEM images of selected examples of the MPDAMe synthesis using various concentrations of the metal sources (listed in **Table 12**) at a single addition timepoint of t = 19 h. **A)** MPDAFe(L), **B)** MPDAFe(H), **C)** MPDAGd(L), **D)** MPDAGd(H), **E)** MPDAMn(L), **F)** MPDAMn(H).

Table 12. Results of the DLS measurements of MPDAMe NPs for various metal sources added at t = 19 h. All measurements were performed in triplicates and are presented as mean±SD.

Sample	**MPDAFe(L)**	**MPDAFe(H)**	**MPDAGd(L)**	**MPDAGd(H)**	**MPDAMn(L)**	**MPDAMn(H)**
Metal source	$FeCl_3 \cdot 6H_2O$	$FeCl_3 \cdot 6H_2O$	$GdCl_3 \cdot 6H_2O$	$GdCl_3 \cdot 6H_2O$	$MnCl_2 \cdot 4H_2O$	$MnCl_2 \cdot 4H_2O$
Mass of Me added/µg	75	150	75	150	75	150
Z-average/d.nm	251.0±13.4	209.5±4.6	243.2±0.6	290.0±10.9	252.3±1.4	246.2±3.9
PDI	0.13±0.02	0.11±0.04	0.10±0.02	0.18±0.02	0.11±0.02	0.12±0.04
Zeta potential/mV	-22.7±4.3	0.9±0.8	-11.6±0.4	-1.9±0.5	-25.4±0.3	-25.6±0.6

The selection of the nanoformulations most suitable for further steps according to the design of the desired drug delivery system was based on the morphology and the DLS physical characterization of the obtained structures. Coating with biological membranes was reported to require a negative zeta potential of the optimal results [85]. Moreover, additional structures attached to the spherical nanoparticles could physically disturb the membrane coating. Potential cytotoxicity was also considered, as the requirements for an ideal DDS highlight biocompatibility and low toxicity of the drug carriers. A comparative study on biosafety Mn-, Gd-, and Fe-based contrast agents revealed the latest to exhibit a considerably more stable safety profile compared to Gd- and Mn-based nanoformulations [144]. Moreover, studies on synthetic melanin NPs containing Fe^{3+} ions for MRI imaging did not show any acute cytotoxicity or morphological changes resulting from the NPs incubation with cells [145]. Considering the above factors, the iron source was chosen as the most suitable for further experiments. However, MPD NPs modified with Gd and Mn were further investigated for their magnetic properties and MRI contrasting potential.

In order to further explore the synthesis conditions, several time points and amounts of the iron source addition were analyzed. TEM images of the examples of this investigation are shown in **Figure 13**. The DLS characterization of those particles is summarized in **Table 13.**

Analysis of the TEM images of MPDAFe NPs synthesized at various conditions shows that generally, the later the addition, the more distinct the shape of the resulting nanoformulations. The early addition times resulted in more of a polymer conglomerate rather than separate spherical nanoparticles.

Previous studies show that the presence of a transition metal in a one-pot synthesis influences the polymerization of dopamine. The work by Yang *et al*. suggests that transition metal ions could mediate the polymerization reaction by interacting with dopamine oligomers [146]. The researchers suggest that such ions can act as a ‘catalyst’, accelerating the PDA formation even when introduced several hours after the initiation of the polymerization process. The presence of transition metal ions, especially Fe(III) cations, is known to have a significant impact on polydopamine synthesis by interfering with the oxidation of dopamine through the formation of metal-catecholate complexes [147–149]. However, it has been observed that in the neutral and basic pH conditions (the latter was employed in the synthesis described in this study), the interaction between metals and polydopamine PDA is facilitated through metal-oxygen coordination bonds [149,150]. Unambiguous determination of the metal-PDA

coordination environment is difficult due to the high complexity and structural disorder of this unique polymer. The oxidation of dopamine is a crucial step in polydopamine synthesis, as it generates reactive intermediates that undergo nucleophilic addition reactions to form the polymer backbone [151]. The influence of transition metals on the polymerization of dopamine into polydopamine nanoparticles is attributed to the catalytic role of their ions in the oxidation of dopamine to dopaquinone [147].

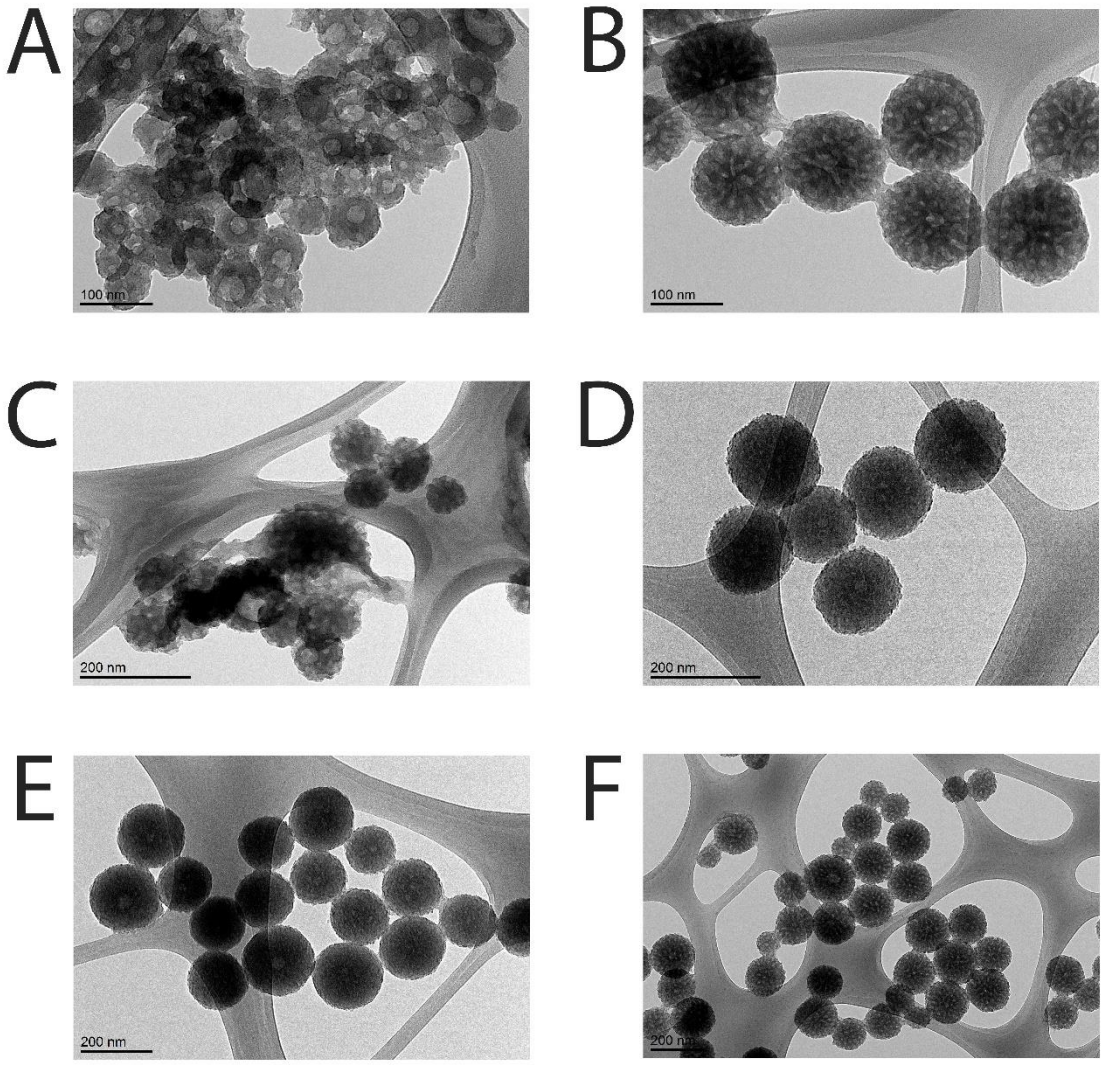

Figure 13. TEM images of selected examples of the MPDAFe synthesis at various conditions (different time points of addition and amount of the Fe source summarized in **Table 13)**. **A)** MPDAFe1, **B)** MPDAFe2, **C)** MPDAFe3, **D)** MPDAFe4/MPDAFe(L), **E)** MPDAFe5, **F)** MPDAFe6.

Table 13. Results of the DLS measurements of MPDAFe NPs for various amounts of metal source added different time points. All measurements were performed in triplicates and are presented as mean±SD. Sample **MPDAFe4** is the same as sample **MPDAFe(L)** in **Table 12**.

Sample	**MPDAFe1**	**MPDAFe2**	**MPDAFe3**	**MPDAFe4**	**MPDAFe5**	**MPDAFe6**
Metal source	$FeCl_3 \cdot 6H_2O$	$FeCl_3 \cdot 6H_2O$	$FeCl_3 \cdot 6H_2O$	$FeCl_3 \cdot 6H_2O$	$FeCl_3 \cdot 6H_2O$	$FeCl_3 \cdot 6H_2O$
Mass of Fe^{3+} added/µg	15	15	75	75	150	150
Timepoint of addition	3 h	21 h	8 h	19 h	7 h	20 h
Z-average/d.nm	447.2±24.91	713.9±59.11	584.5±9,4	251.0±13.4	193.5±3.3	210.6±2.6
PDI	0.46±0.02	0.59±0.03	0.47±0.04	0.13±0.02	0.02±0.01	0.04±0.01
Zeta potential/mV	-27.8±0.8	-31.5±1.3	-12.2±0.9	-22.7±4.3	8.8±0.6	2.1±0.6

These results align well with those presented in this study. It was observed that the early addition of a metal source led to disrupted morphology of the MPDA structures compared to the bare nanoparticles. This suggests that, in the case of porous particles, it is crucial to add the metal source when the porous structure is already established. It is plausible to hypothesize that the metal ions may not only react with dopamine oligomers but also with the template, potentially destabilizing the matrix structure and/or interfering with the interaction between polydopamine structures and emulsion droplets. Consequently, this disruption could hinder the formation of desired porous nanoparticles. On the other hand, if the metal source is added later in the synthesis process, after the PDA polymer has already formed, it can be easily incorporated into the PDA matrix, resulting in the formation of distinct spherical nanoparticles. The delayed addition of the metal source can also prevent the high concentration of metal ions from interfering with the polymerization process.

It is worth noting that the exact mechanism of PDA polymerization and the role of Fe ions, as well as Gd and Mn ions, may depend on the specific synthesis conditions used. For example, the presence of other ions or chemicals, such as oxygen or hydrogen peroxide, can also affect the polymerization process and the resulting MPDA NPs [147]. Different synthesis conditions, such as pH or temperature, may also result in differences in properties and morphology [148,152]. Therefore, a detailed understanding of the molecular-level interactions between dopamine, transition metal ions, and other components of the synthesis system is important for optimizing PDA synthesis and controlling the properties of the resulting nanoparticles. However, in general, the timing and concentration of the metal source addition can play an important role in determining the morphology of the resulting MPDAMe nanoparticles.

Evaluation of metal content

The evaluation of metal content played a crucial role in characterizing the investigated nanoformulations for several reasons. Firstly, it confirms the successful incorporation of metals within the nanoparticles, validating the synthesis process. Secondly, quantification of the metal content was essential for subsequent investigations, such as relaxivity measurements and MRI imaging, where accurate metal concentrations were needed. The metal content assessment was carried out using two complementary techniques: ICP-OES for quantitative analysis and HR-TEM with EDS for visualizing the distribution of metals within the nanoparticles.

The ICP-OES results, summarized in **Table 14**, demonstrated the successful incorporation of iron, gadolinium, and manganese in the respective nanoformulations (MPDAFe, Ferritis, Gadolinis, and Manganis NPs). Interestingly, among the three metals, gadolinium exhibited the highest yield of incorporation into the nanoparticles.

Table 14. Metal content of the four nanoformulations obtained from the ICP-OES analysis.

Sample	Metal content/(μg/mg$_{NPs}$)
MPDAFe	44.3
Ferritis	96.4
Gadolinis	264
Manganis	107

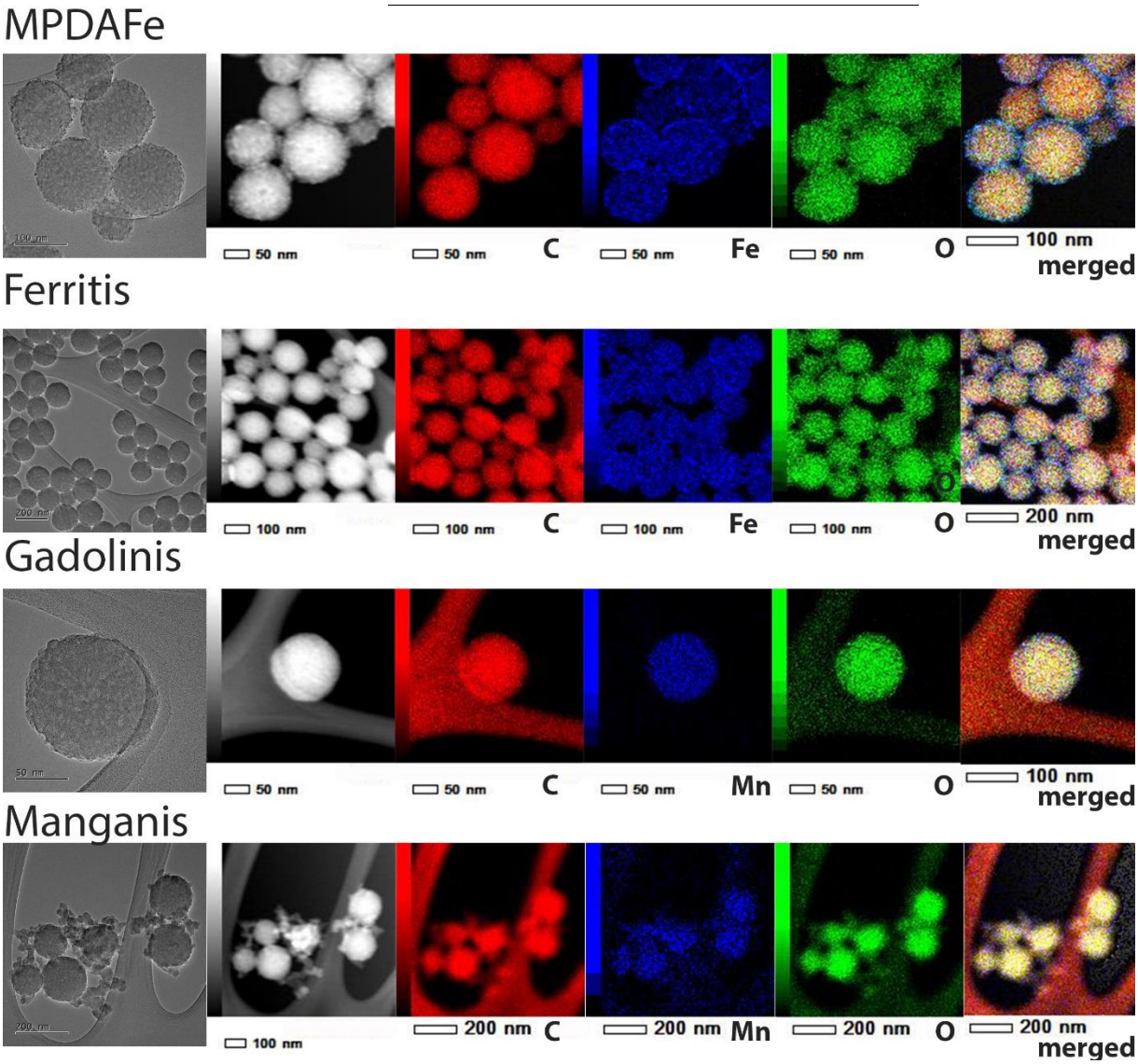

Figure 14. HR-TEM EDS elemental mapping of different nanoformulations. The elements considered in the analysis were: C, Fe/Gd/Mn, and O.

Furthermore, the HR-TEM images with EDS elemental mapping (**Figure 14**) provided visual evidence that all the samples contained metals distributed throughout the entire structure of the nanoparticles rather than being confined only to the surface. This finding confirmed that the chosen time point for the addition of the metal source during the synthesis process was optimal for achieving the incorporation of metal ions within the PDA nanoparticles.

In conclusion, the combined results from ICP-OES and HR-TEM with EDS confirmed the successful and uniform incorporation of metals into the nanoparticles, validating the suitability of the synthesized nanoformulations for further investigation.

Drug loading and release

Investigation of drug release from nanoparticles within diverse buffer solutions, each simulating distinct biological conditions, is an indispensable aspect of studying drug nanocarriers. By replicating various physiological environments, I aimed to comprehensively evaluate the nanoparticles' performance, shedding light on their potential as precise drug delivery systems.

The intracellular pH of healthy cells typically ranges from 7.2 to 7.4 [153]. Cancer tissues tend to have a lower extracellular pH, which is partially connected to a high metabolic rate of tumor cells and reliance on glycolysis for energy production. Additionally, the acidic environment in tumors can be attributed to the accumulation of lactic acid produced by cancer cells as well as the pentose pathway, sodium–hydrogen exchanges, carbonic acid anhydrase activity, and dysfunctional vasculature [154]. Acidic pH between 6.5 and 4.5 is also maintained in endosomes and lysosomes – the intercellular structures through which most drug delivery systems pass when entering a cell [155,156]. This acidity is related to the activity of ATP-dependent proton pumps located in the membranes of endosomes and lysosomes [157]. This difference in pH between healthy and cancer cells can be exploited in DDS by designing drug carriers that are sensitive to changes in pH, allowing for targeted drug delivery to cancer cells while minimizing harm to healthy cells [154].

Glutathione (GSH) is a tripeptide molecule that plays an important role in protecting cells from oxidative stress [158]. It is found at higher concentrations in cancer cells compared to healthy cells, where it helps to maintain the reduced state of the intracellular environment [159]. This higher concentration of GSH in cancer cells can also be exploited in drug delivery systems. Drug carriers can be designed to be responsive to GSH levels, allowing for targeted drug release

in cancer cells where GSH levels are high. Both pH and GSH levels can be designed to trigger drug release from nanocarriers [54,160].

For the drug loading experiments, freshly prepared DOX solution in pH 7.4 PBS buffer was mixed with MPDAFe NPs (0.5:1 w/w of DOX:NPs). After 24 incubation under shaking, the unloaded drug was removed by several cycles of centrifugation. The collected supernatant was then measured using UV-Vis, and the DOX content was evaluated using a standard curve method. The calculated drug loading of DOX into MPDAFe NPs was about 90%, whereas the encapsulation efficiency was around 46%. The drug release from MPDAFe@DOX and NPs in various buffers with and without initial irradiation (808 nm NIR laser with the power of 6 W/cm^2 for 5 min) was evaluated for 72 h. **Figure 15** shows the release of DOX in the tested buffers. The results indicate that the DOX release is the most efficient at pH 4.5+GSH (10 mM), which reflects the tumor microenvironment condition, with the additional stimuli of laser irradiation. The lowest release was observed in pH 7.4, which corresponds to healthy cells. The release of doxorubicin from nanocarriers is higher at lower pH because of the protonation of the amine groups present in the drug molecule, which results in weaker electrostatic interactions between the drug and the carrier matrix [161,162]. Taking advantage of this phenomenon is a common strategy to achieve controlled and targeted release of the drug.

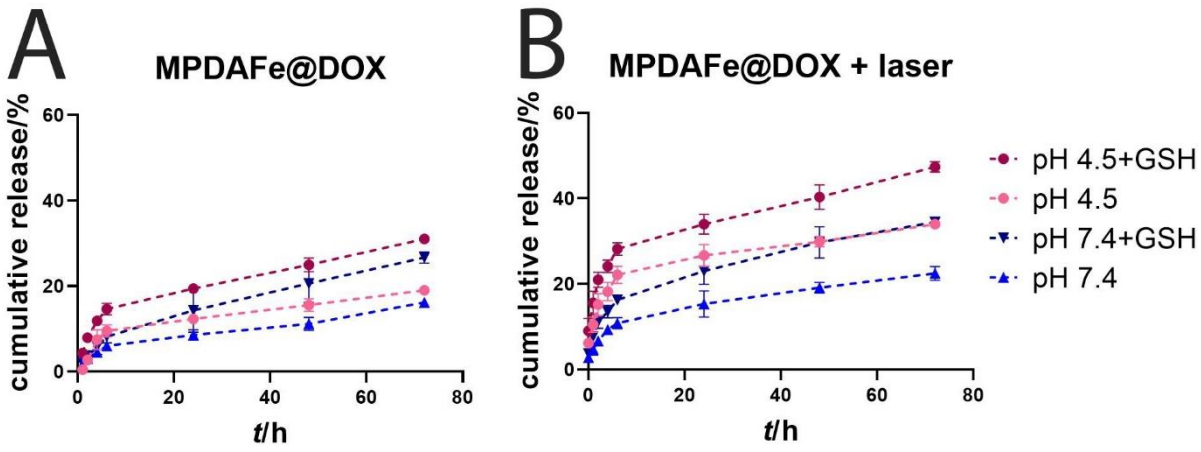

Figure 15. The DOX release from **A)** non-irradiated and **B)** NIR laser-irradiated MPDAFe NPs in various buffers ((citric buffer (10 mM, pH = 4.5); citric buffer (10 mM, pH = 4.5) with 10 mM GSH; PBS buffer (10 mM, pH = 7.4); PBS buffer (10 mM, pH = 7.4) with 10 mM GSH) at 37 °C under shaking (550 rpm). The measurements were performed at chosen time points for 72 h in triplicates. All dashed lines connecting data points on the graphs are guide to the eye of the viewers only.

The obtained release data shows that the presence of GSH also increases the amount of the released active agent. The observed enhancement in drug release can be attributed to the disruption of noncovalent hydrophobic interactions and π–π stacking between the aromatic regions of the PDAFe nanoparticles and DOX. Similar phenomena have been observed in graphene oxide systems [132,163]. Moreover, the findings revealed a substantial increase in the release of DOX from MPDAFe nanoparticles upon NIR laser irradiation, as compared to the release outcomes without laser irradiation. Overall, the presence of glutathione in the biological environment, combined with the lower pH of cancer cells and laser irradiation of the selected region, may stimulate the release of therapeutic agents from MPDAFe nanoparticles, offering a promising approach for controlled drug release and targeted cancer therapy.

Drug release kinetics

Drug delivery systems are designed to control the rate and extent of drug release, which can influence therapeutic efficacy and patient safety. Sustained and controlled release of therapeutic agents is essential for achieving optimal therapeutic outcomes. Mathematical models are useful for describing and predicting drug release kinetics from different types of drug delivery systems. Five commonly used mathematical models of drug release: zero-order model, first-order model, Higuchi's model, Korsmeyer-Peppas model, and Hixson-Crowell model were chosen for the analysis of the obtained release data.

The zero-order model assumes that the rate of drug release is independent of drug concentration and follows a constant release rate over time. This model describes drug dissolution from dosage forms that do not disaggregate and release the drug slowly [164]. The equation for zero-order release is:

$$Q = k_0 t \qquad (4)$$

where Q is the amount of the drug released at time t, k_0 is the release rate constant, and t is time. The slope of the release curve is equal to the release rate constant, which can be determined experimentally. The main advantage of the zero-order model is its simplicity and ease of interpretation. However, it may not accurately describe drug release from systems with finite drug solubility or diffusion-limited release [165].

The first-order model assumes that drug release is proportional to the amount of drug remaining in the nanocarrier, resulting in an exponential decay in drug release over time. This

model is commonly used to describe drug release from porous systems containing water-soluble drugs [164]. The equation for first-order release is:

$$ln\left(\frac{C}{C0}\right) = -kt \qquad (5)$$

where $\boldsymbol{C}$ is the drug concentration at time *t*, $\boldsymbol{C_0}$ is the initial drug concentration, $\boldsymbol{k}$ is the release rate constant, and $\boldsymbol{t}$ is time. The slope of the release curve is equal to the release rate constant, which can be determined experimentally. The first-order model can provide insight into the mechanisms of drug release, however, it may not accurately describe drug release from systems with complex drug-polymer interactions or non-linear release kinetics.

Another popular model is **Higuchi's model**, which describes drug release from a matrix system and assumes that drug release is proportional to the square root of time and is based on Fick's law of diffusion. This model is commonly used to describe drug release from polymeric matrices or gels. The equation for Higuchi's model is:

$$Q = k_H t^{1/2} \qquad (6)$$

where $\boldsymbol{Q}$ is the amount of the drug released at time *t*, $\boldsymbol{k_H}$ is the release rate constant, and **t** is time. The slope of the release curve is proportional to the square root of time and is equal to the release rate constant, which can be determined experimentally. Higuchi's model assumes that drug release occurs by diffusion through a homogeneous matrix and does not account for other mechanisms, such as erosion or swelling [166]. It may not accurately describe drug release from systems with complex polymer structures or drug-polymer interactions.

The Korsmeyer-Peppas model is a semi-empirical model that assumes that drug release occurs by a non-Fickian mechanism combined with more than one type of drug release phenomenon, such as swelling or erosion [165]. This model is commonly used to describe drug release from polymeric matrices, nanoparticles, or hydrogels and assumes that drug release follows a power-law relationship with time. The equation for Korsmeyer-Peppas release is:

$$\frac{M}{M_\infty} = kt^n \qquad (7)$$

where $\boldsymbol{M}$ is the amount of drug released at time *t*, $\boldsymbol{M_\infty}$ is the total amount of the drug in the nanoparticle, $\boldsymbol{k}$ is the release rate constant, n is the release exponent, and the release mechanism is determined by the value of $\boldsymbol{n}$. For example, if $n = 0.5$, the release mechanism is Fickian diffusion, whereas if $n > 0.5$, the release mechanism is non-Fickian and can be attributed to swelling, erosion, or relaxation of the polymer matrix.

The Hixson-Crowell model describes drug release from systems in which the rate-limiting step is the erosion or dissolution of the nanocarrier. This model assumes that the rate of drug release is proportional to the cube root of the amount of drug remaining in the nanoparticle. The mathematical equation for the Hixson-Crowell model is:

$$(M_0 - M_t)^{\frac{1}{3}} = kt \qquad (8)$$

where M_0 is the initial mass of the drug in the formulation, M_t is the mass of the drug remaining in the formulation at time *t,* and k is a constant that depends on the properties of the drug and the formulation, as well as the conditions of the dissolution test.

This equation describes a cubic root relationship between the mass of the drug remaining and time. It assumes that the drug release rate is proportional to the surface area of drug particles, which decreases as the particles dissolve [164]. Therefore, the cubic root term reflects the reduction in surface area as drug particles dissolve over time. The equation is often used to estimate the release kinetics of poorly water-soluble drugs from solid dosage forms, such as tablets and capsules [164].

The model fitting was performed using an Excel add-in program, DD Solver 1.0, developed by Zhang *et al.* [167]. The R^2 values established for all of the release conditions are presented in **Table 15**. Representative fitting curves of MPDAFe@DOX in pH.45+GSH release with and without laser irradiation are shown in **Figure 16**.

Table 15. R^2 values calculated for each of the analyzed models.

Sample	Buffer	Zero-order	First-order	Higuchi	Korsmeyer-Peppas		Hixson-Crowell
		R^2	R^2	R^2	R^2	n	R^2
MPDAFe@DOX	pH 4.5	0.1702	0.2421	0.8298	0.9374	0.341	0.2184
	pH 4,5+GSH	0.3003	0.3965	0.8947	0.9738	0.359	0.3653
	pH 7,4	0.6653	0.6887	0.9603	0.9670	0.448	0.6811
	pH 7,4+GSH	0,8277	0.8626	0.9933	0.9951	0.532	0.8516
MPDAFe@DOX+laser	pH 4.5	-0.9287	-0.7189	0.3348	0.9118	0.216	-0.7888
	pH 4,5+GSH	-0.7407	-0.4591	0.4190	0.9510	0.228	-0.5518
	pH 7,4	0.0999	0.1727	0.7967	0.9636	0.228	0.1487
	pH 7,4+GSH	-0.1317	-0.0203	0.6906	0.9554	0.268	-0.0570

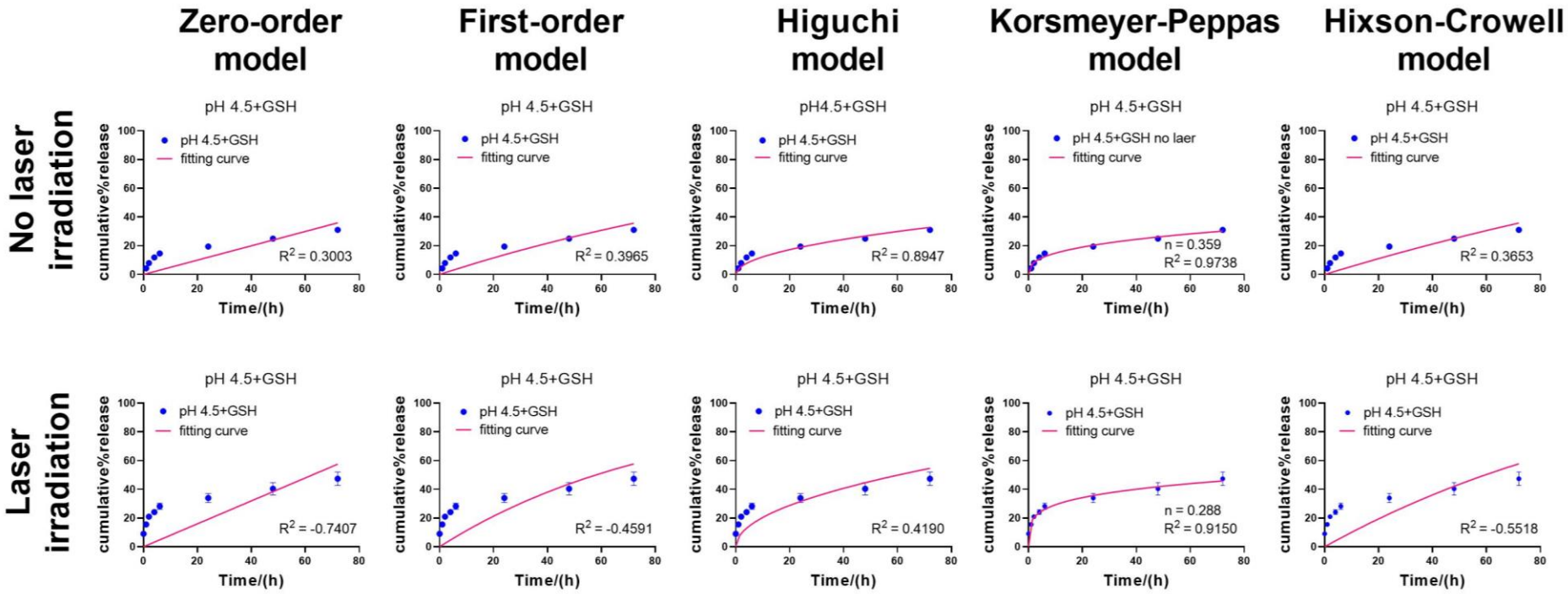

Figure 16. Representative model fitting of five drug release models: Zero-order, first-order, Higuchi, Korsmeyer-Peppas, and Hixson-Crowell, fitted to two release data samples: MPDAFe@DOX NPs in pH 4.5+GSH buffer with and without the laser irradiation. R^2 values are presented on each graph.

Among the tested models, the Korsmeyer-Peppas model demonstrated the best fit for all tested scenarios, exhibiting the highest R-squared (R^2) values. The *n* values, which indicate the release mechanism, ranged from 0.341 to 0.532 for the samples without laser irradiation and from 0.216 to 0.268 for the samples with laser irradiation.

The Korsmeyer-Peppas model is commonly used to analyze drug release from polymeric matrices, and it describes the release behavior by considering both Fickian and non-Fickian diffusion processes. When the release mechanism follows Fickian diffusion, the value of the release exponent *n* is equal to 0.5 [164]. On the other hand, if the value of *n* is lower or higher than 0.5, it indicates a non-Fickian or anomalous transport mechanism, where factors like swelling, erosion, or polymer relaxation contribute significantly to the drug release process [164]. However, several studies showed the interpretation of the *n* values below 0.5 (the reported values oscillate between 0.057 and 0.45) as Fickian diffusion [164,168–170] or even 'quasi-Fickian' [171]. Hence, the definite determination of the diffusion mechanism of DOX from MPDAFe nanoparticles is highly difficult.

Interestingly, the Higuchi model also displayed a high R^2, especially for the samples without laser irradiation. However, the other models, including zero-order and first-order, exhibited poor fitting results, with some cases even displaying negative values. The good fit of the Higuchi model for drug release data indicates that the drug release from the nanoparticles follows a diffusion-controlled mechanism [166]. The observation that the Higuchi model does not fit well for the laser-irradiated samples indicates a change in the drug release mechanism compared to the non-irradiated samples. When the Higuchi model fails to provide a good fit, it suggests that factors other than pure diffusion may be influencing the drug release behavior. The deviation from the Higuchi model for the laser-irradiated samples could indicate that drug release is now affected by multiple factors, such as photothermal-induced drug release or nanoparticle degradation, in addition to diffusion [172]. This complexity could lead to drug release profiles that do not conform to the simple diffusion-based Higuchi model.

In summary, the results indicate that the drug release from MPDAFe@DOX NPs is governed by non-Fickian diffusion and that laser irradiation further enhances this behavior. Understanding the release mechanism and the effect of laser irradiation is essential for optimizing the drug delivery system's therapeutic efficacy and tailoring it to specific applications, such as targeted cancer therapy. These findings suggest that the drug release from MPDAFe@DOX NPs follows a diffusion process, indicating a controlled and sustained release

pattern. The laser irradiation seemed to slightly alter the release mechanism, as evidenced by the variations in the *n* values of the Korsmeyer-Peppas model and the decreased fitting of the Higuchi model. Overall, the results demonstrate the importance of considering the release kinetics when designing drug delivery systems, and the Korsmeyer-Peppas model appears to be the most suitable for predicting drug release from the investigated NPs under different conditions. However, it is worth noting that in drug delivery studies, there is no universal mathematical model that covers all of the issues or that would fit to every drug delivery system.

Membrane coating

Over the past years, membrane coating of the drug nanocarriers has been gaining growing attention due to the relative simplicity, versatility, and wide range of beneficial properties that the natural membrane can offer to artificial nanostructures in drug delivery. Strategies for coating nanoparticles with cell membranes include using sonication or coextrusion to fuse the membranes onto the surface of the NPs. Sonication involves subjecting the NPs and cell membranes to high-frequency sound waves, which disrupt the membranes and create transient pores in their surfaces [18]. When the NPs and membranes are mixed together, the pores allow the membranes to fuse onto the surface of the NPs and form a stable coating. Coextrusion, on the other hand, involves passing a mixture of NPs and cell membrane vesicles through a small pore size filter, which causes the membranes to fuse onto the surface of the NPs as they pass through the filter.

As mentioned earlier, liver cancer was selected as a model cancer type for this project. Hence, the HepG2 cell line of hepatocellular carcinoma was used as a source for the membrane coating. The successful separation of the cell fractions was investigated by performing SDS-PAGE electrophoresis (**Figure 17**). The distinct protein patterns of each fraction (WC – whole cell, Cyt – cytosol, Mem – membrane) confirm the successful isolation of both cytosolic and membrane proteins.

The membrane vesicles were formed using an extrusion technique. The membrane solution in water (1 mg/mL) was mechanically passed 15-20 times through a Mini Extruder with polycarbonate filters with a pore size of 400 nm, followed by 15-20 passes through filters with pores of 200 nm. The size and zeta potential of the resulting vesicles were measured using DLS. At the early stage of the research, just before coating, a solution of MPDA@Fe, MPDAFe, or MPDAFe@DOX in water or PBS buffer was sonicated for 5 min using the bath sonicator.

Subsequently, the solutions of nanoparticles and membranes were mixed at different mass ratios: 1:2 and 1:3 (m_{NPs}:$m_{membranes}$). At first, two methods of coating were examined. For the coextrusion method, the procedure was similar to the formation of membrane vesicles. The mixture of nanoparticles and membrane vesicles was passed through polycarbonate filters with specific pore sizes (400 and 200 nm) for a total of 10 repetitions. The second method involved placing the mixture of nanoparticles and membrane vesicles in the bath sonicator for 2, 5, 6, 8, and 10 min. The resulting solutions were examined using DLS for hydrodynamic diameter and zeta potential measurements, and TEM microscopy was used for imaging.

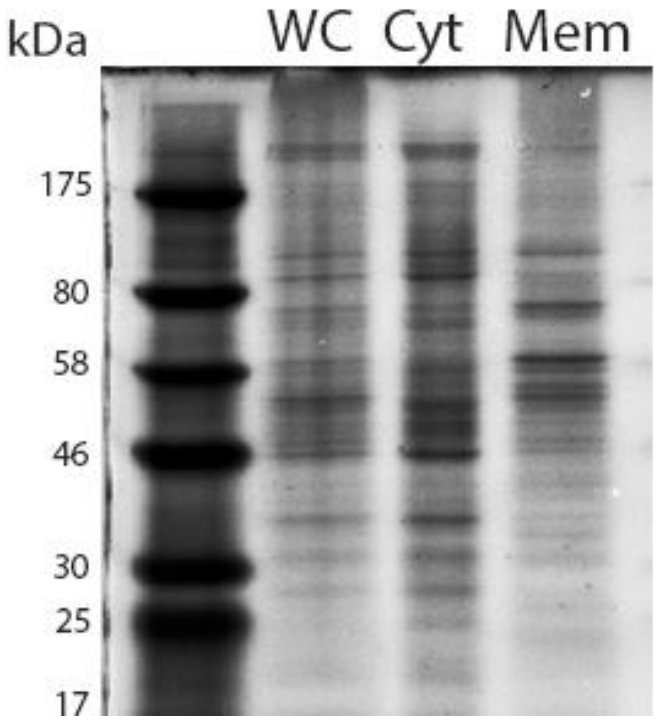

Figure 17. SDS-PAGE electrophoresis of three cell fractions: WC (whole cell), Cyt (cytosol), and Mem (membrane) on 10% polyacrylamide gel. A pre-stained protein market of a broad range (7-175 kDa) was used for size reference.

The initial attempt at coating using the coextrusion method was carried out in PBS buffer, but it failed, possibly due to the buffer-induced aggregation of the nanoformulations. Consequently, the material remaining on the filters blocked the pores of the polycarbonate filters, preventing the coating of nanoparticles. Subsequent tests were conducted in aqueous solutions. The bath sonication method did not yield satisfactory results (data not shown), as the DLS measurements exceeded the reliability limit of the technique (> 1 μm), indicating its inefficiency. Slightly

better results were achieved by coextrusion of aqueous solutions of nanoparticles and membrane vesicles. The DLS measurements are presented in **Figure 18**. Importantly, the data shown on the graph was obtained for nanoparticles modified with iron post-synthesis (MPDA@Fe) loaded with DOX.

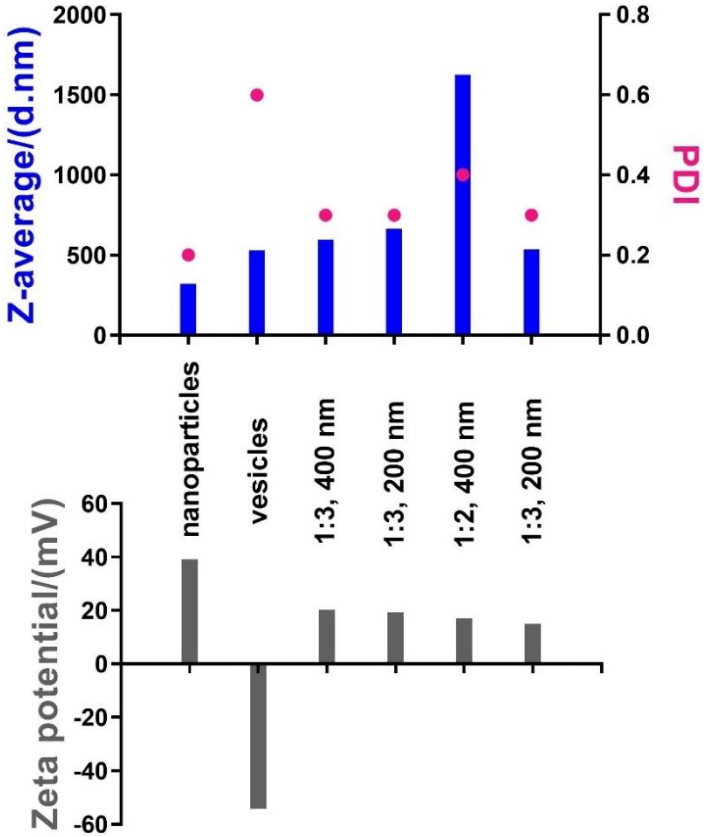

Figure 18. Results of the DLS measurements of MPDA@Fe@DOX nanoparticles coated with HepG2 cell membranes. In the graph from the left: Nanoparticles - uncoated PDA nanoparticles functionalized with iron and loaded with doxorubicin (MPDA@Fe@DOX NPs), Vesicles - vesicles of cell membranes of HepG2 cells, consecutive numbers indicate the mass ratio of NPs:membrane during co-extrusion (1:3/1:2) and the size of the polycarbonate filter (400/200nm).

The sizes of the coated structures obtained were similar to the size of the vesicles, while the zeta potentials were lower than those of the particles but much higher than the potentials of the vesicles themselves. This may indicate incomplete coverage of the particles and the presence of uncoated nanoparticles in the solution. Moreover, extensive clogging of the filters was observed, hence, it was decided to switch to 800 nm filters to avoid material loss. Further investigation focused on negatively charged nanoparticles synthesized with the one-pot methods (MPDAFe). Additionally to the previously mentioned coating techniques, a high

power sonication was included in the investigation. The experimental procedure consisted of two steps: at first, the nanoparticles alone were sonicated using a pulse sequence (1 s on, 2 s off) for a total pulse duration of 1.5 min at the power of 160 W. Next, the nanoparticles were mixed with pre-made using membrane vesicles and sonicated using a similar pulse sequence but at the power of 125 W. The tube containing the sonicated samples was immersed in water during the duration of the procedure. The data obtained from all three methods and two different NPs:membrane protein mass ratios (1:1 and 1:0.1) are summarized in **Figure 19**.

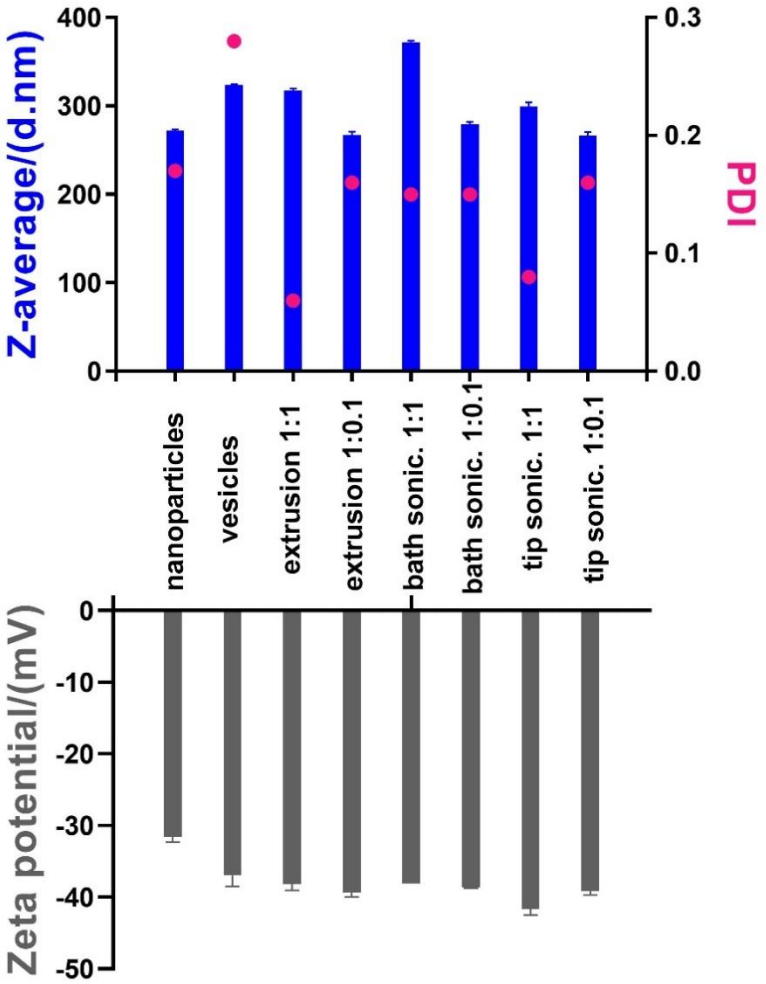

Figure 19. Results of the DLS measurements of MPDAFe nanoparticles coated with HepG2 cell membranes. In the graph from the left: nanoparticles - uncoated MPDAFe nanoparticles, Vesicles - vesicles of cell membranes of HepG2 cells, consecutive numbers indicate the mass ratio of NPs:membrane protein during extrusion, bath sonication, and tip sonication (1:1/1:0.1 w/w).

To understand the composition and stability of membrane-coated nanoparticles, I conducted an SDS-PAGE analysis, which separates proteins based on their molecular weight. This

approach allows for verification of the successful integration of the biomimetic membrane onto the nanoparticle surface and assessment of any potential alterations in protein composition during the coating process. SDS-PAGE electrophoresis was performed to compare the protein composition on the surface of nanoparticles coated with different techniques (**Figure 20**). The samples were centrifuged before the procedure to ensure that the visualized proteins were attached to the surface of nanoformulations. Representative supernatant of the centrifuged samples was also included in the experiment. The obtained results confirmed the presence of proteins on the MPDAFe@Mem NPs obtained using all of the tested methods. The patterns visible in **Figure 20** correspond to the protein pattern of the isolated membrane fraction (Mem). The separation of the Supernatant fraction revealed a similar protein pattern, however, certain bands are missing compared to membrane coated-nanoparticles and pure membrane samples.

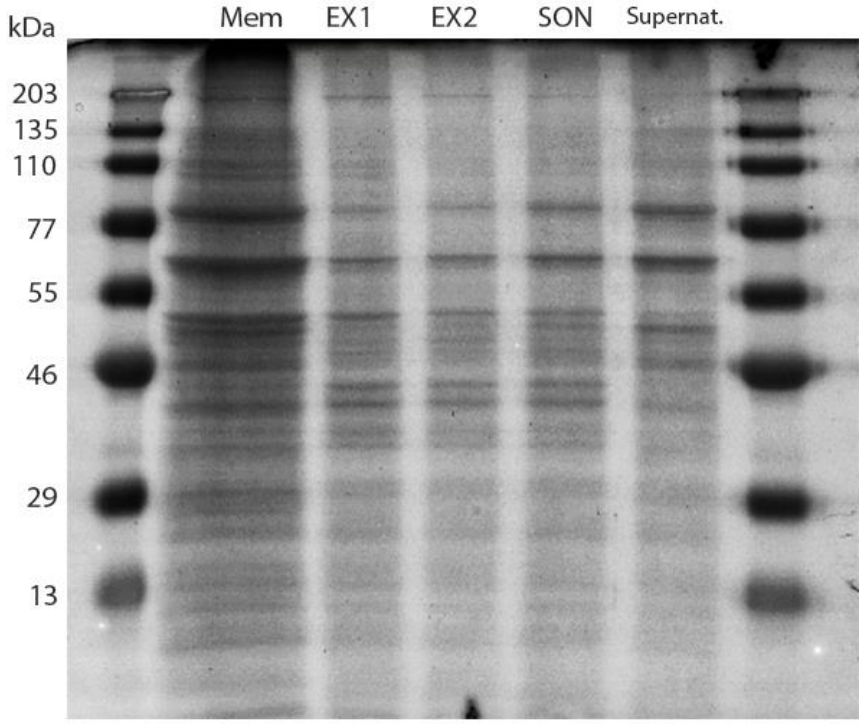

Figure 20. SDS-PAGE electrophoresis of MPDAFe@Mem NPs obtained using different coating techniques. WC – whole cell lysate, Mem – isolated cell membrane fraction, EX1 – extrusion with 800 nm filters, EX2 – extrusion with 400 nm filters, SON – high power sonication, Supernat. – supernatant of the centrifuged MPDAFe@Mem samples. Separation was performed on 10% polyacrylamide gel. Size reference: mPAGE™ Color Protein Standard, 10 to 203 kDa.

Further assessment of the membrane-coated nanoformulations was based on the TEM images (not shown) and was predominantly focused on the extent of the coated particles observed, as well as the coating degree. Careful analysis of the obtained data resulted in selecting extrusion

and high power sonication as the most effective techniques, and the ratio of 1:1 NPs:membrane protein as the most beneficial for the process. The evaluation was based on the increase of the MPDAFe NPs' Z-average after the coating, which matched the theoretical width of the cell membrane [173,174]. Although the zeta potential of the coated nanoformulations in all cases decreased accordingly with the value of the membrane vesicles, the PDI values suggested high polydispersity of the majority of the testes variants except for the extrusion 1:1 and sonication 1:1. Thus, it was decided to combine the two methods: co-extrusion and high power sonication. Importantly, by pre-sonicating the samples, I was able to eliminate the issue of clogging the extrusion filters by the nanoparticles, which increased the efficiency of the process and limited mass loss during the coating procedure. The results of the coating using the final procedure are presented in **Table 16**. The TEM images of the representative MPDAFe@Mem NPs are shown in **Figure 21**. Uracyl acetate staining was used to visualize the membrane coatings on the images.

Table 16. DLS evaluation of the coating efficacy of MPDAFe NPs using combined high power sonication and co-extrusion method.

Sample	Z-average/d.nm	PDI	Zeta potential/mV
MPDAFe	227.6±1.6	0.11±0.01	-17.7±0.7
Vesicles	214.9±71.1	0.47±0.15	-45.5±8.4
MPDAFe@Mem	242.2±0.7	0.05±0.03	-38.4±0.3

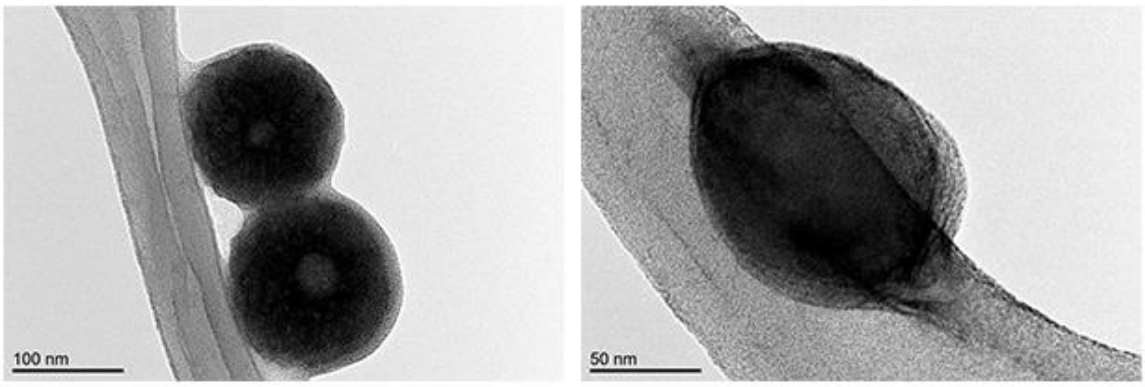

Figure 21. TEM images of MPDAFe@Mem NPs coated using combined high power sonication and co-extrusion technique. The membrane of the MPDAFe@Mem was stained with uranyl acetate.

The final nanoformulations were further examined using SDS-PAGE electrophoresis and Western blotting analysis (**Figure 22**). The SDS-PAGE protein patterns observed in the membrane isolate (Mem), membrane vesicles (Ves), and membrane-coated MPDAFe (NP@Mem) exhibited a significant level of similarity, indicating the successful translocation of membrane proteins onto the nanoparticles (**Figure 22A**). Furthermore, specific proteins that are exclusively present in cell membranes, namely Glypican 3 and Na+/K+ ATPase, were identified in the membrane isolate fractions (**Figure 22B**). These results further confirm the integrity of the membrane proteins and their successful integration into the membrane-coated nanoparticles. Conversely, the cytosolic protein GAPDH was solely detected in the cytosol isolate fraction. This differential distribution reinforces the specificity of the membrane protein isolation process and highlights the selective translocation of membrane proteins onto the nanoparticles.

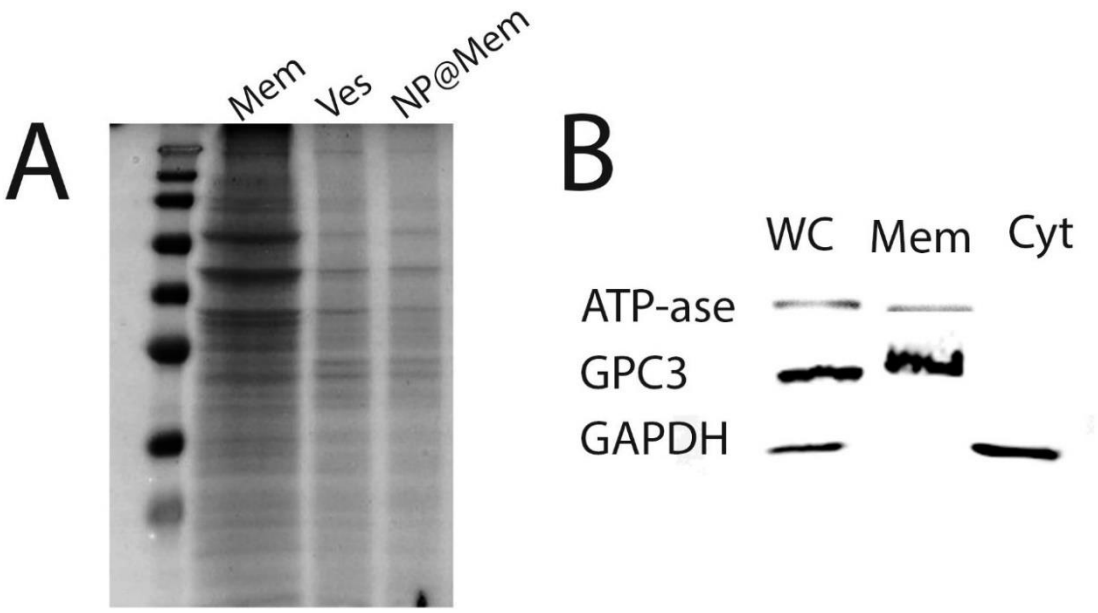

Figure 22. Protein analysis of MPDAFe@Mem NPs. **A)** SDS-PAGE gel separation of membrane fraction (Mem), membrane vesicles (Ves), and membrane-coated NPs (NP@Mam), **B)** Western blotting identification of selected membrane proteins; in whole cell lysate (WC), membrane fraction (Mem) and cytosolic fraction (Cyt) – membrane proteins Na+/K- ATP-ase (110 kDa), Glypican 3 (66 kDa), and a cytosolic protein GAPDH (36 kDa).

The successful preservation and translocation of membrane proteins onto the membrane-coated nanoparticles hold great significance for targeted drug delivery systems. Membrane proteins play key roles in cellular signaling, transport, and recognition processes, making them attractive targets for therapeutic interventions [65]. By incorporating these membrane proteins into the drug delivery system, it becomes possible to enhance the specificity and efficacy of the drug delivery system [65].

Eventually, the stability of the coated nanoparticles over time was evaluated. The results of the DLS measurements are summarized in **Figure 23**, comparing the stability of MPDAFe@DOX@Mem NPs in water and two re-suspended lyophilized nanoformulations: MPDAFe@Mem and MPDAFe@DOX@Mem NPs. For the freshly prepared MPDAFe@DOX@Mem NPs in water, no significant changes were observed in the hydrodynamic diameter, polydispersity, or zeta potential, indicating their excellent stability as membrane-coated nanocarriers. However, in the case of lyophilized nanoparticles re- suspended in water, changes, especially in the hydrodynamic diameter, were detected. These observations suggest that the stability of the coated nanoformulations may decrease after the lyophilization process. Further investigation is necessary to understand the underlying factors contributing to the observed changes in size, providing insights for the optimization of formulation and storage conditions to maintain the stability of these promising nanostructures.

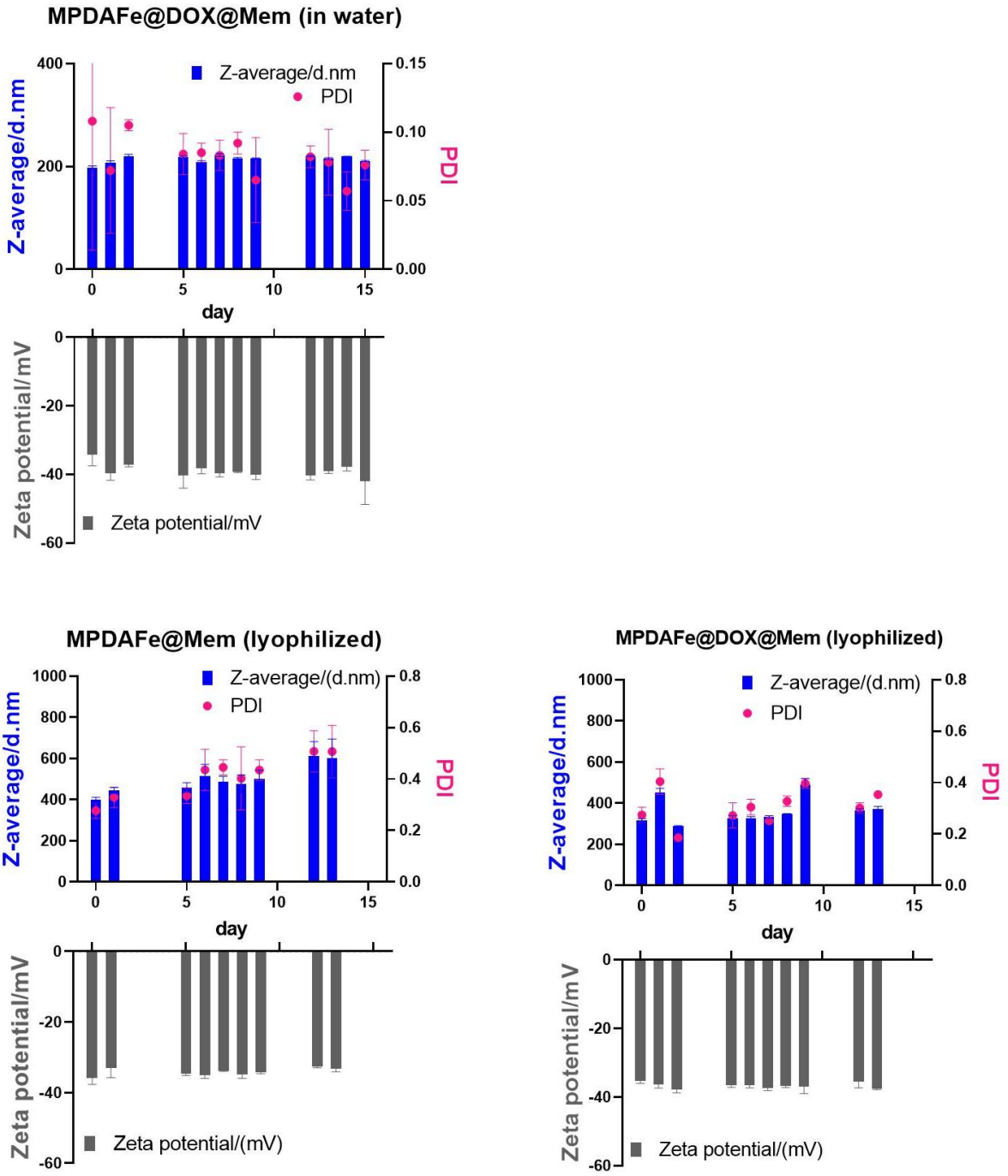

Figure 23. DLS evaluation of the stability of MPDAFe@DOX@Mem NPs in water and re-suspended lyophilized MPDAFe@Mem and MPDAFe@DOX@Mem NPs for the course of two weeks. All solutions were stored at 4 ºC.

Photothermal properties

Photothermal therapy is based on converting near-infrared (650-900 nm) light into heat by a photothermal agent (PTA). The photothermal effect is associated with the energy transition performed by the irradiated PTA, resulting in a local temperature increase that may lead to the thermal ablation of tumor cells. Polymeric PTAs are often superior to inorganic PTAs in various aspects, including low toxicity and biocompatibility [46]. It is often employed as a non-invasive therapeutic modality in cancer treatment owing to its efficiency and spatial targetability [175].

PDA exhibits strong photothermal properties due to the absorption of light in the near-infrared (NIR) region, which is a tissue-penetrating wavelength range in the so-called first biological window [176]. When exposed to NIR light, PDA NPs absorb the energy and convert it into heat through a process known as non-radiative relaxation [176]. This localized heating effect causes the temperature of the surrounding environment to increase, resulting in a photothermal response. The extent of the photothermal response depends on the concentration of PDA nanoparticles, the power of the NIR light, and the duration of the exposure. The photothermal response of MPDAMe NPs (Me = Fe, Gd, or Mn) was examined by irradiating the nanoparticle solutions placed in a quartz cuvette by an 808 nm laser for 5 min. The distance between the laser and the cuvette was 5 cm. The temperature was controlled either by a thermocouple (measurement every 10 s) or by a thermal camera (pictures taken every 30 s).

The investigation into the photothermal properties of MPDAFe nanoparticles commenced with an assessment of the impact of laser power on temperature elevation, as depicted in **Figure 24**. The graphs present a comparison of three MPDAFe NP concentrations: 10, 25, and 50 µg/mL, alongside a water control, subjected to three distinct laser powers: 6, 3, and 2 W/cm^2 (**Figure 24A,B**, and **C**, respectively). The results revealed a direct correlation between concentration and temperature increase upon irradiation, with higher concentrations leading to greater temperature elevations. Moreover, the highest temperatures were achieved with the application of the strongest laser power. For instance, at a concentration of 50 µg/mL, the temperature rose by 30 ºC, while the same concentration experienced temperature increases of 15 ºC and 10 ºC under 3 and 2 W/cm^2, respectively. These observations underscore the photothermal efficacy of the MPDAFe nanoparticles and their potential for thermal applications.

To assess the impact of membrane coating on the photothermal properties of the nanoparticles, three different concentrations of MPDAFe@Mem NPs were subjected to two laser powers, and

the outcomes were measured using a thermocouple, as shown in **Figure 25** (**A** – 3 W/cm^2, **B** – 6 W/cm^2). The data indicates that the membrane coating had minimal influence on the temperature elevation caused by laser irradiation. This result was further corroborated by thermal camera measurements (**Figure 26**), which confirmed that the membrane coating hardly affected the temperature response during irradiation. These compelling findings suggest that the membrane-coated nanoparticles retain their photothermal efficiency, making them promising candidates for targeted photothermal therapy applications.

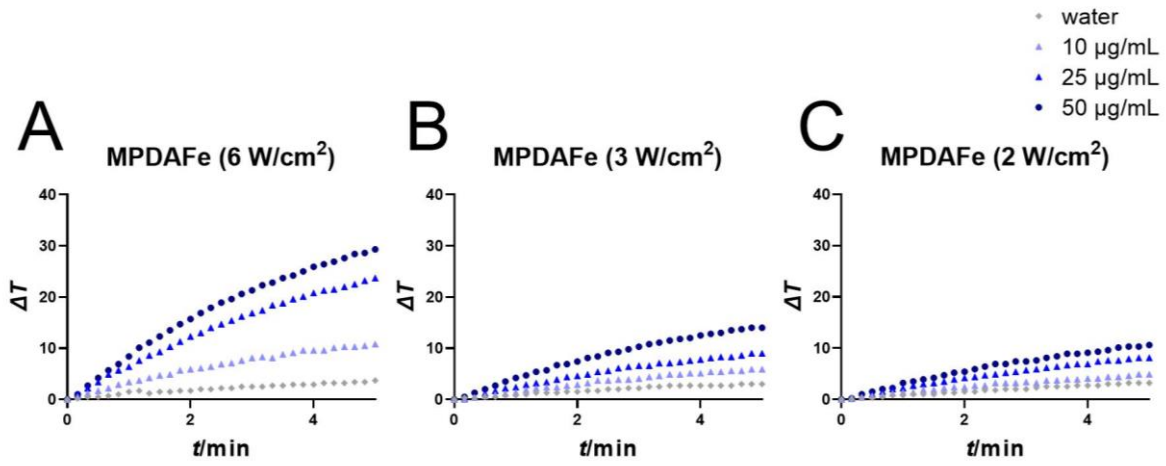

Figure 24. Influence of laser power on temperature increase of various concentrations of MPDAFe solution in water. **A**) 6 W/cm^2, **B)** 3 W/cm^2, **C)** 2 W/cm^2.

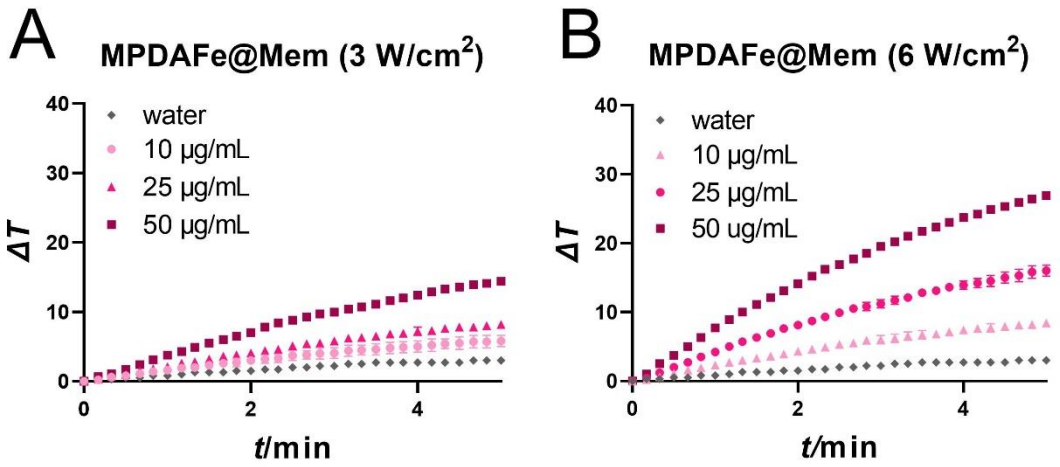

Figure 25. Photothermal properties of MPDAMe@Mem – temperature change of 3 different concentrations (10, 25, and 50 µg/mL) of the nanoformulations under 5 min irradiation with 808 nm laser at the power of **A**) 3 W/cm^2 and **B)** 6 W/cm^2. Temperature change was registered using a thermocouple. Measurements were performed in triplicates. The results are presented as mean±SD. The majority of the error bars are too small to be visible on the graph.

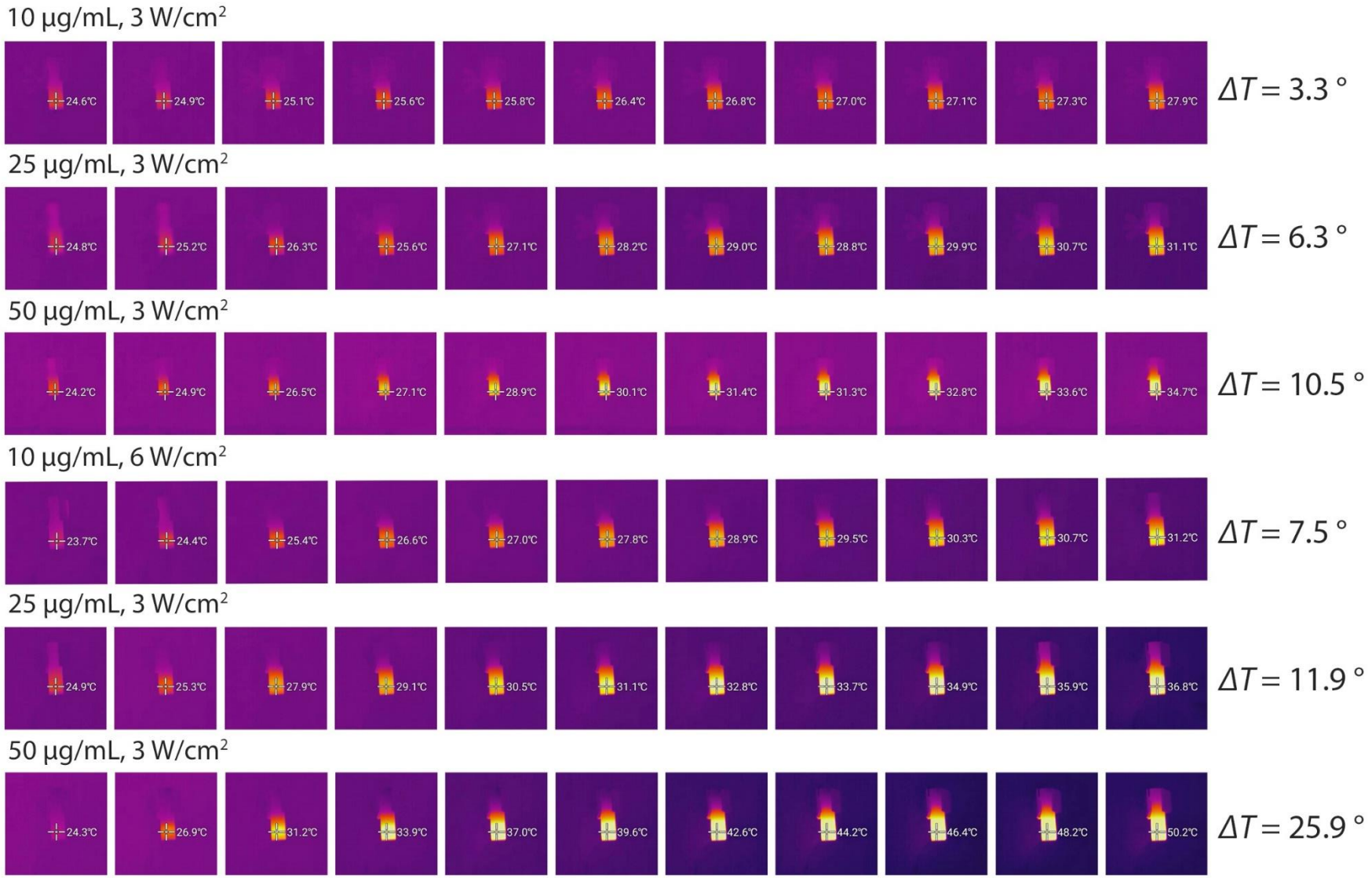

Figure 26. Photothermal properties of MPDAFe@Mem – temperature change of 3 different concentrations (10, 25, and 50 µg/mL) of the nanoformulations under 5 min irradiation with 808 nm laser at the power of 3 and 6 W/cm^2. Temperature change was registered using a thermal camera.

Eventually, the stability of the thermal response was evaluated. Five irradiation cycles of nanoparticle solutions with continuous temperature measurement were carried out. Two laser powers were compared. Moreover, the influence of membrane coating was included in the investigation. The results are presented in **Figure 27**. The temperature increase upon each irradiation repetition was constant in all cases. Moreover, the membrane coating did not cause any visible changes in the thermal stability of the tested materials. The obtained results are significant for the possibility of using the tested materials in photothermal therapy. The constant temperature response ensures the stability of the potential treatment and the reproducibility of the results, which can increase the therapeutic effect of the system.

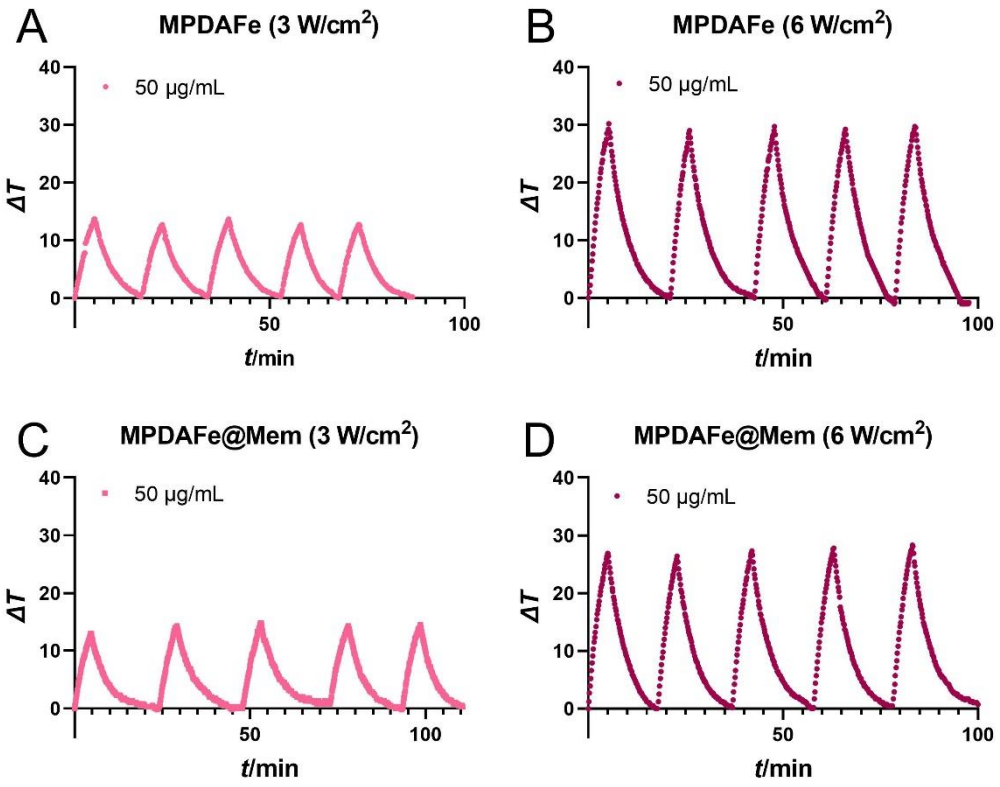

Figure 27. Thermal stability of **A,B)** MPDAFe and **C,D)** MPDAFe@Mem NPs. Five repetitions of laser irradiation-cooling cycle at two different laser powers – 3 and 6 W/cm^2 (808 nm laser, 5 min irradiation from 10 cm distance).

A comparative analysis of photothermal properties was conducted for nanoparticles containing three different metals: Fe, Gd, and Mn (Ferritis, Gadolinis, and Manganis NPs, respectively). The results, presented in **Figure 28**, indicate that all three nanoformulations exhibited a temperature increase of approximately 20 ºC at a concentration of 200 µg/mL and around 10 ºC at 50 µg/mL. Despite slightly lower temperature elevation observed for Gadolinis NPs compared

to the other two formulations, the data suggests that the type of metal had a negligible effect on the photothermal properties of MPDAMe NPs. However, when comparing the thermocouple and thermal camera measurements (**Figure 29**), it is worth noting that the thermal camera data showed a few degrees lower temperature increase. This difference may be attributed to the measurement setup and the possibility of nanoparticle aggregation during irradiation. The thermocouple measurements were performed under stirring, which prevented nanoparticle sedimentation, whereas with the thermal camera, sedimentation of nanoparticles could have occurred, potentially influencing the observed thermal effect. Despite this discrepancy, the overall results underscore the promising photothermal properties of the investigated nanoparticles, highlighting their potential for future applications in photothermal therapy.

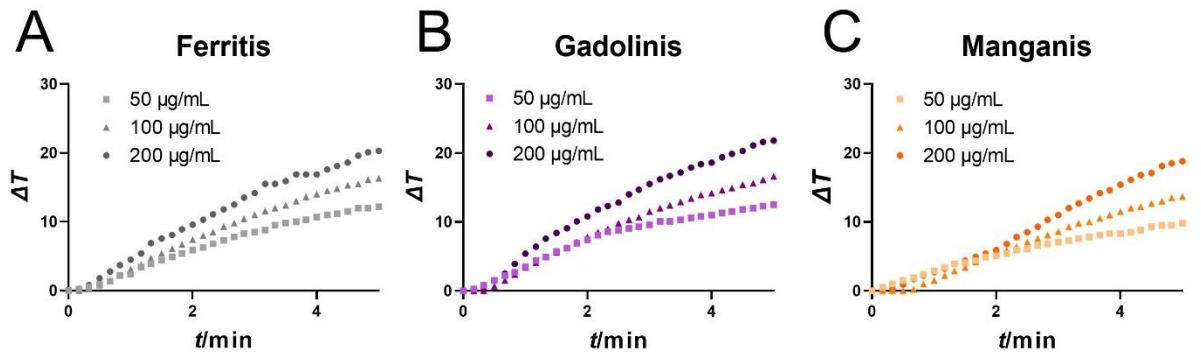

Figure 28. Photothermal properties of **A)** Ferritis, **B)** Gadolinis, and **C)** Manganis NPs – temperature change of 3 concentrations (50, 100, and 200 µg/mL) under 5 min irradiation with 808 nm laser at the power of 3 W/cm^2. Temperature change was registered using a thermocouple.

The impact of metal chelation on the photothermal properties of PDA NPs has been vaguely debated in the literature. Some studies have suggested that the addition of metals may have a neutral or even a negative effect on temperature elevation. For instance, Miao *et al.* reported that Mn-chelated PDA NPs exhibited a slight decrease in temperature change compared to pure PDA NPs [177]. Similarly, Guo *et al.* found negligible differences in the thermal response between their MPDA-Fe(III)-DOX-HA NPs and bare PDA NPs [161]. On the other hand, Xu *et al*. synthesized Fe-PDA NPs with a higher heating rate and stronger heating capacity compared to PDA [178]. Moreover, Hu and co-workers proposed PDA-Fe^{3+}-ICG NPs that exhibited a 14 ºC elevation in photothermal effect compared to PDA NPs, although this effect could be attributed to the presence of indocyanine green (ICG), which enhanced the nanoformulations' adsorption in the UV-Vis NIR region [179].

Figure 29. Photothermal properties of Ferritis, Gadolinis, and Manganis NPs – temperature change of 3 different concentrations (50, 100, and 200 µg/mL) under 5 min irradiation with 808 nm laser at the power of 3 W/cm^2. Temperature change was registered using a thermal camera. The measurements were performed in triplicates, but only one representative repetition is presented.

To the best of my knowledge, a direct comparison of various metals chelated with PDA NPs and their influence on photothermal activity has not been reported. The studies on Ferritis, Gadolinis, and Manganis NPs show that the type of metal appears to have a negligible impact on the heating outcome. Further investigation and systematic studies are needed to fully understand the complex relationship between metal chelation and photothermal properties in PDA NPs. Nevertheless, the results from this study, as well as those from previous research, collectively underscore the potential of these metal-chelated PDA NPs as versatile and promising candidates for various biomedical applications, including photothermal therapy.

Magnetic properties of MPDAMe NPs

Magnetic properties of materials can be classified into three main types: diamagnetism, paramagnetism, and ferromagnetism. The macroscopic magnetic characteristics of materials result from the magnetic moments that individual electrons possess [180]. Moving elementary particles inside atoms, such as electrons, generate a magnetic field. The vector of magnetization is described as a sum of the atomic dipole moments within the given volume of a material [181]. For the diamagnetic materials, in the absence of an external magnetic field, the average value of the dipole moments is considered zero as at least a part of them undergoes random motion, which might cause canceling each other by those dipoles. Consequently, in this situation, both the magnetic moment and the vector of magnetization are equal to zero. When an alternating external magnetic field is applied, the electromagnetic induction causes electron movement around the nucleus, resulting in a magnetic dipole of inductive origin. The law of electromagnetic induction determines that the direction of the moment of this magnetic dipole is opposite to the ambient magnetic field [181]. This phenomenon lays the basis for one of the main characteristics observed in materials with diamagnetic properties, namely the negative magnetic susceptibility. This type of magnetism is relatively weak, nonpermanent, and exists only in the presence of an external field [180]. Since the currents in diamagnetic materials are of induced origin and depend on the mobility of atoms only to a small extent, the dependence of diamagnetism on temperature is considered negligible [181]. Although diamagnetism is present in all materials, it is so faint that it can only be detected when other forms of magnetism are entirely absent [180].

On the contrary, atoms of paramagnetic materials possess a permanent dipole moment that results from an incomplete cancellation of either the electron spin or orbital magnetic moments (or both) [180]. The random orientation of those magnetic moments in the absence of

an external magnetic field originates from the thermal motion of atoms [181]. After an ambient external field is applied, the dipoles line up accordingly. Thus, the vector of magnetization is aligned with the applied field, resulting in a positive susceptibility of the paramagnetic materials [181]. However, similarly to the diamagnetic materials, the paramagnetic materials exhibit magnetization only when an external field is applied [180].

Ferromagnetic materials possess unique properties that set them apart from other substances. One of the most significant characteristics of these materials is their ability to exhibit spontaneous magnetization, which means they can become permanent magnets even without an external magnetic field [180]. This phenomenon occurs due to the strong interaction between the atoms of the material - coupling interactions prompt adjacent atoms' net spin magnetic moments to align with each other, even without an external field [180]. Ferromagnetic materials have a high magnetic susceptibility, which means they are easily magnetized by an external magnetic field and retain their magnetic properties even after the external magnetic field disappears [181].

An MPMS equipped with SQUID was used to establish the magnetic nature of MPDAMe NPs (Me = Fe, Gd, or Mn). MPDA NPs were measured to evaluate if the magnetic properties of MPDAMe NPs resulted from the addition of metal to the material. The graphs in **Figure 30** summarize the results of the susceptibility and magnetization measurements. Fitting of the magnetic susceptibility data was performed using Origin software.

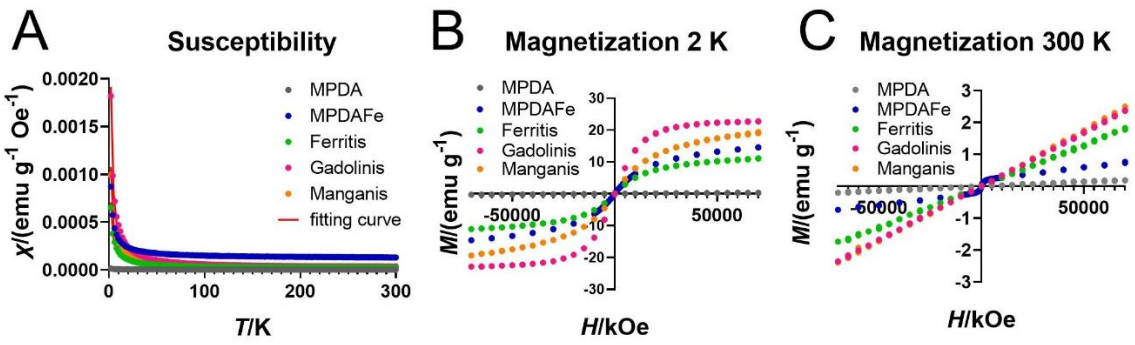

Figure 30. SQUID measurements of **A)** magnetic susceptibility measured in the field of 1 kOe and magnetization at **B)** 2 K and **C)** 300 K of MPDA NPs, MPDAFe NPs, Ferritis NPs, Gadolinis NPs, and Manganis NPs.

The results obtained for MPDAFe, Ferritis, Gadolinis, and Manganis NPs clearly show the paramagnetic nature of the materials. **Figure 30A** shows a plot of χ(T). As temperature increases, the magnetic susceptibility decreases, indicating that the magnetic moment is becoming less aligned with the external magnetic field. The fitting curve (red) follows the Curie law throughout the whole temperature range, suggesting that the measured material is a Curie-type paramagnet, a type of magnetism resulting from atoms with unpaired electrons [115]. The magnetization curves in **Figure 30B** and **C** also confirm the paramagnetic behavior of all of the nanoformulations. The magnetization of the samples increases with the increasing strength of the applied magnetic field. This effect is better observed at lower temperatures, which is also typical for this type of magnetic material. The magnetization of paramagnetic materials is directly proportional to the strength of the magnetic field. This phenomenon is known as the Curie law, which states that the magnetic susceptibility of a paramagnetic material is inversely proportional to the temperature and directly proportional to the magnetic field strength [181]. In other words, as the strength of the magnetic field increases, the magnetic moment of the atoms in the paramagnetic material becomes more aligned with the external field, increasing magnetization. However, as the temperature of the material increases, the thermal energy begins to disrupt the alignment of the magnetic moments, causing the magnetic susceptibility to decrease.

On the contrary, the measurements of MPDA NPs revealed the diamagnetic behavior of this sample. The χ(T) fitting curve follows the Curie law only at higher temperatures. Moreover, the susceptibility of MPDA NPs is negative, which is a clear sign of diamagnetism. The magnetization plots of MPDA NPs are also fundamentally different from the plots of paramagnetic MPDAMe NPs due to an opposing alignment of the magnetic moments compared to the direction of the applied external magnetic field, which is typical for diamagnets. Those results indicate that the paramagnetic nature of MPDAFe, Ferritis, Gadolnis, and Manganis NPs was induced by the addition of metal to the material and could not be observed otherwise.

The assessment of the magnetic properties of PDA materials is challenging due to their complicated and ambiguous structure. However, several attempts have been made to analyze the magnetic behavior of those fascinating structures. In 1964, Blois and co-workers performed detailed electron spin resonance (ESR) studies on natural, synthetic, and Cu-dopped melanins [182]. The researchers suggested a radical-originated paramagnetism of the investigated materials. However, the proposed mechanism was not exclusive – the alternatives of the origin of paramagnetic properties included interference of contaminations of transition metal ions or

the semiconducting behavior of melanins. Moreover, the researchers claim that the investigated materials followed the Curie law from 500 to 4.2 K. However, the susceptibility contribution of MPDA NPs observed in this study was negligible. It could be explained by the physical properties of the investigated materials. Here, the dry sample of nanoparticles was measured. Blois and co-workers did not provide the morphology of the analyzed samples. However, the synthesis of synthetic melanins was performed for 4 days, which might suggest a more bulky form of the material.

Overall, among all the tested materials, similar paramagnetic properties were observed, which were introduced by the addition of metal to PDA NPs. Gadolinis NPs exhibited the highest magnetization among the samples, although the differences in magnetization between the various nanoparticles were insignificant. These results suggest that all the investigated materials possess comparable magnetic characteristics, making them promising candidates for further development in biomedical applications that require magnetic responsiveness.

Relaxivity and contrasting properties

In the field of biomedical imaging, MRI has emerged as a powerful tool for non-invasive visualization and characterization of anatomical structures and physiological processes. The efficiency of MRI largely depends on the use of contrast agents that enhance the image contrast between different tissues or pathological areas. Paramagnetic nanoparticles have gained significant attention as promising MRI contrasting agents due to their unique magnetic properties and tunable relaxivity.

Relaxivity is a critical parameter that quantifies the ability of a contrast agent to alter the longitudinal (T_1) or transverse (T_2) relaxation times of nearby water protons, thus enhancing the signal intensity and providing clearer image contrast. By systematically investigating the relaxivity of the nanoparticles, I aimed to elucidate their potential as effective MRI contrasting agents. In this study, the r_1 relaxivity of the nanoformulations was investigated at two different temperatures, namely 22 ºC and 37 ºC, using T_1 relaxation measurements (inversion-recovery) on NMR spectrometers operating at 16.5 MHz (0.4 T) and 200 MHz (4.7 T).

For the inversion-recovery experiment, a series of NMR pulse sequences were employed. The MPDAFe@Mem, Ferritis, Gadolinis, and Manganis NPs were dispersed in water at various metal concentrations. Each sample underwent an inversion pulse, followed by a variable

recovery time (TR) before acquiring the NMR signal. The resulting T_1 recovery data exhibited mono-exponential behavior, allowing to fit the data using **Equation (9)**:

$$M(0) = M_0 \cdot (1 - 2 \cdot exp(-t/T_1)) \quad (9)$$

Here, $\boldsymbol{M_0}$ represents the magnetization at thermodynamic equilibrium, $\boldsymbol{M}$ is the magnetization at time *t*, and $\boldsymbol{T_1}$ denotes the spin-lattice relaxation time.

A summary of the obtained relaxation values for both positive (T_1-weighted) and negative (T_2-weighted) contrasting is provided in **Table 17**.

Table 17. Relaxation values calculated from the data obtained from the NMR measurements at 22 ºC and 37 ºC using 16.5 MHz and 200 MHz (T_1-weighted), and MRI maps at 400 MHz (T_2- weighted) of MPDAFe@Mem, Ferritis, Gadolinis, and Manganis NPs.

Sample	Metal concentration/ (mM)	R_1/(1/s)				R_2/(1/s)
		22 ºC		37 ºC		400 MHz (9.4 T)
		16.5 MHz (0.4 T)	200 MHz (4.7 T)	16.5 MHz (0.4 T)	200 MHz (4.7 T)	
MPDAFe@Mem	0	0.39	0.35	0.31	0.25	3.23
	0.2	1.14	1.01	0.97	0.91	6.67
	0.4	1.79	1.63	1.59	1.51	9.09
	0.6	2.43	2.20	2.18	2.06	10.00
	0.8	3.13	2.84	2.81	2.69	16.67
	1.0	3.72	3.41	3.28	3.25	20.00
Ferritis	0.0	0.39	-	0.31	-	-
	0.3	1.17	-	1.02	-	-
	0.7	1.76	-	1.68	-	-
	1.0	2.63	-	2.56	-	-
	1.4	3.55	-	3.50	-	-
	1.7	4.30	-	4.24	-	-

Gadolinis	0	0.39	-	0.31	-	-
	0.67	4.16	-	3.74	-	-
	1.01	-	-	4.72	-	-
	1.34	5.92	-	-	-	-
Mangnis	0	0.38	-	0.30	-	-
	0.39	8.00	-	7.56	-	-
	0.78	15.63	-	14.71	-	-
	1.17	22.56	-	21.43	-	-
	1.56	31.25	-	28.57	-	-

C(Me) = $f(R_1)$ graphs (**Figure 31** and **Figure 32**) were plotted based on the acquired relaxation rate values (R_1) and the corresponding molar concentrations of Me (Me = Fe, Fe, Gd, or Mn in the MPDAFe@Mem, Ferritis, Gadolinis, and Manganis NPs, respectively). To determine the relaxivity of the nanoformulations, we performed linear fitting using **Equation (3)** (p.42). The resulting linear fitting curve (shown in red) provided the best fit to the experimental data and allowed to determine the slope, which corresponds to the relaxivity of the nanoformulations.

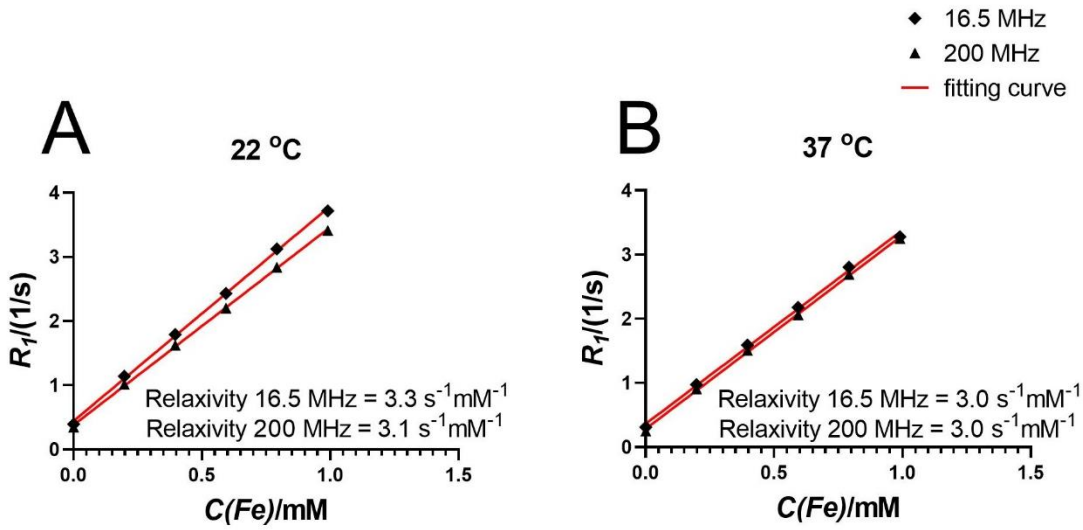

Figure 31. Relaxation times of increasing concentrations of MPDAFe@Mem NPs in water measured at **A)** 22 ºC and **B)** 37 ºC using 16.5 MHz and 200 MHz NMR spectrometers. The relaxivity values were calculated based on the linear fit of the data.

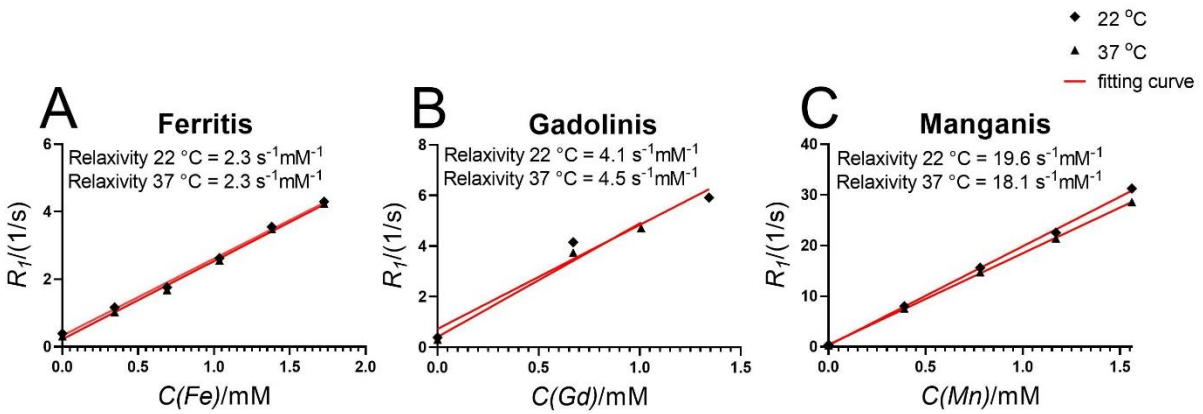

Figure 32. Relaxation times of increasing concentrations of **A)** Ferritis, **B)** Gadolinis, and **C)** Manganis NPs in water measured at 22 ºC and 37 ºC using a 16.5 MHz NMR spectrometer. The relaxivity values were calculated based on the linear fit of the data.

To facilitate comparison with the obtained relaxivity values, **Table 18** presents representative r_1 values of commercially available contrast agents. It is noteworthy that the majority of these agents are based on gadolinium complexes, with the exception of TESLASCAN, which utilizes manganese.

Table 18. Relaxivity (r_1) values of selected clinically used contrasting agents measured in water at 40 ºC (at 0.47 T) and 37 ºC (at 4.7 T) [183].

Trade name	**r_1 at 0.47 T/(s^{-1} mM^{-1})**	**r_1 at 4.7 T/($^{s-1}$ mM^{-1})**
MAGNEVIST	3.4 (3.2-3.6)	3.2 (3.0-3.4)
GADOVIST	3.7 (3.5-3.9)	3.9 (3.6-4.2)
PROHANCE	3.1 (2.9-3.3)	3.4 (3.1-3.7)
MULTIHANCE	4.2 (3.9-4.4)	4.7 (4.4-5.0)
DOTAREM	3.4 (3.2-3.6)	3.3 (3.0-3.6)
OMNISCAN	3.5 (3.3-3.7)	3.8 (3.5-4.1)
TESLASCAN	1.9 (1.8-2.0)	2.3 (2.0-2.6)
OPTIMARK	4.2 (4.0-4.4)	4.5 (4.2-4.8)
Gadomer	16.5 (15.7-17.3)	9.1 (8.6-9.6)

Notably, all the investigated nanoformulations (**Figure 31**, **Figure 32**) exhibited relaxivity values comparable to or higher than the commercially used agents presented in **Table 18**. This suggests that these nanoformulations have the potential to enhance image contrast and improve diagnostic accuracy.

Among the tested nanoformulations, Manganis NPs demonstrated the highest relaxivity. However, it is important to note that the stability of Manganis NPs decreased significantly at the highest concentrations, leading to the exclusion of the corresponding data from the evaluation. This instability might limit the practical applicability of Manganis NPs in clinical settings. Gadolinis NPs exhibited overall instability, which affected the accuracy and reliability of the presented data. Therefore, the relaxation properties of Gadolinis NPs should be considered as a rough estimation based on the obtained results. In contrast, both Ferritis NPs and MPDAFe@Mem NPs demonstrated excellent stability across all tested concentrations and measurement conditions. This stability is crucial in ensuring consistent and reliable contrast enhancement in MRI imaging. However, it is worth noting that the relaxivity of Ferritis and MPDAFe@Mem NPs was approximately five times lower than that of Manganis NPs. This difference in relaxivity values should be taken into account when considering the specific application and desired imaging outcomes. Comparison with other studies on PDA-based MRI contrasting agents further reinforces the exceptional potential of the synthesized structures. Ding *et al*. introduced Mn-containing nanoparticles (Mn_3O_4@PDA) with a reported longitudinal relaxivity of 14.47 s^{-1} mM^{-1} at 1.2 T, which they described as 'ultra-high relaxivity' [184]. In light of our findings that Manganis nanoparticles exhibited an r1 value of 18.1/19.6 $s^{-1}mM^{-1}$, it is justifiable to classify it also as ultra-high relaxivity. In another study, Wang *et al.* reported several Mn-based PDA NPs with r_1 values between 4.7 and 8.3 s^{-1} mM^{-1} (measured at 7 T) [148], whereas a series of Fe-based PDA NPs proposed by Li *et al.* were shown to have r_1 values between 1.2 and 4.6 s^{-1} mM^{-1} (measured at 7 T) [49]. However, examples with extremely high relaxivity were also reported, such as a series of Gd-containing PDA NPs with r_1 values from 35.1 to 74.6 s^{-1} mM^{-1} (measured at 1.4 T) [185]. Nevertheless, the presented results highlight the contrast-enhancing capabilities of the presented nanoparticles and emphasize their potential for highly sensitive and accurate MRI imaging applications.

To further evaluate the potential of MPDAFe@Mem NPs as MRI contrast agents, T_2-weighted imaging was performed across a range of NPs concentrations (0.2 to 1 mM) using a 9.4 T MRI scanner operating at a proton resonance frequency of 400 MHz. A multi-echo sequence was applied for the imaging experiments. The resulting images and the calculated T_2 values derived

from the MRI maps are presented in **Figure 33**. A summary of the obtained relaxation values is provided in **Table 17.** As evidenced by the changes observed in the images in **Figure 33**, the increasing concentration of NPs was connected with a gradual reduction in T_2, resulting in a decrease in signal intensity. This reduction in image brightness signifies the enhanced T_2 relaxation effect induced by the presence of MPDAFe@Mem NPs, thus demonstrating their potential as effective contrast agents for targeted cancer imaging applications.

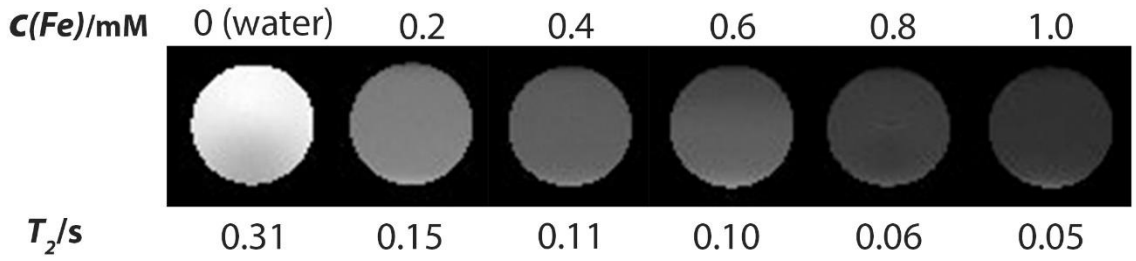

Figure 33. MRI T_2-weighted MRI images of MPDAFe@Mem NPs at concentrations from 0.2 to 1 mM Fe. The T_2 times were determined from the MRI maps.

What is particularly remarkable is that even at the lowest tested concentration of 0.2 mM of Fe, the MPDAFe@Mem NPs exhibited a discernible darkening effect on the T_2-weighted images. This finding highlights the high sensitivity and potential of these NPs for early cancer detection, suggesting that lower concentrations of NPs may be sufficient for successful imaging in such cases.

These results provide valuable insights into the contrasting capabilities of MPDAFe@Mem NPs, emphasizing their ability to generate a negative T_2 contrast. The observed darkening of the images with increasing NPs concentration further underscores their potential for precise and targeted cancer imaging. These findings contribute to the growing body of evidence supporting the use of PDA-based NPs as promising candidates for advancing cancer diagnosis and facilitating early detection, where the sensitivity and accuracy of imaging are of paramount importance.

The stability of nanoparticles plays a crucial role in obtaining accurate and reliable imaging results. A comparative analysis between MPDAFe NPs and MPDAFe@Mem NPs under the same imaging conditions highlighted a distinct difference in their stability. Three-dimensional colormaps (**Figure 34**), constructed based on T_2 MRI maps, provided valuable insights into the behavior of the nanoparticles within the high magnetic field (9.4 T).

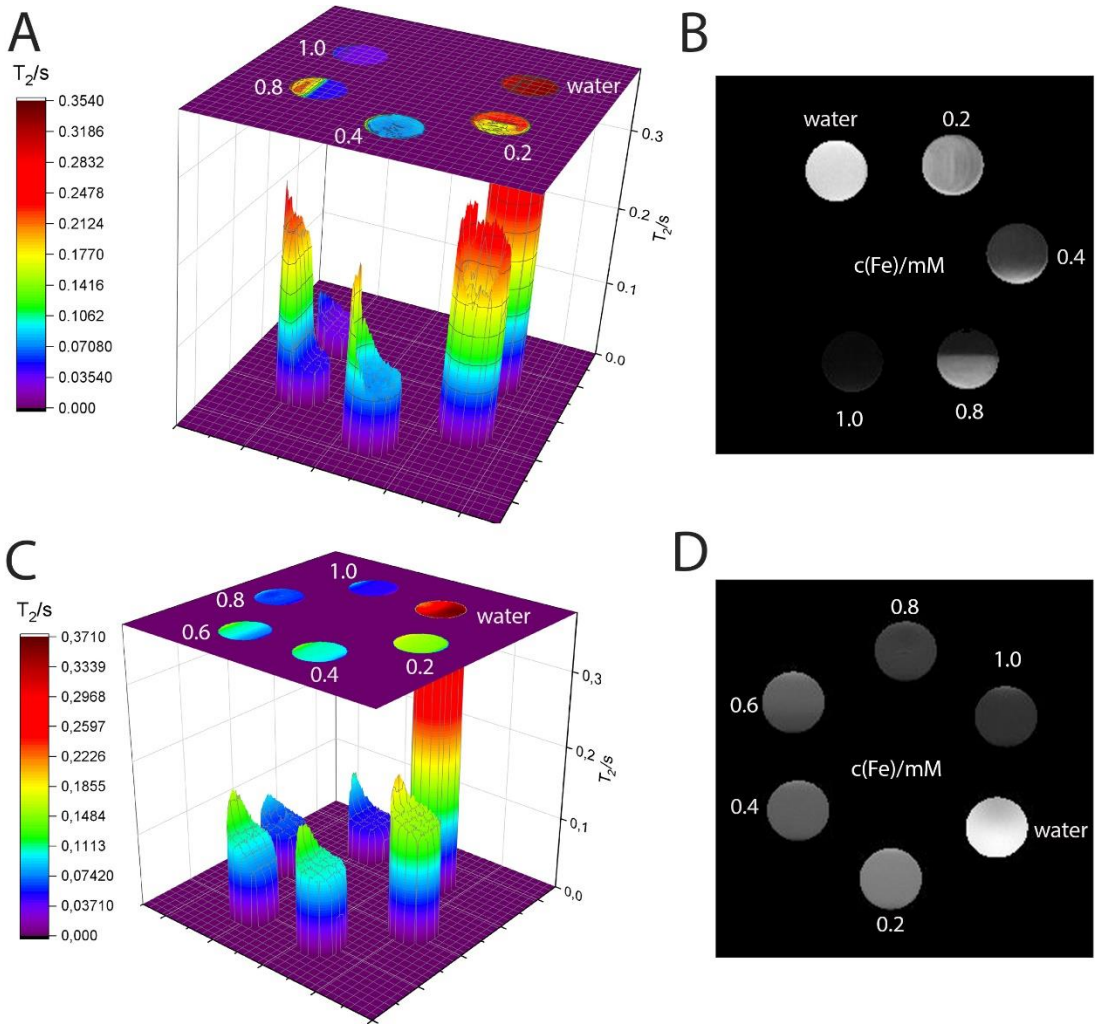

Figure 34. T_2 times of MPDAFe (top) and MPDAFe@Mem (bottom) NPs extracted from the MRI maps. **A)** 3D colormap with a top plane projection of different concentrations of MPDAFe NPs, **B)** Corresponding MRI T_2-weighted images, **C)** 3D colormap with a top plane projection of different concentrations of MPDAFe@Mem NPs, **D)** Corresponding MRI T_2-weighted images.

The colormaps clearly demonstrated that the MPDAFe NPs (**Figure 34A**) exhibited significant sedimentation, as indicated by less defined column shapes and the irregular distribution of colors in the top plane projections. In contrast, the colormaps of the MPDAFe@Mem NPs (**Figure 34C**) showed enhanced stability, characterized by less disturbed column shapes and more even colors on the top plane projections. The sharp increase in the column shape at the edges could be considered an artifact arising from the measurement tube. Regardless, these observations strongly suggest that the membrane coating of MPDAFe@Mem NPs confers improved stability during the T_2-weighted MRI imaging.

The stability of MPDAFe@Mem NPs is of paramount importance for their potential applications in targeted cancer imaging. The consistent and uniform distribution of the nanoparticles ensures accurate contrast enhancement and reliable detection of cancerous tissues. In contrast, the instability of MPDAFe NPs may lead to suboptimal imaging results, hampering their efficacy in clinical applications. By employing the membrane-coating strategy, the MPDAFe@Mem NPs overcome the challenges associated with sedimentation and offer enhanced stability during T_2-weighted MRI imaging. This stability enables the nanoparticles to maintain their optimal contrast-enhancing properties, facilitating their potential use in targeted cancer imaging and improving the accuracy of diagnosis and treatment monitoring.

Overall, the evaluated paramagnetic nanoparticles exhibited promising characteristics for MRI contrasting. The findings presented in this chapter contribute to the development of efficient and tailored paramagnetic nanoparticles for MRI applications. By harnessing the unique properties of these contrast agents, we can improve imaging capabilities, enhance disease detection, and enable more accurate treatment monitoring in clinical settings. The comprehensive evaluation of relaxivity and MRI contrasting properties of the investigated paramagnetic nanoparticles advances the understanding of their potential as contrast agents. The investigations into the relaxivity and contrasting properties of MPDAFe@Mem NPs provided valuable insights into their suitability as MRI contrast agents (both positive and negative). This result highlights the high sensitivity and potential of the membrane-coated NPs for *in vivo* applications, where lower NPs concentrations may be required to be sufficient for successful imaging.

Biological studies *in vitro*

Nanoparticles have emerged as promising tools in various fields within biomedical applications. However, before their widespread implementation, it is crucial to thoroughly investigate their safety profiles, particularly in terms of cytotoxicity. Cytotoxicity assays serve as fundamental tools for assessing the potential adverse effects of nanoparticles on cellular systems. Based on a detailed physicochemical analysis, MPDAFe NPs were selected as possessing the most beneficial properties for the established aims of the project. This chapter aims to explore the cytotoxicity of membrane-coated MPDAFe nanoparticles through a comprehensive evaluation of their impact on cell viability and function. Through a systematic investigation of the cytotoxic effects induced by nanoparticles, this chapter aims to contribute to understanding the potential hazards and challenges associated with exposing living cells to MPDAFe-based nanoformulations.

Biosafety evaluation

The study presented in this chapter focuses on the biosafety evaluation of porous PDAFe NPs coated with cancer cell membranes (MPDAFe@Mem NPs) using two cytotoxicity assays: the Live/Dead assay and the EdU assay. The Live/Dead assay is a fluorescence-based method used to distinguish live cells from dead cells in a population. It employs two fluorescent dyes: calcein AM, which labels live cells with green fluorescence, and EthD-1, which penetrates and labels dead cells with red fluorescence by binding to nucleic acids [186]. Therefore, live cells exhibit green fluorescence, while dead cells display red fluorescence, allowing for quick and reliable assessment of cell viability and cytotoxicity based on cell membrane integrity in various experimental settings. This assay was used to assess the impact of MPDAFe@Mem NPs on both normal cells (MRC5) and liver cancer cells (HepG2) and provide insights into their biosafety, which is a crucial aspect in targeted cancer therapy. Additionally, the EdU assay was employed to investigate the impact of MPDAFe@Mem NPs on cell proliferation. EdU, a thymidine analog, is incorporated into replicating DNA during active cell proliferation [122,187]. The assay enables the identification and quantification of actively proliferating cells, providing valuable data on the potential effects of the nanoformulations on cellular growth and replication. By employing these specific cytotoxicity assays, the study aims to comprehensively assess the biocompatibility and potential therapeutic efficacy of MPDAFe@Mem NPs. The use of both normal and cancer cells in the evaluation allows for a comparative analysis of

the nanoparticles' impact on different cell types, aiding in the development of targeted and safe therapeutic agents for cancer treatment.

For the Live/Dead assay, MRC5 and HepG2 cells were seeded in culture plates and allowed to adhere overnight. The cells were then treated with varying concentrations (0-40 μg/mL) of MPDAFe and MPDAFe@Mem NPs for 48 h. After the treatment period, the cells were stained using a Live/Dead assay kit according to the manufacturer's instructions. The stained cells were imaged using an InCell Analyzer, capturing fluorescence images. The viability of the cells was determined by analyzing the fluorescence signals and quantifying the proportion of live and dead cells using image analysis software.

Both the Live/Dead assay and EdU assay were performed in triplicates, and the results were presented as mean±SD. The InCell Analyzer, a high-content imaging system, provided the capability to capture and analyze multiple images, enabling accurate assessment of cell viability and proliferation in a quantitative manner.

The cell viability evaluation using the Live/Dead assay revealed that the MPDAFe and MPDAFe@Mem NPs exhibited negligible cytotoxicity towards MRC5 cells, which are normal fibroblasts (**Figure 35A,B**). Even at the highest concentration (40 μg/mL), these NPs did not induce significant cell death in MRC5 cells. This finding suggests that the NPs are biocompatible and do not adversely affect the viability of normal cells.

In contrast, a slight decrease in viability was observed in HepG2 cells, which are cancer cells, when treated with the MPDAFe@Mem NPs (**Figure 35C,D**). At the highest concentration (40 μg/mL) of MPDAFe@Mem NPs, the viability of HepG2 cells decreased by approximately 10% compared to the control group. On the other hand, the MPDAFe NPs did not show any significant toxicity towards HepG2 cells. These results indicate that the MPDAFe@Mem NPs may have a minimal impact on the viability of cancer cells. Statistical analysis of the MRC5 and HepG2 cell lines are summarized in **Table 19** and **Table 20**, respectively.

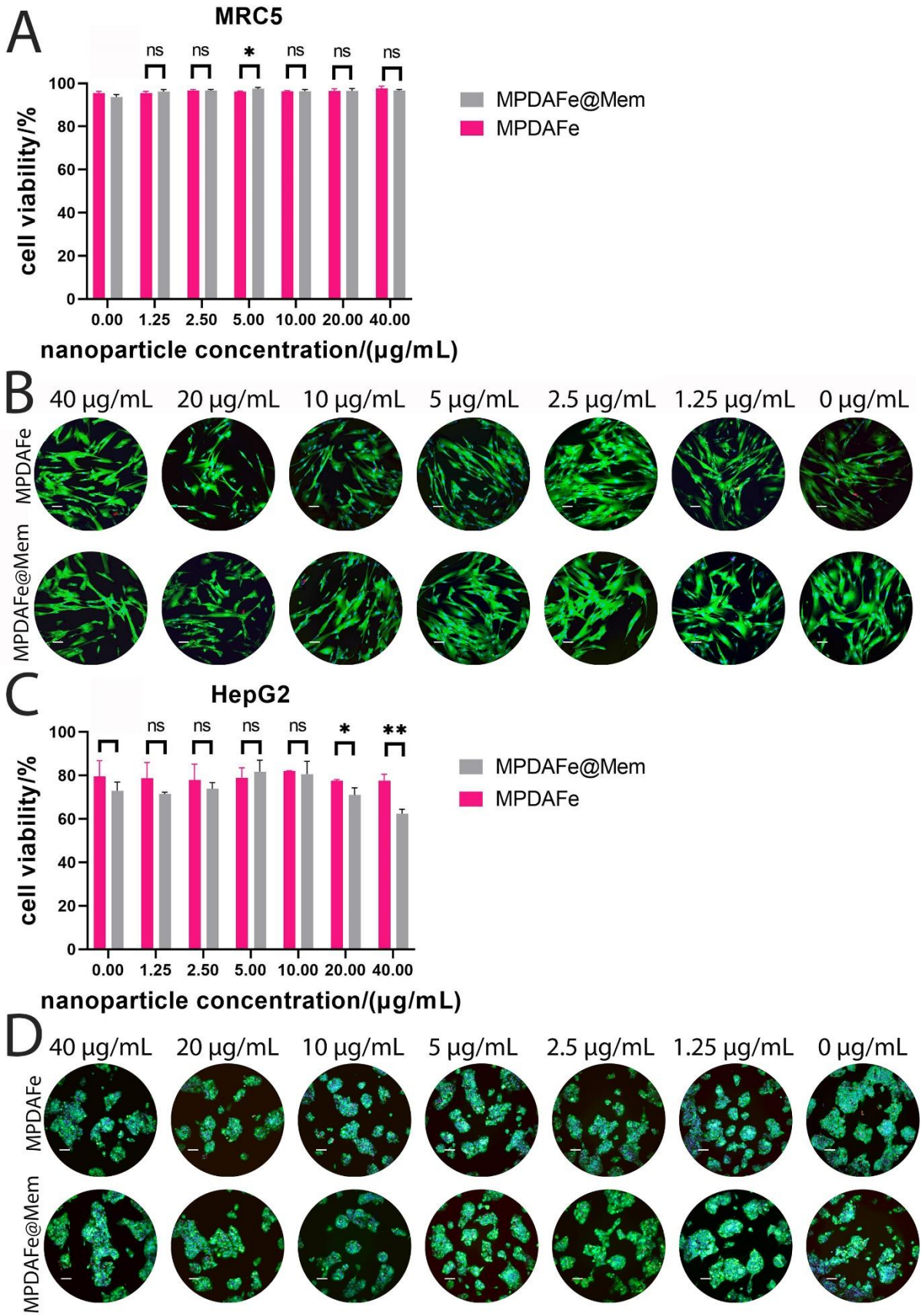

Figure 35. Results of Live/Dead assay comparing biosafety of MPDAFe and MPDAFe@Mem NPs. **A)** Viability of MRC5 cells, **B)** Corresponding images (green – live cells, red – dead nuclei, blue – all

nuclei); the scale marks 70 μm, **C)** Viability of HepG2 cells, **D)** Corresponding images (green –live cells, red – dead nuclei, blue – all nuclei); the scale marks 70 μm.

Table 19. Summary of the unpaired t-test analysis results of the normalized number of proliferating MRC5 cells (Live/Dead assay) incubated with MPDAFe or MPDAFe@Mem NPs (**MPDAFe@Mem vs. MPDAFe**).

Concentration	P value	P value summary	Significantly different? (P < 0.05)
1.25	0.3236	ns	no
2.5	0.8515	ns	no
5	0.0312	*	yes
10	0.9687	ns	no
20	0.9546	ns	no
40	0.3590	ns	no

Table 20. Summary of the unpaired t-test analysis results of the normalized number of proliferating HepG2 cells (Live/Dead assay) incubated with MPDAFe or MPDAFe@Mem NPs (**MPDAFe@Mem vs. MPDAFe**).

Concentration	P value	P value summary	Significantly different? (P < 0.05)
1.25	0.1619	ns	no
2.5	0.4260	ns	no
5	0.5195	ns	no
10	0.6986	ns	no
20	0.0273	*	yes
40	0.0017	**	yes

For the EdU assay, MRC5 and HepG2 cells were seeded in culture plates and allowed to adhere overnight. The cells were then treated with different concentrations (0-40 μg/mL) of MPDAFe and MPDAFe@Mem NPs for 24 h. After incubation, the cells were exposed to EdU. Following the EdU incorporation period, the cells were fixed, permeabilized, and subjected to a click chemistry reaction with a fluorescent dye conjugated to detect EdU. The stained cells were imaged using the InCell Analyzer. The relative number of proliferating cells was determined by analyzing the fluorescence signals and quantifying the proportion of EdU-positive cells using image analysis software.

In the EdU assay, which assesses cell proliferation, both MRC5 and HepG2 cell lines were evaluated for proliferation under incubation with MPDAFe and MPDAFe@Mem NPs. Interestingly, the relative number of proliferating cells did not vary significantly with increasing NPs concentration for both normal cells (**Figure 36A**) and cancer cells (**Figure 36C**). The corresponding images of the MRC5 and HepG2 cells (**Figure 36B** and **D**, respectively) confirm that the proportion of proliferating cells did not exhibit a significant decrease in the range of the tested NPs concentrations. This finding suggests that the presence of MPDAFe and MPDAFe@Mem NPs did not inhibit cell proliferation in either the normal or cancer cell lines. The nanoparticles did not interfere with the cell's ability to actively replicate DNA during the EdU incorporation period, indicating a lack of significant cytotoxic effects on cell proliferation. Statistical analysis of the MRC5 and HepG2 cell lines are summarized in **Table 21** and **Table 22**, respectively.

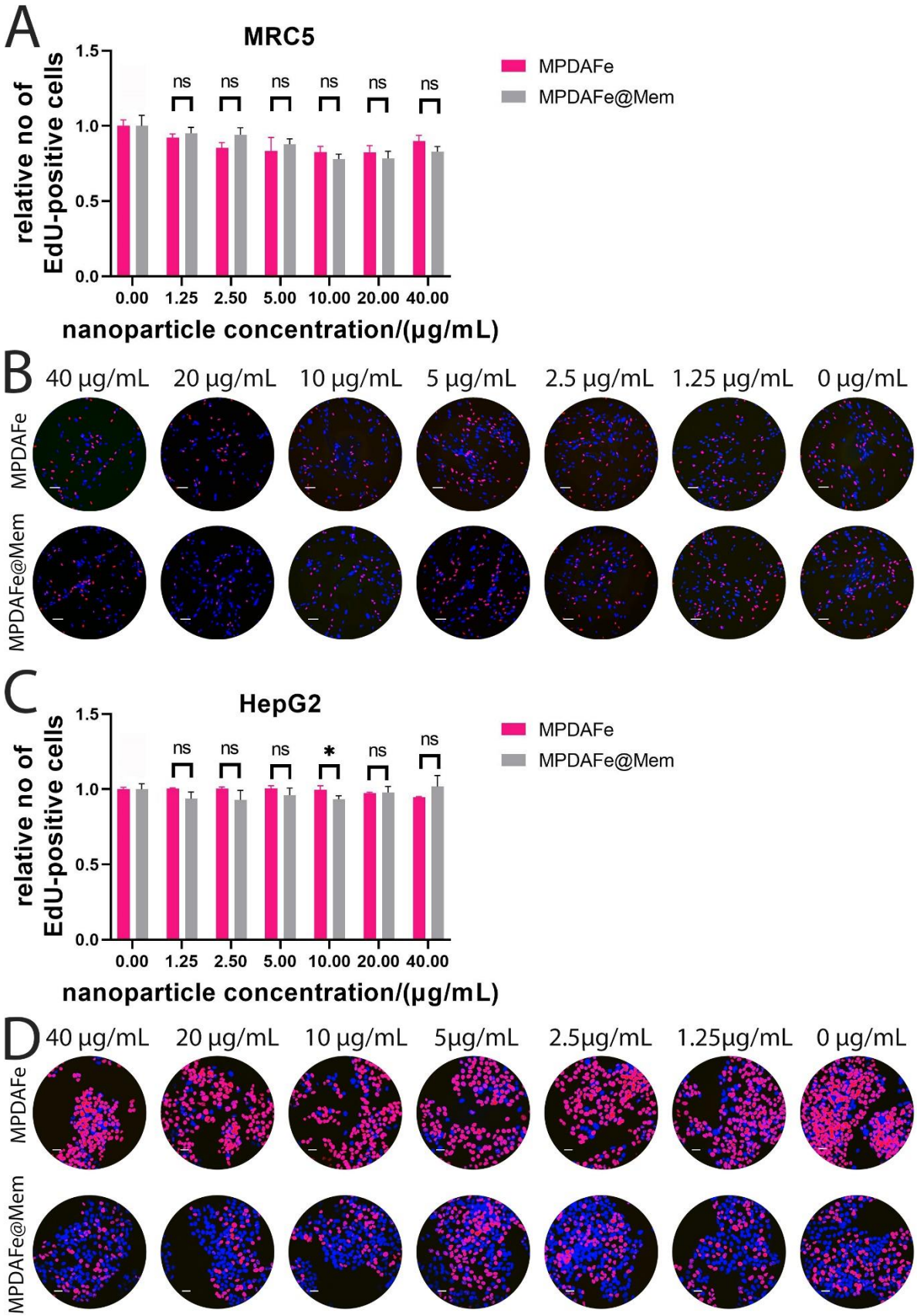

Figure 36. Results of EdU assay comparing biosafety of MPDAFe and MPDAFe@Mem NPs. **A)** Viability of MRC5 cells, **B)** Corresponding images (blue – all nuclei, pink – proliferating nuclei);

the scale marks 70 μm, **C)** Viability of HepG2 cells, **D)** Corresponding images (blue – all nuclei, pink – proliferating nuclei); the scale marks 30 μm.

Table 21. Summary of the unpaired t-test analysis results of the normalized number of proliferating MRC5 cells (EdU assay) incubated with MPDAFe or MPDAFe@Mem NPs (**MPDAFe@Mem vs. MPDAFe**).

Concentration	P value	P value summary	Significantly different? (P < 0.05)
1.25	0.3198	ns	no
2.5	0.0581	ns	no
5	0.4504	ns	no
10	0.1872	ns	no
20	0.3653	ns	no
40	0.1468	ns	no

Table 22. Summary of the unpaired t-test analysis results of the normalized number of proliferating HepG2 cells (EdU assay) incubated with MPDAFe or MPDAFe@Mem NPs (**MPDAFe@Mem vs. MPDAFe**).

Concentration	P value	P value summary	Significantly different? (P < 0.05)
1.25	0.0613	ns	no
2.5	0.2466	ns	no
5	0.2069	ns	no
10	0.0337	*	yes
20	0.8004	ns	no
40	0.1625	ns	no

The negligible toxicity of Fe-modified PDA NPs is consistent with previous studies. Xu and co-workers reported no severe cytotoxicity of Fe (III)-chelated PDA NPs toward normal cells (HUVEC cells), even at concentrations up to 200 μg/mL [178]. Similarly, in another study, PDA-Fe^{3+}-ICG NPs showed no toxicity toward various cancer cell lines [179]. These findings support the presented results, highlighting the intrinsic biosafety of Fe-modified PDA NPs. Additionally, membrane-coated drug carriers have demonstrated excellent biocompatibility in various studies [94,97,188,189]. Interestingly, coating with cancer cells further enhanced

the biocompatibility of upconversion nanoparticles toward different tumor cell lines and macrophage cells [190].

Overall, the results from the cytotoxicity assays demonstrate the biocompatibility and minimal cytotoxicity of the MPDAFe and MPDAFe@Mem NPs towards normal cells (MRC5) and cancer cells (HepG2) at the tested concentrations (1.25 - 40 μg/mL). The slight decrease in viability observed in HepG2 cells treated with the MPDAFe@Mem NPs suggests a potential selectivity towards cancer cells, while the absence of significant effects on cell proliferation indicates the compatibility of the nanoparticles with the cell's replicative processes. These findings support the promising application of the MPDAFe@Mem NPs as a safe and effective drug delivery system for potential use in cancer therapy.

Cell internalization

Understanding the cellular internalization of nanoparticles is essential for assessing their potential as drug delivery systems and targeted therapeutics. In this study, I investigated the uptake of MPDAFe and MPDAFe@Mem NPs by HepG2 cells using flow cytometry. By comparing the uptake of membrane-coated and non-coated nanoparticles at different time points, I aimed to evaluate the influence of the cell membrane coating on the MPDAFe NPs internalization.

Flow cytometry analysis was performed on HepG2 cells incubated with MPDAFe and MPDAFe@Mem NPs stained with RED NHS dye for 1 h and 4 h. The results revealed an increased uptake of membrane-coated nanoparticles already after 1 h (**Figure 37A**), and this effect was further pronounced after 4 h (**Figure 37C**). The corresponding images (**Figure 37B,D**) provided visual evidence of these findings, indicating that after 4 h, a larger number of membrane-coated nanoparticles were internalized compared to the images taken after 1 h incubation.

Furthermore, the images showed a notable difference in nanoparticle localization within the cells between the two time points. After 1 h, the nanoparticles were mainly localized near the cell membrane, suggesting initial interactions and binding. However, after 4 h, the nanoparticles had migrated further inside the cells, indicating successful internalization and intracellular distribution. This shift in localization suggests that the membrane-coated nanoparticles have the ability to traverse the cell membrane and enter the intracellular compartments more efficiently over time.

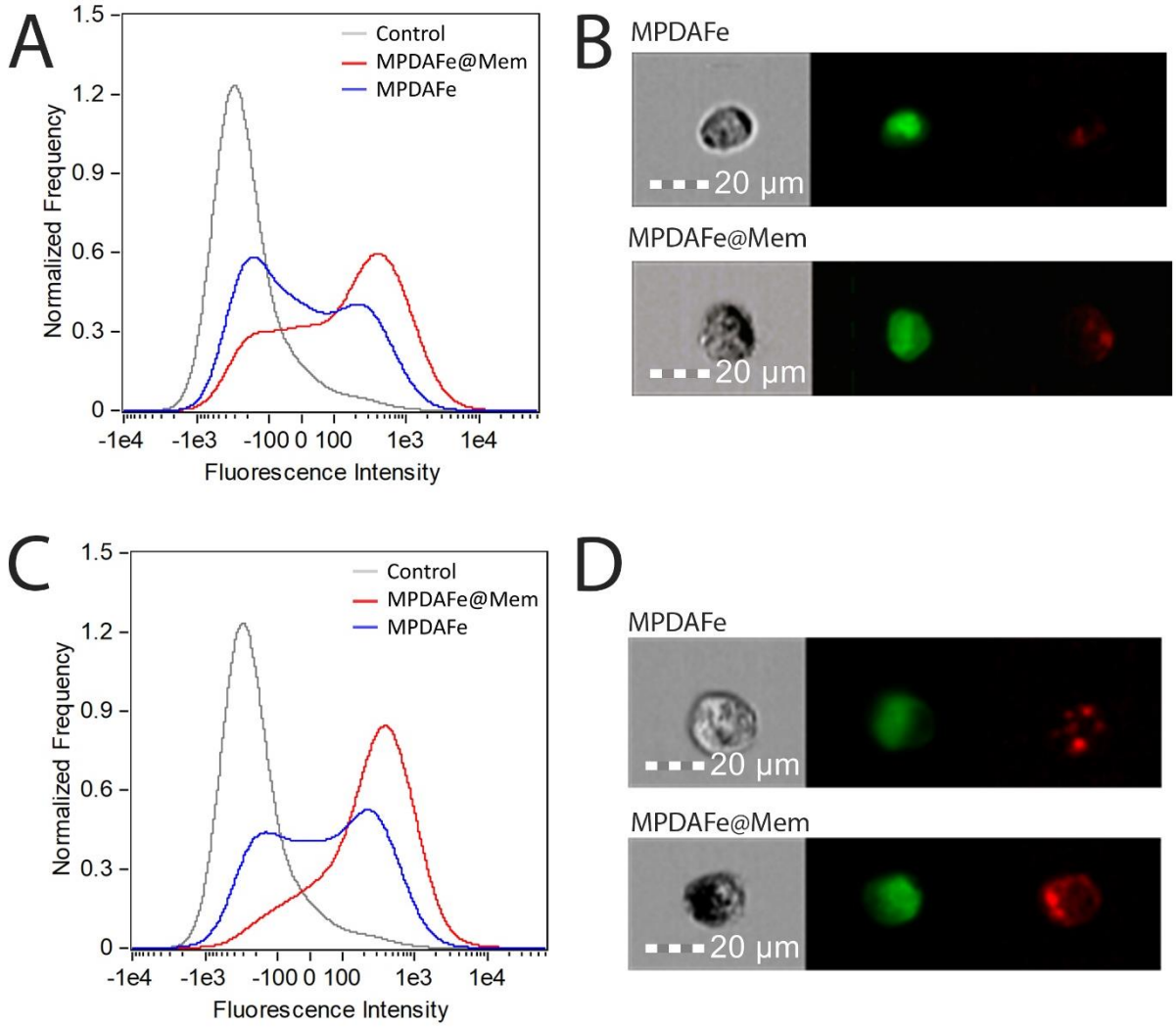

Figure 37. Internalization of MPDAFe and MPDAFe@Mem NPs in HepG2 cells after **A,B)** 1 h and **C,D)** 4 h of incubation measured using flow cytometry. Graphs: grey – control (cells without nanoparticles), red – cells incubated with MPDAFe@Mem NPs, blue – cells incubated with MPDAFe NPs. Images: green – cell membrane, red – nanoparticles stained with a RED NHS fluorescent dye.

The observed increase in internalization of membrane-coated nanoparticles can be attributed to the enhanced cellular uptake facilitated by the membrane coating. The coating likely promotes interactions with specific receptors on the cell membrane, leading to improved cellular recognition and internalization [66]. This selective uptake can be crucial for targeted drug delivery, as it increases the nanoparticles' accumulation at the desired site of action, such as cancer cells. The enhancement of the membrane-coated uptake by cancer cells has been observed in other studies. For instance, ICG and DCT-loaded PLGA NPs coated with 4T1 cell membrane showed 70% higher uptake into the homologous breast cancer cells than their uncoated counterparts [39]. Similarly, in another study, PGT NPs coated with MNNG/HOS cell

membranes demonstrated about 5 times increase in internalization in homologous tumor cells [96]. It is worth noting that cancer cell coatings have been shown to have a superior enhancing effect on homologous cancer cell internalization compared to red blood cell membrane coatings [191].

In conclusion, this study investigated the internalization of MPDAFe and MPDAFe@Mem nanoparticles in HepG2 cells using flow cytometry. The results demonstrated that the membrane coating significantly enhanced nanoparticle internalization. The images provided visual confirmation of the increased internalization and revealed a shift in nanoparticle localization over time. These findings highlight the importance of the membrane coating in promoting efficient cellular uptake and support the potential of MPDAFe@Mem nanoparticles as effective drug delivery carriers for targeted therapeutics.

Photothermal treatment

Photothermal therapy has emerged as a promising approach for targeted cancer treatment, utilizing the photothermal conversion properties of nanoparticles to induce localized hyperthermia and subsequent cell death [46]. In this part of my study, I investigated the photothermal therapy-related cytotoxicity of MPDAFe@Mem NPs towards HepG2 cells using the MUSE flow cytometer with the Count&Viability assay and the Live/Dead assay for visualization of cell death. By comparing the cytotoxic effects of laser-irradiated and non-irradiated nanoparticles on cancer cells, I aimed to assess the photothermal effect of the investigated nanoformulations.

The impact of the photothermal properties of MPDAFe@Mem nanoparticles on the viability of cancer cells was evaluated using a MUSE® cytometer's Count&Viability assay – a flow cytometry-based method used to assess cell viability and determine cell counts in a sample. It utilizes fluorescent dyes that selectively stain live and dead cells, allowing for the differentiation between viable and non-viable populations. By measuring the fluorescence emitted by the stained cells, the MUSE system can provide accurate and rapid quantification of live and dead cells [192]. Cancer cells (HepG2) were treated with MPDAFe@Mem NPs using two sets of conditions: one group irradiated with a 3 W/cm^2 laser and another group without laser irradiation. The results showed a gradual decrease in cell viability with increasing nanoparticle concentration in the laser-treated group, ultimately leading to complete cell elimination at a concentration of 40 μg/mL (**Figure 38A,B)**. The difference in cell viability between the laser-treated and control groups was evident in the graph, with statistical significance established for

the concentrations of 20 and 40 µg/mL (**Table 23**). Notably, irradiation alone (without nanoparticles) did not cause any significant viability reduction. These findings highlight the potent photothermal effect of the nanoparticles, resulting in selective cytotoxicity toward cancer cells when exposed to laser irradiation.

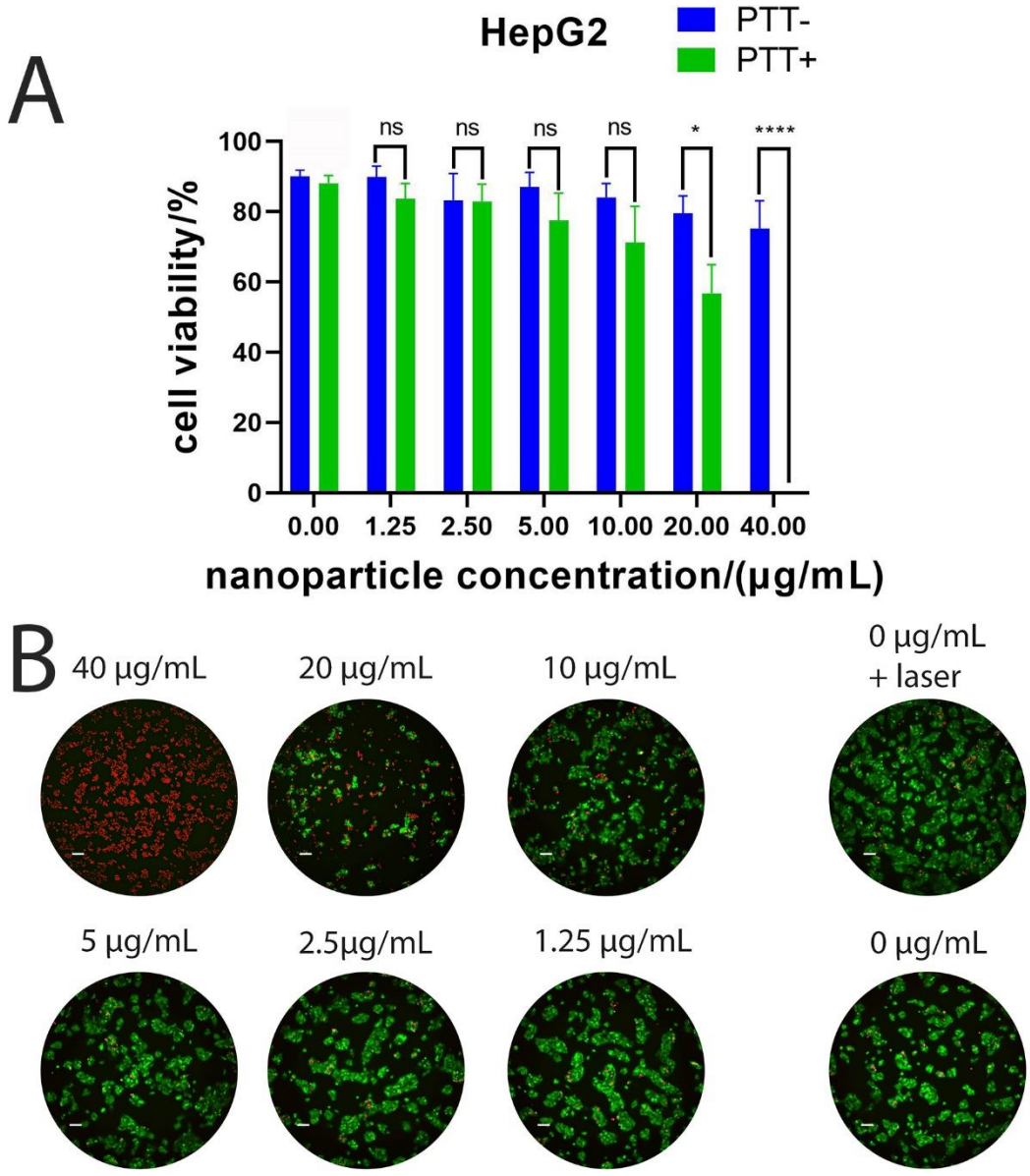

Figure 38. Photothermal evaluation of MPDAFe@Mem NPs. **A)** Cell viability of cancer cells (HepG2) evaluated using MUSE® flow cytometry. Asterisks denote the statistical significance: ns - $p>0.05$, * - $p \leq 0.05$, **** - $p \leq 0.0001$ **B)** Live/Dead assay – visualization of cytotoxic effect of laser (3 W/cm^2)-irradiated MPDAFe@Mem NPs at various concentrations. Cell staining: Calcein, AM (green) – live cells, ethidium homodimer-1 (red) – dead cells; the scale marks 100 µm.

Table 23. Summary of the unpaired t-test results of **PTT+ vs PTT** - cell viability.

Concentration	P value	P value summary	Significantly different? (P < 0.05)
1.25	0.1118	ns	no
2.5	0.9572	ns	no
5	0.1345	ns	no
10	0.1118	ns	no
20	0.0153	*	yes
40	<0.0001	****	yes

Further evidence of the photothermal effect was obtained through Live/Dead assay images. At concentrations of 40 μg/mL nanoparticles, the images showed predominantly red cells (dead cells), indicating the photothermal-induced cell death. Moreover, as the nanoparticle concentration decreased, the number of red cells decreased, suggesting a dose-dependent response to photothermal treatment. These observations confirm that the photothermal properties of MPDAFe@Mem nanoparticles effectively induce cell death, reinforcing their potential as a photothermal therapeutic agent for cancer treatment.

The obtained results show the great potential of MPDAFe@Mem NPs compared to other similar systems that were previously reported. In a study conducted by Hu *et al.,* Fe-PDA NPs irradiated with an NIR laser caused complete elimination of tumor cells at a concentration of 100 μg/mL [178]. However, differences in cell killing ability may be attributed to the conditions of laser exposure; the researchers irradiated cells for 15 min with 1 W/cm^2, while in the study presented here, cells were exposed to 3 W/cm^2 for 5 min. In another work, PDA-Fe3^{+}-ICG NPs reduced cancer cell viability to approximately 0% at a concentration of 100 μg/mL when irradiated with 1 W/cm^2 for 5 min [179]. These results highlight the significance of optimizing irradiation conditions when designing photothermal therapeutic approaches. It has also been shown that the membrane coating might improve the outcome of the photothermal treatment [94,188]. This effect is likely attributed to the enhanced internalization of membrane-coated nanoformulations into tumor cells.

In conclusion, the presented study focused on investigating the photothermal properties of MPDAFe@Mem nanoparticles as a potential photothermal therapy agent. The results demonstrated a significant decrease in cell viability with laser-irradiated nanoparticles, leading

to complete cell elimination at the highest tested concentration (40 μg/mL). The comparison between the laser-treated and non-treated groups further validated the photothermal effect of the nanoparticles. Live/Dead assay images provided additional visual evidence of the photothermal-induced cell death, emphasizing the potential of MPDAFe@Mem nanoparticles for photothermal therapy applications.

Chemotherapeutical effect

The development of efficient drug delivery systems is of utmost importance in cancer therapy to enhance therapeutic efficacy while minimizing systemic toxicity. Traditional chemotherapy often suffers from limitations such as poor drug solubility, rapid clearance, and lack of tumor selectivity [32,193]. To overcome these challenges, various nanoscale drug delivery systems have emerged as promising strategies to improve drug delivery and enhance the chemotherapeutic effect. These systems can encapsulate anticancer drugs, protect them from premature degradation, and selectively deliver them to tumor cells [193]. Evaluation of the chemotherapeutic efficacy of such drug delivery systems is crucial to determine their effectiveness in inhibiting cancer cell growth, inducing cytotoxicity, and minimizing adverse effects. In this study, I investigated the chemotherapeutic effect of DOX-loaded MPDAFe@Mem NPs, aiming to provide insights into their potential as a targeted drug delivery system for cancer therapy. Doxorubicin is a widely used anthracycline chemotherapeutic agent known for its potent anticancer activity. It functions primarily by intercalating with DNA, disrupting DNA replication and transcription processes, inhibiting topoisomerase II activity, and generating reactive oxygen species [194]. These mechanisms collectively induce DNA damage and apoptosis in cancer cells. However, doxorubicin is also associated with side effects such as cardiotoxicity, myelosuppression, and gastrointestinal disturbances [137,194].

Evaluation of the chemotherapeutic effect aimed to assess the efficacy of doxorubicin-loaded MPDAFe@Mem NPs (MPDAFe@DOX@Mem) in inducing cytotoxicity towards HepG2 cells. Multiple assays were performed, including the WST-1 assay, confocal microscopy measurements, and the EdU assay. The WST-1 is a colorimetric cell viability assay commonly used in cell biology and drug discovery research. It is based on the reduction of WST-1, a water-soluble tetrazolium salt, by cellular mitochondrial dehydrogenases to produce a water-soluble formazan dye. The formazan dye is directly proportional to the number of metabolically active cells, and its absorbance can be measured using a spectrophotometer to determine cell viability [195]. HepG2 cells were exposed to various concentrations (from 1.25 to 40 μg/mL) of

MPDAFe, MPDAFe@DOX@Mem, MPDAFe@DOX, and free DOX. The results demonstrated distinct cytotoxicity profiles among the formulations (**Figure 39A**). MPDAFe NPs alone exhibited negligible cytotoxicity across most tested concentrations (ranging from 1.25 to 20 μg/mL), with minimal effect on cell viability. However, at the highest concentration (40 μg/mL), a decrease in viability of approximately 20% was observed. These findings suggest that MPDAFe NPs alone have limited cytotoxicity and may serve as a suitable carrier for drug delivery. In contrast, MPDAFe@DOX@Mem NPs displayed a potent chemotherapeutic effect. Remarkably, even at a concentration of 20 μg/mL, MPDAFe@DOX@Mem NPs completely eliminated the cancer cells. The membrane-coated NPs efficiently delivered the drug to the target cells, resulting in enhanced cytotoxicity. MPDAFe@DOX NPs induced a significant decrease in cell viability, although to a lesser extent than MPDAFe@DOX@Mem NPs - approximately 10% cell viability was observed at the highest concentration, indicating a moderate cytotoxic effect. In contrast, free DOX displayed a relatively lesser decrease in viability, with approximately 30% cell viability observed at the highest concentration. These results suggest that the drug-loaded nanoparticles, particularly MPDAFe@DOX@Mem NPs, exerted a more potent chemotherapeutic effect compared to free doxorubicin, likely due to improved cellular uptake and sustained release of the drug within the cells. The statistical analysis of the WST-1 assay results is summarized in **Table 24**.

Furthermore, the EdU assay was utilized to evaluate the influence of MPDAFe@DOX NPs and MPDAFe@DOX@Mem NPs on cell proliferation (**Figure 39B,C**). Similarly to the WST-1 results, both formulations exhibited a decrease in the relative number of proliferating cells. Notably, with increasing concentrations, the impact of MPDAFe@DOX@Mem NPs became more pronounced, further reducing the population of proliferating cells. This finding highlights the efficacy of MPDAFe@DOX@Mem NPs in inhibiting cell proliferation, an important aspect of cancer treatment. The statistical analysis of the EdU assay results is summarized in **Table 25.**

Confocal microscopy measurements were employed to visualize the intracellular distribution of DOX and assess its uptake by HepG2 cells (**Figure 39D**). MPDAFe@DOX@Mem NPs demonstrated the ability of the nanoformulations to internalize into cancer cells and supported the time-dependence of this process suggested by the imaging flow cytometry (**Figure 37**). After 1 h, the DOX signal inside the cells was relatively weak, whereas after 4 h it was clearly observable, indicating successful uptake of the nanoformulations. This finding confirms the effective encapsulation and successful intracellular delivery of the drug by the nanocarriers, supporting their potential as a drug delivery system for targeted cancer therapy.

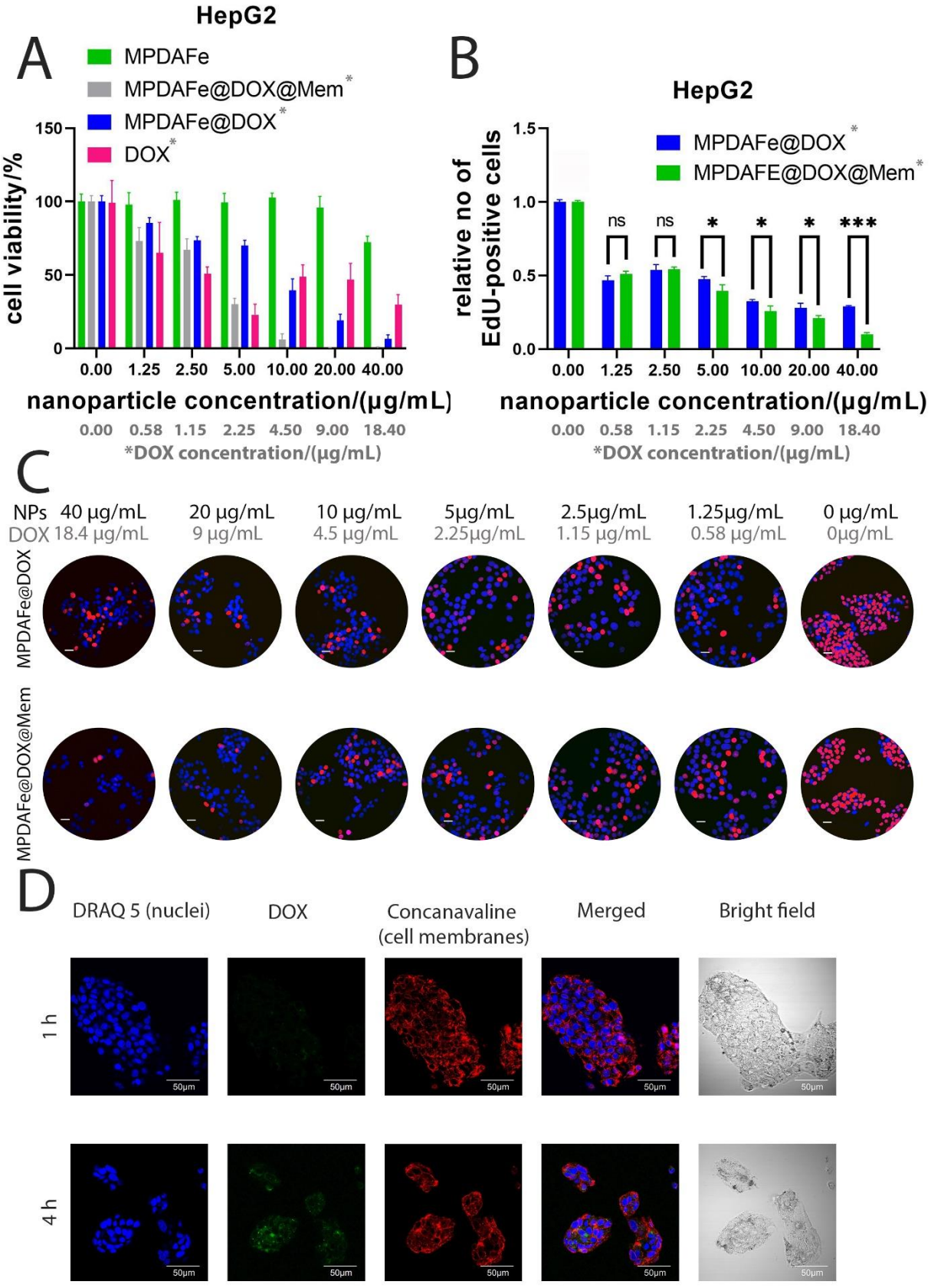

Figure 39. Chemotherapeutic evaluation. **A)** WST-1 assay of viability of cancer cells (HepG2) under incubation with different nanoformulations and free drug (DOX), **B)** Edu assay of HepG2 cells incubated with MPDAFe@DOX and MPDAFe@DOX@Mem NPs. Asterisks denote the statistical

significance: ns - $p>0.05$, * - $p \leq 0.05$, *** - $p \leq 0.001$ **C)** corresponding images of cells from EdU assay (blue – all nuclei, pink – proliferating nuclei); the scale marks 30 μm, **D)** Confocal microscopy images of HepG2 cells incubated with MPDAFe@DOX@Mem NPs for 1 h and 4 h.

Table 24. Summary of the results of the Turkey's multiple comparison tests of the cell viability data obtained from the WST-1 assay of various formulations. Prior the Turkey's analysis, one-way ANOVA evaluation was applied to establish statistically significant differences between the samples.

PDAFe vs. DOX

Concentration	Adjusted P value	P value summary	Significantly different? (P < 0.05)
1.25	0.0435	*	yes
2.5	<0.0001	****	yes
5	<0.0001	****	yes
10	<0.0001	****	yes
20	0.0001	***	yes
40	<0.0001	****	yes

PDAFe@DOX@Mem vs. DOX

Concentration	P value	P value summary	Significantly different? (P < 0.05)
1.25	0.8537	ns	no
2.5	0.0252	*	yes
5	0.4203	ns	no
10	0.0001	***	yes
20	0.0002	***	yes
40	0.0001	***	yes

PDAFe@DOX vs. DOX

Concentration	P value	P value summary	Significantly different? (P < 0.05)
1.25	0.2525	ns	no
2.5	0.0035	**	yes
5	<0.0001	****	yes
10	0.3203	ns	no
20	0.0056	**	yes
40	0.0007	***	yes

PDAFe@DOX@Mem vs. MPDAFe@DOX

Concentration	P value	P value summary	Significantly different? (P < 0.05)
1.25	0.6229	ns	no
2.5	0.4636	ns	no
5	<0.0001	****	yes
10	0.0007	***	yes
20	0.0484	*	yes
40	0.3235	Ns	no

Table 25. Summary of the unpaired t-test analysis results of the normalized number of proliferating HepG2 cells (EdU assay) incubated with MPDAFe@DOX or MPDAFe@DOX@Mem NPs.

MPDAFe@DOX@Mem vs. MPDAFe@DOX

Concentration	P value	P value summary	Significantly different? (P < 0.05)
1.25	0.1159	ns	no
2.5	0.8055	ns	no
5	0.0378	*	yes
10	0.0338	*	yes
20	0.0307	*	yes
40	0.0002	***	yes

Previous studies on PDA-PEG-DOX NPs demonstrated a reduction in 4T1 cancer cell viability to about 40% at a DOX concentration of 10 μg/mL [57], similar to the cytotoxicity observed in this study for uncoated MPDAFe@DOX NPs. Meanwhile, the membrane-coated MPDAFe@DOX@Mem NPs completely eliminated tumor cells at the same concentration. However, in the case of PDA-PEG-DOX NPs, the incubation time was 24 h, whereas in this study, the nanoparticles were incubated with cells for 48 h. The enhanced chemotherapy effect is a common feature of membrane-coated drug delivery systems. For instance, RBC membrane-coated curcumin-loaded PLGA NPs showed increased inhibition of H22 cell proliferation, which was attributed to the membrane-related enhanced endocytosis into the cancer cells [196]. Additionally, membranes from HepG2 and L02 cells enhanced the anticancer effect of DOX-PLGA NPs on their respective homologous cells [81]. Similar effects were observed with platelet membrane-coated DOX-loaded MPDA NPs against MDA-MB-231 cancer cells [97] and paclitaxel-loaded PLGA NPs coated with HeLa cell membranes [197].

In summary, the chemotherapeutic evaluation of the DOX-loaded MPDAFe@Mem NPs (MPDAFe@DOX@Mem) demonstrated their remarkable cytotoxicity towards HepG2 cells. The membrane-coated NPs exhibited enhanced cytotoxicity compared to free doxorubicin, likely attributed to improved cellular uptake and sustained release of the drug. The observed decrease in cell viability, intracellular doxorubicin localization, and inhibition of cell proliferation emphasize the potential of MPDAFe@DOX@Mem NPs as a promising targeted drug delivery system, offering improved therapeutic outcomes while minimizing off-target effects.

Combined therapy

The combination of chemotherapy and photothermal therapy holds great promise as an effective strategy for cancer treatment [198,199]. By combining these two therapeutic approaches, I aimed to enhance treatment efficacy and achieve synergistic effects that could lead to improved outcomes for cancer patients. In this study, I investigated the combined therapy using MPDAFe@DOX@Mem NPs, which can deliver the chemotherapeutic drug and also induce photothermal effects upon laser irradiation. The rationale for conducting these experiments is to assess the cytotoxicity and therapeutic potential of the nanoformulations under different conditions, considering varying concentrations of nanoparticles and laser power levels.

Figure 40 shows the results of the WST-1 assay for MPDAFe@DOX NPs with and without NIR laser irradiation (6 W/cm^2). At lower NP concentrations of 1.25 and 2.5 μg/mL, a gradual reduction in cell viability was observed in both the irradiated and non-irradiated samples, albeit without a significant difference between the two groups. However, a notable disparity emerged as the NPs concentration increased to 5 μg/mL. The viability of the irradiated samples decreased more significantly compared to their non-irradiated counterparts, indicating a synergistic effect of combined therapy. The most striking result was observed at an NPs concentration of 10 μg/mL. In this case, the irradiated MPDAFe@DOX NPs exhibited a remarkable capacity to eliminate cancer cells entirely, achieving a complete reduction in cell viability. In contrast, the non-irradiated NPs at the same concentration still left approximately 40% of the cancer cells viable and were not able to completely eliminate the cancer cells even at the highest tested concentration (40 μg/mL). These findings underscore the advantages of a combined therapeutic approach that merges chemotherapy with PTT. The results not only affirm the potential of MPDAFe@DOX NPs as an effective drug delivery system but also highlight the transformative impact of laser irradiation in enhancing the therapeutic outcome. Statistically significant differences (**Table 26**) were observed in the samples with NPs concentrations of 10-40 μg/mL.

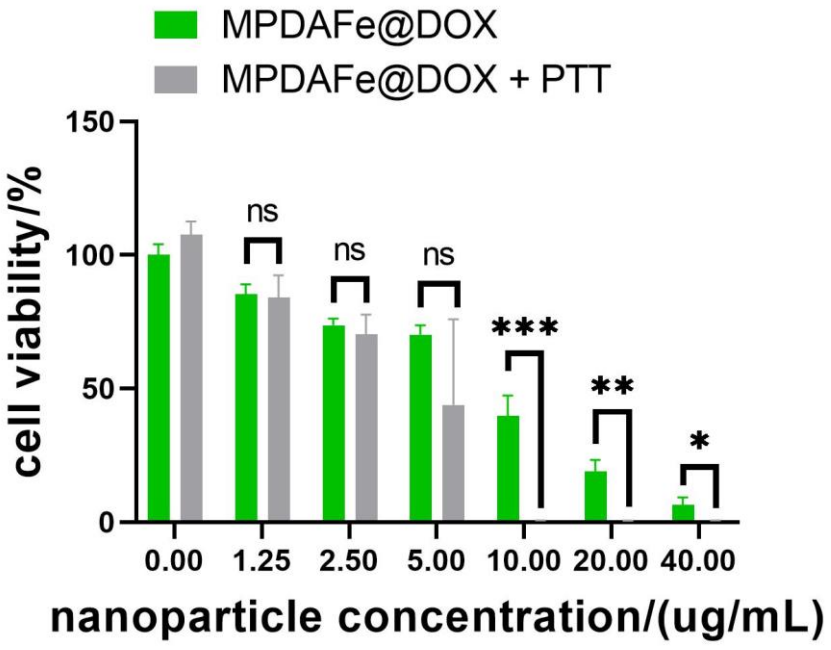

Figure 40.WST-1 results of cell viability study of MPDAFe@DOX NPs with and without NIR laser irradiation (6 W/cm^2).

Table 26. Summary of the unpaired t-test results of the impact of MPDAFe@DOX NPs with and without NIR laser irradiation on cell viability (**MPDAFe@DOX+PTT vs. MPDAFe@DOX).**

Concentration	P value	P value summary	Significantly different? (P < 0.05)
1.25	0.8304	ns	no
2.5	0.4947	ns	no
5	0.2220	ns	no
10	0.0009	***	yes
20	0.0017	**	yes
40	0.0154	*	yes

The cytotoxicity dependence of photothermal nanosystems on irradiation conditions has been previously reported. Silica-coated Gd-chelated melanin nanoparticles showed increased cytotoxicity toward prostate cancer cells with increasing laser power [200]. This effect could be connected to increased heat generation upon laser irradiation, as shown in **Figure 24**. The laser powers used in literature vary from below 1 W/cm^2 [200] to 6 W/cm^2 [163]. However, with MPDAFe NPs, the cancer cell-killing potential of MPDAFe@DOX was more pronounced at the power of 6 W/cm^2.

In the second experiment, the efficacy of combined therapy was evaluated by assessing the viability of HepG2 cancer cells incubated with MPDAFe@DOX@Mem NPs, both with and without irradiation by a NIR laser (6 W/cm^2) (**Figure 41**). The outcomes revealed a concentration-dependent decrease in cell viability for both nanoformulations. Notably, at a concentration of 10 μg/mL, both of the nanoformulations demonstrated a remarkable ability to eradicate cancer cells – irradiated NPs decreased the cell viability completely, whereas the non-irradiated NPs resulted in a mere 6% cell viability. The results affirm that the membrane-coated MPDAFe@DOX NPs offer a highly effective approach for eradicating cancer cells. The details of the statistical analysis of the results are summarized in **Table 27**.

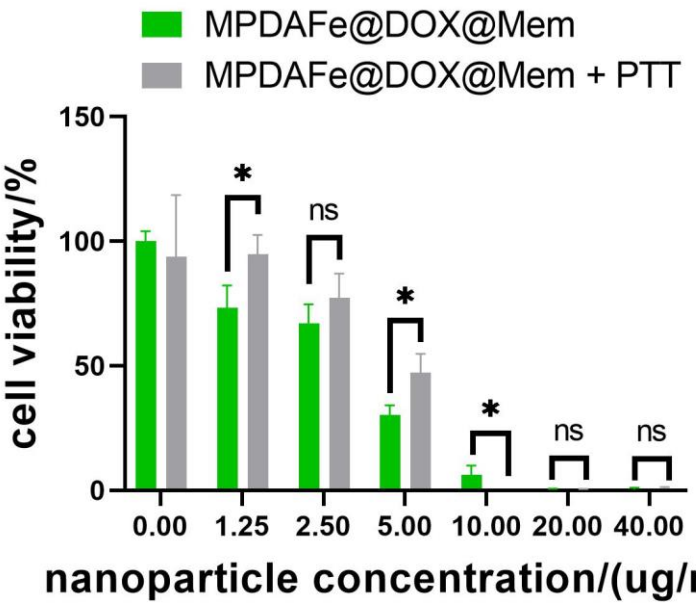

Figure 41. WST-1 results of cell viability study of MPDAFe@DOX@Mem NPs with and without NIR laser irradiation (6 W/cm^2).

Table 27. Summary of the unpaired t-test results of the impact of MPDAFe@DOX@Mem NPs with and without NIR laser irradiation on cell viability (**MPDAFe@DOX@Mem+PTT vs. MPDAFe@DOX@Mem).**

Concentration	P value	P value summary	Significantly different? (P < 0.05)
1.25	0.0353	*	yes
2.5	0.2241	ns	no
5	0.0272	*	yes
10	0.0416	*	yes
20	0.3506	ns	no
40	0.5656	ns	no

Cell membrane-coating has demonstrated beneficial effects on the outcomes of synergistic chemo- and photothermal therapy in various studies. Curcumin-loaded PLGA/PDA NPs irradiated with NIR laser exhibited stronger cell-killing ability when coated with RBC membranes [201]. However, there is also evidence suggesting that the cell membrane coating may not significantly enhance the synergistic therapy efficacy. For instance, Fe_3O_4@PDA NPs combining gene therapy with photothermal treatment displayed similar cytotoxicity with or without stem cell membrane coating [202]. These findings suggest that in certain cases,

the membrane coating primarily aids in delivering the cargo to tumor cells and contributes to the overall therapeutic outcome to a lesser extent.

In conclusion, our two experimental investigations have highlighted the exceptional cytotoxicity of MPDAFe@DOX NPs and MPDAFe@DOX@Mem NPs toward cancer cells. The results suggest a nuanced interplay between drug delivery enhancement due to membrane coating and the PTT component. In the case of non-coated NPs, the effect of combined therapy is more pronounced, highlighting the substantial contribution of photothermal treatment to overall cancer cell eradication. Conversely, membrane coating appears to enhance drug delivery into the cells, which may mask the photothermal therapy's contribution despite its efficacy in eliminating cancer cells. Taken together, these experiments emphasize the promise of MPDAFe@DOX@Mem for targeted cancer therapy. The combined strategies of chemotherapy and photothermal therapy offer a compelling avenue for achieving highly efficient cancer cell eradication.

Oxidative stress

Comparative analysis of ROS generation is an important aspect when investigating drug delivery systems, especially in the context of cancer therapy. ROS are highly reactive molecules containing oxygen, such as superoxide anion (O^{2-}), hydrogen peroxide (H_2O_2), and hydroxyl radical (OH^-) [203]. While low levels of ROS play crucial roles in various cellular processes, excessive ROS generation can lead to oxidative stress, causing damage to biomolecules and triggering multiple diseases, including cancer [203]. In the context of drug delivery systems, it can be harnessed for enhancing therapeutic efficacy, such as in photothermal therapy, where ROS production induced by laser irradiation can lead to selective cancer cell destruction [176]. Additionally, understanding the ROS generation by drug-loaded nanoparticles is vital to assess their potential cytotoxic effects and optimize their therapeutic application.

In the evaluation of ROS generation, I compared several nanoformulations, including MPDAFe@Mem NPs, MPDA@DOX@Mem NPs, MPDAFe@DOX@Mem NPs, and MPDAFe@DOX@Mem irradiated with a laser power of 6 W/cm^2. The results of the ROS production evaluation are presented in **Figure 42**. Among these nanoformulations, MPDAFe@Mem NPs exhibited the lowest ROS levels. This result could be attributed to the absence of doxorubicin in these nanoparticles, as doxorubicin is known to generate ROS upon cellular internalization and subsequent activation [203,204]. In contrast, both MPDA@DOX@Mem and MPDAFe@DOX@Mem NPs demonstrated higher ROS levels

compared to MPDAFe@Mem NPs. The presence of DOX in the MPDA@DOX@Mem and MPDAFe@DOX@Mem NPs likely accounts for the higher ROS levels observed in these formulations. Furthermore, the irradiated sample of MPDAFe@DOX@Mem NPs exhibited a significant increase in ROS levels at concentrations of 20 and 40 µg/mL. Previous reports show that laser irradiation could enhance ROS production in tumor cells caused by nanoformulations [205]. Hence, the laser irradiation likely triggered additional ROS production resulting from exposure to MPDAFe@DOX@Mem NPs, further enhancing the therapeutic effect of the combined chemotherapy and photothermal therapy. It has been shown that increased ROS generation can lead to oxidative damage of cellular components and subsequent cell death [206,207].

Another aspect that I was interested in was the impact of iron on ROS generation. Thus. I compared two membrane-coated nanoformulations containing doxorubicin with and without Fe (MPDAFe@DOX@Mem and MPDA@DOX@Mem, respectively) to explore the possibility of ferroptosis induction by Fe ions. Ferroptosis is a form of regulated cell death characterized by the accumulation of intracellular iron and ROS that lead to subsequent cell membrane damage [208]. Fe has long been linked to toxicity due to its ability to induce hydroxyl radicals (OH·) through the Fenton reaction [209]. Previously reported iron-chelated DOX@PDA NPs were shown to increase ROS production in cancer cells compared to nanoparticles without iron [160]. Given the presence of iron in the formulation of MPDAFe@DOX@Mem, it was hypothesized that the nanoformulations might trigger ferroptosis in cancer cells, which would result in increased ROS generation. Surprisingly, the two formulations did not show a significant difference in ROS profiles, indicating that the presence of Fe-modified nanoparticles does not influence ROS generation by HepG2 cells. This suggests that the observed cytotoxic effects and therapeutic efficacy of MPDAFe@DOX@Mem are likely not related to ferroptosis induction in this particular cell line. **Table 28** –**31** summarize the results of the statistical analysis of the Oxidative stress evaluation assay of various formulations.

In conclusion, the investigation of ROS production in the context of drug delivery systems holds immense significance for understanding the cytotoxicity and therapeutic potential of nanomaterials. MPDAFe@Mem NPs demonstrated the lowest ROS levels, while the presence of doxorubicin in the nanoformulations, such as MPDA@DOX@Mem and MPDAFe@DOX@Mem NPs, led to increased ROS generation. Laser irradiation further enhanced ROS production in the irradiated sample, contributing to the synergistic effect of

combined chemotherapy and photothermal therapy. While the presence of iron in MPDAFe@DOX@Mem suggested a possible association with ferroptosis, the results did not support this hypothesis.

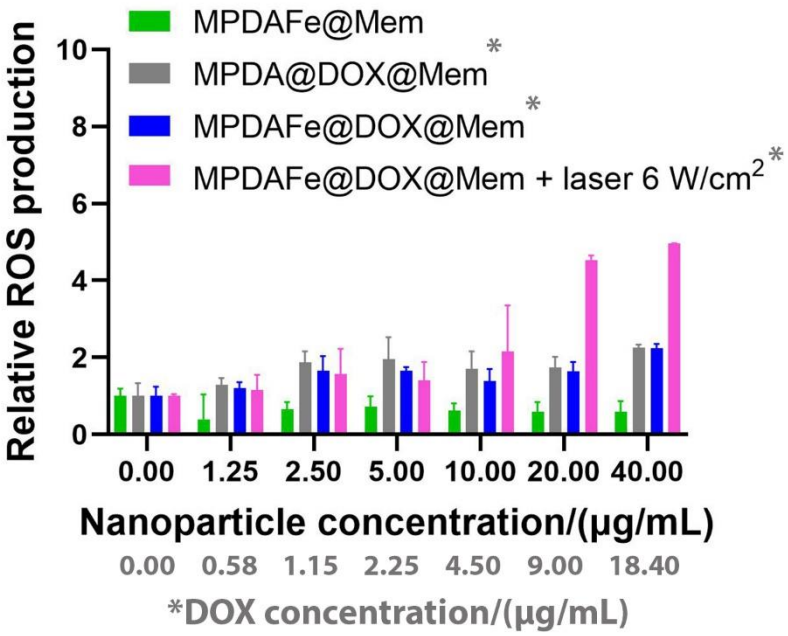

Figure 42. Relative ROS production (The data are shown as mean and SD (n=3)). Results were obtained using the MUSE® Oxidative Stress assay.

Table 28. Results of the Turkey's multiple comparison tests of the cell viability of **PDAFe@Mem vs. MPDA@DOX@Mem**. Prior the Turkey's analysis, one-way ANOVA evaluation was applied to establish statistically significant differences between the samples.

Concentration	Adjusted P value	P value summary	Significantly different? (P < 0.05)
1.25	0.0924	ns	no
2.5	0.0288	*	yes
5	0.0221	*	yes
10	0.2666	ns	no
20	0.0016	**	yes
40	<0.0001	****	yes

Table 29. Results of the Turkey's multiple comparison tests of the cell viability of **PDAFe@Mem vs. MPDAFe@DOX@Mem**. Prior the Turkey's analysis, one-way ANOVA evaluation was applied to establish statistically significant differences between the samples.

Concentration	P value	P value summary	Significantly different? (P < 0.05)
1.25	0.1309	ns	no
2.5	0.0711	ns	no
5	0.0778	ns	no
10	0.5286	ns	no
20	0.0029	**	yes
40	<0.0001	****	yes

Table 30. Results of the Turkey's multiple comparison tests of the cell viability of **PDAFe@Mem vs. MPDAFe@DOX@Mem+PTT**. Prior the Turkey's analysis, one-way ANOVA evaluation was applied to establish statistically significant differences between the samples.

Concentration	P value	P value summary	Significantly different? (P < 0.05)
1.25	0.1641	ns	no
2.5	0.1021	ns	no
5	0.2268	ns	no
10	0.0822	ns	no
20	<0.0001	****	yes
40	<0.0001	****	yes

Table 31. Results of the Turkey's multiple comparison tests of the cell viability of **PDAFe@DOX@Mem vs. MPDAFe@DOX@Mem**. Prior the Turkey's analysis, one-way ANOVA evaluation was applied to establish statistically significant differences between the samples.

Concentration	P value	P value summary	Significantly different? (P < 0.05)
1.25	0.9942	ns	no
2.5	0.9149	ns	no
5	0.8040	ns	no
10	0.9339	ns	no
20	0.9518	ns	no
40	0.9989	ns	no

Homotypic targeting

Homotypic targeting is one of the most appealing features of the cancer cell membrane-coated nanocarriers. This concept is based on the fact that membrane coating preserves the protein profile close to that of the source cells [210]. As a result, it was observed that the homologous cells show selectively increased uptake of the cancer cell membranes compared to other membranes, such as RBC [191] or even other cancer cell lines (non-homologous) [211]. The investigation of homotypic targeting in cancer cell membrane-coated drug delivery systems is important to understand their selectivity and effectiveness in cancer therapy. This study aimed to assess the impact of homotypic targeting on the cytotoxicity of two nanoformulations, MPDAFe@DOX and MPDAFe@DOX@Mem, on HepG2 (homologous cells) and U118 cells (non-homologous cells).

To evaluate the effectiveness of homotypic targeting, the WST-1 assay was employed to measure the cell viability of both HepG2 and U118 cells treated with MPDAFe@DOX and MPDAFe@DOX@Mem nanoparticles at various concentrations (from 1.25 to 40 μg/mL) (**Figure 43**). The MPDAFe@DOX@Mem NPs demonstrated enhanced cytotoxicity toward the homologous cells (HepG2) compared to the U118 cell line. At concentrations of 10 and 20 μg/mL, the cytotoxic effects of the nanoparticles on HepG2 cells were statistically different from the U118 cells (**Table 32**), indicating enhanced cell killing potentially connected to the homotypic targeting scenario. At a concentration of 40 μg/mL, both HepG2 and U118 cells were completely eliminated. The study revealed that the non-coated nanoparticles, MPDAFe@DOX, also exhibited significant differences in cytotoxicity between HepG2 and U118 cells. However, the cytotoxicity of MPDAFe@DOX NPs was much lower than that of

their membrane-coated counterparts. This observation suggests that the selective cytotoxicity against different cell types could not be exclusively related to the membrane coating. Notably, the membrane-coated nanoparticles, MPDAFe@DOX@Mem, demonstrated improved cell killing of heterotypic U118 cells compared to the non-coated nanoparticles. These results are consistent with previously reported studies, which demonstrate that while homologous cells indeed exhibit significantly increased uptake through homotypic targeting, other cell lines can also internalize the membrane-coated drug carriers to a varying extent [81,211,212]. However, in specific instances, such as HeLa cell membrane-coated PLGA NPs, the cytotoxic effect on the homologous cells is much more evident [213].

In conclusion, the performed targeting experiments demonstrated enhanced cytotoxicity in homologous cells (HepG2 cells) as well as nonhomologous cells (U118 cells) compared to non-coated nanoparticles. The intrinsic properties of the nanoparticles also played a role in their selective cytotoxicity against different cell types. Nevertheless, the findings of this study underscore the potential benefits of membrane coating, which may extend beyond homologous cell lines.

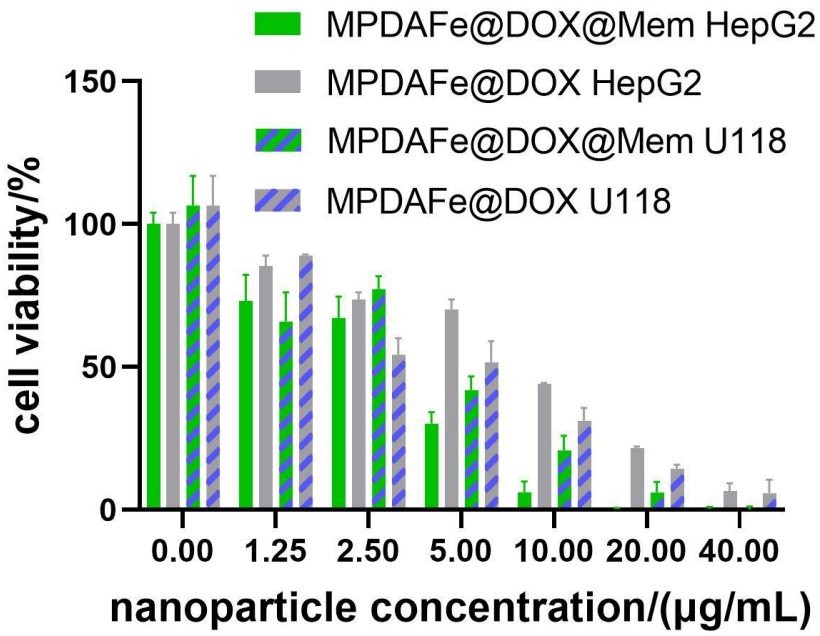

Figure 43. Homotypic targeting. WST-1 results of viability of two cell lines: HepG2 (homologous) and U118 (non-homologous) under incubation with MPDAFe@DOX or MPDAFe@DOX@Mem NPs.

Overall, MPDAFe@DOX@Mem NPs showed promising anticancer properties with a synergistic effect of chemo-and photothermal therapy enhanced by increased internalization resulting from the cancer cell membrane. Based on those results, the nanoparticles were decided to be tested further for the anticancer treatment on the mice model.

Table 32. Summary the results of the Turkey's multiple comparison tests of the cell viability data obtained from the WST-1 assay of various formulations. Prior the Turkey's analysis, one-way ANOVA evaluation was applied to establish statistically significant differences between the samples.

MPDAFe@DOX@Mem HepG2 vs. U118

Concentration	Adjusted P value	P value summary	Significantly different? (P < 0.05)
1.25	0.6234	ns	no
2.5	0.1674	ns	no
5	0.0715	ns	no
10	0.0078	**	yes
20	0.0405	*	yes
40	0.8314	ns	no

PDAFe@DOX HepG2 vs. U118

Concentration	P value	P value summary	Significantly different? (P < 0.05)
1.25	0.9228	ns	no
2.5	0.0101	*	yes
5	0.0007	***	no
10	0.0153	*	yes
20	0.0118	*	yes
40	0.9904	ns	no

PDAFe@DOX@Mem vs. MPDAFe@DOX U118

Concentration	P value	P value summary	Significantly different? (P < 0.05)
1.25	0.0176	*	yes
2.5	0.0036	**	yes
5	0.2034	ns	no
10	0.0494	*	no
20	0.0043	**	yes
40	0.0676	ns	no

In vivo pilot study

The following studies were performed in consortium with Poznań University of Medical Sciences.

Therapeutic efficacy

In vivo studies involving animal models, particularly mice, are crucial for translating potential therapeutic interventions from preclinical to clinical stages [61]. They aim to evaluate the therapeutic efficacy of drug delivery systems in a biologically relevant setting [214]. Mouse models provide valuable insights into the safety and effectiveness of drug delivery systems, allowing a better understanding of the behavior and response of the nanoparticles within a living organism [214].

Balb/c nude mice are a strain of laboratory mice that lack a functional immune system, making them particularly useful in studies related to cancer research [215]. These mice are also commonly used in xenograft studies, in which human tumor cells are implanted into the mice to create subcutaneous tumor models for further investigation [215]. The use of Balb/c nude mice in research has contributed significantly to our understanding of cancer biology and the development of potential cancer therapies [216].

In vivo pilot studies were conducted in Balb/c nude mice to investigate the effectiveness of MPDAFe@DOX@Mem NPs as a potential anticancer therapy. The schematic plan of the studies is presented in **Figure 44**. The animals were divided into 8 experimental groups, listed in **Table 33**.

Table 33. Experimental animal groups for the pilot *in vivo* study.

Group	**Applied therapy**	**Initial no of animals (N)**
I (control)	PBS	8
II	PBS+laser irradiation (phototherapy)	8
III	DOX (chemotherapy)	8
IV	MPDAFe@Mem NPs	8
V	MPDAFe@DOX@Mem NPs (chemotherapy)	8
VI	MPDAFe@Mem NPs + laser irradiation (phototherapy)	8
VII	DOX + laser irradiation (chemo- + phototherapy),	8
VIII	MPDAFe@DOX@Mem NPs + laser irradiation (chemo- + phototherapy)	8

Subcutaneous tumor models were established by injecting tumor cells (HepG2 cells, 2 x 10^6 cells per mouse, 100 µL) into the flanks of the mice. After the tumors reached 5-10 mm^3, the mice were administrated in tail vain with 100 µL of either MPDAFe@Mem NPs, MPDAFe@DOX@Mem NPs, or 10 mM pH 7.4 PBS buffer, depending on the experimental group. The concentration applied concentration of DOX was 2 mg/kg, which corresponds to 4.44 mg/kg of NPs. The groups that involved phototherapy treatment were irradiated with an 808 nm laser the day after the injection. The animals were then monitored for the following 38 days, including body weight and tumor size measurements (using a caliper) every two days. The therapeutic efficacy of the NPs was evaluated by measuring tumor growth inhibition rates and survival rates.

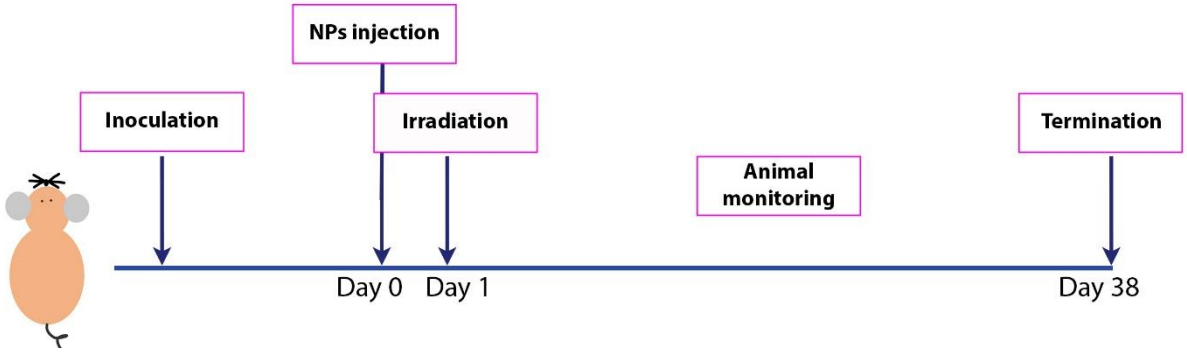

Figure 44. Schematic illustration of the pilot *in vivo* studies plan.

Figure 45A summarizes the tumor size measurements obtained to assess the impact of the different therapeutic interventions on tumor growth. Remarkably, all groups subjected to laser irradiation demonstrated smaller tumor sizes compared to their respective non-irradiated counterparts. This finding suggests that the photothermal effect induced by the laser contributed to inhibiting tumor growth in the irradiated groups. Notably, complete tumor elimination was observed in two groups: the PBS+laser irradiation group and the MPDAFe@DOX@Mem + laser irradiation group. These results indicate that laser irradiation alone and combined with MPDAFe@DOX@Mem NPs exhibited the most significant tumor suppression and eradication capabilities, suggesting that the applied laser power masked the potential therapeutic effect of the nanoformulations. The results for the groups treated with MPDAFe@Mem NPs, MPDAFe@DOX@Mem NPs, and DOX alone showed limited efficacy in decreasing the tumor size comparable with the PBS control group. This suggests that the dosage of the nanoformulations would require adjustment in the next stage of the research. It is worth noting that later MRI investigation revealed that some tumors might have been omitted in

the assessment as they were growing inside the muscle and could not have been noticeable palpably or visually. Such a variety in the tumor location could have been caused by faulty inoculation.

In the literature, various laser powers have been utilized for *in vivo* irradiation of nanoparticles, ranging from lower values such as 1.3 W/cm^2 [217] or 1.0 W/cm^2 [97] to higher values like 5 W/cm^2 [218] and even 9.5 W/cm^2 [219]. Another crucial factor contributing to the diverse outcomes could be the post-injection time of irradiation. In this study, irradiation was conducted 24 h after the NP injection, while other investigations implemented shorter intervals, such as 4 h [220], 6 h [217], 12 h [97], or even as short as 30 min [219]. Increasing the DOX dosage could yield different results, as examples can be found where 5 mg/kg doses were employed [97]. Moreover, some studies apply the therapy repeatedly throughout the study, such as every two days [97] or *via* intratumoral injection [219], which could also enhance the efficacy of the applied treatment.

In assessing the safety of the treatments, the body weight of the mice in all groups remained stable and comparable (**Figure 45B**). This indicates that the treatments did not lead to significant weight loss or adverse effects on the general health of the animals. On the other hand, the survival rate of the mice varied among the different groups. Interestingly, the PBS group, which received no therapeutic intervention, exhibited the highest survival rate of 100%. This outcome may be attributed to the relatively slower tumor growth observed in some mice. Since the lowest survival rates were observed in the laser-treated groups, it further confirms the hypotheses that the laser power might have been inadequate.

Overall, the *in vivo* studies using Balb/c nude mice provided valuable insights into the therapeutic efficacy and safety of MPDAFe@Mem NPs and MPDAFe@DOX@Mem NPs, both with and without laser irradiation. The observed tumor suppression and eradication capabilities in some groups highlight the potential of these nanoparticle-based therapies. However, the study also indicates the need for further optimization, such as adjusting the laser power and nanoparticle concentration, to improve therapeutic outcomes and enhance long-term survival rates. The high laser power of 6 W/cm^2 may have induced unintended side effects or affected the overall therapeutic outcome. Similarly, adjusting the nanoparticle concentration might enhance the drug delivery efficiency and overall therapeutic efficacy. Continued investigations and modifications are warranted to fine-tune the therapeutic approaches and maximize their potential for clinical applications.

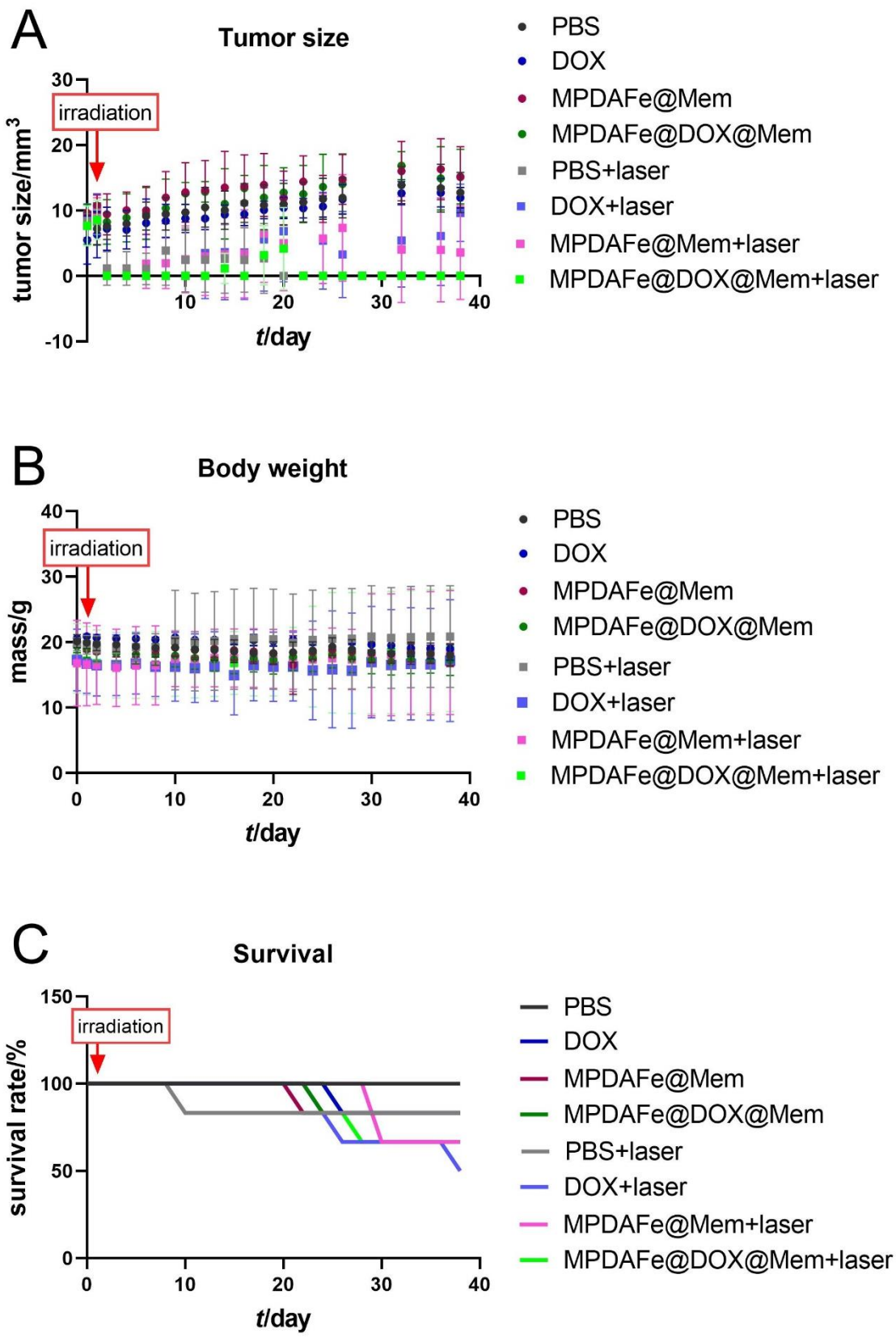

Figure 45. Results of the pilot *in vivo* studies on Balb/c nude mice. **A)** Tumor size, **B)** Body weight, **C)** Survival of the animals.

In vivo imaging

Bioimaging is an important tool for studying biological processes and diseases at the cellular and molecular levels. It allows to visualize and quantify the distribution, behavior, and interactions of cells, tissues, and molecular targets in living organisms. This information can provide valuable insights into the pathogenesis of diseases, the mechanisms of drug action, and the efficacy of therapies. Bioimaging also enables the development of new diagnostic and therapeutic tools, such as imaging agents, targeted drug delivery systems, and nanomedicines. The use of MPDAFe@Mem nanoparticles in MRI imaging of mice has the potential to provide valuable insights into the physiology and pathology of the tumor and aid in the development of new diagnostic and therapeutic strategies.

The MRI contrasting properties of MPDAFe@Mem NPs were assessed on a subcutaneous tumor model using six mice inoculated with HepG2 tumor cells. The mice were intravenously injected with 100 µL of MPDAFe@Mem NPs (4.44 mg/kg) using a catheter while inside the MRI scanner. T_1-weighted images were acquired at various time points: before NPs administration, immediately after administration, and at 20 min, 24 h, and 7 days post-administration. Representative images are presented in **Figure 46**. The selected cross-sections present different areas of the abdomen area. The tumor was marked with red arrows. The images showed a contrasting effect, with an enhanced signal-to-noise ratio, resulting in improved visualization of details and overall contrast enhancement throughout the body, although not specifically within the tumor area. The images taken after 24 h and 7 days no longer contain the contrasting effect.

The contrasting effect observed in the MRI images indicates the successful distribution of MPDAFe@Mem NPs in the body. The increased signal-to-noise ratio suggests that the nanoparticles can be detected effectively in the tissue, improving the visibility of anatomical structures and tissue details. However, the specific enhancement within the tumor area was not prominent, which might be attributed to several factors. Previous studies show that PEG-Fe-PDA NPs, which exhibited similar r_1 values to MPDAFe@Mem, were successful in contrasting within the tumor region [217]. One possible explanation for the lack of specific contrast enhancement in the tumor area of MPDAFe@Mem NPs could be related to the distribution and pharmacokinetics of the nanoparticles. The tumor microenvironment is known for its complex and heterogeneous characteristics, which can influence the accumulation and retention of nanoparticles [156]. Depending on factors such as tumor vascularization, permeability, and interstitial fluid pressure, the nanoparticles might not accumulate uniformly

within the tumor, leading to variations in contrast enhancement. In the future, another administration route could be investigated, such as intratumoral injection, which is also used for examining MRI candidates [217]. The dose could also be considered, as studies show the applied concentrations of nanoformulations to range from x to even 10 mg/kg body weight [218].

In conclusion, the MRI study proves the contrasting potential of MPDAFe@Mem as they demonstrated the successful overall contrasting effect throughout the body. However, specific contrast enhancement within the tumor area was not evident in the selected time points and imaging sequence. Further investigations could include adjustment of the administrated dose or administration route. Moreover, complementary imaging techniques such as fluorescent imaging could be applied to assess whether the nanoparticles are capable of accumulating in the tumor region. The results of this study provide valuable insights and lay the foundation for future optimization and development of nanoparticle-based MRI contrast agents for cancer imaging and therapeutics.

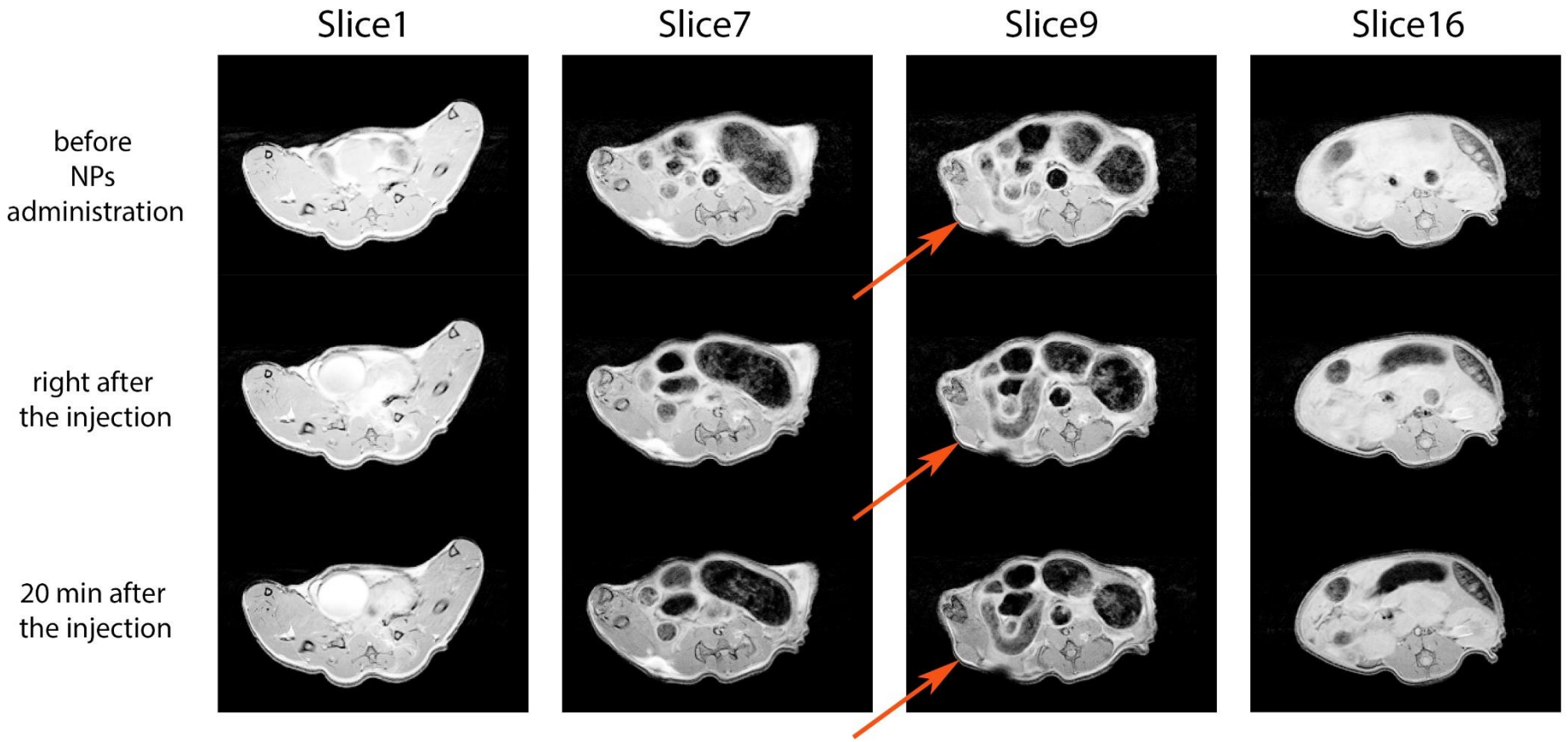

Figure 46. Representative example of the *in vivo* transversal cross-sectional MR images of nude mice bearing tumor. The red arrows point at the tumor.

5

CONCLUSIONS

In this final chapter, I present the conclusive findings of my doctoral thesis, substantiating the significance of the undertaken research. By summarizing the outcomes and implications of my study, I aim to address the identified research gap in the realm of cancer therapy. The conclusions drawn from the results shed light on the efficacy of the employed materials and solutions, paving the way for further advancements in nanotechnology-based treatments.

The presented study successfully bridged the gap between nanoscience theory and practical applications, paving the way for advanced nanotechnology-based cancer therapies. This research lays the groundwork for future studies to optimize PDA-based cancer therapies to achieve better therapeutic outcomes. Below are listed the most significant aspects of the presented work.

1. **Successful development of multifunctional nanoparticles**: The research resulted in the successful synthesis and characterization of multifunctional polydopamine-coated iron nanoparticles (MPDAFe NPs) and their variations, including drug-loaded MPDAFe@DOX NPs and membrane-coated MPDAFe@DOX@Mem NPs. Based on the established synthesis, the possibility of using other metals, including gadolinium and manganese, was also presented. Through metal addition, the PDA nanoparticles gained paramagnetic properties, proving promising for MRI applications.
2. **Biosafety:** Several cytotoxicity studies proved negligible toxicity of MPDAFe nanocarriers.
3. **Tumor targeting**: Introducing cancer cell membrane coatings on the nanoparticles (MPDAFe@DOX@Mem NPs) led to improved homologous cell targeting, enhancing drug delivery to cancer cells through increased cell internalization.
4. **Synergistic chemotherapy and photothermal therapy:** Combining chemotherapy with photothermal therapy using MPDAFe@DOX@Mem NPs demonstrated enhanced eradication of HepG2 cells supported by a range of *in vitro* assays.
5. ***In vivo* pilot studies**: *In vivo* experiments on Balb/c nude mice did not dismiss potential therapeutic effects with tumor size reduction after laser irradiation. However, varying factors like laser power, post-injection time of irradiation, and DOX dosage need to be adjusted to reveal the full potential of the described drug delivery system.

The application of MPDAFe@Mem NPs in MRI imaging showed an improved signal-to-noise ratio and enhanced contrast in general, with the potential for further optimization.

In conclusion, the described research has made notable strides in the field of cancer therapy strategies based on multifunctional nanoparticles, demonstrating promising results in targeted drug delivery and synergistic treatment. The findings contribute to the growing body of knowledge in nanotechnology and provide insights for the development of safer and more effective nanomedicine. Further studies and refinements can lead to transformative advancements in cancer treatment and nanotechnology applications in various domains. To paraphrase the words of Dr. Feynman: *I described a field in which little has been done but in which an enormous amount can be done in principle*.

LIST OF ABBREVIATIONS

APS	ammonium persulfate
CNTs	carbon nanotubes
CP	cisplatin
CT	computed tomography
DA	dopamine
DDS	drug delivery systems
DFT	density functional theory
DHE	dihydroethidium
DHI	5,6-Dihydroxyindole
DLS	dynamic light scattering
DMEM	Dulbecco's Modified Eagle Medium
DNA	deoxyribonucleic
DOX	doxorubicin
DPBS	Dulbecco's phosphate-buffered saline
DSC	differential scanning calorimetry
EDS	energy-dispersive X-ray spectroscopy
EdU	5-ethynyl 2´-deoxyuridine
EDX	energy-dispersive X-ray
EPR	electron plasmon resonance
EPR	enhanced permeability and retention
ET	echo time
ETL	echo train lenght
FBS	fetal bovine serum
FTIR	Fourier-transform infrared spectroscopy
GSH	glutathione
HBSS	Hank's balanced salt solution
HCA	high-content analysis
HR-MS	high-resolution mass spectroscopy
ICF	imaging flow cytometry
ICG	indocyanine green
ICP-OES	inductively coupled plasma optical emission spectroscopy
MEM	minimum essential medium Eagle
MEMS	multi-echo multi-slice
MPDA	porous PDA nanoparticles
MPDAFe	porous Fe-modified PDA nanoparticles
MPMS	magnetic property measurement system
MRI	magnetic resonance imaging
MSOT	multispectral optoacoustic tomography
MWCNTs	multi-walled carbon nanotubes
NIR	near-infrared
NMR	nuclear magnetic resonance

NPs	nanoparticles
PAA	acrylamide (30%)/bisacrylamide (0.8%)
PAI	photoacoustic imaging
PAMAM	poly(amidoamine)
PAN	polyaniline
PBS	phosphate-buffered saline
PCL	poly(caprolactone)
PDA	polydopamine
PDI	polydispersity index
PDT	photodynamic therapy
PEG	polyethylene glycol
PET	positron emission tomography
PLGA	poly(lactic-co-glycolic acid)
PMMA	poly(methyl methacrylate)
PPI	poly(propylene imine)
PPy	polypyrrole
PTA	photothermal agent
PTT	photothermal therapy
PVDF	polyvinylidene fluoride
QD	quantum dots
RBC	red blood cells
RES	reticuloendothelial system
RF	radiofrequency
RIT	radioisotope therapy
ROS	reactive oxygen species
RT	room temperature
RT	repetition time
SDS-PAGE	sodium dodecyl-sulfate polyacrylamide gel electrophoresis
SEMS	single-echo multi-slice
SQUID	superconducting quantum interference devices
STA/FTIR	simultaneous thermal analysis and Fourier-transform infrared spectroscopy
SWCNTs	single-walled carbon nanotubes
TEM/HR	transmission electron microscopy/high-resolution transmission electron
TEM	microscopy
TEMED	N,N,N’,N’-Tetramethylethylenediamine
TGA	thermogravimetry
TRIS	Tris(hydroxymethyl)aminomethane
WBC	white blood cells
XRD	X-ray diffraction

INDEX OF FIGURES

INDEX OF TABLES

REFERENCES

[1] R.P. Feynman, There's Plenty of Room at the Bottom, J. MICROELECTROMECHANICAL Syst. 1 (1992) 60–66.

[2] H.F. Tibbals, Medical Nanotechnology and Nanomedicine, 1st ed., Taylor & Francis, 2011.

[3] S. Bayda, M. Adeel, T. Tuccinardi, M. Cordani, F. Rizzolio, The History of Nanoscience and Nanotechnology: From Chemical–Physical Applications to Nanomedicine, Molecules. 25 (2019) 112. https://doi.org/10.3390/molecules25010112.

[4] M.C. Roco, National Nanotechnology Initiative - Past, Present, Future, in: Handb. Nanosci. Eng. Technol. 2nd Ed, John Wiley & Sons, Inc., Hoboken, NJ, USA, 2007: pp. 3.1-3.26. https://doi.org/10.1002/9780470114735.hawley11400.

[5] V.K. Varadan, A.S. Pillai, D. Mukherji, M. Dwivedi, L. Chen, Nanoscience and Nanotechnology in Engineering, WORLD SCIENTIFIC, 2010. https://doi.org/10.1142/7364.

[6] L. Zhang, T.J. Webster, Nanotechnology and nanomaterials: Promises for improved tissue regeneration, Nano Today. 4 (2009) 66–80. https://doi.org/10.1016/j.nantod.2008.10.014.

[7] V. Bhardwaj, A. Kaushik, Biomedical Applications of Nanotechnology and Nanomaterials, Micromachines. 8 (2017) 298. https://doi.org/10.3390/mi8100298.

[8] P. Iqbal, J.A. Preece, P.M. Mendes, Nanotechnology: The "Top-Down" and "Bottom-Up" Approaches, Supramol. Chem. (2012). https://doi.org/10.1002/9780470661345.smc195.

[9] J.M. Zuo, J.C.H. Spence, Advanced Transmission Electron Microscopy - Imaging and Diffraction in Nanoscience-, Springer, 2017.

[10] N. Joudeh, D. Linke, Nanoparticle classification, physicochemical properties, characterization, and applications: a comprehensive review for biologists, J. Nanobiotechnology. 20 (2022) 262. https://doi.org/10.1186/s12951-022-01477-8.

[11] S. Anu Mary Ealia, M.P. Saravanakumar, A review on the classification, characterisation, synthesis of nanoparticles and their application, IOP Conf. Ser. Mater. Sci. Eng. 263 (2017) 032019. https://doi.org/10.1088/1757-899X/263/3/032019.

[12] C. Vauthier, G. Ponchel, Polymer Nanoparticles for Nanomedicines, Springer International Publishing, Cham, 2016. https://doi.org/10.1007/978-3-319-41421-8.

[13] J.L. Arias, ed., Nanotechnology and Drug Delivery, Volume One: Nanoplatforms in Drug Delivery, CRC Press, 2015. https://doi.org/10.1201/b17271.

[14] A. Zielińska, F. Carreiró, A.M. Oliveira, A. Neves, B. Pires, D.N. Venkatesh, A. Durazzo, M. Lucarini, P. Eder, A.M. Silva, A. Santini, E.B. Souto, Polymeric Nanoparticles: Production, Characterization, Toxicology and Ecotoxicology, Molecules. 25 (2020) 3731. https://doi.org/10.3390/molecules25163731.

[15] N. Mendoza-Munoz, D. Quintanar-Guerrero, E. Allemann, The Impact of the Salting-Out Technique on the Preparation of Colloidal Particulate Systems for Pharmaceutical

Applications, Recent Pat. Drug Deliv. Formul. 6 (2012) 236–249. https://doi.org/10.2174/187221112802652688.

[16] S. Pedroso-Santana, N. Fleitas-Salazar, Ionotropic gelation method in the synthesis of nanoparticles/microparticles for biomedical purposes, Polym. Int. 69 (2020) 443–447. https://doi.org/10.1002/pi.5970.

[17] N.H. Abd Ellah, S.A. Abouelmagd, Surface functionalization of polymeric nanoparticles for tumor drug delivery: approaches and challenges, Expert Opin. Drug Deliv. 14 (2017) 201–214. https://doi.org/10.1080/17425247.2016.1213238.

[18] M. Li, Y. Xuan, W. Zhang, S. Zhang, J. An, Polydopamine-containing nano-systems for cancer multi-mode diagnoses and therapies: A review, Int. J. Biol. Mthisromol. 247 (2023) 125826. https://doi.org/10.1016/j.ijbiomac.2023.125826.

[19] M.J. Mitchell, M.M. Billingsley, R.M. Haley, M.E. Wechsler, N.A. Peppas, R. Langer, Engineering precision nanoparticles for drug delivery, Nat. Rev. Drug Discov. 20 (2021) 101–124. https://doi.org/10.1038/s41573-020-0090-8.

[20] S. Desgouilles, C. Vauthier, D. Bazile, J. Vacus, J.-L. Grossiord, M. Veillard, P. Couvreur, The Design of Nanoparticles Obtained by Solvent Evaporation: A Comprehensive Study, Langmuir. 19 (2003) 9504–9510. https://doi.org/10.1021/la034999q.

[21] H. Lee, S.M. Dellatore, W.M. Miller, P.B. Messersmith, Mussel-Inspired Surface Chemistry for Multifunctional Coatings, Science (80-.). 318 (2007) 426–430. https://doi.org/10.1126/science.1147241.

[22] K.-Y. Ju, Y. Lee, S. Lee, S.B. Park, J.-K. Lee, Bioinspired Polymerization of Dopamine to Generate Melanin-Like Nanoparticles Having an Excellent Free-Radical-Scavenging Property, Biomacromolecules. 12 (2011) 625–632. https://doi.org/10.1021/bm101281b.

[23] H.C. Longuet-Higgins, On the origin of the free radical property of melanins, Arch. Biochem. Biophys. 86 (1960) 231–232. https://doi.org/10.1016/0003-9861(60)90410-0.

[24] D.R. Dreyer, D.J. Miller, B.D. Freeman, D.R. Paul, C.W. Bielawski, Elucidating the Structure of Poly(dopamine), Langmuir. 28 (2012) 6428–6435. https://doi.org/10.1021/la204831b.

[25] M.L. Tran, B.J. Powell, P. Meredith, Chemical and Structural Disorder in Eumelanins: A Possible Explanation for Broadband Absorbance, Biophys. J. 90 (2006) 743–752. https://doi.org/10.1529/biophysj.105.069096.

[26] K. Tadyszak, R. Mrówczyński, R. Carmieli, Electron Spin Relaxation Studies of Polydopamine Radicals, J. Phys. Chem. B. 125 (2021) 841–849. https://doi.org/10.1021/acs.jpcb.0c10485.

[27] J. Liebscher, R. Mrówczyński, H.A. Scheidt, C. Filip, N.D. Hădade, R. Turcu, A. Bende, S. Beck, Structure of Polydopamine: A Never-Ending Story?, Langmuir. 29 (2013) 10539–10548. https://doi.org/10.1021/la4020288.

[28] Y. Liu, K. Ai, L. Lu, Polydopamine and its derivative materials: Synthesis and promising applications in energy, environmental, and biomedical fields, Chem. Rev. 114 (2014) 5057–5115. https://doi.org/10.1021/cr400407a.

[29] J. Liebscher, Chemistry of Polydopamine – Scope, Variation, and Limitation, European J. Org. Chem. 2019 (2019) 4976–4994. https://doi.org/10.1002/ejoc.201900445.

[30] R.A. Burrell, N. McGranahan, J. Bartek, C. Swanton, The causes and consequences of genetic heterogeneity in cancer evolution, Nature. 501 (2013) 338–345. https://doi.org/10.1038/nature12625.

[31] J. Ferlay, M. Ervik, F. Lam, M. Colombet, L. Mery, M. Piñeros, Global Cancer Observatory: Cancer Today., Lyon Int. Agency Res. Cancer; 2020. (2023). https://gco.iarc.fr/today.

[32] V. Gyanani, J.C. Haley, R. Goswami, Challenges of Current Anticancer Treatment Approaches with Focus on Liposomal Drug Delivery Systems, Pharmaceuticals. 14 (2021) 835. https://doi.org/10.3390/ph14090835.

[33] S. Parveen, R. Misra, S.K. Sahoo, Nanoparticles: A boon to drug delivery, therapeutics, diagnostics and imaging, Nanomedicine Nanotechnology, Biol. Med. 8 (2012) 147–166. https://doi.org/10.1016/j.nano.2011.05.016.

[34] M.M. Gottesman, T. Fojo, S.E. Bates, Multidrug resistance in cancer: role of ATP–dependent transporters, Nat. Rev. Cancer. 2 (2002) 48–58. https://doi.org/10.1038/nrc706.

[35] S. Kwon, S. Jung, S.H. Baek, Combination Therapy of Radiation and Hyperthermia, Focusing on the Synergistic Anti-Cancer Effects and Research Trends, Antioxidants. 12 (2023) 924. https://doi.org/10.3390/antiox12040924.

[36] M. Kordi, Z. Borzouyi, S. Chitsaz, M. hadi Asmaei, R. Salami, M. Tabarzad, Antimicrobial peptides with anticancer activity: Today status, trends and their computational design, Arch. Biochem. Biophys. 733 (2023) 109484. https://doi.org/10.1016/j.abb.2022.109484.

[37] G. Shumi, T. Desalegn, T.B. Demissie, V.P. Ramachandran, R. Eswaramoorthy, Metal Complexes in Target-Specific Anticancer Therapy: Recent Trends and Challenges, J. Chem. 2022 (2022) 1–19. https://doi.org/10.1155/2022/9261683.

[38] X. Mu, J. Li, S. Yan, H. Zhang, W. Zhang, F. Zhang, J. Jiang, siRNA Delivery with Stem Cell Membrane-Coated Magnetic Nanoparticles for Imaging-Guided Photothermal Therapy and Gene Therapy, ACS Biomater. Sci. Eng. 4 (2018) 3895–3905. https://doi.org/10.1021/acsbiomaterials.8b00858.

[39] P. Zhao, M. Wang, M. Chen, Z. Chen, X. Peng, F. Zhou, J. Song, J. Qu, Programming cell pyroptosis with biomimetic nanoparticles for solid tumor immunotherapy, Biomaterials. 254 (2020) 120142. https://doi.org/10.1016/j.biomaterials.2020.120142.

[40] W. Fan, B. Yung, P. Huang, X. Chen, Nanotechnology for Multimodal Synergistic Cancer Therapy, Chem. Rev. 117 (2017) 13566–13638. https://doi.org/10.1021/acs.chemrev.7b00258.

[41] S.D. Jo, S.H. Ku, Y.-Y. Won, S.H. Kim, I.C. Kwon, Targeted Nanotheranostics for Future Personalized Medicine: Recent Progress in Cancer Therapy, Theranostics. 6 (2016) 1362–1377. https://doi.org/10.7150/thno.15335.

[42] M. Liu, R. Anderson, X. Lan, P.S. Conti, K. Chen, Recent advances in the development of nanoparticles for multimodality imaging and therapy of cancer, Med. Res. Rev. 40 (2020) 909–930. https://doi.org/10.1002/med.21642.

[43] Y. Yeo, ed., Nanoparticulate drug delivery systems: strategies, technologies, and applications, John Wiley & Sons, Inc., 2013.

[44] P. Zheng, B. Ding, G. Li, Polydopamine-Incorporated Nanoformulations for Biomedical Applications, Macromol. Biosci. 20 (2020) 1–13. https://doi.org/10.1002/mabi.202000228.

[45] S. Sur, A. Rathore, V. Dave, K.R. Reddy, R.S. Chouhan, V. Sadhu, Recent developments in functionalized polymer nanoparticles for efficient drug delivery system, Nano-Structures & Nano-Objects. 20 (2019) 100397. https://doi.org/10.1016/j.nanoso.2019.100397.

[46] Y. Shi, M. Liu, F. Deng, G. Zeng, Q. Wan, X. Zhang, Y. Wei, Recent progress and development on polymeric nanomaterials for photothermal therapy: a brief overview, J. Mater. Chem. B. 5 (2017) 194–206. https://doi.org/10.1039/C6TB02249A.

[47] X. Zhang, S. Wang, L. Xu, L. Feng, Y. Ji, L. Tao, S. Li, Y. Wei, Biocompatible polydopamine fluorescent organic nanoparticles: facile preparation and cell imaging, Nanoscale. 4 (2012) 5581. https://doi.org/10.1039/c2nr31281f.

[48] S.H. Hong, Y. Sun, C. Tang, K. Cheng, R. Zhang, Q. Fan, L. Xu, D. Huang, A. Zhao, Z. Cheng, Chelator-Free and Biocompatible Melanin Nanoplatform with Facile-Loading Gadolinium and Copper-64 for Bioimaging, Bioconjug. Chem. 28 (2017) 1925–1930. https://doi.org/10.1021/acs.bioconjchem.7b00245.

[49] Y. Li, Y. Xie, Z. Wang, N. Zang, F. Carniato, Y. Huang, C.M. Andolina, L.R. Parent, T.B. Ditri, E.D. Walter, M. Botta, J.D. Rinehart, N.C. Gianneschi, Structure and Function of Iron-Loaded Synthetic Melanin, ACS Nano. 10 (2016) 10186–10194. https://doi.org/10.1021/acsnano.6b05502.

[50] J.E. Lemaster, Z. Wang, A. Hariri, F. Chen, Z. Hu, Y. Huang, C. V Barback, R. Cochran, N.C. Gianneschi, J. V Jokerst, Gadolinium Doping Enhances the Photoacoustic Signal of Synthetic Melanin Nanoparticles: A Dual Modality Contrast Agent for Stem Cell Imaging, Chem. Mater. 31 (2019) 251–259. https://doi.org/10.1021/acs.chemmater.8b04333.

[51] J. Wang, H. Cui, Nanostructure-Based Theranostic Systems, Theranostics. 6 (2016) 1274–1276. https://doi.org/10.7150/thno.16479.

[52] Z. Zhu, M. Su, Polydopamine Nanoparticles for Combined Chemo- and Photothermal Cancer Therapy, Nanomaterials. 7 (2017) 160. https://doi.org/10.3390/nano7070160.

[53] X. Wang, J. Zhang, Y. Wang, C. Wang, J. Xiao, Q. Zhang, Y. Cheng, Multi-responsive photothermal-chemotherapy with drug-loaded melanin-like nanoparticles for synergetic tumor ablation, Biomaterials. 81 (2016) 114–124. https://doi.org/10.1016/j.biomaterials.2015.11.037.

[54] Y. Li, C. Jiang, D. Zhang, Y. Wang, X. Ren, K. Ai, X. Chen, L. Lu, Targeted polydopamine nanoparticles enable photoacoustic imaging guided chemo-photothermal synergistic therapy of tumor, Acta Biomater. 47 (2017) 124–134. https://doi.org/10.1016/j.actbio.2016.10.010.

[55] D. Zhang, M. Wu, Y. Zeng, L. Wu, Q. Wang, X. Han, X. Liu, J. Liu, Chlorin e6 Conjugated Poly(dopamine) Nanospheres as PDT/PTT Dual-Modal Therapeutic Agents for Enhanced Cancer Therapy, ACS Appl. Mater. Interfaces. 7 (2015) 8176–

8187. https://doi.org/10.1021/acsami.5b01027.

[56] J. Han, W. Park, S. Park, K. Na, Photosensitizer-Conjugated Hyaluronic Acid-Shielded Polydopamine Nanoparticles for Targeted Photomediated Tumor Therapy, ACS Appl. Mater. Interfaces. 8 (2016) 7739–7747. https://doi.org/10.1021/acsami.6b01664.

[57] X. Zhong, K. Yang, Z. Dong, X. Yi, Y. Wang, C. Ge, Y. Zhao, Z. Liu, Polydopamine as a Biocompatible Multifunctional Nanocarrier for Combined Radioisotope Therapy and Chemotherapy of Cancer, Adv. Funct. Mater. 25 (2015) 7327–7336. https://doi.org/10.1002/adfm.201503587.

[58] Q. Lu, S. Qi, P. Li, L. Yang, S. Yang, Y. Wang, Y. Cheng, Y. Song, S. Wang, F. Tan, N. Li, Photothermally activatable PDA immune nanomedicine combined with PD-L1 checkpoint blockade for antimetastatic cancer photoimmunotherapy, J. Mater. Chem. B. 7 (2019) 2499–2511. https://doi.org/10.1039/C9TB00089E.

[59] X. Wang, S. Li, S. Wang, S. Zheng, Z. Chen, H. Song, Protein Binding Nanoparticles as an Integrated Platform for Cancer Diagnosis and Treatment, Adv. Sci. 9 (2022) 2202453. https://doi.org/10.1002/advs.202202453.

[60] H. Maeda, H. Nakamura, J. Fang, The EPR effect for macromolecular drug delivery to solid tumors: Improvement of tumor uptake, lowering of systemic toxicity, and distinct tumor imaging in vivo, Adv. Drug Deliv. Rev. 65 (2013) 71–79. https://doi.org/10.1016/j.addr.2012.10.002.

[61] S. Wilhelm, A.J. Tavares, Q. Dai, S. Ohta, J. Audet, H.F. Dvorak, W.C.W. Chan, Analysis of nanoparticle delivery to tumours, Nat. Rev. Mater. 1 (2016) 16014. https://doi.org/10.1038/natrevmats.2016.14.

[62] Q.-V. Le, J. Lee, H. Lee, G. Shim, Y.-K. Oh, Cell membrane-derived vesicles for delivery of therapeutic agents, Acta Pharm. Sin. B. 11 (2021) 2096–2113. https://doi.org/10.1016/j.apsb.2021.01.020.

[63] L. Wang, S. Chen, W. Pei, B. Huang, C. Niu, Magnetically targeted erythrocyte membrane coated nanosystem for synergistic photothermal/chemotherapy of cancer, J. Mater. Chem. B. 8 (2020) 4132–4142. https://doi.org/10.1039/D0TB00364F.

[64] M. Guo, C. Xia, Y. Wu, N. Zhou, Z. Chen, W. Li, Research Progress on Cell Membrane-Coated Biomimetic Delivery Systems, Front. Bioeng. Biotechnol. 9 (2021) 1–14. https://doi.org/10.3389/fbioe.2021.772522.

[65] M.J. Bigaj-Józefowska, B.F. Grześkowiak, Polymeric nanoparticles wrapped in biological membranes for targeted anticancer treatment, Eur. Polym. J. 176 (2022) 111427. https://doi.org/10.1016/j.eurpolymj.2022.111427.

[66] P. Dash, A.M. Piras, M. Dash, Cell membrane coated nanocarriers - an efficient biomimetic platform for targeted therapy, J. Control. Release. 327 (2020) 546–570. https://doi.org/10.1016/j.jconrel.2020.09.012.

[67] Q. Xia, Y. Zhang, Z. Li, X. Hou, N. Feng, Red blood cell membrane-camouflaged nanoparticles: a novel drug delivery system for antitumor application, Acta Pharm. Sin. B. 9 (2019) 675–689. https://doi.org/10.1016/j.apsb.2019.01.011.

[68] P.A. Oldenborg, A. Zheleznyak, Y.F. Fang, C.F. Lagenaur, H.D. Gresham, F.P. Lindberg, Role of CD47 as a marker of self on red blood cells, Science (80-.). 288 (2000) 2051–2054. https://doi.org/10.1126/science.288.5473.2051.

[69] Z. He, Y. Zhang, N. Feng, Cell membrane-coated nanosized active targeted drug delivery systems homing to tumor cells: A review, Mater. Sci. Eng. C. 106 (2020) 110298. https://doi.org/10.1016/j.msec.2019.110298.

[70] L. Wu, W. Xie, H.M. Zan, Z. Liu, G. Wang, Y. Wang, W. Liu, W. Dong, Platelet membrane-coated nanoparticles for targeted drug delivery and local chemo-photothermal therapy of orthotopic hepatocellular carcinoma, J. Mater. Chem. B. 8 (2020) 4648–4659. https://doi.org/10.1039/d0tb00735h.

[71] Y. Shi, L. Du, L. Lin, Y. Wang, Tumour-associated mesenchymal stem/stromal cells: emerging therapeutic targets, Nat. Rev. Drug Discov. 16 (2017) 35–52. https://doi.org/10.1038/nrd.2016.193.

[72] X. Mu, M. Zhang, A. Wei, F. Yin, Y. Wang, K. Hu, J. Jiang, Doxorubicin and PD-L1 siRNA co-delivery with stem cell membrane-coated polydopamine nanoparticles for the targeted chemoimmunotherapy of PCa bone metastases, Nanoscale. 13 (2021) 8998–9008. https://doi.org/10.1039/D0NR08024A.

[73] Y. Xia, L. Rao, H. Yao, Z. Wang, P. Ning, X. Chen, Engineering Macrophages for Cancer Immunotherapy and Drug Delivery, Adv. Mater. 32 (2020) 2002054. https://doi.org/10.1002/adma.202002054.

[74] S. Krishnamurthy, M.K. Gnanasammandhan, C. Xie, K. Huang, M.Y. Cui, J.M. Chan, Monocyte cell membrane-derived nanoghosts for targeted cancer therapy, Nanoscale. 8 (2016) 6981–6985. https://doi.org/10.1039/c5nr07588b.

[75] D. Dehaini, X. Wei, R.H. Fang, S. Masson, P. Angsantikul, B.T. Luk, Y. Zhang, M. Ying, Y. Jiang, A. V. Kroll, W. Gao, L. Zhang, Erythrocyte-Platelet Hybrid Membrane Coating for Enhanced Nanoparticle Functionalization, Adv. Mater. 29 (2017) 1606209. https://doi.org/10.1002/adma.201606209.

[76] C. Gong, X. Yu, B. You, Y. Wu, R. Wang, L. Han, Y. Wang, S. Gao, Y. Yuan, Macrophage-cancer hybrid membrane-coated nanoparticles for targeting lung metastasis in breast cancer therapy, J. Nanobiotechnology. 18 (2020) 92. https://doi.org/10.1186/s12951-020-00649-8.

[77] J.G. Piao, L. Wang, F. Gao, Y.Z. You, Y. Xiong, L. Yang, Erythrocyte membrane is an alternative coating to polyethylene glycol for prolonging the circulation lifetime of gold nanocages for photothermal therapy, ACS Nano. 8 (2014) 10414–10425. https://doi.org/10.1021/nn503779d.

[78] C.M.J. Hu, R.H. Fang, K.C. Wang, B.T. Luk, S. Thamphiwatana, D. Dehaini, P. Nguyen, P. Angsantikul, C.H. Wen, A. V. Kroll, C. Carpenter, M. Ramesh, V. Qu, S.H. Patel, J. Zhu, W. Shi, F.M. Hofman, T.C. Chen, W. Gao, K. Zhang, S. Chien, L. Zhang, Nanoparticle biointerfacing by platelet membrane cloaking, Nature. 526 (2015) 118–121. https://doi.org/10.1038/nature15373.

[79] X. Zhang, S. He, B. Ding, C. Qu, Q. Zhang, H. Chen, Y. Sun, H. Fang, Y. Long, R. Zhang, X. Lan, Z. Cheng, Cancer cell membrane-coated rare earth doped nanoparticles for tumor surgery navigation in NIR-II imaging window, Chem. Eng. J. 385 (2020) 123959. https://doi.org/10.1016/j.cej.2019.123959.

[80] Z. Chen, P. Zhao, Z. Luo, M. Zheng, H. Tian, P. Gong, G. Gao, H. Pan, L. Liu, A. Ma, H. Cui, Y. Ma, L. Cai, Cancer Cell Membrane–Biomimetic Nanoparticles for Homologous-Targeting Dual-Modal Imaging and Photothermal Therapy, ACS Nano.

10 (2016) 10049–10057. https://doi.org/10.1021/acsnano.6b04695.

[81] X. Liu, Y. Sun, S. Xu, X. Gao, F. Kong, K. Xu, B. Tang, Homotypic Cell Membrane-Cloaked Biomimetic Nanocarrier for the Targeted Chemotherapy of Hepatocellular Carcinoma, Theranostics. 9 (2019) 5828–5838. https://doi.org/10.7150/thno.34837.

[82] L. Rao, B. Cai, L.L. Bu, Q.Q. Liao, S.S. Guo, X.Z. Zhao, W.F. Dong, W. Liu, Microfluidic Electroporation-Facilitated Synthesis of Erythrocyte Membrane-Coated Magnetic Nanoparticles for Enhanced Imaging-Guided Cancer Therapy, ACS Nano. 11 (2017) 3496–3505. https://doi.org/10.1021/acsnano.7b00133.

[83] R.H. Fang, C.M.J. Hu, B.T. Luk, W. Gao, J.A. Copp, Y. Tai, D.E. O'Connor, L. Zhang, Cancer cell membrane-coated nanoparticles for anticancer vaccination and drug delivery, Nano Lett. 14 (2014) 2181–2188. https://doi.org/10.1021/nl500618u.

[84] H. Li, K. Jin, M. Luo, X. Wang, X. Zhu, X. Liu, T. Jiang, Q. Zhang, S. Wang, Z. Pang, Size Dependency of Circulation and Biodistribution of Biomimetic Nanoparticles: Red Blood Cell Membrane-Coated Nanoparticles, Cells. 8 (2019) 881. https://doi.org/10.3390/cells8080881.

[85] B.T. Luk, C.M. Jack Hu, R.H. Fang, D. Dehaini, C. Carpenter, W. Gao, L. Zhang, Interfacial interactions between natural RBC membranes and synthetic polymeric nanoparticles, Nanoscale. 6 (2014) 2730–2737. https://doi.org/10.1039/c3nr06371b.

[86] E. Ben-Akiva, R.A. Meyer, H. Yu, J.T. Smith, D.M. Pardoll, J.J. Green, Biomimetic anisotropic polymeric nanoparticles coated with red blood cell membranes for enhanced circulation and toxin removal, Sci. Adv. 6 (2020) 1–9. https://doi.org/10.1126/sciadv.aay9035.

[87] L. Florez, C. Herrmann, J.M. Cramer, C.P. Hauser, K. Koynov, K. Landfester, D. Crespy, V. Mailänder, How Shape Influences Uptake: Interactions of Anisotropic Polymer Nanoparticles and Human Mesenchymal Stem Cells, Small. 8 (2012) 2222–2230. https://doi.org/10.1002/smll.201102002.

[88] S. Shukla, F.J. Eber, A.S. Nagarajan, N.A. DiFranco, N. Schmidt, A.M. Wen, S. Eiben, R.M. Twyman, C. Wege, N.F. Steinmetz, The Impact of Aspect Ratio on the Biodistribution and Tumor Homing of Rigid Soft-Matter Nanorods, Adv. Healthc. Mater. 4 (2015) 874–882. https://doi.org/10.1002/adhm.201400641.

[89] S. Rampersaud, J. Fang, Z. Wei, K. Fabijanic, S. Silver, T. Jaikaran, Y. Ruiz, M. Houssou, Z. Yin, S. Zheng, A. Hashimoto, A. Hoshino, D. Lyden, S. Mahajan, H. Matsui, The Effect of Cage Shape on Nanoparticle-Based Drug Carriers: Anticancer Drug Release and Efficacy via Receptor Blockade Using Dextran-Coated Iron Oxide Nanocages, Nano Lett. 16 (2016) 7357–7363. https://doi.org/10.1021/acs.nanolett.6b02577.

[90] L. Liu, X. Bai, M.V. Martikainen, A. Kårlund, M. Roponen, W. Xu, G. Hu, E. Tasciotti, V.P. Lehto, Cell membrane coating integrity affects the internalization mechanism of biomimetic nanoparticles, Nat. Commun. 12 (2021) 1–12. https://doi.org/10.1038/s41467-021-26052-x.

[91] X. Mu, J. Li, S. Yan, H. Zhang, W. Zhang, F. Zhang, J. Jiang, SiRNA Delivery with Stem Cell Membrane-Coated Magnetic Nanoparticles for Imaging-Guided Photothermal Therapy and Gene Therapy, ACS Biomater. Sci. Eng. 4 (2018) 3895–3905. https://doi.org/10.1021/acsbiomaterials.8b00858.

[92] W. Liu, T. Liu, M. Zou, W. Yu, C. Li, Z. He, M. Zhang, M. Liu, Z. Li, J. Feng, X. Zhang, Aggressive Man-Made Red Blood Cells for Hypoxia-Resistant Photodynamic Therapy, Adv. Mater. 30 (2018) 1802006. https://doi.org/10.1002/adma.201802006.

[93] W. Pan, X. Zhang, P. Gao, N. Li, B. Tang, An anti-inflammatory nanoagent for tumor-targeted photothermal therapy, Chem. Commun. 55 (2019) 9645–9648. https://doi.org/10.1039/c9cc04486h.

[94] M. Zhang, F. Zhang, T. Liu, P. Shao, L. Duan, J. Yan, X. Mu, J. Jiang, Polydopamine Nanoparticles Camouflaged by Stem Cell Membranes for Synergistic Chemo-Photothermal Therapy of Malignant Bone Tumors, Int. J. Nanomedicine. Volume 15 (2020) 10183–10197. https://doi.org/10.2147/IJN.S282931.

[95] H. Cao, B. Jiang, Y. Yang, M. Zhao, N. Sun, J. Xia, X. Gao, J. Li, Cell membrane covered polydopamine nanoparticles with two-photon absorption for precise photothermal therapy of cancer, J. Colloid Interface Sci. 604 (2021) 596–603. https://doi.org/10.1016/j.jcis.2021.07.004.

[96] H. Guo, W. Zhang, L. Wang, Z. Shao, X. Huang, Biomimetic cell membrane-coated glucose/oxygen-exhausting nanoreactor for remodeling tumor microenvironment in targeted hypoxic tumor therapy, Biomaterials. 290 (2022) 121821. https://doi.org/10.1016/j.biomaterials.2022.121821.

[97] D. Ren, G.R. Williams, Y. Zhang, R. Ren, J. Lou, L.-M. Zhu, Mesoporous Doxorubicin-Loaded Polydopamine Nanoparticles Coated with a Platelet Membrane Suppress Tumor Growth in a Murine Model of Human Breast Cancer, ACS Appl. Bio Mater. 5 (2022) 123–133. https://doi.org/10.1021/acsabm.1c00926.

[98] Y. Xiao, T. Zhu, Q. Zeng, Q. Tan, G. Jiang, X. Huang, Functionalized biomimetic nanoparticles combining programmed death-1/programmed death-ligand 1 blockade with photothermal ablation for enhanced colorectal cancer immunotherapy, Acta Biomater. 157 (2023) 451–466. https://doi.org/10.1016/j.actbio.2022.11.043.

[99] M.J. Bigaj, B.F. Grześkowiak, Targeted drug delivery system based on biomimetic coating for synergistic liver cancer treatment, 11 (2019) 9588.

[100] F. Chen, Y. Xing, Z. Wang, X. Zheng, J. Zhang, K. Cai, Nanoscale Polydopamine (PDA) Meets π–π Interactions: An Interface-Directed Coassembly Approach for Mesoporous Nanoparticles, Langmuir. 32 (2016) 12119–12128. https://doi.org/10.1021/acs.langmuir.6b03294.

[101] A. Elmas, G. Akyüz, A. Bergal, M. Andaç, Ö. Andaç, Mathematical Modelling of Drug Release, Res. Eng. Struct. Mater. 6 (2020) 327–350. https://doi.org/10.17515/resm2020.178na0122.

[102] M. Winey, J.B. Meehl, E.T. O'Toole, T.H. Giddings, Conventional transmission electron microscopy, Mol. Biol. Cell. 25 (2014) 319–323. https://doi.org/10.1091/mbc.e12-12-0863.

[103] A.-L. Robson, P.C. Dastoor, J. Flynn, W. Palmer, A. Martin, D.W. Smith, A. Woldu, S. Hua, Advantages and Limitations of Current Imaging Techniques for Characterizing Liposome Morphology, Front. Pharmacol. 9 (2018) 1–8. https://doi.org/10.3389/fphar.2018.00080.

[104] D. Shindo, T. Oikawa, Energy Dispersive X-ray Spectroscopy, in: Anal. Electron

Microsc. Mater. Sci., Springer Japan, Tokyo, 2002: pp. 81–102. https://doi.org/10.1007/978-4-431-66988-3_4.

[105] V.-D. Hodoroaba, Energy-dispersive X-ray spectroscopy (EDS), in: Charact. Nanoparticles, Elsevier, 2020: pp. 397–417. https://doi.org/10.1016/B978-0-12-814182-3.00021-3.

[106] J. Stetefeld, S.A. McKenna, T.R. Patel, Dynamic light scattering: a practical guide and applications in biomedical sciences, Biophys. Rev. 8 (2016) 409–427. https://doi.org/10.1007/s12551-016-0218-6.

[107] S. Bhattacharjee, DLS and zeta potential – What they are and what they are not?, J. Control. Release. 235 (2016) 337–351. https://doi.org/10.1016/j.jconrel.2016.06.017.

[108] S. Karmakar, Particle Size Distribution and Zeta Potential Based on Dynamic Light Scattering: Techniques to Characterize Stability and Surface Charge Distribution of Charged Colloids, in: Recent Trends Mater. Phys. Chem., 2019: pp. 117–159.

[109] G. Tyler, J. Yvon, ICP-OES , ICP-MS and AAS Techniques Compared, Tech. Note 05 ICP Opt. Spectrosc. (2003) 1–11.

[110] S.R. Khan, B. Sharma, P.A. Chawla, R. Bhatia, Inductively Coupled Plasma Optical Emission Spectrometry (ICP-OES): a Powerful Analytical Technique for Elemental Analysis, Food Anal. Methods. 15 (2022) 666–688. https://doi.org/10.1007/s12161-021-02148-4.

[111] A. Schindler, G. Neumann, A. Rager, E. Füglein, J. Blumm, T. Denner, A novel direct coupling of simultaneous thermal analysis (STA) and Fourier transform-infrared (FT-IR) spectroscopy, J. Therm. Anal. Calorim. 113 (2013) 1091–1102. https://doi.org/10.1007/s10973-013-3072-9.

[112] and A.R. R. Bruce Prime, Harvey E. Bair, Sergey Vyazovkin, Patrick K. Gallagher, Thermal Analysis of Polymers, John Wiley & Sons, Inc., Hoboken, NJ, USA, 2009. https://doi.org/10.1002/9780470423837.

[113] M. Naderi, Surface Area: Brunauer– Emmett–Teller (BET), in: Prog. Filtr. Sep., Elsevier, 2015: pp. 585–608. https://doi.org/10.1016/B978-0-12-384746-1.00014-8.

[114] A.K. Ladavos, A.P. Katsoulidis, A. Iosifidis, K.S. Triantafyllidis, T.J. Pinnavaia, P.J. Pomonis, The BET equation, the inflection points of N2 adsorption isotherms and the estimation of specific surface area of porous solids, Microporous Mesoporous Mater. 151 (2012) 126–133. https://doi.org/10.1016/j.micromeso.2011.11.005.

[115] M. McElfresh, Fundamentals of Magnetism and Magnetic Measurements Featuring Quantum Design's Magnetic Property Measurement system, Quantum Des. 11578 (1994) 1–38.

[116] J.C. McGowan, Basic Principles of Magnetic Resonance Imaging, Neuroimaging Clin. N. Am. 18 (2008) 623–636. https://doi.org/10.1016/j.nic.2008.06.004.

[117] K.H. Hausser, H.R. Kalbitzer, NMR w biologii i medycynie, Wydawnictwo Naukowe Uniwersytetu im. Adama Mickiewicza, Poznań, 1993.

[118] S.R. Gallagher, SDS-Polyacrylamide Gel Electrophoresis (SDS-PAGE), in: Curr. Protoc. Essent. Lab. Tech., John Wiley & Sons, Inc., Hoboken, NJ, USA, 2012: pp. 1–28. https://doi.org/10.1002/9780470089941.et0703s06.

[119] B. KURIEN, R. SCOFIELD, Western blotting, Methods. 38 (2006) 283–293. https://doi.org/10.1016/j.ymeth.2005.11.007.

[120] Ö.S. Aslantürk, In Vitro Cytotoxicity and Cell Viability Assays: Principles, Advantages, and Disadvantages, in: Genotoxicity - A Predict. Risk to Our Actual World, InTech, 2018: pp. 1–18. https://doi.org/10.5772/intechopen.71923.

[121] D.J. Brayden, S.-A. Cryan, K.A. Dawson, P.J. O'Brien, J.C. Simpson, High-content analysis for drug delivery and nanoparticle applications, Drug Discov. Today. 20 (2015) 942–957. https://doi.org/10.1016/j.drudis.2015.04.001.

[122] Y. Yu, A. Arora, W. Min, C.M. Roifman, E. Grunebaum, EdU incorporation is an alternative non-radioactive assay to [3H]thymidine uptake for in vitro measurement of mice T-cell proliferations, J. Immunol. Methods. 350 (2009) 29–35. https://doi.org/10.1016/j.jim.2009.07.008.

[123] M.J. Stoddart, Mammalian Cell Viability: Methods and Protocols - Cell Viability Assays, in: Methods Mol. Biol., 2011: pp. 1–6. https://doi.org/10.1007/978-1-61779-108-6.

[124] M. Doan, I. Vorobjev, P. Rees, A. Filby, O. Wolkenhauer, A.E. Goldfeld, J. Lieberman, N. Barteneva, A.E. Carpenter, H. Hennig, Diagnostic Potential of Imaging Flow Cytometry, Trends Biotechnol. 36 (2018) 649–652. https://doi.org/10.1016/j.tibtech.2017.12.008.

[125] N.S. Barteneva, E. Fasler-Kan, I.A. Vorobjev, Imaging Flow Cytometry: Coping with Heterogeneity in Biological Systems, J. Histochem. Cytochem. 60 (2012) 723–733. https://doi.org/10.1369/0022155412453052.

[126] W.B. Amos, J.G. White, How the Confocal Laser Scanning Microscope entered Biological Research, Biol. Cell. 95 (2003) 335–342. https://doi.org/10.1016/S0248-4900(03)00078-9.

[127] S.W. Paddock, Confocal Laser Scanning Microscopy, Biotechniques. 27 (1999) 992–1004. https://doi.org/10.2144/99275ov01.

[128] J.E. Long, M. Jankovic, D. Maddalo, Drug discovery oncology in a mouse: concepts, models and limitations, Futur. Sci. OA. 7 (2021). https://doi.org/10.2144/fsoa-2021-0019.

[129] R.C. Oliveira, A.M. Abrantes, J.G. Tralhão, M.F. Botelho, The role of mouse models in colorectal cancer research—The need and the importance of the orthotopic models, Anim. Model. Exp. Med. 3 (2020) 1–8. https://doi.org/10.1002/ame2.12102.

[130] C. Qi, L.-H. Fu, H. Xu, T.-F. Wang, J. Lin, P. Huang, Melanin/polydopamine-based nanomaterials for biomedical applications, Sci. China Chem. 62 (2019) 162–188. https://doi.org/10.1007/s11426-018-9392-6.

[131] L. Tian, X. Li, H. Ji, Q. Yu, M. Yang, L. Guo, L. Huang, W. Gao, Melanin-like nanoparticles: advances in surface modification and tumour photothermal therapy, J. Nanobiotechnology. 20 (2022) 485. https://doi.org/10.1186/s12951-022-01698-x.

[132] Y. Xing, J. Zhang, F. Chen, J. Liu, K. Cai, Mesoporous polydopamine nanoparticles with co-delivery function for overcoming multidrug resistance via synergistic chemo-photothermal therapy, Nanoscale. 9 (2017) 8781–8790. https://doi.org/10.1039/C7NR01857F.

[133] H.-P. Lin, S.-T. Wong, C.-Y. Mou, C.-Y. Tang, Extensive Void Defects in Mesoporous Aluminosilicate MCM-41, J. Phys. Chem. B. 104 (2000) 8967–8975. https://doi.org/10.1021/jp001569p.

[134] M. Tanhaei, A.R. Mahjoub, V. Safarifard, Energy-efficient sonochemical approach for the preparation of nanohybrid composites from graphene oxide and metal-organic framework, Inorg. Chem. Commun. 102 (2019) 185–191. https://doi.org/10.1016/j.inoche.2019.02.024.

[135] M. Ziółek, I. Nowak, Kataliza heterogeniczna. Wybrane zagadnienia, Wydawnictwo Naukowe Uniwersytetu im. Adama Mickiewicza, Poznań, 1999.

[136] B. Lu, A. Atala, Small Molecules: Controlling Cell Fate and Function, Situ Tissue Regen. Host Cell Recruit. Biomater. Des. (2016) 87–110. https://doi.org/10.1016/B978-0-12-802225-2.00006-4.

[137] C. Carvalho, R. Santos, S. Cardoso, S. Correia, P. Oliveira, M. Santos, P. Moreira, Doxorubicin: The Good, the Bad and the Ugly Effect, Curr. Med. Chem. 16 (2009) 3267–3285. https://doi.org/10.2174/092986709788803312.

[138] Q.T. Phung, N. Maes, S. Seetharam, Pitfalls in the use and interpretation of TGA and MIP techniques for Ca-leached cementitious materials, Mater. Des. 182 (2019) 108041. https://doi.org/10.1016/j.matdes.2019.108041.

[139] T.L. Tan, G.B. Lebron, Determination of Carbon Dioxide, Carbon Monoxide, and Methane Concentrations in Cigarette Smoke by Fourier Transform Infrared Spectroscopy, J. Chem. Educ. 89 (2012) 383–386. https://doi.org/10.1021/ed200178s.

[140] NIST Standard Reference Database 69: NIST Chemistry WebBook; carbon monoxide spectrum, (n.d.). https://webbook.nist.gov/cgi/cbook.cgi?ID=C630080&Type=IR-SPEC&Index=1#Refs.

[141] NIST Benchmark Spray Combustion Database, (n.d.). https://webbook.nist.gov/chemistry/special/spray-combust/baseline-case/ftir/.

[142] B. Smith, The Grand Review II: Why Do Different Functional Groups Have Different Peak Heights and Widths?, Spectroscopy. 36 (2021) 9–15. https://cdn.sanity.io/files/0vv8moc6/spectroscopy/bebe6e4cd6b11a3d0624acb3894eab540aff6251.pdf.

[143] K.M. Im, T.-W. Kim, J.-R. Jeon, Metal-Chelation-Assisted Deposition of Polydopamine on Human Hair: A Ready-to-Use Eumelanin-Based Hair Dyeing Methodology, ACS Biomater. Sci. Eng. 3 (2017) 628–636. https://doi.org/10.1021/acsbiomaterials.7b00031.

[144] R. Chen, D. Ling, L. Zhao, S. Wang, Y. Liu, R. Bai, S. Baik, Y. Zhao, C. Chen, T. Hyeon, Parallel Comparative Studies on Mouse Toxicity of Oxide Nanoparticle- and Gadolinium-Based T1 MRI Contrast Agents, ACS Nano. 9 (2015) 12425–12435. https://doi.org/10.1021/acsnano.5b05783.

[145] K.-Y. Ju, J.W. Lee, G.H. Im, S. Lee, J. Pyo, S.B. Park, J.H. Lee, J.-K. Lee, Bio-Inspired, Melanin-Like Nanoparticles as a Highly Efficient Contrast Agent for T 1 -Weighted Magnetic Resonance Imaging, Biomacromolecules. 14 (2013) 3491–3497. https://doi.org/10.1021/bm4008138.

[146] L. Yang, J. Kong, D. Zhou, J.M. Ang, S.L. Phua, W.A. Yee, H. Liu, Y. Huang, X. Lu,

Transition-metal-ion-mediated polymerization of dopamine: Mussel-inspired approach for the facile synthesis of robust transition-metal nanoparticle-graphene hybrids, Chem. - A Eur. J. 20 (2014) 7776–7783. https://doi.org/10.1002/chem.201402241.

[147] M. Salomäki, T. Ouvinen, L. Marttila, H. Kivelä, J. Leiro, E. Mäkilä, J. Lukkari, Polydopamine Nanoparticles Prepared Using Redox-Active Transition Metals, J. Phys. Chem. B. 123 (2019) 2513–2524. https://doi.org/10.1021/acs.jpcb.8b11994.

[148] Z. Wang, Y. Xie, Y. Li, Y. Huang, L.R. Parent, T. Ditri, N. Zang, J.D. Rinehart, N.C. Gianneschi, Tunable, Metal-Loaded Polydopamine Nanoparticles Analyzed by Magnetometry, Chem. Mater. 29 (2017) 8195–8201. https://doi.org/10.1021/acs.chemmater.7b02262.

[149] Z. Wang, Y. Zou, Y. Li, Y. Cheng, Metal-Containing Polydopamine Nanomaterials: Catalysis, Energy, and Theranostics, Small. 16 (2020) 1907042. https://doi.org/10.1002/smll.201907042.

[150] J.H. Waite, Mussel adhesion – essential footwork, J. Exp. Biol. 220 (2017) 517–530. https://doi.org/10.1242/jeb.134056.

[151] J. Liebscher, Chemistry of Polydopamine – Scope, Variation, and Limitation, European J. Org. Chem. 2019 (2019) 4976–4994. https://doi.org/10.1002/ejoc.201900445.

[152] H. Li, J. Xi, A.G. Donaghue, J. Keum, Y. Zhao, K. An, E.R. McKenzie, F. Ren, Synthesis and catalytic performance of polydopamine supported metal nanoparticles, Sci. Rep. 10 (2020) 1–7. https://doi.org/10.1038/s41598-020-67458-9.

[153] S. Lee, A. Shanti, Effect of Exogenous pH on Cell Growth of Breast Cancer Cells, Int. J. Mol. Sci. 22 (2021) 9910. https://doi.org/10.3390/ijms22189910.

[154] Z. Imtiyaz, J. He, Q. Leng, A.K. Agrawal, A.J. Mixson, pH-Sensitive Targeting of Tumors with Chemotherapy-Laden Nanoparticles: Progress and Challenges, Pharmaceutics. 14 (2022) 2427. https://doi.org/10.3390/pharmaceutics14112427.

[155] Y.-B. Hu, E.B. Dammer, R.-J. Ren, G. Wang, The endosomal-lysosomal system: from acidification and cargo sorting to neurodegeneration, Transl. Neurodegener. 4 (2015) 18. https://doi.org/10.1186/s40035-015-0041-1.

[156] S. Behzadi, V. Serpooshan, W. Tao, M.A. Hamaly, M.Y. Alkawareek, E.C. Dreaden, D. Brown, A.M. Alkilany, O.C. Farokhzad, M. Mahmoudi, Cellular uptake of nanoparticles: journey inside the cell, Chem. Soc. Rev. 46 (2017) 4218–4244. https://doi.org/10.1039/C6CS00636A.

[157] M. Ko, A. Quiñones-Hinojosa, R. Rao, Emerging links between endosomal pH and cancer, Cancer Metastasis Rev. 39 (2020) 519–534. https://doi.org/10.1007/s10555-020-09870-1.

[158] J.M. Estrela, A. Ortega, E. Obrador, Glutathione in Cancer Biology and Therapy, Crit. Rev. Clin. Lab. Sci. 43 (2006) 143–181. https://doi.org/10.1080/10408360500523878.

[159] E. V. Kalinina, L.A. Gavriliuk, Glutathione Synthesis in Cancer Cells, Biochem. 85 (2020) 895–907. https://doi.org/10.1134/S0006297920080052.

[160] X.-J. Li, W.-T. Li, Z.-H.-R. Li, L.-P. Zhang, C.-C. Gai, W.-F. Zhang, D.-J. Ding, Iron-Chelated Polydopamine Decorated Doxorubicin-Loaded Nanodevices for Reactive Oxygen Species Enhanced Cancer Combination Therapy, Front. Pharmacol. 10 (2019)

1–9. https://doi.org/10.3389/fphar.2019.00075.

[161] M. Guo, J. Ling, X. Xu, X. Ouyang, Delivery of Doxorubicin by Ferric Ion-Modified Mesoporous Polydopamine Nanoparticles and Anticancer Activity against HCT-116 Cells In Vitro, Int. J. Mol. Sci. 24 (2023) 6854. https://doi.org/10.3390/ijms24076854.

[162] A.M. Jazani, C. Shetty, H. Movasat, K.K. Bawa, J.K. Oh, Imidazole-Mediated Dual Location Disassembly of Acid-Degradable Intracellular Drug Delivery Block Copolymer Nanoassemblies, Macromol. Rapid Commun. 42 (2021) 2100262. https://doi.org/10.1002/marc.202100262.

[163] H. Kim, D. Lee, J. Kim, T. Kim, W.J. Kim, Photothermally Triggered Cytosolic Drug Delivery via Endosome Disruption Using a Functionalized Reduced Graphene Oxide, ACS Nano. 7 (2013) 6735–6746. https://doi.org/10.1021/nn403096s.

[164] S. Dash, P.N. Murthy, L. Nath, P. Chowdhury, Kinetic modeling on drug release from controlled drug delivery systems., Acta Pol. Pharm. 67 (2010) 217–23. http://www.ncbi.nlm.nih.gov/pubmed/20524422.

[165] N.S. Heredia, K. Vizuete, M. Flores-Calero, K. Pazmiño V., F. Pilaquinga, B. Kumar, A. Debut, Comparative statistical analysis of the release kinetics models for nanoprecipitated drug delivery systems based on poly(lactic-co-glycolic acid), PLoS One. 17 (2022) e0264825. https://doi.org/10.1371/journal.pone.0264825.

[166] P. Trucillo, Drug Carriers: A Review on the Most Used Mathematical Models for Drug Release, Processes. 10 (2022) 1094. https://doi.org/10.3390/pr10061094.

[167] Y. Zhang, M. Huo, J. Zhou, A. Zou, W. Li, C. Yao, S. Xie, DDSolver: An Add-In Program for Modeling and Comparison of Drug Dissolution Profiles, AAPS J. 12 (2010) 263–271. https://doi.org/10.1208/s12248-010-9185-1.

[168] J. Supramaniam, R. Adnan, N.H. Mohd Kaus, R. Bushra, Magnetic nanocellulose alginate hydrogel beads as potential drug delivery system, Int. J. Biol. Macromol. 118 (2018) 640–648. https://doi.org/10.1016/j.ijbiomac.2018.06.043.

[169] I. Permanadewi, A.C. Kumoro, D.H. Wardhani, N. Aryanti, Modelling of controlled drug release in gastrointestinal tract simulation, J. Phys. Conf. Ser. 1295 (2019) 012063. https://doi.org/10.1088/1742-6596/1295/1/012063.

[170] I.S. Bayer, Controlled Drug Release from Nanoengineered Polysaccharides, Pharmaceutics. 15 (2023) 1364. https://doi.org/10.3390/pharmaceutics15051364.

[171] S.C. Basak, K.S. Kumar, M. Ramalingam, Design and release characteristics of sustained release tablet containing metformin HCl, Rev. Bras. Ciências Farm. 44 (2008) 477–483.

[172] W. Wang, Y. Zhao, B.-B. Yan, L. Dong, Y. Lu, S.-H. Yu, Calcium carbonate-doxorubicin@silica-indocyanine green nanospheres with photo-triggered drug delivery enhance cell killing in drug-resistant breast cancer cells, Nano Res. 11 (2018) 3385–3395. https://doi.org/10.1007/s12274-017-1950-3.

[173] & S.N.B. Curtis, Helena, Biology, 5th editio, Worth Publishers, New York, 1989.

[174] R. Hine, “Membrane.” The Facts on File Dictionary of Biology, 3rd editio, Checkmark, New York, n.d.

[175] H. Hou, L. Chen, H. He, L. Chen, Z. Zhao, Y. Jin, Fine-tuning the LSPR response of

gold nanorod-polyaniline core-shell nanoparticles with high photothermal efficiency for cancer cell ablation, J. Mater. Chem. B. 3 (2015) 5189–5196. https://doi.org/10.1039/c5tb00556f.

[176] M. Farokhi, F. Mottaghitalab, M.R. Saeb, S. Thomas, Functionalized theranostic nanocarriers with bio-inspired polydopamine for tumor imaging and chemo-photothermal therapy, J. Control. Release. 309 (2019) 203–219. https://doi.org/10.1016/j.jconrel.2019.07.036.

[177] Z.-H. Miao, H. Wang, H. Yang, Z.-L. Li, L. Zhen, C.-Y. Xu, Intrinsically Mn 2+ -Chelated Polydopamine Nanoparticles for Simultaneous Magnetic Resonance Imaging and Photothermal Ablation of Cancer Cells, ACS Appl. Mater. Interfaces. 7 (2015) 16946–16952. https://doi.org/10.1021/acsami.5b06265.

[178] N. Xu, A. Hu, X. Pu, J. Li, X. Wang, J. Wang, Z. Huang, X. Liao, G. Yin, Fe(III)-Chelated Polydopamine Nanoparticles for Synergistic Tumor Therapies of Enhanced Photothermal Ablation and Antitumor Immune Activation, ACS Appl. Mater. Interfaces. 14 (2022) 15894–15910. https://doi.org/10.1021/acsami.1c24066.

[179] D. Hu, C. Liu, L. Song, H. Cui, G. Gao, P. Liu, Z. Sheng, L. Cai, Indocyanine green–loaded polydopamine–iron ions coordination nanoparticles for photoacoustic/magnetic resonance dual-modal imaging-guided cancer photothermal therapy, Nanoscale. 8 (2016) 17150–17158. https://doi.org/10.1039/C6NR05502H.

[180] W.D. Callister Jr, D.G. Rethwisch, Materials Science and Engineering - An introduction, 10th ed., 2018.

[181] A.A. Kaufman, R.O. Hansen, R.L.K. Kleinberg, Chapter 6 Paramagnetism, Diamagnetism, and Ferromagnetism, in: Methods Geochemistry Geophys., 2008: pp. 207–254. https://doi.org/10.1016/S0076-6895(08)00006-1.

[182] M.S. Blois, A.B. Zahlan, J.E. Maling, Electron Spin Resonance Studies on Melanin, Biophys. J. 4 (1964) 471–490. https://doi.org/10.1016/S0006-3495(64)86797-7.

[183] M. Rohrer, H. Bauer, J. Mintorovitch, M. Requardt, H.-J. Weinmann, Comparison of Magnetic Properties of MRI Contrast Media Solutions at Different Magnetic Field Strengths, Invest. Radiol. 40 (2005) 715–724. https://doi.org/10.1097/01.rli.0000184756.66360.d3.

[184] X. Ding, J. Liu, J. Li, F. Wang, Y. Wang, S. Song, H. Zhang, Polydopamine coated manganese oxide nanoparticles with ultrahigh relaxivity as nanotheranostic agents for magnetic resonance imaging guided synergetic chemo-/photothermal therapy, Chem. Sci. 7 (2016) 6695–6700. https://doi.org/10.1039/c6sc01320a.

[185] Z. Wang, F. Carniato, Y. Xie, Y. Huang, Y. Li, S. He, N. Zang, J.D. Rinehart, M. Botta, N.C. Gianneschi, High Relaxivity Gadolinium-Polydopamine Nanoparticles, Small. 13 (2017) 1–7. https://doi.org/10.1002/smll.201701830.

[186] S. Zhou, Z. Cui, J. Urban, Dead cell counts during serum cultivation are underestimated by the fluorescent live/dead assay, Biotechnol. J. 6 (2011) 513–518. https://doi.org/10.1002/biot.201000254.

[187] P. Cappella, F. Gasparri, M. Pulici, J. Moll, A novel method based on click chemistry, which overcomes limitations of cell cycle analysis by classical determination of BrdU incorporation, allowing multiplex antibody staining, Cytom. Part A. 73A (2008) 626–

636. https://doi.org/10.1002/cyto.a.20582.

[188] J. Zhang, Y. Miao, W. Ni, H. Xiao, J. Zhang, Cancer cell membrane coated silica nanoparticles loaded with ICG for tumour specific photothermal therapy of osteosarcoma, Artif. Cells, Nanomedicine, Biotechnol. 47 (2019) 2298–2305. https://doi.org/10.1080/21691401.2019.1622554.

[189] D. Wang, C. Liu, S. You, K. Zhang, M. Li, Y. Cao, C. Wang, H. Dong, X. Zhang, Bacterial Vesicle-Cancer Cell Hybrid Membrane-Coated Nanoparticles for Tumor Specific Immune Activation and Photothermal Therapy, ACS Appl. Mater. Interfaces. 12 (2020) 41138–41147. https://doi.org/10.1021/acsami.0c13169.

[190] L. Rao, L.L. Bu, B. Cai, J.H. Xu, A. Li, W.F. Zhang, Z.J. Sun, S.S. Guo, W. Liu, T.H. Wang, X.Z. Zhao, Cancer Cell Membrane-Coated Upconversion Nanoprobes for Highly Specific Tumor Imaging, Adv. Mater. 28 (2016) 3460–3466. https://doi.org/10.1002/adma.201506086.

[191] R.H. Fang, C.-M.J. Hu, B.T. Luk, W. Gao, J.A. Copp, Y. Tai, D.E. O'Connor, L. Zhang, Cancer Cell Membrane-Coated Nanoparticles for Anticancer Vaccination and Drug Delivery, Nano Lett. 14 (2014) 2181–2188. https://doi.org/10.1021/nl500618u.

[192] E. Millipore, Precise and Accurate Counts and Viability Measurements Across Multiple Cell Lines Using the Muse^{TM} Cell Count & Viability Assay, Biotechniques. 52 (2012) 200–203. https://doi.org/10.2144/000113827.

[193] Y. Xin, M. Yin, L. Zhao, F. Meng, L. Luo, Recent progress on nanoparticle-based drug delivery systems for cancer therapy, Cancer Biol. Med. 14 (2017) 228–241. https://doi.org/10.20892/j.issn.2095-3941.2017.0052.

[194] R.E. Nicoletto, C.M. Ofner, Cytotoxic mechanisms of doxorubicin at clinically relevant concentrations in breast cancer cells, Cancer Chemother. Pharmacol. 89 (2022) 285–311. https://doi.org/10.1007/s00280-022-04400-y.

[195] P. Ngamwongsatit, P.P. Banada, W. Panbangred, A.K. Bhunia, WST-1-based cell cytotoxicity assay as a substitute for MTT-based assay for rapid detection of toxigenic Bacillus species using CHO cell line, J. Microbiol. Methods. 73 (2008) 211–215. https://doi.org/10.1016/j.mimet.2008.03.002.

[196] X. Xie, H. Wang, G.R. Williams, Y. Yang, Y. Zheng, J. Wu, L.-M. Zhu, Erythrocyte Membrane Cloaked Curcumin-Loaded Nanoparticles for Enhanced Chemotherapy, Pharmaceutics. 11 (2019) 429. https://doi.org/10.3390/pharmaceutics11090429.

[197] C. Xu, W. Liu, Y. Hu, W. Li, W. Di, Bioinspired tumor-homing nanoplatform for co-delivery of paclitaxel and siRNA-E7 to HPV-related cervical malignancies for synergistic therapy, Theranostics. 10 (2020) 3325–3339. https://doi.org/10.7150/thno.41228.

[198] J. Lu, L. Cai, Y. Dai, Y. Liu, F. Zuo, C. Ni, M. Shi, J. Li, Polydopamine-Based Nanoparticles for Photothermal Therapy/Chemotherapy and their Synergistic Therapy with Autophagy Inhibitor to Promote Antitumor Treatment, Chem. Rec. 21 (2021) 781–796. https://doi.org/10.1002/tcr.202000170.

[199] D.C. Phung, H.T. Nguyen, T.T. Phuong Tran, S.G. Jin, C.S. Yong, D.H. Truong, T.H. Tran, J.O. Kim, Combined hyperthermia and chemotherapy as a synergistic anticancer treatment, J. Pharm. Investig. 49 (2019) 519–526. https://doi.org/10.1007/s40005-019-

00431-5.

[200] S. Cho, W. Park, D.-H. Kim, Silica-Coated Metal Chelating-Melanin Nanoparticles as a Dual-Modal Contrast Enhancement Imaging and Therapeutic Agent, ACS Appl. Mater. Interfaces. 9 (2017) 101–111. https://doi.org/10.1021/acsami.6b11304.

[201] H. Wang, G.R. Williams, X. Xie, M. Wu, J. Wu, L.-M. Zhu, Stealth Polydopamine-Based Nanoparticles with Red Blood Cell Membrane for the Chemo-Photothermal Therapy of Cancer, ACS Appl. Bio Mater. 3 (2020) 2350–2359. https://doi.org/10.1021/acsabm.0c00094.

[202] X. Mu, J. Li, S. Yan, H. Zhang, W. Zhang, F. Zhang, J. Jiang, Controlled Release and Delivery Systems siRNA delivery with stem cell membrane-coated magnetic nanoparticles for imaging-guided photothermal therapy and gene therapy siRNA Delivery with Stem Cell Membrane-Coated Magnetic Nanoparticles for Imaging-Guided P, (2018). https://doi.org/10.1021/acsbiomaterials.8b00858.

[203] E.G. Russell, T.G. Cotter, New Insight into the Role of Reactive Oxygen Species (ROS) in Cellular Signal-Transduction Processes, Elsevier Ltd, 2015. https://doi.org/10.1016/bs.ircmb.2015.07.004.

[204] M. Volkova, R. Russell, Anthracycline Cardiotoxicity: Prevalence, Pathogenesis and Treatment, Curr. Cardiol. Rev. 7 (2012) 214–220. https://doi.org/10.2174/157340311799960645.

[205] C. Mei, N. Wang, X. Zhu, K.-H. Wong, T. Chen, Photothermal-Controlled Nanotubes with Surface Charge Flipping Ability for Precise Synergistic Therapy of Triple-Negative Breast Cancer, Adv. Funct. Mater. 28 (2018) 1805225. https://doi.org/10.1002/adfm.201805225.

[206] P.T. Schumacker, Reactive Oxygen Species in Cancer: A Dance with the Devil, Cancer Cell. 27 (2015) 156–157. https://doi.org/10.1016/j.ccell.2015.01.007.

[207] Z. Zhou, J. Song, L. Nie, X. Chen, Reactive oxygen species generating systems meeting challenges of photodynamic cancer therapy, Chem. Soc. Rev. 45 (2016) 6597–6626. https://doi.org/10.1039/C6CS00271D.

[208] S.J. Dixon, K.M. Lemberg, M.R. Lamprecht, R. Skouta, E.M. Zaitsev, C.E. Gleason, D.N. Patel, A.J. Bauer, A.M. Cantley, W.S. Yang, B. Morrison, B.R. Stockwell, Ferroptosis: An Iron-Dependent Form of Nonapoptotic Cell Death, Cell. 149 (2012) 1060–1072. https://doi.org/10.1016/j.cell.2012.03.042.

[209] S.J. Dixon, B.R. Stockwell, The role of iron and reactive oxygen species in cell death, Nat. Chem. Biol. 10 (2014) 9–17. https://doi.org/10.1038/nchembio.1416.

[210] R.H. Fang, A. V. Kroll, W. Gao, L. Zhang, Cell Membrane Coating Nanotechnology, Adv. Mater. 30 (2018) 1706759. https://doi.org/10.1002/adma.201706759.

[211] D. Nie, Z. Dai, J. Li, Y. Yang, Z. Xi, J. Wang, W. Zhang, K. Qian, S. Guo, C. Zhu, R. Wang, Y. Li, M. Yu, X. Zhang, X. Shi, Y. Gan, Cancer-Cell-Membrane-Coated Nanoparticles with a Yolk–Shell Structure Augment Cancer Chemotherapy, Nano Lett. 20 (2020) 936–946. https://doi.org/10.1021/acs.nanolett.9b03817.

[212] Y. Ren, C. Miao, L. Tang, Y. Liu, P. Ni, Y. Gong, H. Li, F. Chen, S. Feng, Homotypic Cancer Cell Membranes Camouflaged Nanoparticles for Targeting Drug Delivery and Enhanced Chemo-Photothermal Therapy of Glioma, Pharmaceuticals. 15 (2022) 157.

https://doi.org/10.3390/ph15020157.

[213] M. Chen, M. Chen, J. He, Cancer cell membrane cloaking nanoparticles for targeted co-delivery of doxorubicin and PD-L1 siRNA, Artif. Cells, Nanomedicine, Biotechnol. 47 (2019) 1635–1641. https://doi.org/10.1080/21691401.2019.1608219.

[214] A.K. Jain, S. Thareja, In vitro and in vivo characterization of pharmaceutical nanocarriers used for drug delivery, Artif. Cells, Nanomedicine, Biotechnol. 47 (2019) 524–539. https://doi.org/10.1080/21691401.2018.1561457.

[215] I.J. Fidler, Rationale and methods for the use of nude mice to study the biology and therapy of human cancer metastasis, Cancer Metastasis Rev. 5 (1986) 29–49. https://doi.org/10.1007/BF00049529.

[216] W.M. van Weerden, J.C. Romijn, Use of nude mouse xenograft models in prostate cancer research, Prostate. 43 (2000) 263–271. https://doi.org/10.1002/1097-0045(20000601)43:4<263::AID-PROS5>3.0.CO;2-I.

[217] F. Liu, X. He, J. Zhang, H. Chen, H. Zhang, Z. Wang, Controllable synthesis of polydopamine nanoparticles in microemulsions with pH-activatable properties for cancer detection and treatment, J. Mater. Chem. B. 3 (2015) 6731–6739. https://doi.org/10.1039/C5TB01159K.

[218] Y.-C. Chuang, C.-J. Lin, S.-F. Lo, J.-L. Wang, S.-C. Tzou, S.-S. Yuan, Y.-M. Wang, Dual functional AuNRs@MnMEIOs nanoclusters for magnetic resonance imaging and photothermal therapy, Biomaterials. 35 (2014) 4678–4687. https://doi.org/10.1016/j.biomaterials.2014.02.026.

[219] H. Green, S. Crockett, D. Martyshkin, K. Singh, W. Grizzle, E. Rosenthal, S. Mirov, A histological evaluation and in vivo assessment of intratumoral near infrared photothermal nanotherapy-induced tumor regression, Int. J. Nanomedicine. 9 (2014) 5093. https://doi.org/10.2147/IJN.S60648.

[220] C. Ayala-Orozco, C. Urban, M.W. Knight, A.S. Urban, O. Neumann, S.W. Bishnoi, S. Mukherjee, A.M. Goodman, H. Charron, T. Mitchell, M. Shea, R. Roy, S. Nanda, R. Schiff, N.J. Halas, A. Joshi, Au Nanomatryoshkas as Efficient Near-Infrared Photothermal Transducers for Cancer Treatment: Benchmarking against Nanoshells, ACS Nano. 8 (2014) 6372–6381. https://doi.org/10.1021/nn501871d.

PUBLICATIONS AND CONFERENCES

- **PUBLICATIONS RELATED TO THIS WORK**

Bigaj-Jozefowska, M.J., Grzeskowiak, B. F., *Polymeric nanoparticles wrapped in biological membranes for targeted anticancer treatment*. European Polymer Journal, 2022, 176: 111427. DOI: 10.1016/j.eurpolymj.2022.111427

Submitted: Bigaj-Jozefowska, M.J., et al., *Biomimetic theranostic nanoparticles for effective anticancer therapy and MRI imaging*

In preparation: Bigaj-Jozefowska, M.J., et al., *Three musketeers of PDA-based paramagnetic nanoparticles for MRI contrasting*

- **OTHER PUBLICATIONS**

Sultanov, Fail, et al. Influence of Metal Oxide Particles on Bandgap of 1D Photocatalysts Based on SrTiO3/PAN Fibers. Nanomaterials, 2020, 10.9: 1734. DOI: 10.3390/nano10091734

Sultanov, Fail, et al. Aligned composite SrTiO3/PAN fibers as 1D photocatalyst obtained by electrospinning method. Chemical Physics Letters, 2019, 737: 136821. DOI: 10.1016/j.cplett.2019.136821

- **CONFERENCES**

Nanotech Poland 2023, 14-16 June 2023, Poznań, Poland
Oral presentation: *In Vitro Study of Biomimetic and Paramagnetic Nanoparticles for Targeted Treatment of Liver Cancer*
M. J. Bigaj-Józefowska, K. Załęski, T. Zalewski, B. F. Grześkowiak
★1st prize for the best oral presentation within the Young Researchers Forum

7th International Conference on Multi-functional, Hybrid and Nanomaterials 2022, 19-22 October 2022, Genoa, Italy
Poster: *Biomimetic paramagnetic nanoparticles for advanced treatment of liver cancer*
M. J. Bigaj-Józefowska, E. L. Coy, K. Załęski, R.Mrówczyński, B. F. Grześkowiak

6th International Soft Matter Conference 2022, 19-23 September 2022, Poznań, Poland
Oral presentation*: Paramagnetic porous PDA nanoparticles for combined therapy and imaging of liver cancer*
M. J. Bigaj-Józefowska, E. L. Coy, K. Załęski, T. Zalewski, R. Mrówczyński, B. F. Grześkowiak

11th International Colloids Conference, 12-15 June 2022, Lisbon, Portugal
Poster: Cancer c*ell-membrane coated mesoporous polydopamine NPs for multimodal therapy of hepatocellular carcinoma*,
M. J. Bigaj-Józefowska, E.L. Coy, K. Załęski, R. Mrówczyński, B. F. Grześkowiak

Nanotech Poland 2022, 1-3 June 2022, Poznań, Poland
Oral presentation: *Superior antitumor properties of multimodal biomimetic doxorubicin-loaded PDA-Fe nanoparticles*,
M. J. Bigaj-Józefowska, E. L. Coy, K. Załęski, B. F. Grześkowiak
★Distinction for the oral presentation within the Young Researchers Forum

Nanotech Poland 2022, 1-3 June 2022, Poznań, Poland
Oral presentation: *Cell membrane coated polymeric nanoparticles for targeted anticancer therapy*,
M. J. Bigaj-Józefowska, B. F. Grześkowiak

NanoMedicine International Conference 2021, 20-22 October 2021, Milan, Italy
Poster: *In vitro evaluation of biomimetic nanoparticles for liver cancer treatment*
M. J. Bigaj-Józefowska, E. L. Coy, M. Grabowska, S. Jurga, B. F. Grześkowiak

3rd International Workshop on Functional Nanostructured Materials, 6-8 October 2021, Kraków, Poland
Poster, rapid presentation: *The synergistic strategy of hepatocellular carcinoma treatment based on membrane-coated biomimetic nanoparticles*
M. J. Bigaj-Józefowska, E. L. Coy, M. Grabowska, S. Jurga, B. F. Grześkowiak

Nanotech Poland 2021, 9-11 June 2021, Poznań, Poland
Oral presentation: *Targeted drug delivery system based on biomimetic coating for synergistic liver cancer treatment*
M. J. Bigaj-Józefowska, B. F. Grześkowiak